

# ATMOSPHERIC PROCESSING OF AEROSOLS

NICHOLAS MARK DAVIDSON



A thesis submitted to the University of Birmingham for the degree of DOCTOR OF PHILOSOPHY

Environmental Health and Risk Management  
School of Geography, Earth & Environmental Sciences  
College of Life & Environmental Sciences  
University of Birmingham  
September 2017

UNIVERSITY OF  
BIRMINGHAM

**University of Birmingham Research Archive**

**e-theses repository**

This unpublished thesis/dissertation is copyright of the author and/or third parties. The intellectual property rights of the author or third parties in respect of this work are as defined by The Copyright Designs and Patents Act 1988 or as modified by any successor legislation.

Any use made of information contained in this thesis/dissertation must be in accordance with that legislation and must be properly acknowledged. Further distribution or reproduction in any format is prohibited without the permission of the copyright holder.

## Acknowledgements

First and foremost I would like to thank my supervisors, Francis Pope and Zongbo Shi, for granting me the opportunity to learn and to carry out this research, and for their continual guidance, expertise and patience over the last four years. Thanks to the National Environmental Research Council for funding it. Thanks also to Bill Bloss and Eugenia Valsami-Jones for the use of their lab space.

Thanks to the lab managers and researchers who facilitated my analytical work, including Maria Thompson, Eimear Orgill, Jackie Deans, Richard Johnson, Steve Baker, Chris Stark, Christine Elgy, Michala Pettitt and Paul Stanley. Thanks also to Konstantin Ignatyev, Jörg Göttlicher and Ralph Steininger who guided our work at the Diamond and ANKA synchrotrons, and to Andy Ward, Benji Bateman and Stan Botchway for their guidance and expertise at the Central Laser Facility. Additional thanks to the Science and Technology Research Council for the use of their facilities.

Thanks to post-doctoral researchers Leigh Crilley and Louisa Kramer for their help, guidance and expertise during the design and use of my simulated atmospheric processing chamber, and to Steve West in the workshop for turning our schematics into a functional device.

Thanks to Clare Fitzgerald, Thanos Athanasiadis, Rosalie Shepherd and Peter Gallimore for the opportunities to co-operate and contribute to research at the Central Laser Facility, to Martin King and Markus Kalberer for their guidance there and Marina Kuimova for her oversight and expertise.

Thanks to all the students I worked beside at Birmingham and all the times they acted as sounding board, idea filter or extra pair of hands, including but not limited to Zhe Tian, Ajit Singh, Marliyyah Mahmoud, Jenny Kirby, Pallavi Pant, Adam, Fatima, Laura, Isabella, Tassos, Emily, Max, Ying, Tony, Ian, Paul, Clemens, Uzoma, Alice, Vicki, Becky, Katie, Sam, Helen, James and Steven.

Thanks to Bruce Ravel, the SLIM curve team, and all the creators of specialised software whose time, dedication and expertise make research like mine possible.

Last but certainly not least, thanks to my parents, Marion and Neil, for supporting me and keeping my chin up throughout the writing of this thesis, and to all my old friends back home and the new friends I've made in Birmingham since 2013.

And you know what? Thank *you*, anyone who's read down this far. I appreciate it.

## Contents

Introduction .....	1
Chapter 1 Iron speciation in source and ambient aerosol samples using X-ray Absorbance Near-Edge Spectroscopy.....	3
1. Introduction .....	3
2. Methods and Materials.....	4
2.1 Synchrotron Preparations.....	4
2.2 Iron Standards.....	4
2.3 Sample List .....	6
2.4 X-ray Absorbance Near-Edge Structure .....	9
2.5 Synchrotron Facilities.....	11
2.6 Analysis Software.....	11
2.7 Linear Combination Fitting.....	13
2.8 Sample Preparation for Standard Addition.....	15
2.9 Sample Preparation for Beamline Exposure .....	15
3. Results and discussion .....	16
3.1a Contrast Between Standards .....	16
3.1b Comparing and Contrasting Standards by Linear Combination Fit.....	17
3.2 Standard Addition .....	20
3.3 Mineral Dust Precursors .....	26
3.4 Further Mineral Dust & Haze Samples.....	29
3.5 Particulate Aerosol Samples: Beijing .....	32
3.6 Particulate Aerosol Samples: Ji'nan dust storm.....	35
3.7 Particulate Aerosol Samples: Bermuda & Loess Plateau .....	38
3.8 Soil Samples: Libya .....	42
3.9 Soil Samples: Bodélé Depression .....	45
3.10 Natural mineral sample overview.....	47
3.11 Ship emitted particles .....	48
3.12 Particles from Biomass Burning .....	53
4. Summary and future work .....	62
Works Cited.....	63
Chapter 2 Analysis of chloride in particles produced from a model diesel engine .....	69
1. Introduction .....	69
1.1 Tropospheric importance of chloride .....	69

1.2 Sources of tropospheric chloride .....	69
2. Methods and Materials.....	71
2.1 Sample collection .....	71
2.2 Synchrotron analysis .....	71
2.3 Scanning Electron Microscopy with Energy Dispersive X-ray Spectroscopy (SEM-EDX) .....	71
2.4 Software .....	71
3. Results .....	72
3.1 X-ray Absorbance Near Edge Structure (XANES) comparisons.....	72
3.2 Scanning Electron Microscopy with Energy Dispersive X-ray Spectroscopy (SEM-EDX) .....	73
3.3 X-Ray Fluorescence Map.....	75
4. Discussion.....	77
5. Summary and further work.....	78
Works Cited.....	79
Chapter 3 Atmospheric Processing of iron in Coal Fly Ash .....	82
1. Introduction .....	82
2. Methods and materials .....	84
2.1 Coal Fly Ash samples: .....	84
2.2 PM10 separation:.....	84
2.3 Selective extraction of soluble iron by ammonium acetate at pH 4.7.....	85
2.4 Ascorbate extraction of exchangeable iron .....	85
2.5 Timed dissolution.....	86
2.6 Colorimetric determination of soluble iron .....	86
2.7 Multi-element analysis by Inductively Coupled Plasma Mass Spectrometer (ICP-MS).....	87
2.8 Simulated Atmospheric Processing.....	87
2.9 Metal analysis of processed ash by Inductively Coupled Plasma Optical Emission Spectroscopy (ICP-OES).....	89
2.10 ICP-OES versus ICP-MS.....	89
2.11 Water-soluble cations by ion chromatography .....	89
2.12 Temperature moderation and humidity maintenance in processing chamber .....	90
2.13 Elemental Composition by X-Ray Fluorescence.....	90
2.14 X-ray Absorbance Near Edge Structure (XANES) .....	91
2.15 XANES Standards.....	91
3. Results .....	92
3.1 Elemental composition .....	92

3.2 Oxalate-promoted acid dissolution – ICP-MS analysis.....	95
3.3 Readily soluble iron quantification .....	99
3.4 Initial atmospheric processing .....	100
3.5 Water soluble ion content .....	101
3.6 X-ray Absorbance Near Edge Structure .....	103
3.7 Simulated Atmospheric Processing with Temperature/RH stabilisation.....	109
4. Discussion.....	110
4.1 Oxalate-promoted timed dissolution.....	110
4.2 Exchangeable & non-crystalline iron and siderite – ascorbate vs ammonium acetate extraction .....	110
4.3 Initial Simulated Atmospheric Processing – transition metal solubility enhancement .....	111
4.4 Initial Simulated Atmospheric Processing – ion chromatography of water leachate.....	111
4.5 Initial Simulated Atmospheric Processing – X-ray Absorbance Near Edge Structure.....	112
4.6 Simulated atmospheric processing with stabilised temperature / RH .....	114
5. Conclusions and Future Work.....	115
Works Cited.....	116
Chapter 4 Measurement of the extended refractive index of Green Fluorescent Protein via Fluorescence Lifetime Imaging Microscopy.....	121
1. Introduction .....	121
2. Methods and Materials.....	122
2.1 Calculation of RI of sucrose/water solutions under different RH conditions .....	122
2.2 Green Fluorescent Protein solutions .....	122
2.3 Sample delivery.....	124
2.4 Optical trap setup .....	125
2.5 FLIM & droplet imaging setup.....	126
2.6 Data Processing.....	126
3. Results .....	128
3.1 Dependence of inverse fluorescence lifetime on relative permittivity .....	128
3.2 Hygroscopicity and the refractive index of GFP.....	129
3.3 Droplet volume changes at different RH .....	131
4. Conclusions .....	132
Works Cited.....	133
Chapter 5 Measurement of the Raman spectra and hygroscopicity of four pharmaceutical aerosols as they travel from pressurised metered dose inhalers (pMDI) to a model lung.....	136
1. Introduction .....	136

1.1 Respiratory drugs and drug delivery .....	136
1.2 Significance of relative humidity and temperature on delivery efficiency .....	137
2. Methods and Materials.....	138
2.1 Counter propagating dual beam optical trap .....	138
2.2 Raman Spectroscopy.....	139
2.3 Lung-like Environment & Particle Imaging.....	140
2.4 pMDI injection.....	141
2.5 SEM imaging.....	141
2.6 Chemical Structures of the asthma drugs investigated .....	142
3. Results and Discussion .....	143
3.1 Thermodynamic Calculations of Particle Hygroscopicity.....	143
3.2 Drug Particle Crystallography .....	145
3.3 SEM imaging and Trapping Logistics .....	146
3.4 Raman spectrum changes from hygroscopic properties and additional compounds .....	147
3.5 Salbutamol sulfate / Salamol™ .....	147
3.6 Salmeterol xinafoate / Serevent™ .....	149
3.7 Fluticasone propionate / Flixotide .....	150
3.8 Ciclesonide / Alvesco™ .....	151
3.9 Specific advantages and limitations of procedure to drug delivery .....	152
4. Conclusions .....	153
Works Cited.....	154
Overall Summary.....	160
Appendix .....	162

*The work contained in chapter 5 has been published under the following:*

**Measurement of the Raman spectra and hygroscopicity of four pharmaceutical aerosols as they travel from pressurised metered dose inhalers (pMDI) to a model lung**

**International Journal of Pharmaceutics**, 30 March 2017, volume 520 issues 1-2, pages 59-69

N. M. Davidson, H. -J. Tong, M. Kalberer, P. C. Seville, A. D. Ward, M. K. Kuimova and F. D. Pope

*The paper as published is included in the appendix.*

## **Introduction**

The following work represents the culmination of five separate but thematically related sets of experiments involving analysis of 1 – 10  $\mu\text{m}$  scale aerosol particles and their response to the gaseous composition of the surrounding atmosphere. The majority of sample sets were analysed by the synchrotron-based technique X-ray Absorbance Near Edge Structure, or XANES, which was employed to determine the oxidation state and, where feasible, speciation of iron and chlorine compounds present therein. Samples included emissions from a model diesel engine, mineral dust gathered in geological campaigns in North Africa, South America and the Mediterranean, ambient aerosol samples collected from air quality monitoring campaigns across China and in the Caribbean, samples of soil from Libya and the unique environment of the Bodélé depression in Chad, coal fly ash from power stations, and for the first time by this technique, aerosol samples from agricultural biomass burning and from ship emissions collected close to or directly from the stacks of research vessels.

Particulates from diesel emissions collected from the exhaust stream of a model engine were found upon initial examination by X-Ray Fluorescence to contain unexpectedly high concentrations of chlorine. This led to further analysis by multiple techniques involving scanning electron microscopy, XRF mapping and XANES linear combination fitting to determine the distribution and speciation of chlorine across the samples in an effort to identify potential sources and impacts on air quality and human health.

Samples of coal fly ash were collected from three different power stations in Wales, Poland and China to be compared and contrasted. PM10 material was separated from bulk samples and exposed to a litany of chemical extraction methods to determine the potential bioavailability of various biologically significant elements. The ashes were exposed to simulated atmospheric processing in a custom made chamber to promote changes in iron speciation that may occur during real world atmospheric transport prior to deposition, specifically with regard to increases in water solubility and bioavailability.

In addition to chemical analysis and synchrotron-based techniques, analyses were also carried out on suspended aerosol particles held in optical traps to observe rapid (over the course of seconds) changes to their attributes upon raising and lowering the relative humidity of the surrounding air. Changes in the fluorescence lifetime of green fluorescent protein were monitored by Fluorescence Lifetime Imaging Microscopy as the surrounding relative humidity was raised and lowered, and the changes were plotted to construct a humidigram to predict the refractive index of green fluorescent protein outside of a liquid medium, with the aim of providing the value as a reference to researchers intending to use the protein as a marker in high refractive index media or as an aerosol tracer in its own right.

Optical trapping and humidity adjustment was also employed to examine the behaviour of four inhalable bronchodilator drugs used in the treatment of asthma and COPD, specifically the potential changes in diameter as particles with hygroscopic properties take on layers of water under high humidity conditions like the inside of the human respiratory tract. Changes were monitored by observing any changes in peak width around polar groups in the Raman spectrum. Drug particles found to have hygroscopic properties were also tested at higher temperatures to better emulate conditions within the respiratory system.

Due to the distinct nature of the samples sets and analytical techniques employed in each chapter, and the potential for each chapter to be turned into a publishable paper in the future, the chapters are formatted to be discrete and can be read in any order. Each is self-contained with its own literature review, methodology, results and discussion sections. The chapters are arranged by type so that related subjects are adjacent.

# Chapter 1 Iron speciation in source and ambient aerosol samples using X-ray Absorbance Near-Edge Spectroscopy

## 1. Introduction

Wet and dry deposition of dust is a major source of nutrients for both terrestrial (Chadwick, et al., 1999) (Balestrini, et al., 2000) (Avila, et al., 1998) (Allen, et al., 2010) and marine environments (Nenes, et al., 2011) (Herut, et al., 2016). Iron is a key micronutrient, particularly in marine environments where it is the limiting nutrient for most High Nutrient, Low Chlorophyll regions (Edwards, et al., 2004) (Pitchford & Brindley, 1999). Measuring the total iron content of dust is of limited relevance since bioavailability is dictated by speciation (Journet, et al., 2008) (Shi, et al., 2011) (Formenti, et al., 2014). Iron bound within clay particles due to isomorphous substitution is generally inaccessible to physical or biological solubilisation processes, while large crystalline iron oxide species like goethite and hematite are more readily soluble, and amorphous or poorly crystalline iron oxides and more reactive species like iron sulfates are more soluble again and thus of greatest significance from a bioavailability standpoint (Usher, et al., 2003).

The solubility of Fe in atmospheric aerosol particles is largely determined by its speciation (Schroth, et al., 2009). Iron sulfate is highly water soluble and is thus considered readily bioavailable. Ferrihydrite is considered partially bioavailable to eukaryotes (Nodwell & Price, 2001) while goethite and hematite are poorly bioavailable (Wells, et al., 1983) (Rich & Morel, 1990). Reactive Fe content in Saharan dust has been shown to correlate positively with Fe bioavailability in bivalves (Visser, et al., 2003), although even the most soluble dust Fe species were not as bioavailable as readily soluble species like  $\text{FeCl}_3$ .

Atmospheric processing, in this case the action of oxidising gases in the atmosphere on the surface chemistry of solid particles, can cause more of the total iron present in dust particles to become bioavailable (Majestic, et al., 2007) (Longo, et al., 2016) (Shi, et al., 2015) (Li, et al., 2017). Combustion products such as oil fly ash produced by container ships may have a high proportion of readily bioavailable iron species such as iron(III) sulfate (Schroth, et al., 2009) (Wang, et al., 2015), thus these emissions may significantly enhance the flux of bioavailable Fe to the oceans (Ito & Shi, 2016).

Methods for identifying the species of iron present in solid samples, and thus predicting the bioavailability of said iron, have included sequential extraction with select solvents (Tessler, et al., 1979) (Chao & Zhou, 1982) (Poulton & Canfield, 2005), along with in-situ analysis by techniques such as Cathodic Stripping Voltammetry (CSV) (Croot & Johansson, 1999) (Buck, et al., 2007) and X-Ray Diffraction (XRD) (Schulze, 1980). Each method has its advantages and its drawbacks- sequential extraction and CSV can accurately quantify iron by reactivity but cannot identify specific mineral phases, while XRD can qualitatively identify iron species but cannot accurately quantify them (Leslie, et al., 1990). This chapter explores the use of synchrotron-based analytical techniques in examining the distribution of iron in environmental particulate samples, as well as positively identifying the species of iron present and the relative proportion of species with a single scan.

## 2. Methods and Materials

### 2.1 Synchrotron Preparations

Some analytical techniques prior to or following synchrotron analysis can be advantageous and can streamline data processing:

- Field study: understanding the parent material around the sample and mineral species likely to be present can guide the application of suitable standards for fitting (see section 2.7)
- X-Ray Fluorescence: XRF can quantify the total content of a specific element in samples and add absolute values to the proportions generated by XANES fitting
- X-Ray Diffraction: XRD can verify the presence of specific chemical species identified by XANES fitting
- Sequential extraction: chemical extraction of transition metals in different extractants targeted at specific mineral phases followed by quantification by ICP or colorimetry can also act as confirmation of mineral species identification by XANES fitting

A combination of XRF, XRD and sequential extraction can achieve similar results to even well calibrated XANES analysis, but XANES has three major advantages over them:

- 1) Sample throughput. A XANES spectrum can be generated in 10-20 minutes depending on desired resolution. A single researcher can prepare and run more than 70 samples in one 24 hour beamline session, while other techniques require extensive preparation and handling
- 2) Sample size. A viable XANES spectrum can be generated from a few micrograms of solid material as long as it contains the elements in question in parts per million concentrations or higher, while chemical extraction can require much larger sample masses to yield quantifiable results
- 3) Synchrotrons are cool. A synchrotron is a vast facility filled with equipment and scenery that would look good on the cover of any scientific journal, and synchrotron-based techniques produce visually interesting data. This factor is rarely acknowledged in research outcomes but to ignore it entirely would be disingenuous.

### 2.2 Iron Standards

11 iron standards (Table 1) were prepared to compare against the environmental particulate standards. The iron oxide standards (goethite, hematite, ferrihydrite and magnetite) were synthesised by Leeds University. The ferrous and Ferric sulfate standards were purchased as 99% purity powders from Sigma Aldrich. The clay (illite, illite-smectite mixed layer, Na-rich Montmorillonite and chlorite) and feldspar standards were purchased from the Clay Minerals Society (Clay Minerals Society, 2017).

Table 1 Iron mineral standards including chemical &amp; structural characteristics

Standard	Repeating unit	Crystal structure	% Fe	%Fe(II)	%Fe(III)
Goethite	$\alpha$ -FeOOH	Dipyramidal	62.9%	0%	100%
Hematite	$\alpha$ -Fe <sub>2</sub> O <sub>3</sub>	Rhombohedral	69.9%	0%	100%
Magnetite	Fe <sub>3</sub> O <sub>4</sub>	Hexoctahedral	77.7%	33%	67%
Ferrihydrite	Fe <sub>2</sub> O <sub>3</sub> ·½H <sub>2</sub> O	Dihexagonal pyramidal	66.2%	0%	100%
Iron(II) sulfate heptahydrate	FeSO <sub>4</sub> ·7H <sub>2</sub> O	Monoclinic	20.1%	100%	0%
Iron(III) sulfate	Fe <sub>2</sub> (SO <sub>4</sub> ) <sub>3</sub>	Trigonal hexagonal scalenohedral	27.9%	0%	100%
Illite	(Al,Mg,Fe) <sub>2</sub> (Si,Al) <sub>4</sub> O <sub>10</sub> [(OH) <sub>2</sub> , (H <sub>2</sub> O)]	2:1 layer clay	5.5%	7.7%	92.3%
Illite-smectite mixed layer	(Layers of Illite & Montmorillonite)	2:1 layer clay	0.9%	9.1%	90.9%
Montmorillonite	(Na,Ca) <sub>1/3</sub> (Al,Mg) <sub>2</sub> (Si <sub>4</sub> O <sub>10</sub> )(OH) <sub>2</sub> ·nH <sub>2</sub> O	2:1 layer clay	2.6%	9.6%	90.4%
Chlorite	(Mg,Fe) <sub>3</sub> (Si,Al) <sub>4</sub> O <sub>10</sub> (OH) <sub>2</sub> ·(Mg,Fe) <sub>3</sub> (OH) <sub>6</sub>	2:1 layer phyllosilicate	34.8%	53.5%	46.5%
Feldspar	KAISi <sub>3</sub> O <sub>8</sub>	Monoclinic (tetrahedral Fe)	0.2%	0%	100%

## 2.3 Sample List

All of the sample sets were sent to Dr Zongbo Shi (the lead scientist on our synchrotron beamline applications) from external sources. Specific source locations and conditions that were recorded are reported here, but some samples were dispatched with limited documentation. Requests to the supplying researchers yielded some more information but others did not respond and a few, such as the Chinese ship emission samples, specifically asked not to be identified. This limits the usefulness of analysis from these samples as sampling conditions cannot be established, but some information can be gleaned from comparison with other samples in the same groups.

The mineral dust samples in Table 2 were provided by Dr Nick Drake and Dr Charlie Bristow from separate sampling campaigns in North Africa. Two samples were also provided from Crete and Argentina from previous campaigns. Dust was collected from the ground and the PM10 fraction was separated and collected by resuspension. A full description of the resuspension apparatus is provided in chapter 3.

Table 2 Mineral dust samples

Date	Dust source/location	sample name	Fraction
2015	Agoufou, Hombori, Mali N15°22' W1°28'	Mali	PM10
2015	Western Sahara	W. Sahara	PM10
2015	Tibesti mountains, Libya, N25°35' E16°31'	Tibesti	PM10
2015	Bodélé Depression, Chad, N16°41' E17°47'	Bodélé	PM10
2015	Wadi al Hyatt, Libya	Libya	PM10
2015	Cave of Beasts, Egypt, N23.652954 E25.160638	Cave of Beasts	PM10
2015	Qarat paleolake, Libya, N 28.4038190 E 12.5803670	Qarat Mor Plaga	PM10
2015	Crete	Crete	
2015	Dakhla Oasis, Libya, N25.71140, E 38.81397	DAK_HLA	PM10
2015	Comodoro Rivadavia, Argentina, S45°97', W67°30'	Patagonia	PM10
2015	Chott el Djerid, Tunisia	Tunisia CD80	PM10

Haze samples from China (Table 3) were collected by Junji Cao of the Chinese Academy of Sciences and fractionated in a similar manner to the North Africa samples.

Table 3 China haze samples

Date	Dust source/location	sample name/date	Fraction
2015	Loess Plateau, China	LC10-20	PM10
2015	Loess Plateau, China	LC10-57	PM10
2015	Loess Plateau, China	LC10-74	PM10

Airborne aerosol samples from Bermuda (Table 4) were provided on filter papers by Dr Angela Milne, a postdoctoral researcher from the University of Plymouth (Fishwick, et al., 2014). There was not enough material to separate size fractions.

Table 4 Particulate aerosol samples

Date	Aerosol source/location	sample name/date	Fraction
2015	Bermuda aerosol	AER1	
2015	Bermuda aerosol	AER2	
2015	Bermuda aerosol	AER3	
2015	Bermuda aerosol	AER4	

Larger samples of aerosol particles (Table 5) were supplied by Shandong University in China.

Table 5 China aerosol samples

Date	Aerosol source/location	sample name/date	Fraction
2015	Beijing, China	09.03.2010	PM10
2015	Beijing, China	10.03.2010	PM10
2015	Beijing, China	11.03.2010	PM10
2015	Beijing, China	23.10.2014	PM2.5
2015	Beijing, China	23-24.10.2014	PM2.5
2015	Beijing, China	25-26.10.2014	PM2.5
2015	Beijing, China	08.11.2014	PM2.5
2015	Ji'nan, China	Win-2_dust	PM10
2015	Ji'nan, China	Win-3_dust	PM10
2015	Ji'nan, China	Win-5_dust	PM10
2015	Ji'nan, China	Win-8_dust	PM10
2015	Ji'nan, China	Win-20_dust	PM10

Samples of topsoil were collected by Professor Nick Drake of King's College, London, during a campaign at Wadi al Ramlah in Libya (Table 6).

Table 6 Libya soil samples

Date	Soil source/location	Sample name	Fraction
2015	Libya, near main channel of river	Soil 1	PM20
2015	Libya, Fine grained fluvial sediment; overban flood deposit, deposited in an embankment	Soil 2	PM20
2015	Libya, Fine sediment deposited in main channel	Soil 3	PM20
2015	Libya, Vegetated inland in etc middle of the main channel	Soil 4	PM20
2015	Libya, Soil next to main channel at soil 4	Soil 5	PM20
2015	Libya, Crust pellet trapped in mall gully created by runoff into northern channel ground on lake	Soil 6	PM20
2015	Libya, Active channel of EC meclili delta. Ploughed flied, dust seen	Soil 7	PM20
2015	Libya, Sand on alive delta surface, same surface as soils	Soil 8	PM20
2015	Libya, Soili in headwaters of vain	Soil 9	PM20
2015	Libya, Channel sediments in headwaters of the vain	Soil 10	PM20

Professor Charlie Bristow from Birkbeck, University of London collected samples from the Bodélé depression in Chad (Bristow, et al., 2009) (Table 7). The Bodélé samples were size-separated by sieving rather than resuspension and thus have a larger particle size than the aerosol samples.

Table 7 Bodélé soil/sediment samples

Date	Soil source/location	Sample name	Fraction
2015	Bodélé, Dark Dune Quartz Sand and diatomite	CH8	PM63
2015	Bodélé, Diatomite	CH10	PM63
2015	Bodélé, Diatomite with Fe	CH19	PM63
2015	Bodélé, Diatomie with clay distal Angamma	CH34	PM63
2015	Bodélé, Angama Delta mudstone	CH39	PM63
2015	Bodélé, Delta muds Bahrel Qhcical kaolinite	CH62	PM63

Particulate emissions from ship stacks (Table 8) were collected by Dr Jana Moldanová in two sampling campaigns off the coast of Norway and Sweden (Moldanova, et al., 2009). Further samples were provided by Chinese research vessels that asked not to be identified.

Table 8 Ship emission samples

Date	Ship emission source/location	sample name/date	Fraction
2015	Ship B, Moldanová (Sweden)	IVL380199	
2015	Ship T, Moldanová (Norway)	1026T1	PM10
2015	Ship G, Moldanová (Norway)	342527_ship	PM10
2015	Ship B, Moldanová (Sweden)	poly3_sonic	
2016	Ship B, Moldanová (Sweden)	poly4_ship	
2016	Ship emitted (China)	CB_116P_ship – hotspot	
2016	Ship emitted (China)	CB_116P_ship – background	
2016	Ship emitted (China)	Ship_Chao	

Samples of ash from biomass burning (Table 9) were collected by Dr Adewale Taiwo's research group at the Federal University of Agriculture in Abeokuta, Nigeria. No identifying information could be provided on the nature of the samples beyond their collection in 2016 from natural burning events in savannah, farmland and forested areas in the area surrounding Abeokuta.

Table 9 Biomass burning samples

Date	Biomass Burning Source/location	sample name
2016	Nigerian field BB	ZS5
2016	Nigerian field BB	ZS11
2016	Nigerian field BB	ZS12
2016	Nigerian field BB	ZS13
2016	Nigerian field BB	ZS15
2016	Nigerian field BB	ZB5
2016	Nigerian field BB	ZB15
2016	Nigerian field BB	ZB18_forestfire
2016	FUA Lab-based sampling	Cornstalk_flaming
2016	FUA Lab-based sampling	Cornstalk_smouldering

All samples were stored in sealed containers in the dark at room temperature.

## 2.4 X-ray Absorbance Near-Edge Structure

X-ray Absorbance Near-Edge Structure (XANES) spectroscopy is a synchrotron-based analytical technique. The intense x-ray photon exposure generates a detailed absorbance spectrum for specific elements within samples, which can be compared against standards to identify and, to an extent, quantify the different species based on subtle changes to x-ray absorbance from the influence of oxidation state and the identity and arrangement of heteroatoms (Bianconi, 1980) (Hicks, 2015).

X-ray absorbance occurs when photons transferring sufficient energy to electrons to elevate the electron from a lower energy level to a higher level when the energy imparted matches the binding energy of a particular electron shell (Hirayama, 2000). The absorption cross section (the probability of an absorption event occurring) varies with the inbound photon's kinetic energy, decreasing with increasing photon energy up to the energy equivalent to the binding energy of the innermost 1s electron shell (known as a K-transition in Siegbahn notation (Jenkins, et al., 1991) where the probability rises sharply. Figure 1 shows the absorption cross section of iron with increasing photon energy, produced by NIST's Physical Measurement Laboratory (Chantler, et al., 2005) with the K-transition region highlighted at around 7100 eV.

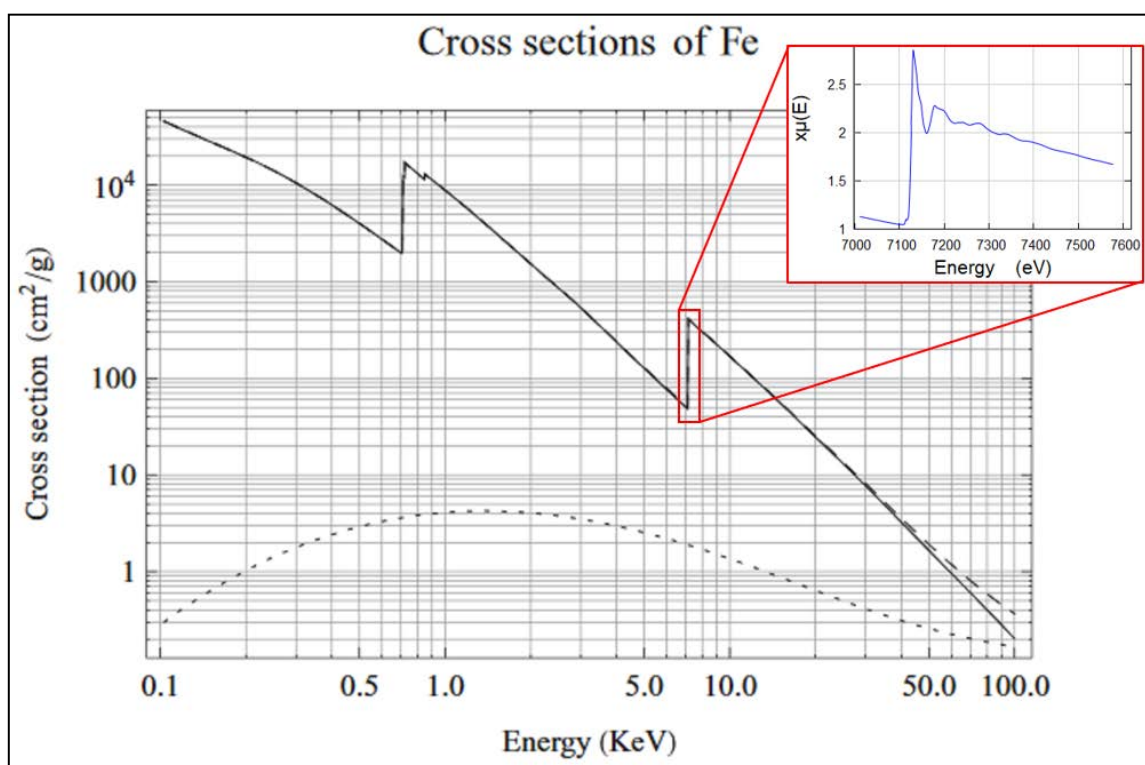


Figure 1 Plot of photon energy versus absorption cross-section (the possibility of a photon being absorbed) for iron, from Chantler et al's "X-ray Form Factor, Attenuation and Scattering Tables". Photoelectric absorption cross section is represented by the solid line, scattering by the dotted line, and total cross section by the dashed line. The XANES spectrum of the iron oxide mineral goethite is used to illustrate the fine structure of the K-transition at 7100 eV.

Figure 2 shows a normalised Fe XANES spectrum of goethite, a common iron oxide mineral. In each spectrum the x axis  $Energy/eV$  shows the range of emission energy from the beamline in electron volts, and the y axis  $x\mu(E)$  plots the relative intensity in terms of energy at the detector. The 7000 – 7300 eV range covers K-transitions for iron, where electrons are excited in the 1s orbital and shifted to higher orbitals.

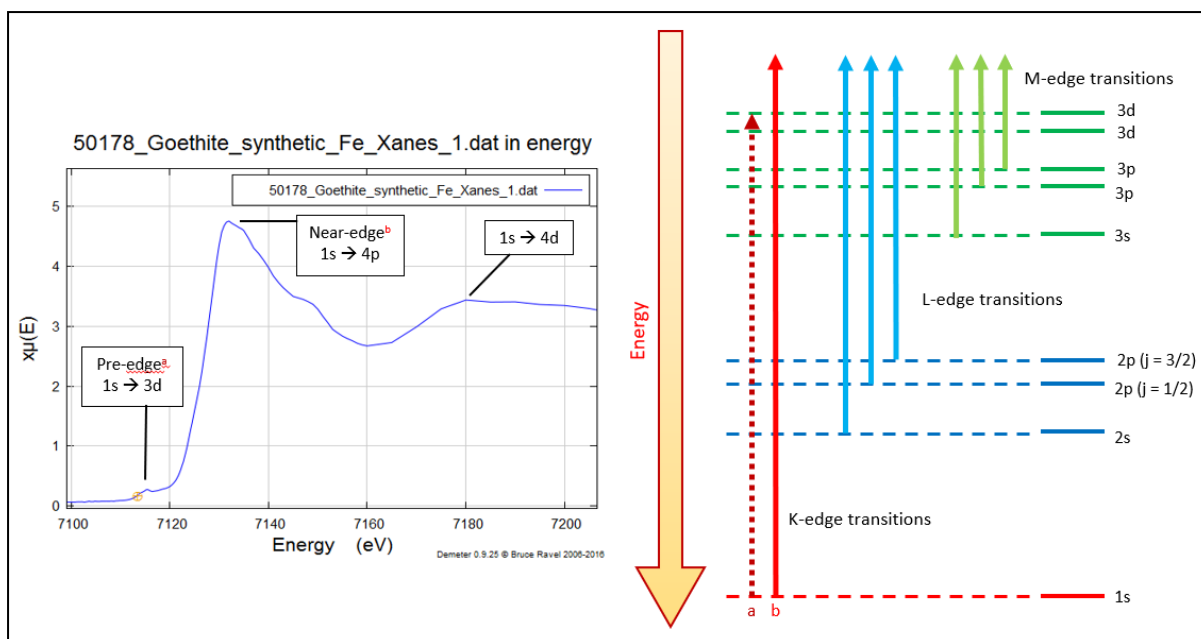


Figure 2 K-edge XANES spectrum of the iron oxide mineral goethite with the peak regions tagged by specific electron transition (left), and an energy level diagram plotting the transitions (right).

Upon excitation by an x-ray photon, electrons in the 1s shell of an iron atom can be promoted to either the unfilled 3d shell, a transition that appears as pre-edge peaks at around 7113eV, or further to the 4p shell- the latter transition appearing as a series of overlapping near-edge peaks at 7120-7140 eV (George & Pickering, 2006). Different species of heteroatom shift relative peak height and oxidation state influences the energy of each peak, with Fe(III) compound transitions shifted to higher energy by 2-3 eV (Westre, et al., 1997) (Wilke, et al., 2001). Co-ordination of heteroatoms influences both the number and intensity of allowable electron transitions (Roe, et al., 1984) (Randall, et al., 1995) which causes scattering effects in the resulting signals which split what would be one transition for an isolated atom into a series of gaussian peaks (figure 3).

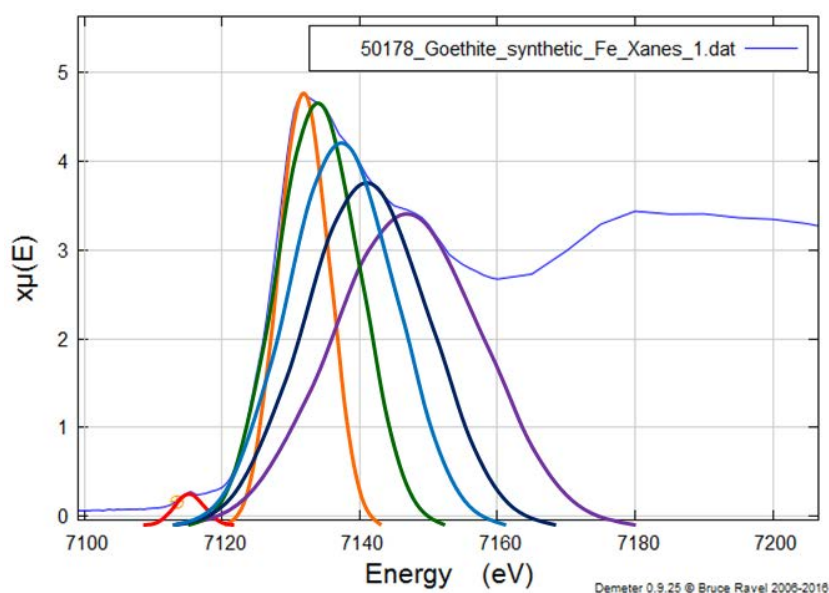


Figure 3 The XANES spectrum of goethite, with the pre-edge 1s-3d (red) and near edge 1s-4p (orange-violet) electron transitions visually distinguished. The 1s-4p absorption signal is split into multiple peaks by the presence and orientation of bonded oxygen atoms. The position and relative intensity of these peaks allow XANES to identify specific mineral species and their relative abundance in samples.

## 2.5 Synchrotron Facilities

All of the standards and samples reported in this chapter were analysed at the Diamond Light Source in Harwell, Oxfordshire, in the I18 beamline, in three sessions carried out in February 2015, February 2016 and January 2017. The x-ray source was set to emit at 9.5 kilo electron volts (KeV) unless otherwise stated.

The detector on the I18 beamline is known to “drift” by  $\pm 1$  eV over time, so all spectra were standardised against the 2015 results to ensure direct comparability. Spectra collected in 2016 were found to be shifted by +0.75 eV from their positions in 2015. Samples run in January 2017 by Dr Angela Milne’s group from the University of Plymouth were found to be shifted by -0.6eV from 2015.

## 2.6 Analysis Software

Analysis of the XANES spectra is carried out using the *Athena* program (ver. 0.9.25), part of the *Demeter* EXAFS software package created by Bruce Ravel (Ravel, 2015). Demeter is based on the IFEFFIT program by Matt Newville. XRF and XRF map data were handled using PyMCA v5.1.1.

The pre-edge background line of each spectrum was correctly set by the software automatically. Athena assigns the post-edge line (the background signal following excitation) as a third-order polynomial by default, but second-order was found to generate a line that runs closer to the readings so second order post-edge lines were set for both standards and samples. The post-edge line represents the average post-excitation energy level and accurate placement should be through the middle of the post-excitation signal.

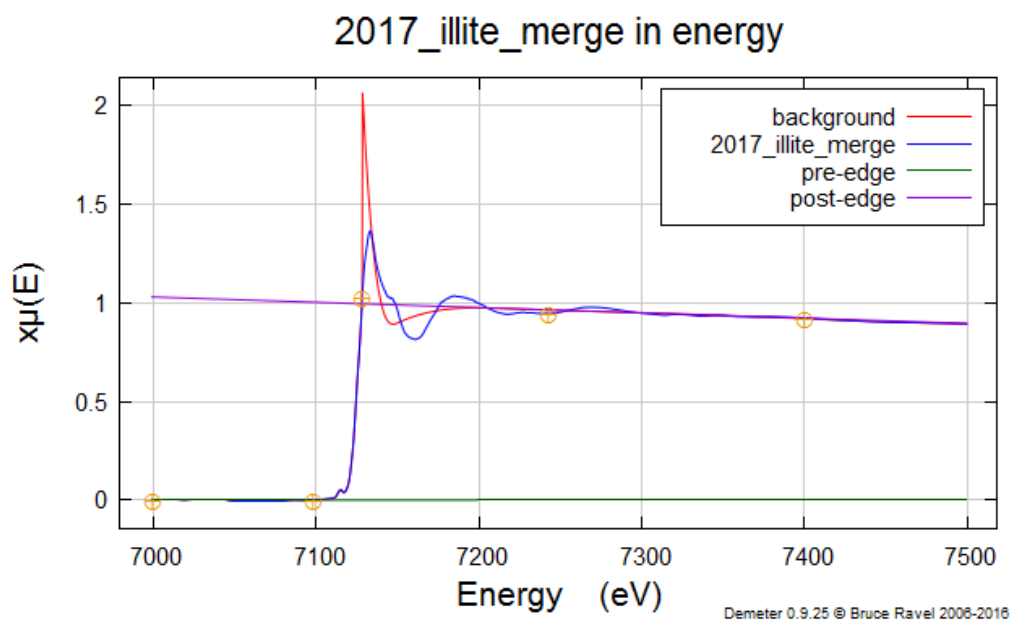


Figure 4 An example of pre-edge and post-edge line placement in an iron standard generated by the Athena software. Correct post-edge line placement can significantly alter the output of linear combination fitting, and thus the accurate quantification of various standard species

The Linear Combination Fitting function compares different combinations of pre-selected standards against sample spectra, with the success of the fit depicted both graphically (figure 5) and numerically via the **reduced chi-squared** and the relationship or **R factor**.

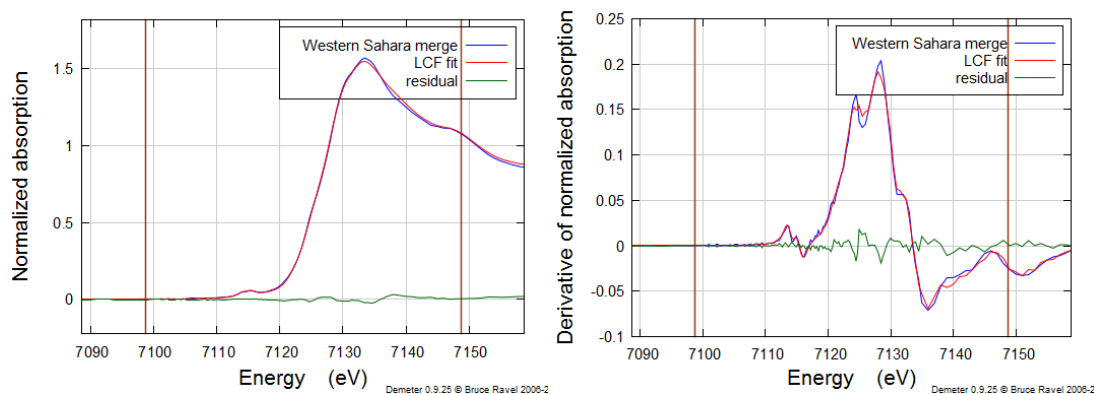


Figure 5 Athena Linear Combination Fits of a mineral dust sample using the normalised (left) and derived (right) spectra. For samples with complex mixtures of iron species, the derived spectra yield more accurate results (Formenti, et al., 2008). The difference between the sample spectrum (blue) and the best fit line using combinations of sample spectra (red) at each data point is plotted as a residual line (green).

Since measurement uncertainty cannot be determined from individual spectra, reduced chi-squared is not as useful as in other statistical methods and R-factor is recommended as the best available means for measuring the quality of the fit. R-factor is calculated as follows:

$$R \text{ factor} = \frac{\sum_i (data - fit)^2}{\sum_i data^2}$$

and a value closer to zero indicates a better fit. An R-factor around 0.05 represents a threshold of viability for a given fit (Kelly, et al., 2008) (Siebecker, 2016). A value of less than 0.05 represents an acceptable fit with the given standards, while any result above 0.05 means that no combination of the available standards can accurately describe the mineral speciation of the iron present in the sample. This can indicate that a sample spectrum has too low a signal - noise ratio to be usefully compared, or it implies that a significant proportion of the sample's iron content is present as mineral species other than those represented by the available standards.

Throughout this chapter, R-factors are stated above the plots of the results of each fit. As an easy visual reference, values in green represent R-factors significantly lower than the threshold of viability, while purple represents values closer to the threshold, implying either that the sample spectrum is of low signal – noise ratio or the sample composition includes a minor fraction of iron in a form outside of those found in the available standards. Any fit with an R-factor in red is above the 0.05 threshold, meaning that no useful speciation information can be gleaned from the spectrum with the available standards.

Time permitting, each sample was analysed at three sites across the surface of each pellet or powder spot. After aligning the post-edges of each individual spectrum, the spectra were plotted together to check for significant differences caused by high noise or low signal (figure 6), and any significantly different spectra were removed. The remaining spectra were merged to form an averaged spectrum for each sample. The iron standards were loaned to a group from Plymouth Marine Laboratories under Dr Angela Milne for their own XANES study in January 2017. Their clay standard spectra were run in triplicate and the merged spectra were used for fitting this data set instead of the single readings taken along with the 2015 samples.

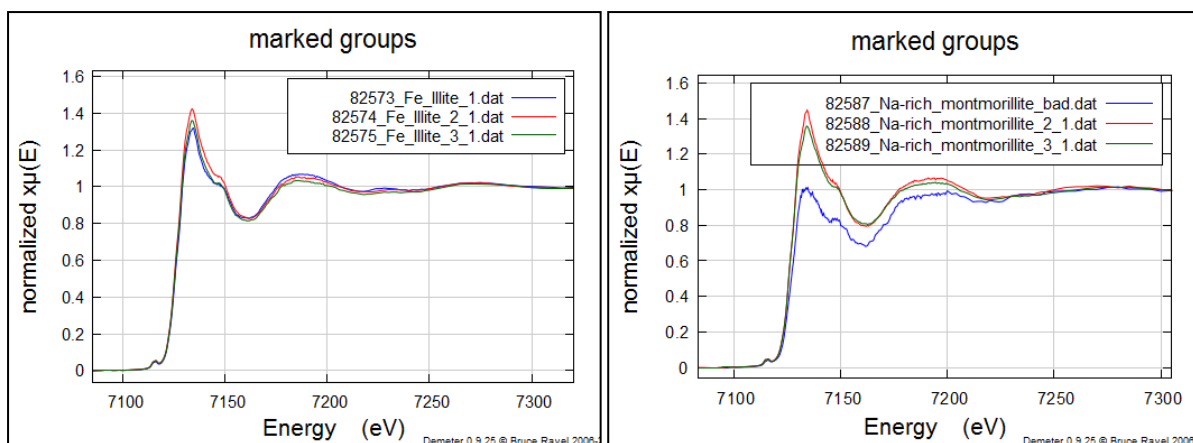


Figure 6 Two sets of replicate XANES spectra. The illite standard spectra (left) are well matched, while one of the sodium-rich montmorillonite spectra (right) shows a visible loss in intensity. This results in a poorly shaped spectrum that is not directly comparable to replicates and would render the merged spectrum useless if included.

## 2.7 Linear Combination Fitting

XANES has been employed to identify and quantify the relative concentrations of iron species in samples since its early use (Bianconi, et al., 1982) and is increasingly popular for the analysis of iron speciation in complex environmental samples (Oakes, et al., 2012) (Ingall, et al., 2013) (Formenti, et al., 2014). Deconvolution software (see section 2.6) can identify mineral species and quantify their relative proportions by contrasting the positions and relative intensities of 1s-4p transition peaks in sample spectra against different combinations of standard spectra.

XANES is a relatively new technique and work is ongoing to improve data quality (Diaz-Moreno, et al., 2017). Even published literature contains XANES results that do not align with the results of chemical testing within the same data set- in particular the over-representation of highly soluble iron species like ferrihydrite (Takahashi, et al., 2011). Ferrihydrite is known to be difficult to analyse due to its reactivity and non-uniform structure, as well as its tendency to react and change conformation under x-ray exposure (Pan, et al., 2006) (Peak & Regier, 2012).

When the Athena software carries out a Linear Combination fit, the sample spectrum is compared against every possible combination of standards selected for the fit. For example:

3 standards -> 7 fits: A, A+B, A+C, A+B+C, B, B+C, C

Running 4 standards requires 11 fits, 5 requires 25, 6 requires 57 and 7 requires 120 fits. To reduce processing time and select appropriate standards efficiently, a series of fits were run using groups of 4 standards, with similar standards run together to eliminate those least similar to the sample and thus least likely to be present. The “winning” standards from each group were gathered into a second round of fittings until only the standards most likely to be present in the sample remained. For example, when fitting Western Sahara mineral dust:

## Round 1

- Iron oxides only
  - 48.8% hematite, 42.3% goethite, 6.2% magnetite, 2.7% ferrihydrite **R-factor 0.0226**
- Clays only
  - 77.2% illite-smectite, 11.3% illite, 9.9% montmorillonite, 1.6% chlorite **R-factor 0.0125**
- Remaining standards
  - 87.9% feldspar, 10.9%  $\text{Fe}_2(\text{SO}_4)_3$ , 1.3%  $\text{FeSO}_4 \cdot 7\text{H}_2\text{O}$  **R-factor 0.0123**

Round 2 – since no standards were eliminated in round 1, minor components from each group were run together with more likely standards to push out the least likely

- Iron oxides + chlorite &  $\text{FeSO}_4 \cdot 7\text{H}_2\text{O}$ 
  - 40.8% hematite, 33.8% goethite, 21.3% ferrihydrite, 10.7% chlorite **R-factor 0.0184**
  - (magnetite &  $\text{FeSO}_4 \cdot 7\text{H}_2\text{O}$  eliminated)
- Clays + feldspar &  $\text{Fe}_2(\text{SO}_4)_3$ 
  - 57.8% feldspar, 14.7% illite-smectite, 13.1% illite, 6.7%  $\text{Fe}_2(\text{SO}_4)_3$ , 6.1% chlorite, 3.3% montmorillonite **R-factor 0.00937**

Round 3 – most likely iron oxides run with most likely other standards, then all remaining standards

- Iron oxides (minus magnetite) + feldspar, illite-smectite & illite
  - 34.1% illite, 31.9% feldspar, 18.5% hematite, 17.9% goethite **R-factor = 0.00434**
  - (ferrihydrite & illite-smectite eliminated)
- All remaining standards
  - **36% feldspar, 19.8% illite, 18.8% hematite, 18.3% goethite, 7.5% montmorillonite, 1.5% chlorite** **R-factor 0.00347**
  - ( $\text{Fe}_2(\text{SO}_4)_3$  eliminated)

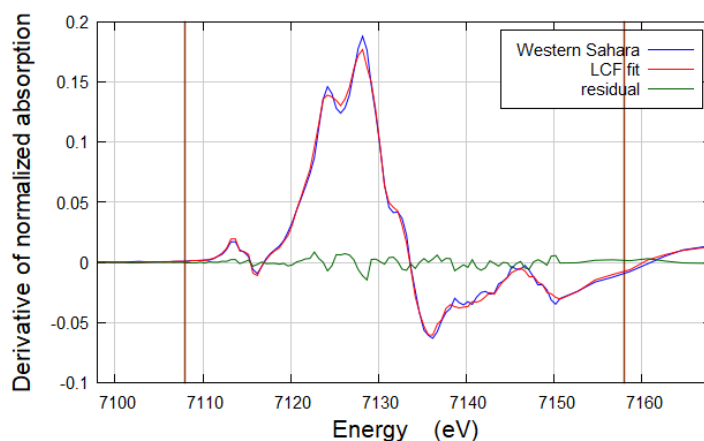


Figure 7 Linear combination fit of the first derivatives of the Western Sahara mineral dust sample contrasted with all available standards

In this study a series of experiments were carried out to test the accuracy of species identification and quantification by XANES by direct analysis of predetermined mixtures of standards, and with comparison to conventional chemical testing of well-defined mineral dust samples from across North Africa. In addition to these samples, further sample sets were analysed including windborne aerosols and particles from ship emission and biomass burning. Biomass burning samples and samples collected directly from ship stacks were analysed by XANES for the first time.

Samples were compared against standards using the Linear Combination Fitting (LCF) function, in the range of 7107 to 7157 eV. LCF can be carried out on normalised, derived or  $\chi(k)$  (which plots

wavenumber rather than energy) spectra. Normalised spectra adjust the relative intensity of the signal so that samples with significantly greater or lesser Fe content can be directly compared. Derived spectra plot the changes in the gradient of the line of intensity vs energy, and are better suited to analysing complex multicomponent samples (Formenti, et al., 2008) so fits were carried out on derived spectra where possible. Due to low Fe content and thus high Fe signal-noise ratio of ship emission and biomass burning samples, they could only be analysed using normalised spectra.

## 2.8 Sample preparation for standard addition

The main advantage of XANES over other analytical techniques is its capacity to both identify and quantify the relative proportions of different chemical species simultaneously, dependent on the availability of suitable standards. However, since some iron standards can be difficult to distinguish from others (see section 3.1), the accuracy of quantification may vary with mineral species. In order to test this hypothesis, 100mg samples of mineral dust with well described iron speciation by sequential extraction and XRD (Shi, et al., 2011) were spiked by mixing and manually grinding with either 1, 2, 3, 4 or 5 mg of an iron oxide known to be present in it. The proportion of total iron present in the samples was calculated in advance based on the amount of material added and its % iron content, and compared against the concentration estimated by Linear Combination Fitting of the various spiked samples.

## 2.9 Sample preparation for beamline exposure

In 2015, the standards were prepared for loading into the beamline by mixing with laboratory grade cellulose and hand grinding with a pestle and mortar prior to being pressed into a 20mm diameter pellet of 1mm thickness. Iron standards were mixed with cellulose in a ratio determined by the initial standard's iron concentration to produce a pellet containing ~3% iron.

e.g.     4.3 mg goethite (63% Fe) + 85.7 mg cellulose = 90 mg @ 3% Fe  
       34.3 mg illite IMt-1 (7.8% Fe) + 55.7 mg cellulose = 90 mg @ 3% Fe

Powder and fine particulate samples, particularly environmental samples, are likely to contain low concentrations of Fe and would thus be unsuitable for pressing into composite pellets with cellulose. These samples were prepared for loading into the beamline by collecting <1mg of solid material and suspending it in ~5  $\mu$ L of methanol dispensed from a 10  $\mu$ L pipette. Each suspension was drawn back into the pipette and dispensed onto a segment of Kapton film where the methanol dries rapidly, leaving a ~1 mm spot of solid sample bound sufficiently well to the film to allow it to be mounted vertically inside the beamline. In the I18 beamline the beam window is 25 x 25 mm. The methanol spotting technique allows up to 100 well separated samples to be loaded onto a single film.

### 3. Results and discussion

#### 3.1a Contrast between standards

Ideal XANES standards have visible differences in both their pre-edge and near-edge structures, as illustrated in figure 8.

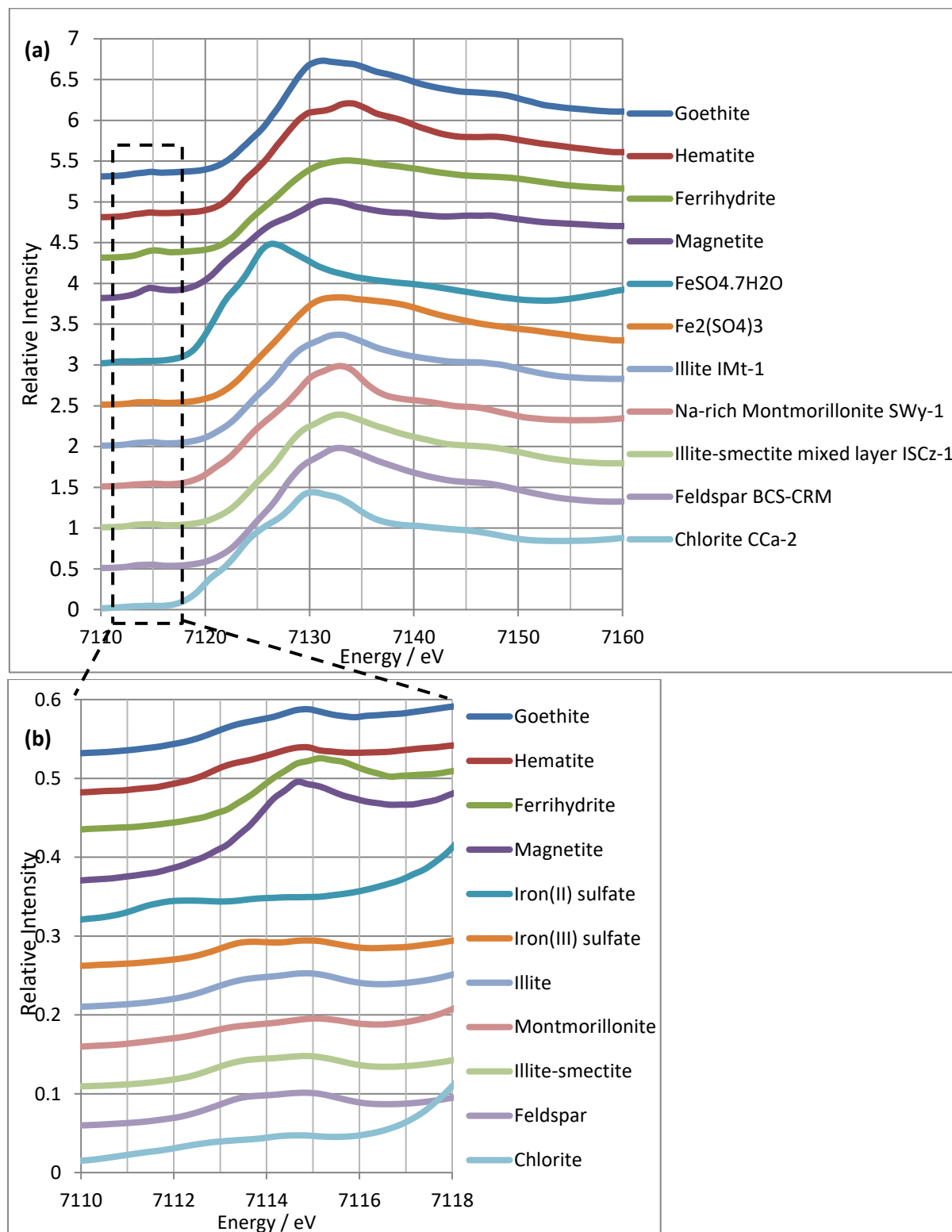


Figure 8 XANES spectra of Fe standards (a), and a close-up of the pre-edge region (b)

Figure 8a allows the main structural differences between the standard spectra to be visualised. Of particular note:

- The Fe(III) rich standard spectra show their two most significant absorption peaks at around 7130 and 7134 eV, while the major peak of iron(II) sulfate (the only exclusively Fe<sup>2+</sup> compound among the standards) is shifted down to 7127 eV, magnetite that shows a single visible peak at 7132 eV and Fe(II) rich chlorite which shows its strongest peak at 7130 eV.
- Ferrihydrite, with its non-crystalline structure, shows a comparatively smooth and featureless spectrum with no significant shoulders or troughs.
- The relative heights of the 7131 and 7134 eV peaks allow Fe(III) oxides goethite and hematite to be readily distinguished- a result that is difficult to achieve through other speciation techniques due to the two compounds' similar reactivity.
- Magnetite, chlorite and to a lesser extent the other clays show a pronounced shoulder at 7125 eV, indicative of their measurable Fe(II) content which is less visible among the Fe(III) oxides. Fe(II) sulfate contains Fe(II) exclusively, so again the shoulder is shifted down to 7122 eV.
- All of the Fe(III) oxides show a shoulder at 7139 eV that is not visible in the Fe(III) sulfate spectrum, indicating a difference in permitted 1s – 4p transitions between the two types of ligand.
- The illite, illite-smectite and feldspar spectra are difficult to distinguish visually, implying similar charge and orientation of heteroatoms around their resident iron.

Zooming in closer on the pre-edge region in figures 8b shows some differences in common with the near-edge. All of the Fe(III)-rich standards show pre-edge excitation peaks at 7113.5 and 7115 eV, except for ferrihydrite where the pre-edge appears as a single, large peak at 7115 eV. Magnetite is similar but displaced towards 7114.5 eV by the high Fe(II) content. Iron(III) sulfate shows a more pronounced pre-edge peak at 7113.5 eV while the iron oxides have a more pronounced peak at 7115 eV. Chlorite and iron(II) sulfate, the two most Fe(II)-rich standards, show pre-edge peaks displaced towards 7112 and 7113 eV respectively. Again, the illite, illite-smectite and feldspar pre-edge peaks are visibly similar while the montmorillonite standard's peaks are less pronounced.

### 3.1b Comparing and Contrasting Standards by Linear Combination Fit

Each one of the 11 iron standards was fitted against the other ten in the manner of an unknown sample as described in section 2.6. The purpose of this exercise was to determine which standards are readily distinguishable from the others, and which are more difficult to tell apart.

Unlike the fits of samples in the following sections, a high R-factor represents a positive outcome for these results. If one standard is fitted against all the others and the best fit has an R-factor of >0.05, it means that that particular iron species cannot be mistaken for a combination of other standards if it is present in a sample.

to compare its spectrum to those of the other standards and determine which standards are readily distinguishable and which are more difficult to differentiate using the Athena software. The fits are tabulated in figure 9.

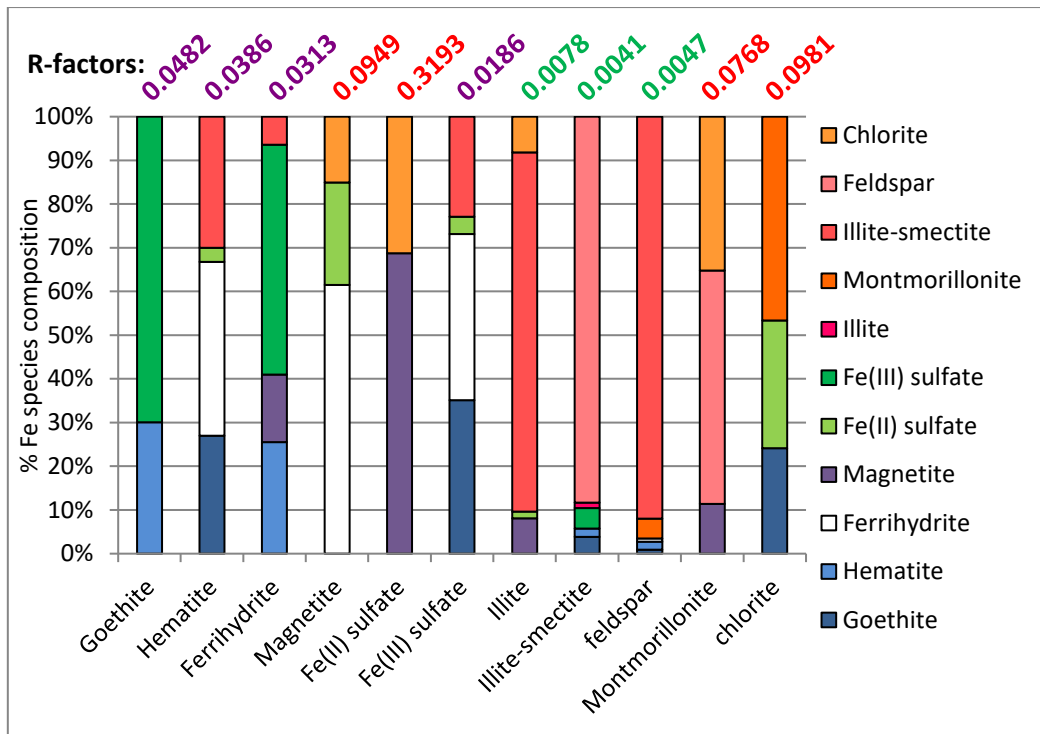


Figure 9 Results of Athena Linear Combination Fit, comparing each standard to all other standards. Each bar shows the relative composition of the best fit i.e. the Goethite standard most closely resembles a mix of 30% hematite and 70% Fe(III) sulfate, but with a high R-factor of 0.0482.

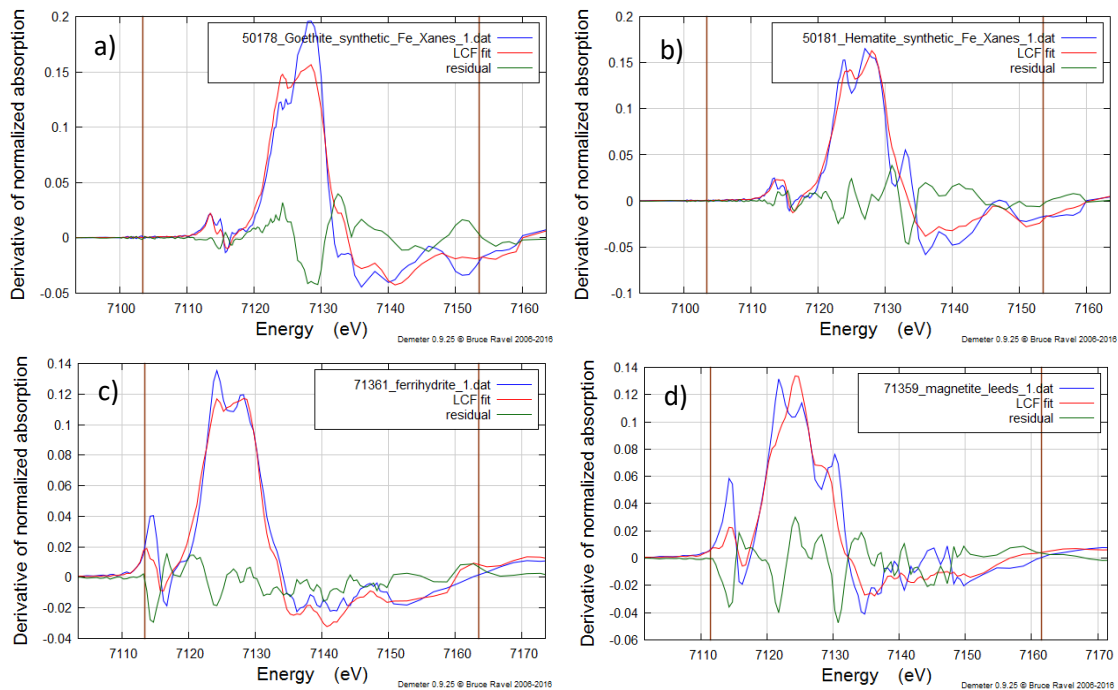


Figure 10 Fits of the first derivative spectra of the four iron oxide compounds, goethite (a), hematite (b), ferrihydrate (c) and magnetite (d)

The four iron oxides are quite distinct, with poor fits against the other standards as seen in figure 10 and high R-factors meaning that they are readily distinguishable from each other. For example, the goethite standard is best fitted to a mixture of 30% hematite and 70% Fe(III) sulfate. Thus any sample whose fit implies that it contains goethite, is more likely to contain goethite than a mixture of hematite and ferric sulfate so long as its R-factor is lower than 0.0482.

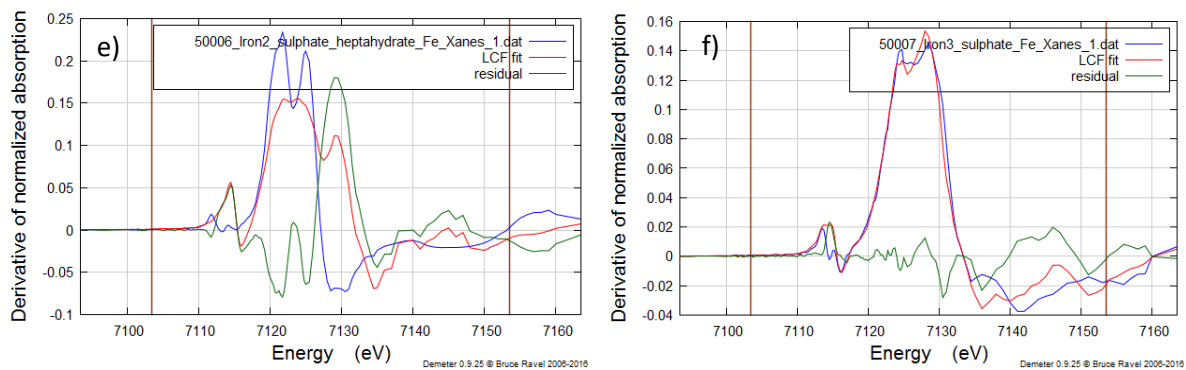


Figure 11 Linear Combination Fits of the first derivative spectra of Fe(II) sulfate heptahydrate (e) and Fe(III) sulfate (f) against all other standards.

Fe(II) sulfate, as the only pure Fe(II) compound among the standards, is by far the most distinct. None of the other standards in any combination come close to resembling its spectrum in figure 11. Fe(III) sulfate, however, can be mistaken for a mixture of goethite, ferrihydrite, illite-smectite and Fe(II) sulfate in a sample if its fit has an R-factor above 0.0186.

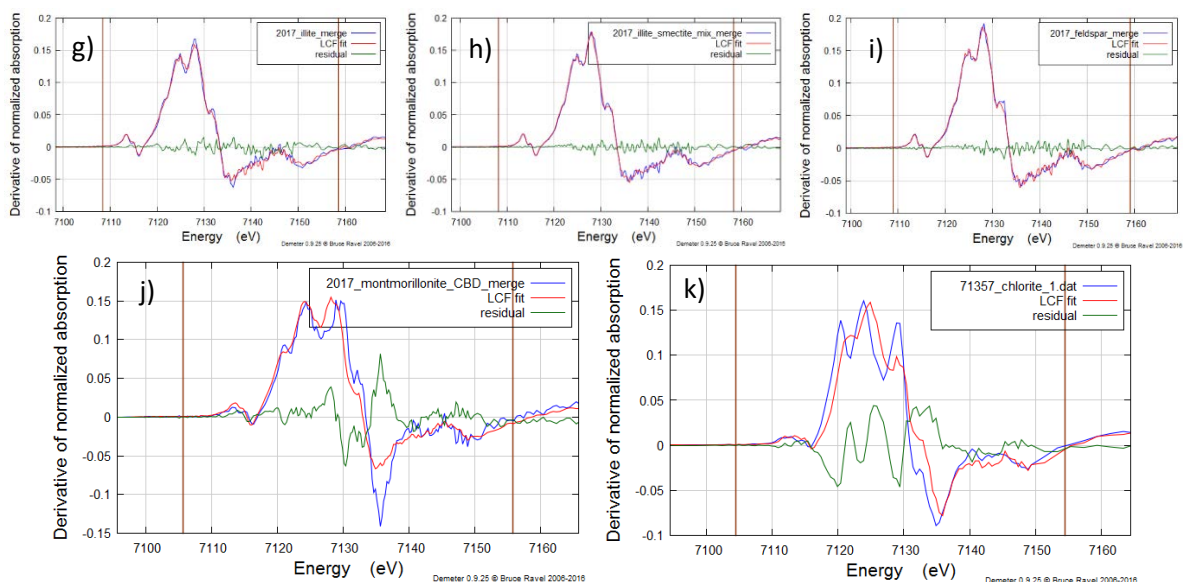


Figure 12 Linear Combination Fits of the first derivative spectra of illite (g), illite-smectite (h), feldspar (i), montmorillonite (j) and chlorite (k).

Figure 12 illustrates that montmorillonite and chlorite are very distinct, with poor fits and R-factors both over 0.05 for any combination of other standards. By comparison, the illite, illite-smectite and feldspar standards resemble each other quite strongly. The similarity between the illite clay and feldspar standards makes them particularly challenging to distinguish. Iron, specifically Fe(III), is found within montmorillonite almost exclusively in the octahedral configuration surrounded by oxygen and hydroxyl groups, while illite clays tend towards a mixture of octahedral and tetrahedral sites within the clay lattices (Johnson & Cardile, 1987). Feldspars vary in composition but tend towards heterogeneity with Fe(III) present in octahedral and tetrahedral configurations (Dyar, et al., 2001) thus the type and orientation of heteroatoms around the iron in the feldspar and illite samples generate very similar spectra, while the montmorillonite spectrum is distinct. The significantly higher Fe content

of clays compared to feldspars (see table 6, (Shi, et al., 2011)) suggests that any Fe signal in dust samples is more likely to be from clays.

### 3.2 Standard Addition

Mali mineral dust is known to contain poorly crystalline ferrihydrite (Shi, et al., 2011), and was thus used as the baseline for standard addition of ferrihydrite.

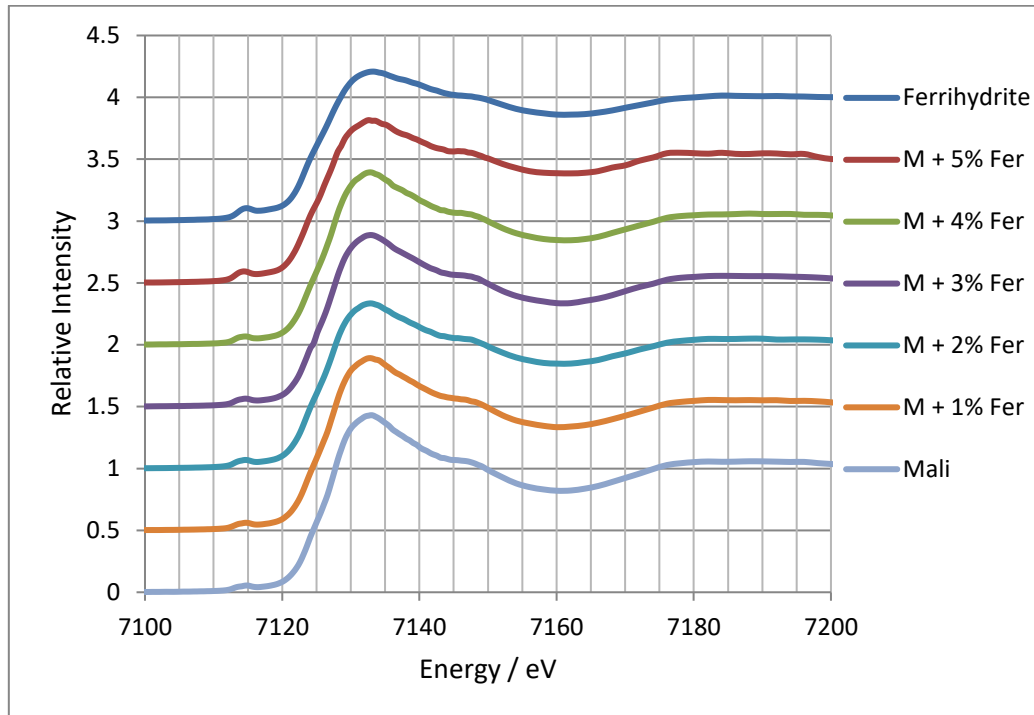


Figure 13 Displaced spectra of samples of Mali mineral dust, illustrating the shift from raw dust towards pure ferrihydrite with increased spiking

In principle, increasing the concentration of ferrihydrite present in the dust sample should cause the spectrum of the sample to more closely resemble that of pure ferrihydrite, and the Linear Combination Fit should reflect the rise in concentration. Furthermore, plotting the concentration of ferrihydrite against the amount of added material and drawing a trendline through them should have the trendline cross the y-axis (0 mg added ferrihydrite) at the concentration of ferrihydrite in the unspiked sample.

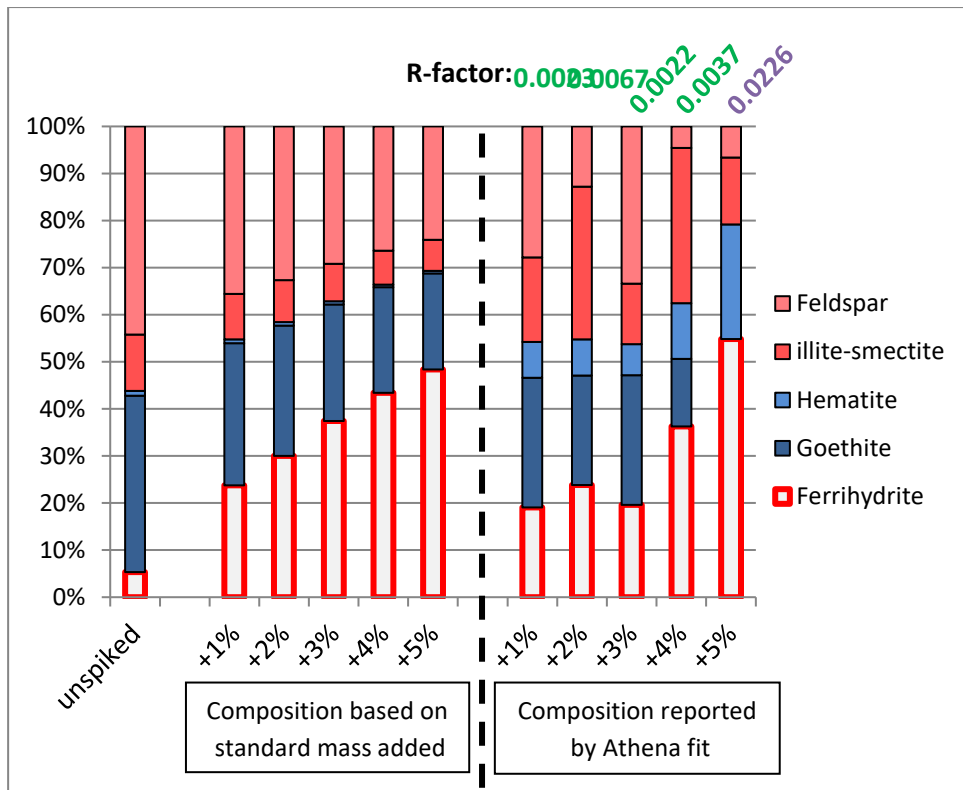


Figure 14 Composition of Mali dust sample prior to spiking, calculated composition of spiked samples based on mass of ferrihydrite added, and composition reported by Athena linear combination fit using first derivative spectra. R-factors are stated above the Athena fit results.

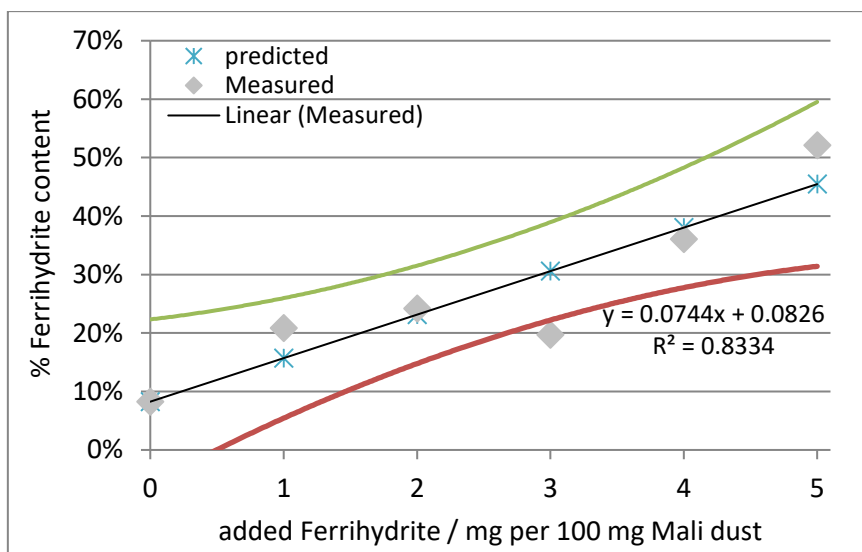


Figure 15 Ferrihydrite addition vs the measured % ferrihydrite content with the calculated values based on the mass added to the sample and the measured result of linear combination fit of the derived XANES spectra. The trendline and CI95 upper (green) and lower (red) bounds are based on the measured values

While the trendline in figure 15 follows the predicted ferrihydrite concentrations well, the individual measurements vary significantly from the true values and the 95% confidence interval, at its most narrow, is  $\pm 15\%$  of the total iron content. The standard comparisons in section 3.1 show that the spectra of ferrihydrite and hematite have some similarities, but hematite accounts for  $<10\%$  of the iron detected in the Mali sample and cannot account for the wide variation in reported ferrihydrite concentrations.

Western Sahara mineral dust is known to contain iron in both goethite and hematite forms in sufficiently high concentrations to be useful as a standard addition baseline for both minerals.

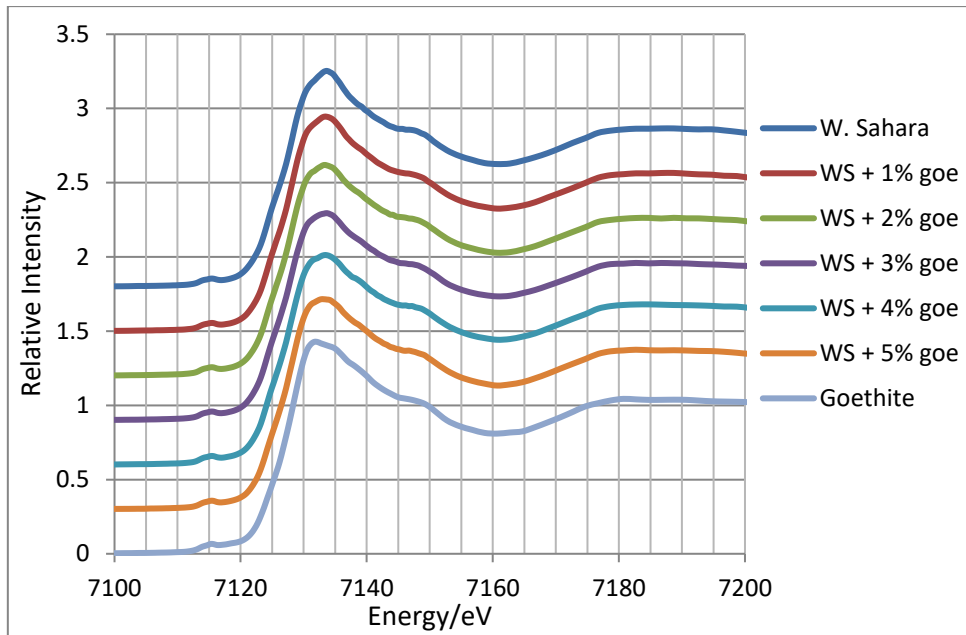


Figure 16 Displaced spectra of samples of Western Sahara mineral dust, illustrating the shift from raw dust towards pure goethite with increased spiking

Figure 16 shows clearer differences in the spectra with increasing spiking, due to goethite’s more distinct and featured spectrum. The rising peak at 7131 eV is the clearest visual indicator of rising concentration.

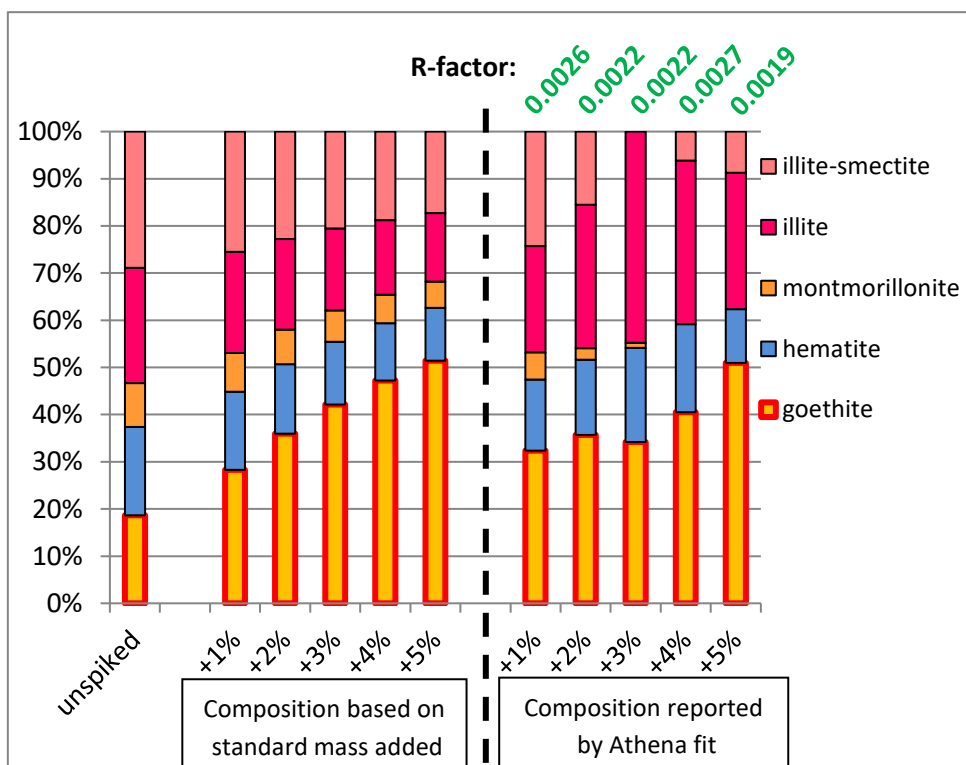


Figure 17 Composition of Western Sahara dust prior to spiking, calculated composition of spiked samples based on mass of goethite added, and composition reported by Athena linear combination fit using first derivative spectra.

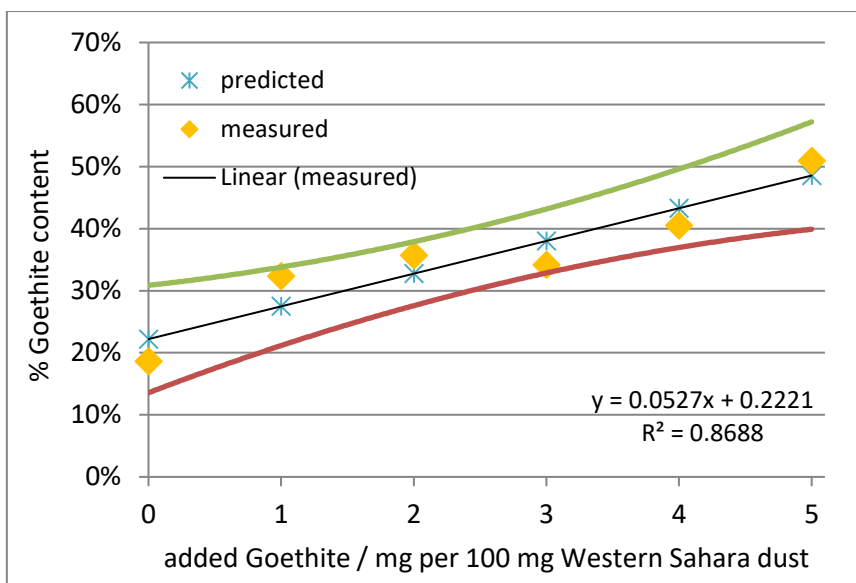


Figure 18 Goethite addition vs the measured % goethite content with the calculated values based on the mass added to the sample and the measured result of linear combination fit of the first derivative XANES spectra. The trendline and CI95 upper (green) and lower (red) bounds are based on the measured values

More accurate results were collected from samples spiked with goethite, with no readings more than  $\pm 4\%$  from the predicted concentration. As with ferrihydrite, the trendline generated by the measurements aligns well with the predicted concentrations, which implies that the variations are random.

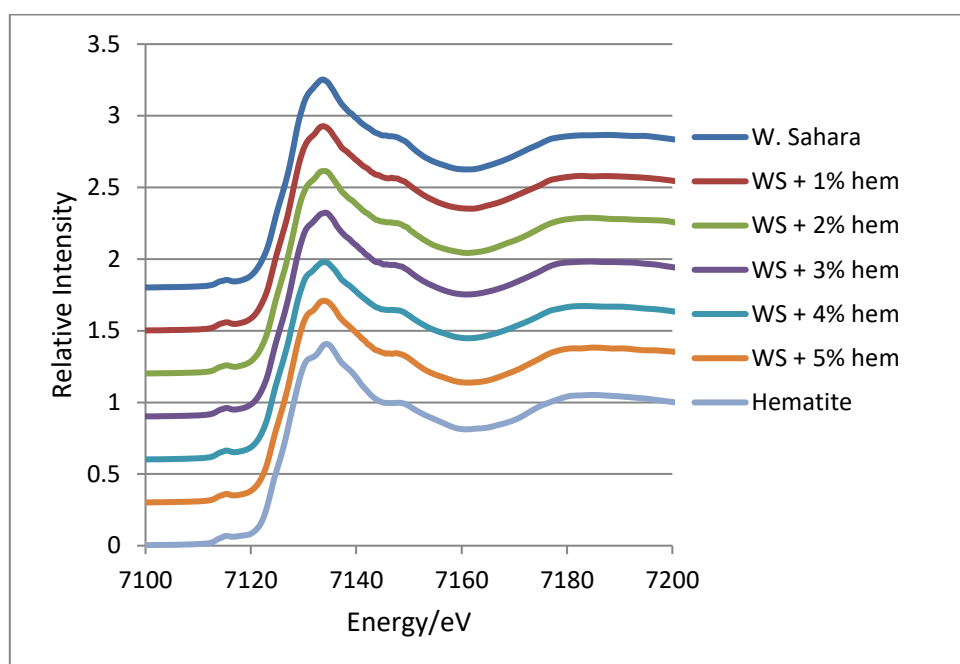


Figure 19 Displaced spectra of samples of Western Sahara mineral dust, illustrating the shift from raw dust towards pure hematite with increased spiking

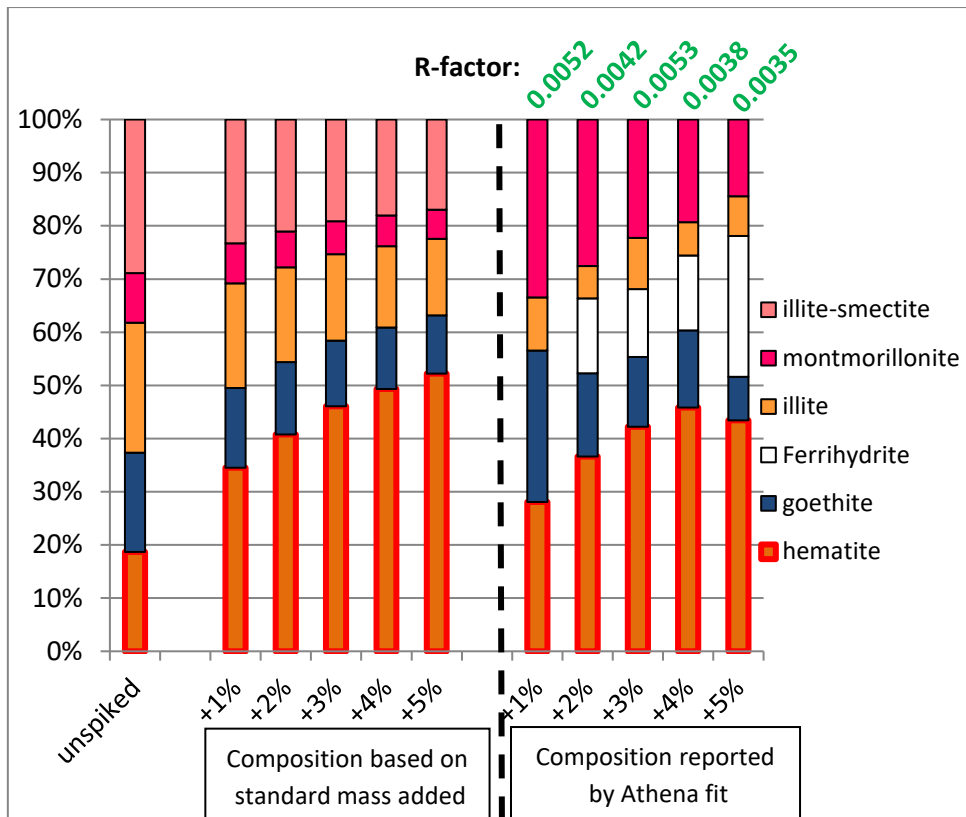


Figure 20 Composition of Western Sahara dust prior to spiking, calculated composition of spiked samples based on mass of hematite added, and composition reported by Athena linear combination fit using first derivative spectra

The Western Sahara dust in figure 20 show features in their spectra that Athena recognises as ferrihydrite at higher levels of spiking with hematite. This lends credence to the observations in section 3.1 that ferrihydrite can be difficult to distinguish from other iron oxides- hematite and ferric sulfate in particular. Due to the lack of significant ascorbate-extractable iron in the sequential extraction of this sample (Shi, et al., 2011) ferrihydrite was eliminated as a possible standard in fittings and the sample spectra were fitted again. The quality of the fits were slightly improved by removing ferrihydrite as an option, as shown in figure 21.

Since no ferrihydrite was added to the spiked samples, this shift in result is a source of some concern and highlights the importance of having access to chemical or XRD-based options for confirming XANES results until the technique is further refined.

The varying concentrations of montmorillonite, illite and illite-smectite across the samples in figure 21 illustrates the difficulty in distinguishing the spectra of clays.

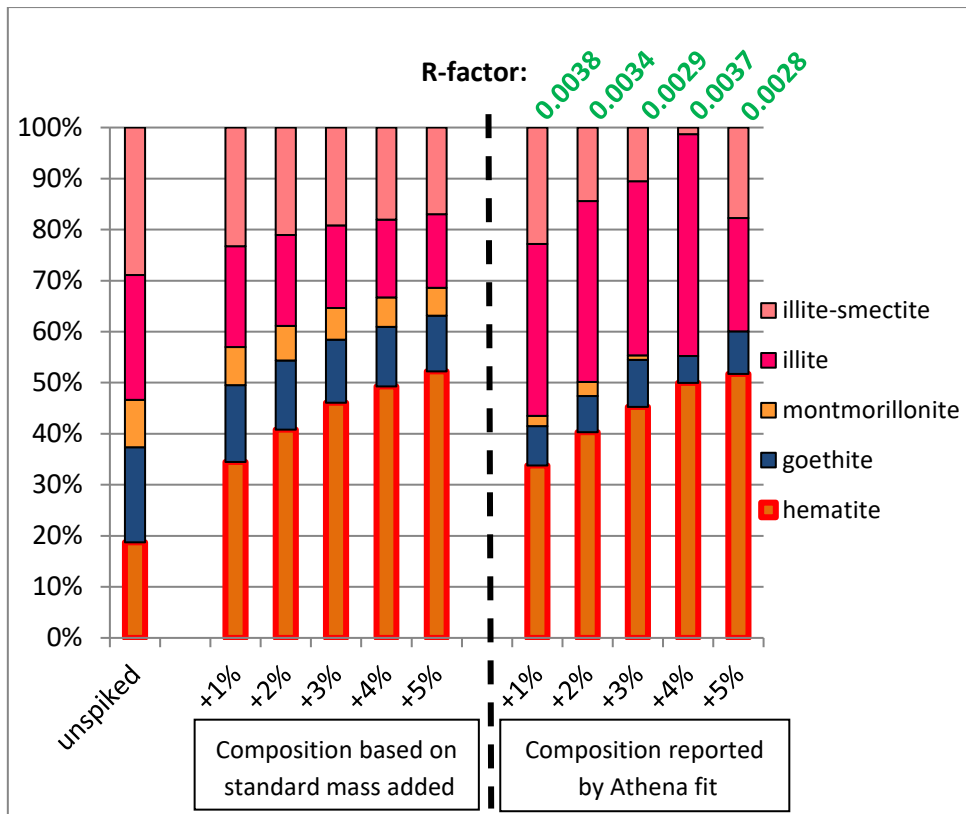


Figure 21 Composition of Western Sahara dust prior to spiking, calculated composition of spiked samples based on mass of hematite added, and composition reported by Athena linear combination fit using first derivative spectra without ferrihydrite as a possible standard.

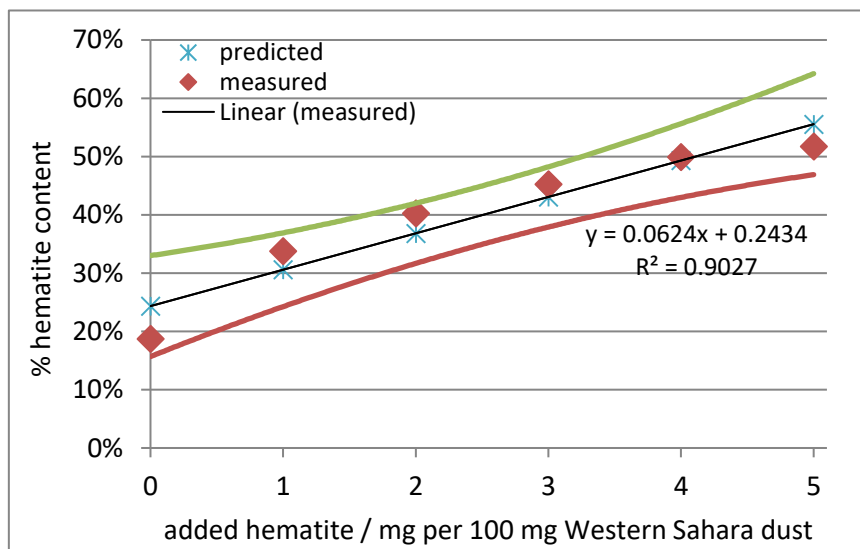


Figure 22 Hematite addition vs the measured % hematite content with the calculated values based on the mass added to the sample and the measured results of linear combination fit of the derived XANES spectra. The trendline and CI95 upper (green) and lower (red) bounds are based on the measured values

Figure 22 shows that hematite quantification is also reliable, with measured concentrations within  $\pm 4\%$  of the predicted values. Again the trendline from the fitting results runs through the predicted values.

### 3.3 Mineral dust precursors

To further test the identification and quantification capabilities of the XANES technique, a series of mineral dust samples were analysed whose iron content had been well-characterised previously by sequential extraction and X-Ray Diffraction (XRD) (Shi, et al., 2011).

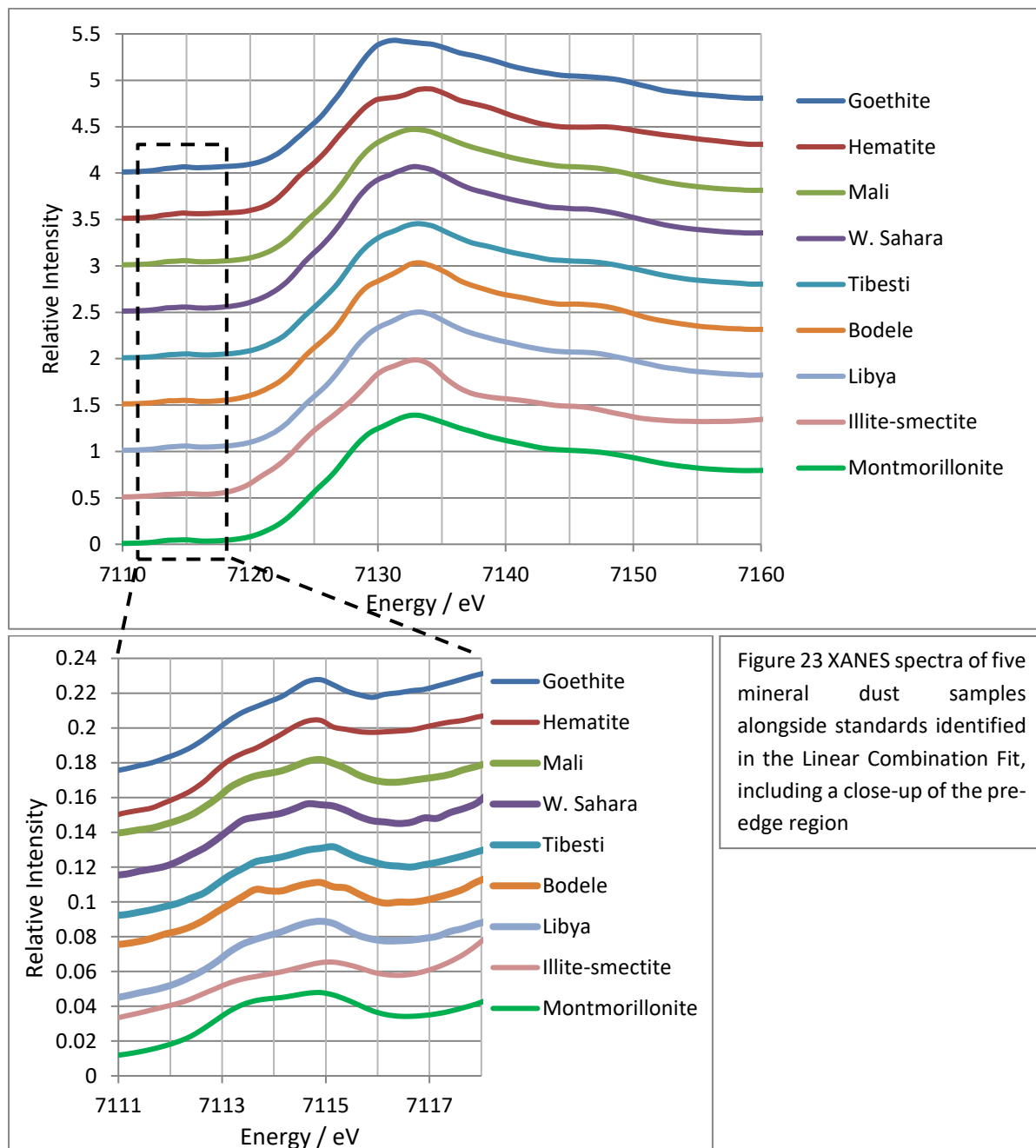


Figure 23 XANES spectra of five mineral dust samples alongside standards identified in the Linear Combination Fit, including a close-up of the pre-edge region

As figure 23 illustrates, the Fe spectra of the North African mineral dust precursors show features in common with the common iron oxides and clay minerals. While all samples show a main excitation peak at around 7134 eV, the Tibesti, Libya and Bodélé samples also show a substantial shoulder at around 7125 eV, more in common with hematite. Hematite is not reported in the XRD results (Shi, et al., 2011), although the samples contain 1-5% Fe so a minor fraction of Fe present as hematite may have been below the detection limit for the equipment. Pre-edge positioning indicates that the samples are all rich in Fe(III), with the main excitation peaks occurring at or near 7113.5 and 7115 eV.

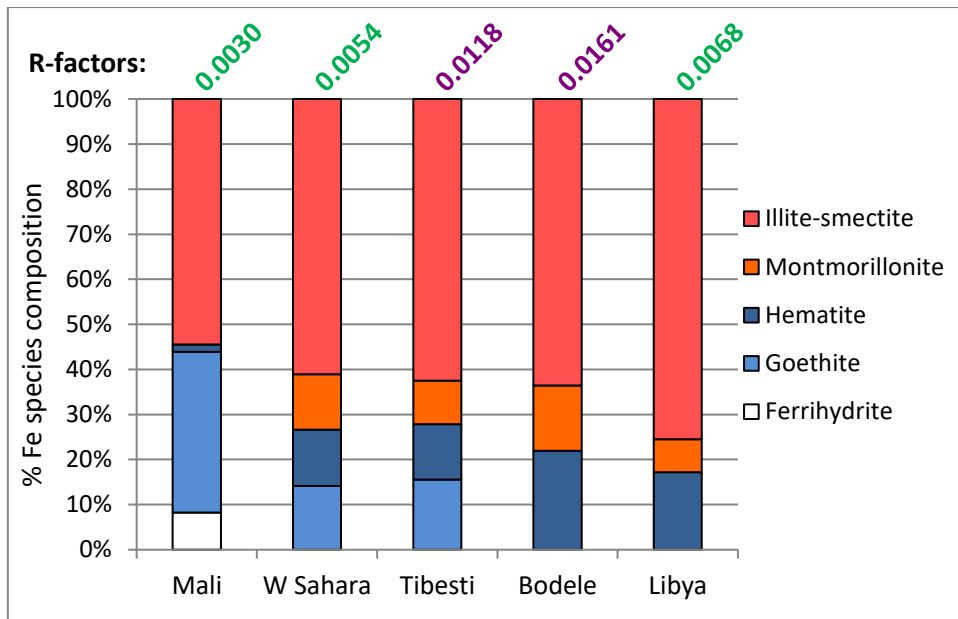


Figure 24 Iron speciation in North African mineral dust precursors according to Athena Linear Combination Fitting of the derived XANES spectra

Figure 24 shows the results of LCF, where three of the five samples fit the available sample spectra well while the Tibesti and Bodélé spectra exhibit less reliable fits that might merit further verification. The comparison with chemical sequential extraction (figure 25) indicates that the LCF (XAS columns) disagrees with the chemical analysis (CHEM column) by around 10% in the Tibesti sample, and misses the ~3% readily available Fe (Ascorbate extractable, or FeA, while FeD pertains to Dithionite extractable species like goethite & hematite, and Residual refers to insoluble species like Fe bound within clay particles) that is assumed to indicate the presence of ferrihydrite. This variation should be considered when analysing all further sample sets. Shi et al's XRD reports feldspar in the Western Sahara sample, but between the low Fe content and similarity to illite-smectite (see figure 9) it was not distinguishable using XANES.

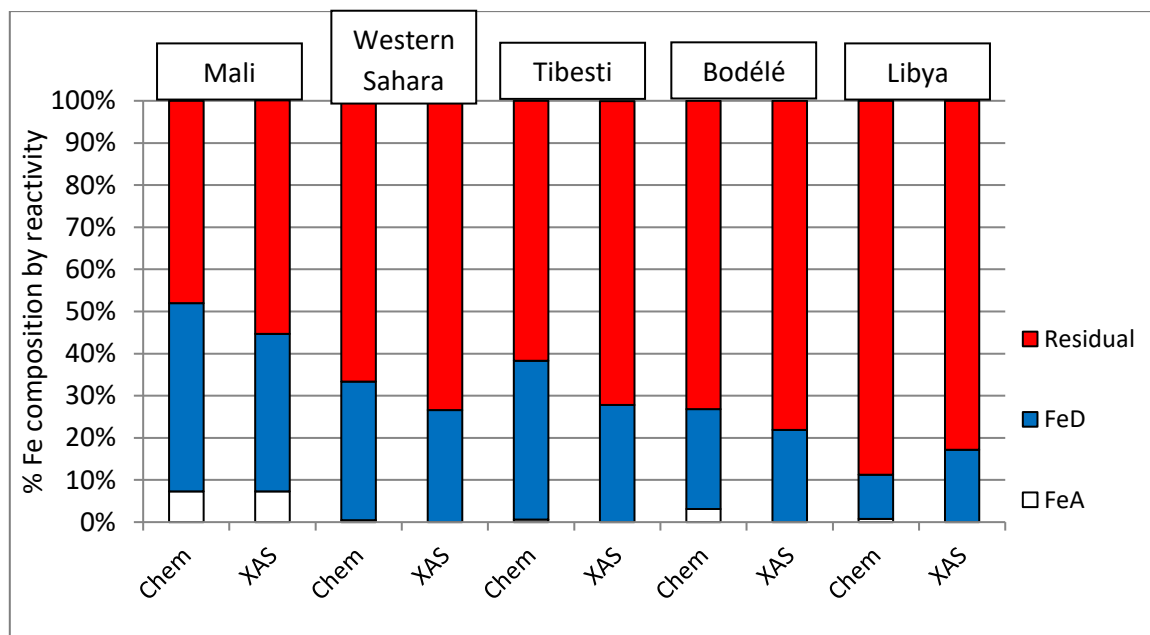


Figure 25 Comparison of Fe speciation reported by sequential extraction vs XANES Linear Combination Fit

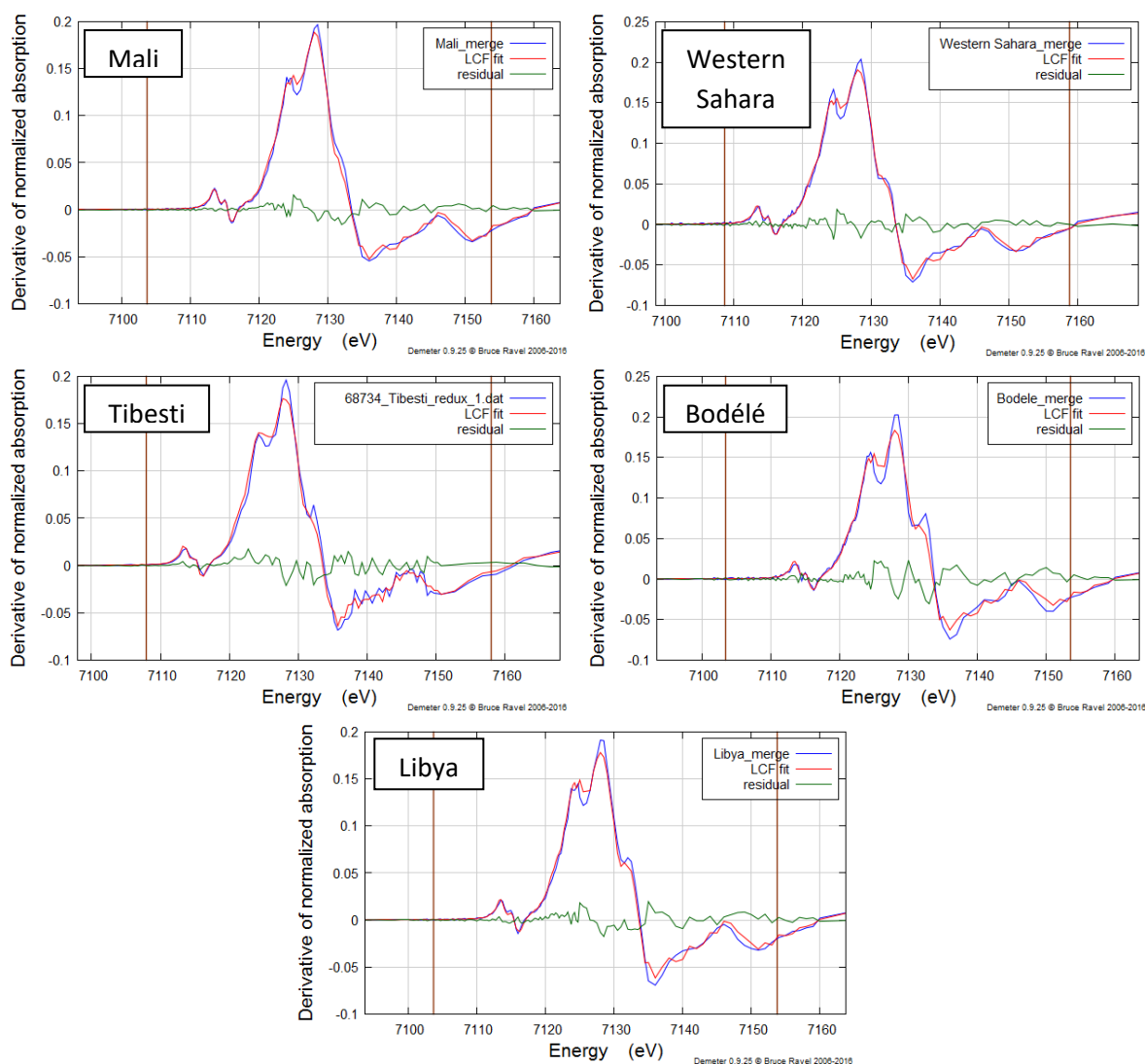


Figure 26 Graphical representation of Linear Combination Fit of derived mineral dust spectra, with the sample spectrum in blue, the best fit combination of standards in red, and the difference at each point represented as a residual line in green. The brown lines indicate the fitted range.

Examination of the fit graphs in figure 26 reveals the exact energy ranges where each sample spectrum separates from the best fit combination of standards. The dust samples from the Tibesti Mountains and the Bodélé Depression show the greatest deviation from the best fit. The Tibesti spectrum shows small but significant variations over the energy range from 7128 – 7135 eV, while the Bodélé sample fits most poorly around 7125-7133 eV. To improve the fit, further standards could be introduced to the set based on documented XANES spectra that have peaks that are significantly different from the available standards in these regions. Fits are close across all samples in the pre-edge region, indicating that the Fe(II):Fe(III) ratios in the samples is close to that of the selected standards.

### 3.4 Further mineral dust & haze samples

Further samples of mineral dust from North Africa (Shi, et al., 2011), South America and the Mediterranean (Stockdale, et al., 2016) were analysed by XANES. The samples will be analysed by sequential extraction by another student prior to publication in order to compare against the results of linear combination fitting.

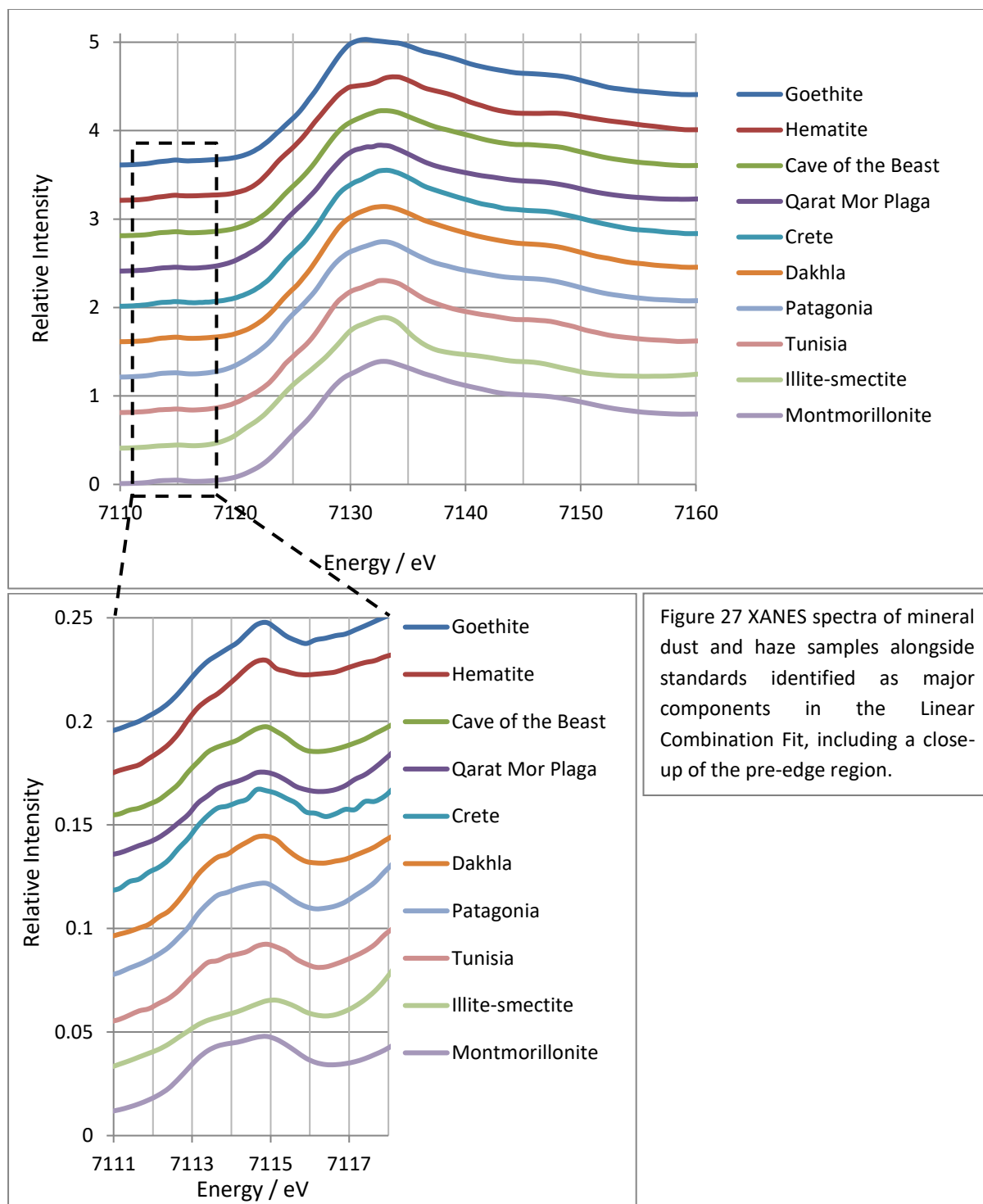


Figure 27 XANES spectra of mineral dust and haze samples alongside standards identified as major components in the Linear Combination Fit, including a close-up of the pre-edge region.

The North African mineral dust samples, with their peak near-edge excitation at around 7134 eV and more pronounced shoulder at around 7125 eV, more closely resemble hematite than goethite

although the lack of pronounced shoulders at 7139 eV among many of the samples (Tunisia in particular) causes the spectra to more closely resemble those of the clays. Examination of the pre-edge regions implies that all of the samples are very Fe(III) rich.

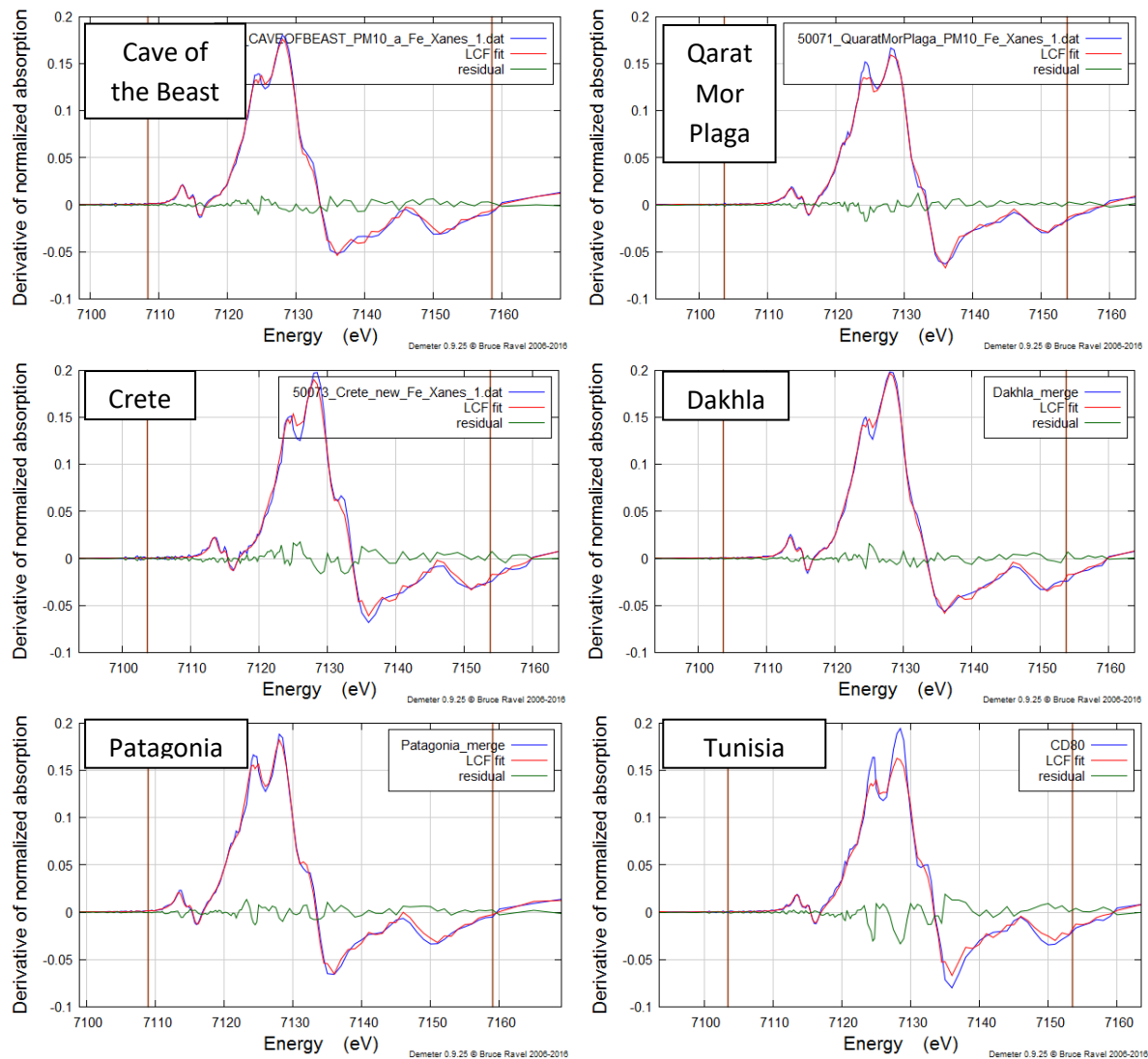


Figure 28 Graphical representation of the Linear Combination Fits of derived mineral dust spectra, with the sample spectrum in blue, the best fit combination of standards in red, and the difference at each point represented as a residual line in green. The brown lines indicate the fitted range.

All of the samples can be fitted to the available standard curves relatively well, although the consistent deviation of the derived sample curves from the best fit at around 7124 eV implies that at least one iron species present in the dust is not accounted for by the standards. The Patagonian sample is unusually dark which implies a high organic matter content, although the solid fit with the mineral Fe samples indicates that the organic fraction does not contain a significant proportion of the total iron in the dust.

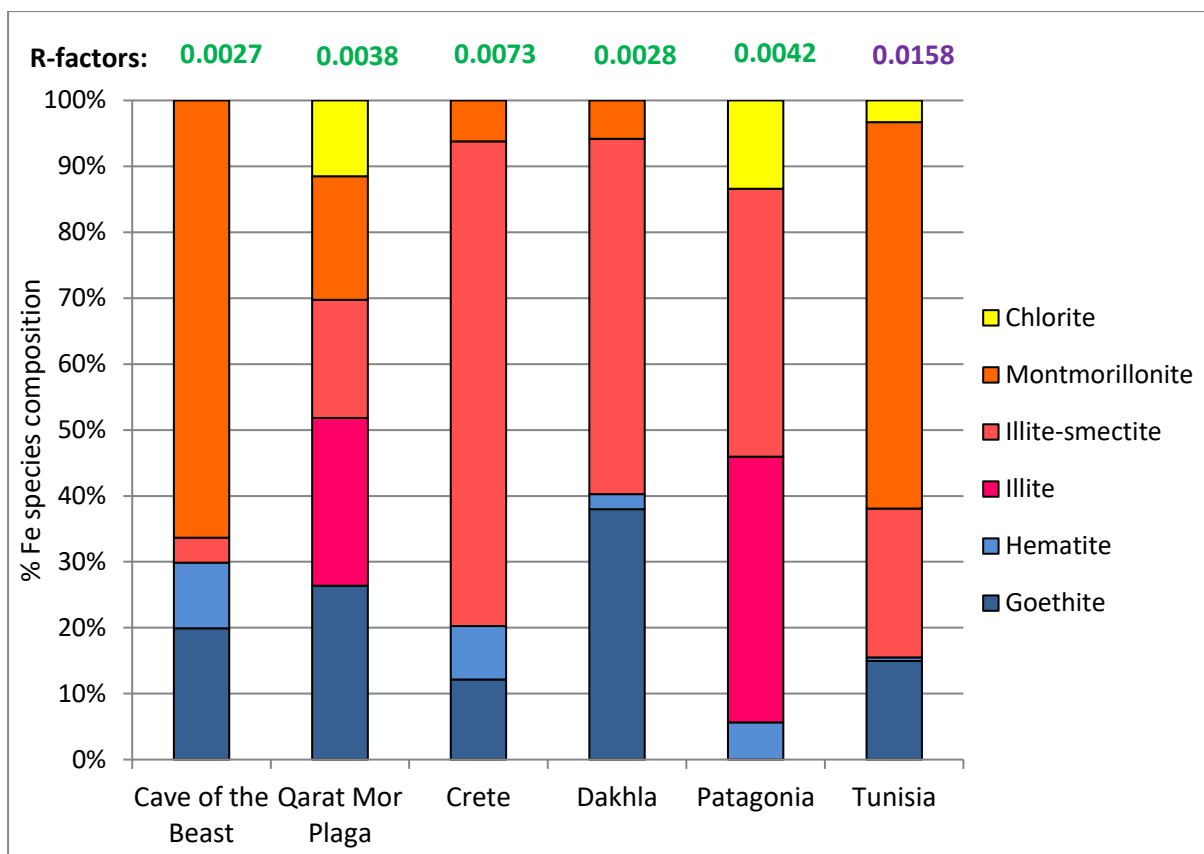


Figure 29 Iron speciation in mineral dust precursors according to Athena Linear Combination Fitting of the derived XANES spectra

The results of fitting show that, of the two common iron oxides, goethite appears to be more dominant in the North African and Mediterranean samples, in accordance with existing literature on the nature of dust from that region (Formenti, et al., 2014). In common with the mineral dust samples in section 3.3, the extractable iron content is low with 60-90% of the Fe in the samples contained within clay particles.

### 3.5 Particulate Aerosol Samples: Beijing

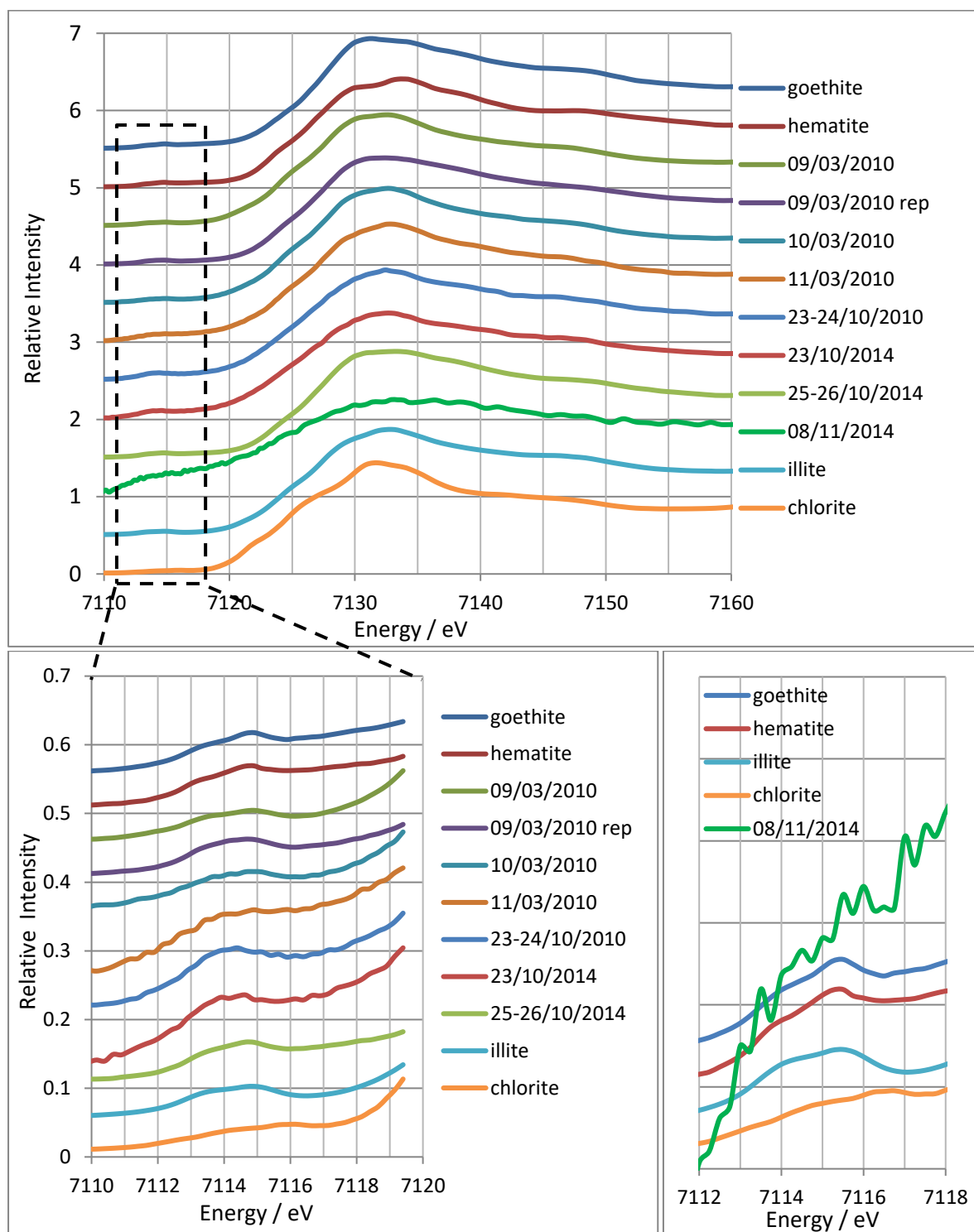


Figure 30 XANES spectra of Beijing aerosols, including the excitation region (a) and close-up of pre-edge regions (b and c) of samples and relevant standards

The sample collected on 08/11/2014 was particularly low in iron, and this is reflected in the noisy and shapeless XANES spectrum. Such spectra are difficult to normalise (see 7112-7118 eV plot) and thus any attempt at fitting with standards is unlikely to yield useful information. Close examination of the pre-edge regions reveal signal noise in the 23-24/10/2010 and 23/10/2014 samples which were collected during days without haze events. The remaining samples taken during haze events,

09/03/2010 to 11/03/2010 & 25-26/03/2014, show pre-edge shapes and positions similar to that of the clay illite. Some of the Beijing samples, most notably the 09/03/2010 and 25-26/10/2014 samples, show their highest excitation at 7131 rather than 7134 eV, indicative of a high proportion of goethite. The repeat spectrum taken from a new area on the 09/03/2010 sample differs visually from the previous spectrum, particularly in the 7140-7145 eV region, and implies a certain level of heterogeneity.

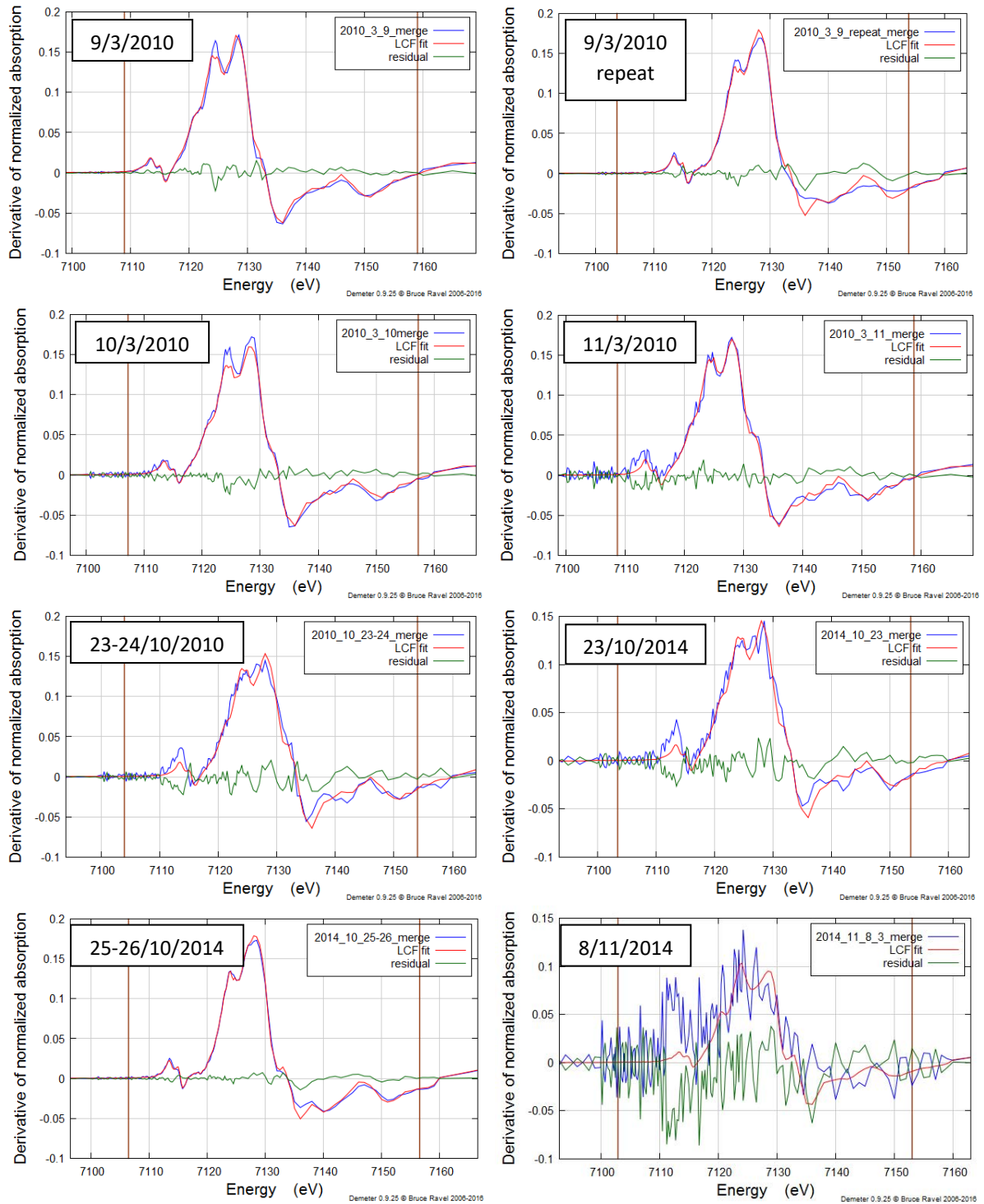


Figure 31 Linear Combination Fits of derived Beijing aerosol spectra, with the sample spectra in blue, the best fit combinations of standards in red, and the difference at each point represented as a residual line in green. The brown lines indicate the fitted range.

Figure 31, particularly the 08/11/2014 fit, illustrates the difficulty of fitting standards to noisy sample spectra.

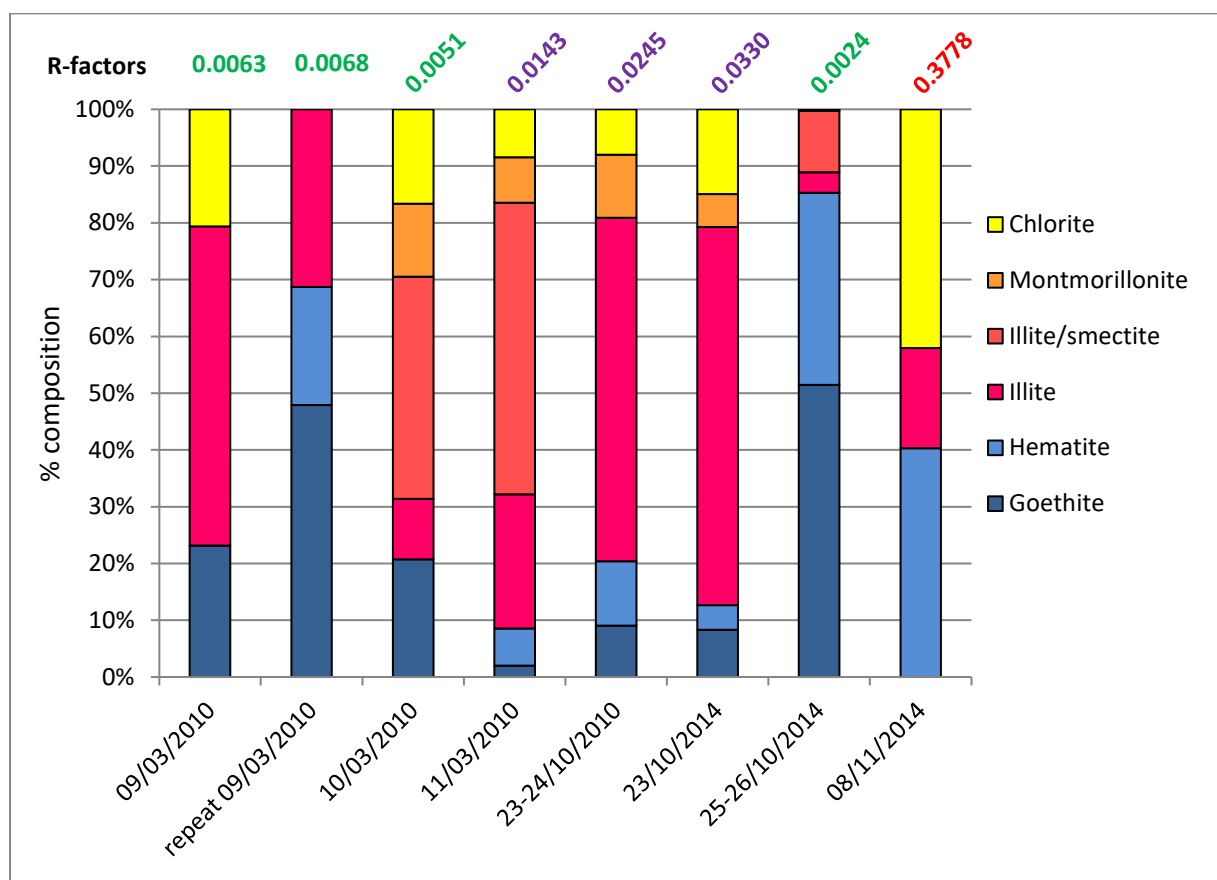


Figure 32 Iron speciation in Beijing aerosol samples according to Athena LCF

Previous examination of iron speciation in particulates from dust storm events in Beijing (Shi, et al., 2005) using XRD reports that illite-smectite is the dominant clay mineral, but the XANES LCF results report that the majority of iron is present in illite. The similarity between the illite and illite-smectite Fe XANES spectra (figure 9) is enumerated with an R-factor of 0.0045, lower than the R-factors for the majority of the Beijing samples, so XANES result does not necessarily contradict the 2005 XRD readings (table 2, (Shi, et al., 2005)).

As previously discussed, the 8/11/2014 sample is too noisy to be fitted and the R-factor of 0.3778 renders the result meaningless. By contrast, the most accurate fit is to the 25-26/10/2014 sample which contains iron mostly as goethite and hematite. The second 9/03/2010 reading reports a similar composition, which implies two distinct types of material within the iron-rich aerosol- one with Fe mostly present in illite clay as reported by Shi et al's XRD results and one with Fe mostly in iron oxides. Further source apportionment studies in the area would effectively trace these components.

### 3.6 Particulate Aerosol Samples: Ji'nan dust storm

Five aerosol samples were collected from dust storm events in Jinan by collaborators at Shandong University. The displacement of the pre-edge centroids in figure 33, most visibly in the Win-5 sample, towards 7114 eV indicates that the dust has a high proportion of Fe(II), more in line with the chlorite standard (close to 50:50) than the illite (90% Fe(III)) that the rest of the samples closely resemble. Comparison with other Fe(II) rich clays or micas such as biotite, glauconite or celadonite (Weaver & Pollard, 1973) might yield closer fits than the available standards.

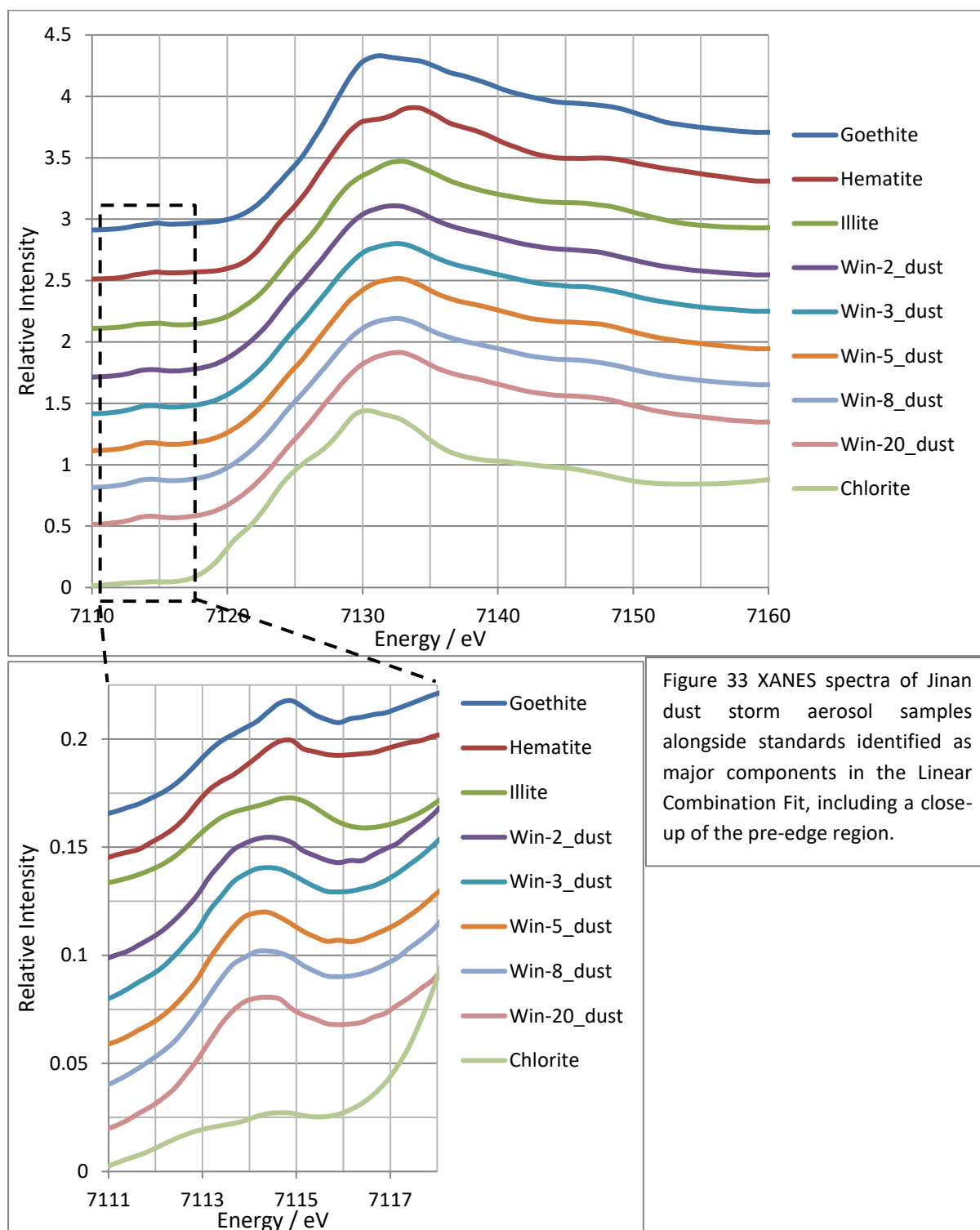


Figure 33 XANES spectra of Jinan dust storm aerosol samples alongside standards identified as major components in the Linear Combination Fit, including a close-up of the pre-edge region.

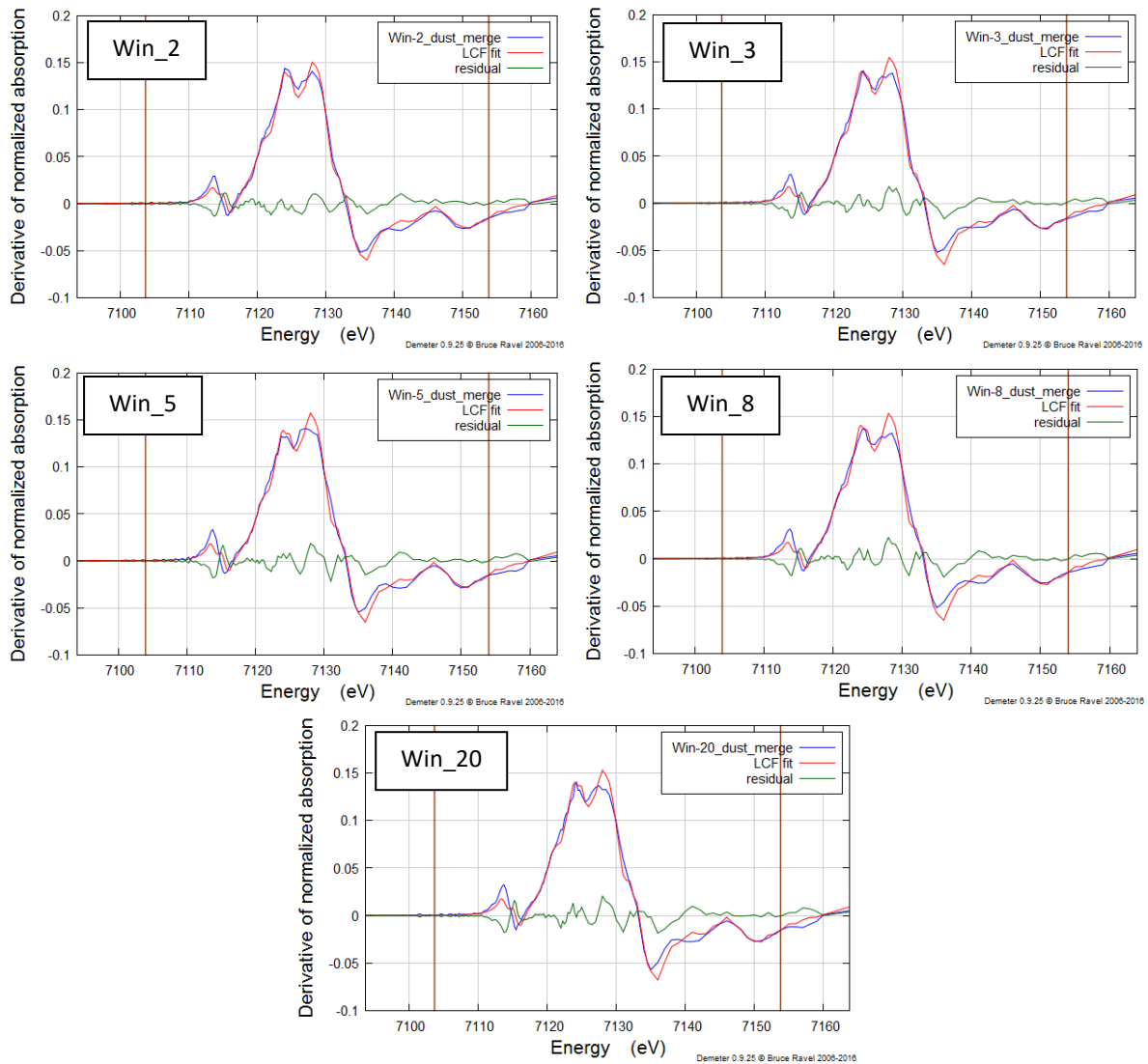


Figure 34 Linear combination fits of aerosol samples from dust storms in Jinan, with the sample spectrum in blue, the best fit combination of standards in red, and the difference at each point represented as a residual line in green. The brown lines indicate the fitted range.

Appraisal of the linear combination fits in figure 34 shows that no combination of available standards effectively represents the pre-edge region and, along with the pre-edge shapes visible in figure 33, implies that further analysis with other minerals rich in Fe(II) would yield a more reliable fit.

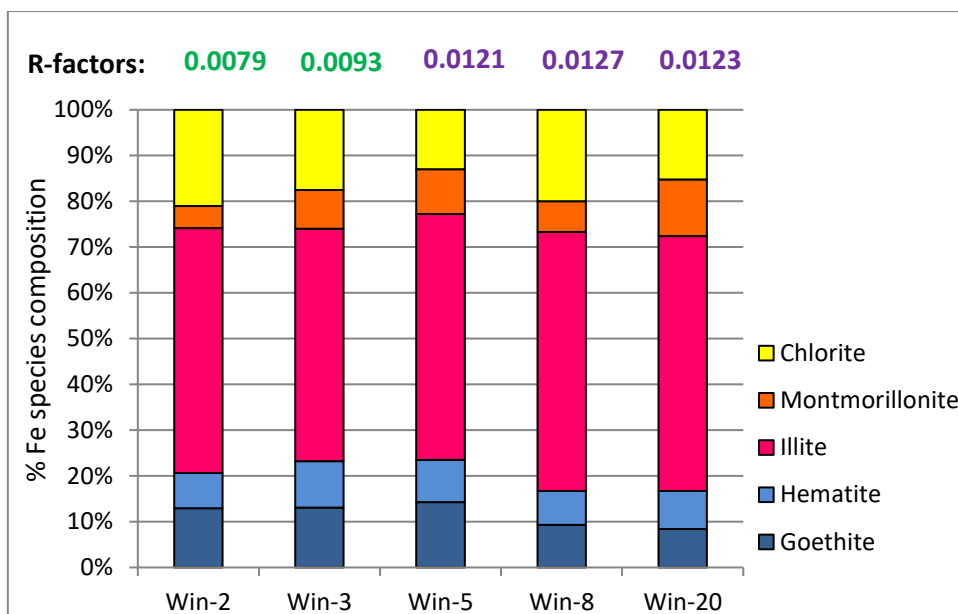
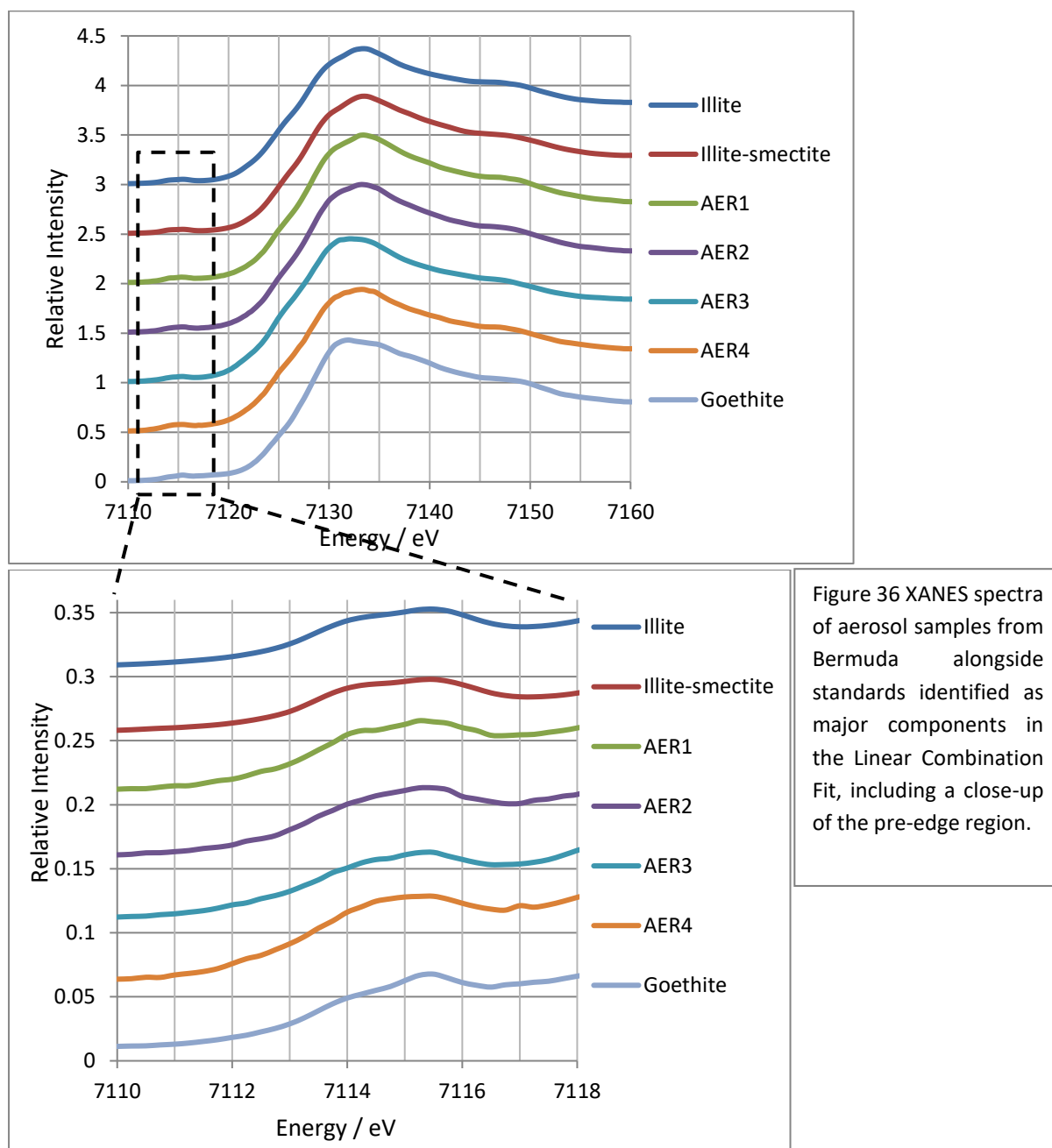


Figure 35 Iron speciation in Jinan dust storm aerosol samples according to Athena LCF

The linear combination fit results in figure 35 imply a small (~20%) contribution of common iron oxides towards the XANES spectrum of the dust storm samples, while the majority of the resident iron is bound in clay particles. The high chlorite content, combined with the fitting issues around the pre-edge region visible in figure 34 imply that another Fe(II) rich clay mineral is likely to be present in the dust that is not represented by the standards.

### 3.7 Particulate Aerosol Samples: Bermuda & Loess Plateau

Four aerosol samples were collected in Bermuda over periods of several days from July 2009 to December 2010, selected to analyse the content of four different North American air masses (Fishwick, et al., 2014). The XANES spectra in figure 36 closely resemble those of illite or illite-smectite, although the shift in maximum excitation particularly in the AER3 sample suggests a higher concentration of goethite. Close examination of the pre-edge regions show that the samples are mostly Fe(III)-rich.



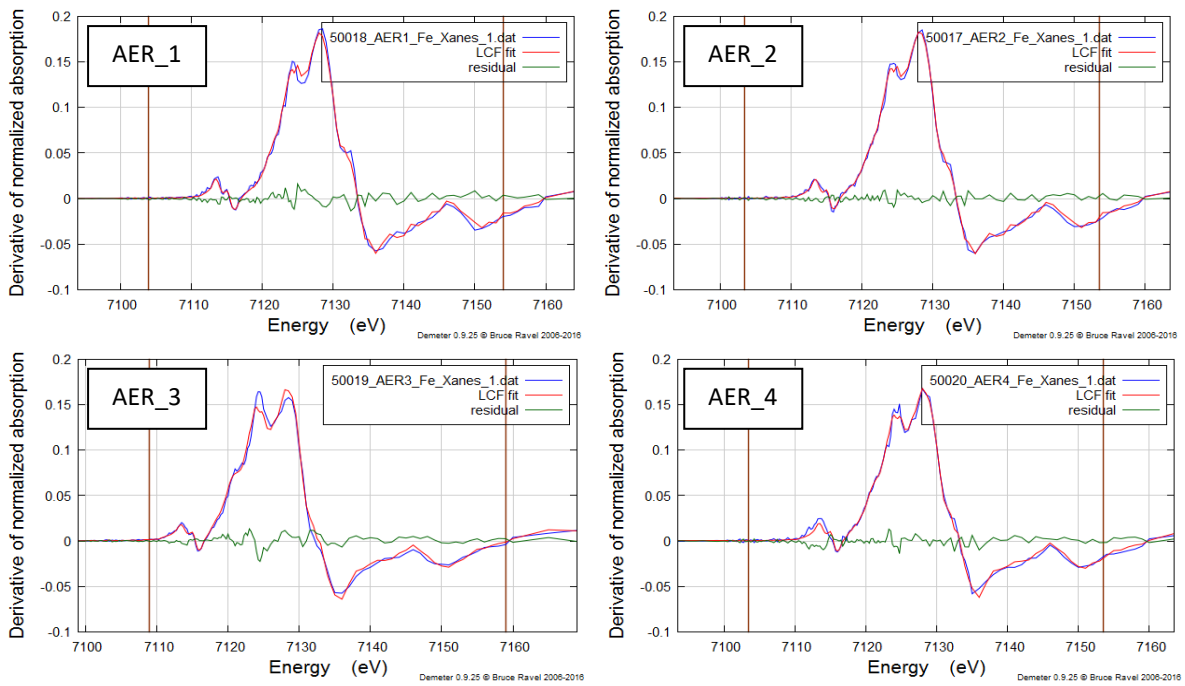


Figure 37 Linear Combination Fits of aerosol samples collected in Bermuda

Figure 37 shows that the Bermuda samples all fit the available standards well, although the discrepancy between the fit and the sample curve around the pre-edge region of AER4 implies the presence of at least one iron species in the sample that is not represented by the standards. Figure 38 shows that, again, the Athena software has difficulty distinguishing between iron in illite/smectite and in pure illite.

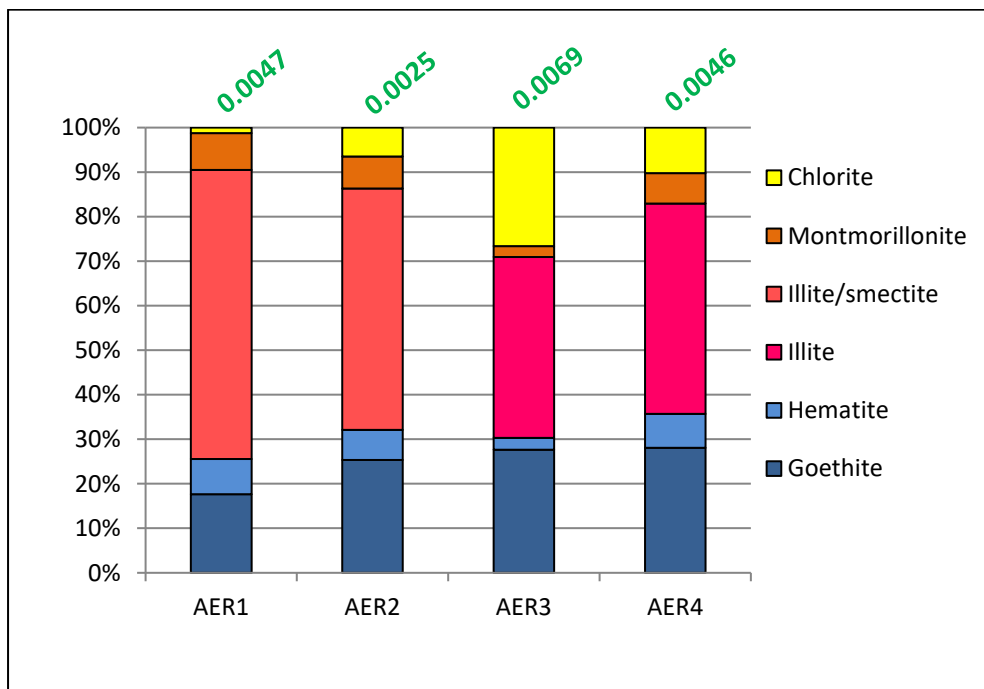


Figure 38 Iron speciation in Bermuda aerosol samples according to Athena LCF

The three LC10 samples were collected in three separate flights across the Loess Plateau in eastern China during a haze event in December 2010 (Li, et al., 2012). The shape of the spectrum of sample LC10-20 in the range of 7130-7137 eV closely resembles the spectrum of chlorite, while the other Loess samples have a more prominent excitation peak at 7134 eV more in common with the illite clays. The pre-edge peak positioning implies that Fe(III) dominates the iron content of the haze particles, and the overall shape of the pre-edges resemble illite across the board. Since the haze was generated primarily from coal combustion in the Taiyuan basin, it was not expected to contain a significant fraction of Fe(II).

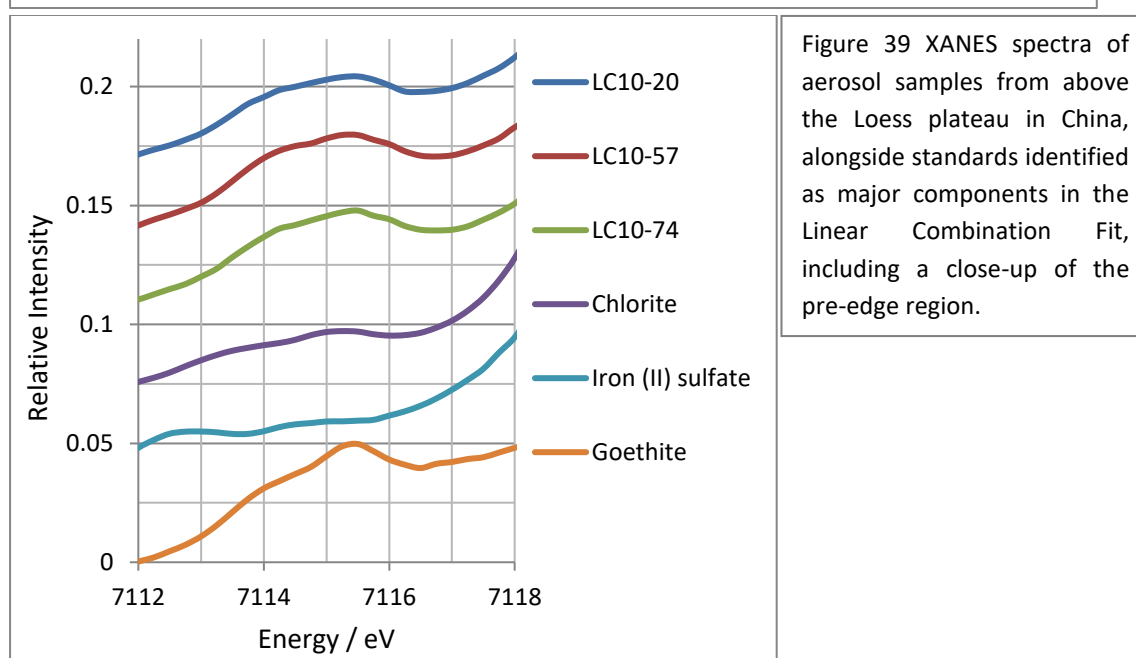
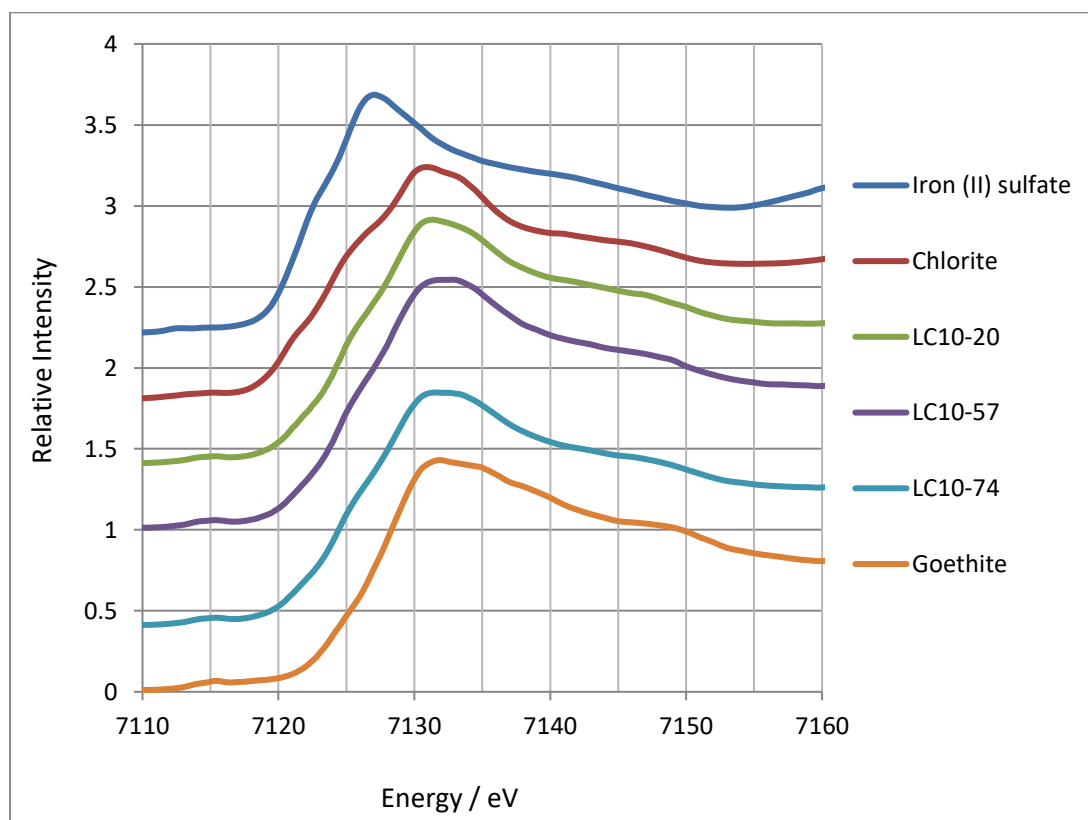


Figure 39 XANES spectra of aerosol samples from above the Loess plateau in China, alongside standards identified as major components in the Linear Combination Fit, including a close-up of the pre-edge region.

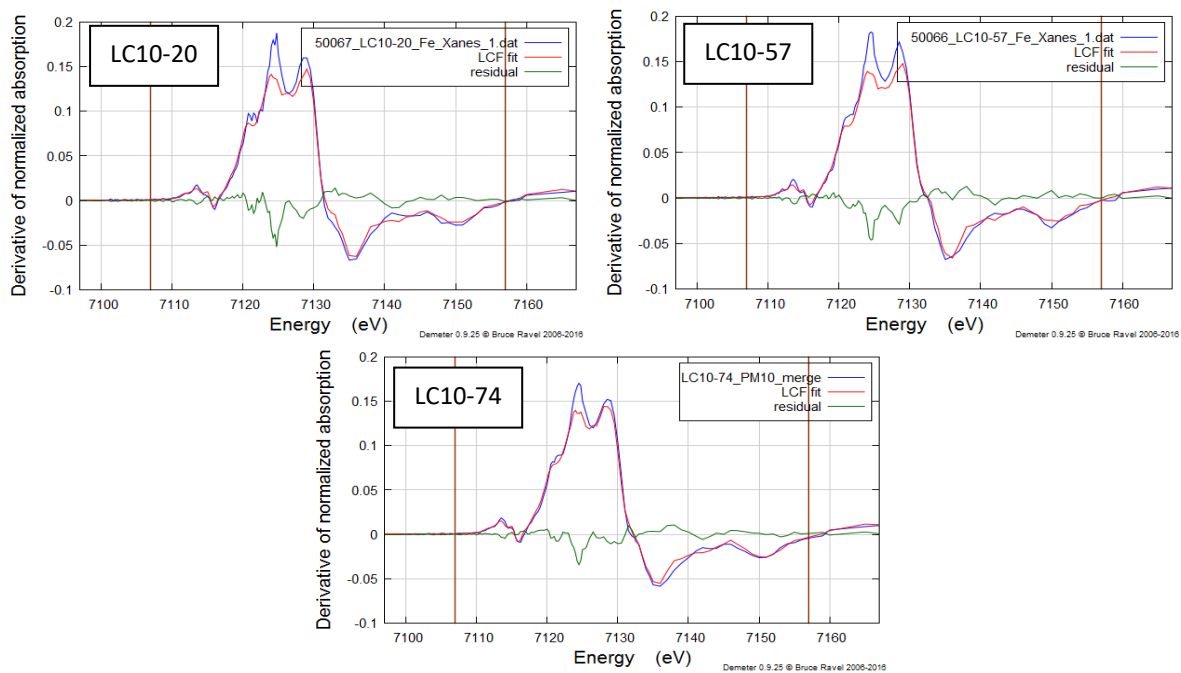


Figure 40 Linear Combination Fits of aerosol samples collected during flights over the Loess plateau, China, with the sample spectrum in blue, the best fit combination of standards in red, and the difference at each point represented as a residual line in green. The brown lines indicate the fitted range.

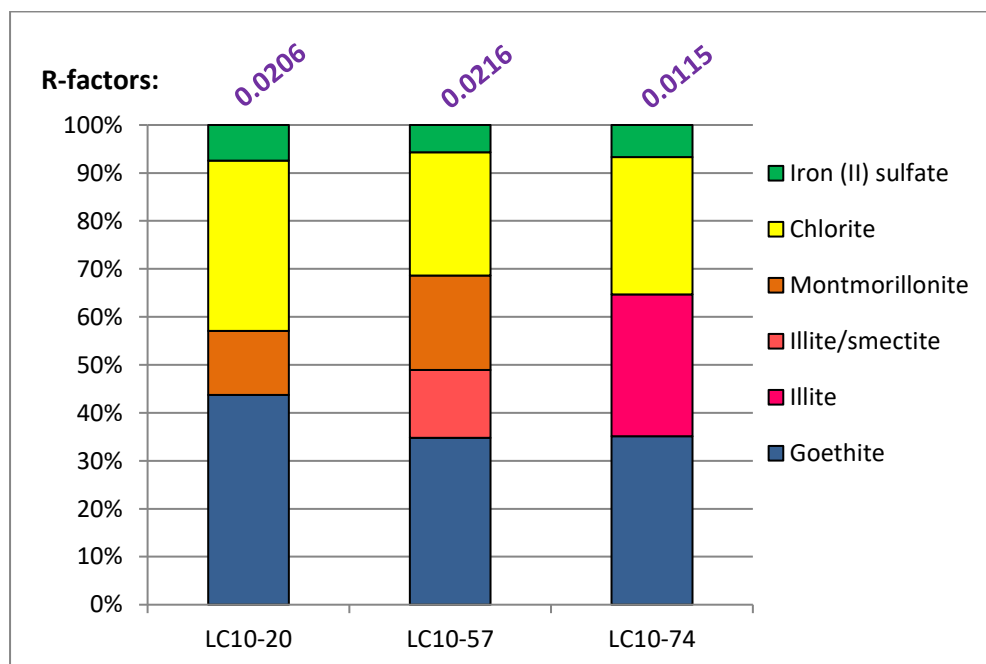


Figure 41 Iron speciation in Bermuda aerosol samples according to Athena LCF

The Loess plateau haze samples in figure 40 fit less well, particularly in the region of 7122-7126 eV where major excitation peaks occur in Fe(II)-rich species like magnetite and chlorite. The LCF speciation reported in figure 41 identifies a small proportion of iron present as ferrous sulfate, although the position of the variation in the fit implies that this may be better represented as another Fe(II) species. It is noteworthy that the iron speciation in the haze samples do not resemble that of coal fly ash (see chapter 3 section 3.6) and are more similar to mineral dust. This implies that coal fly ash did not provide a significant proportion of the iron found in the haze during the sampling period.

### 3.8 Soil Samples: Libya

Ten soil samples were collected by Professor Nick Drake from the area close to Wadi al Ramlah in northeast Libya. The XANES spectra of the samples in figure 42 are quite consistent and strongly resemble the spectrum of the illite-smectite standard. The pre-edge regions show peak positions consistent with Fe(III) rich standards and the peak shapes are again consistent with illite-smectite.

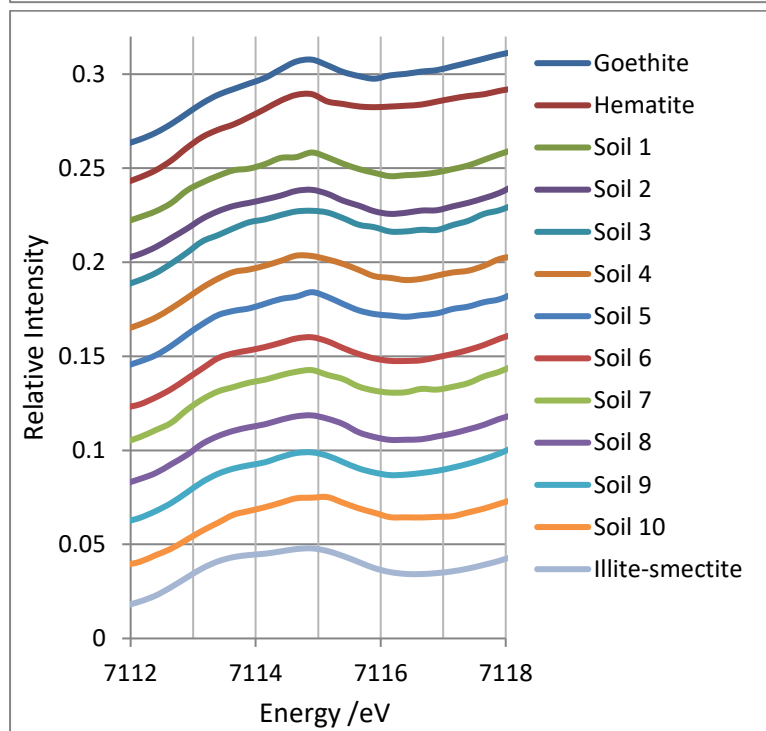
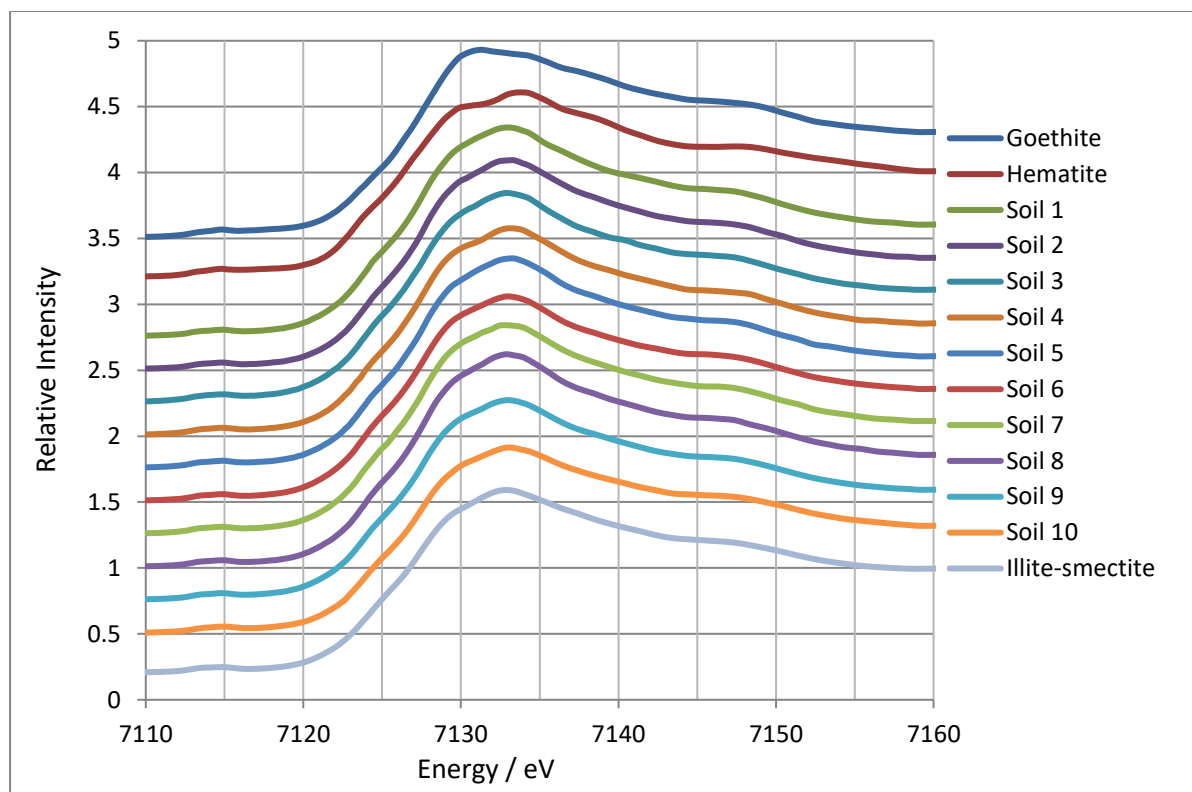


Figure 42 XANES spectra of 10 soil samples from northern Libya alongside standards identified as major components in the Linear Combination Fit, including a close-up of the pre-edge region.

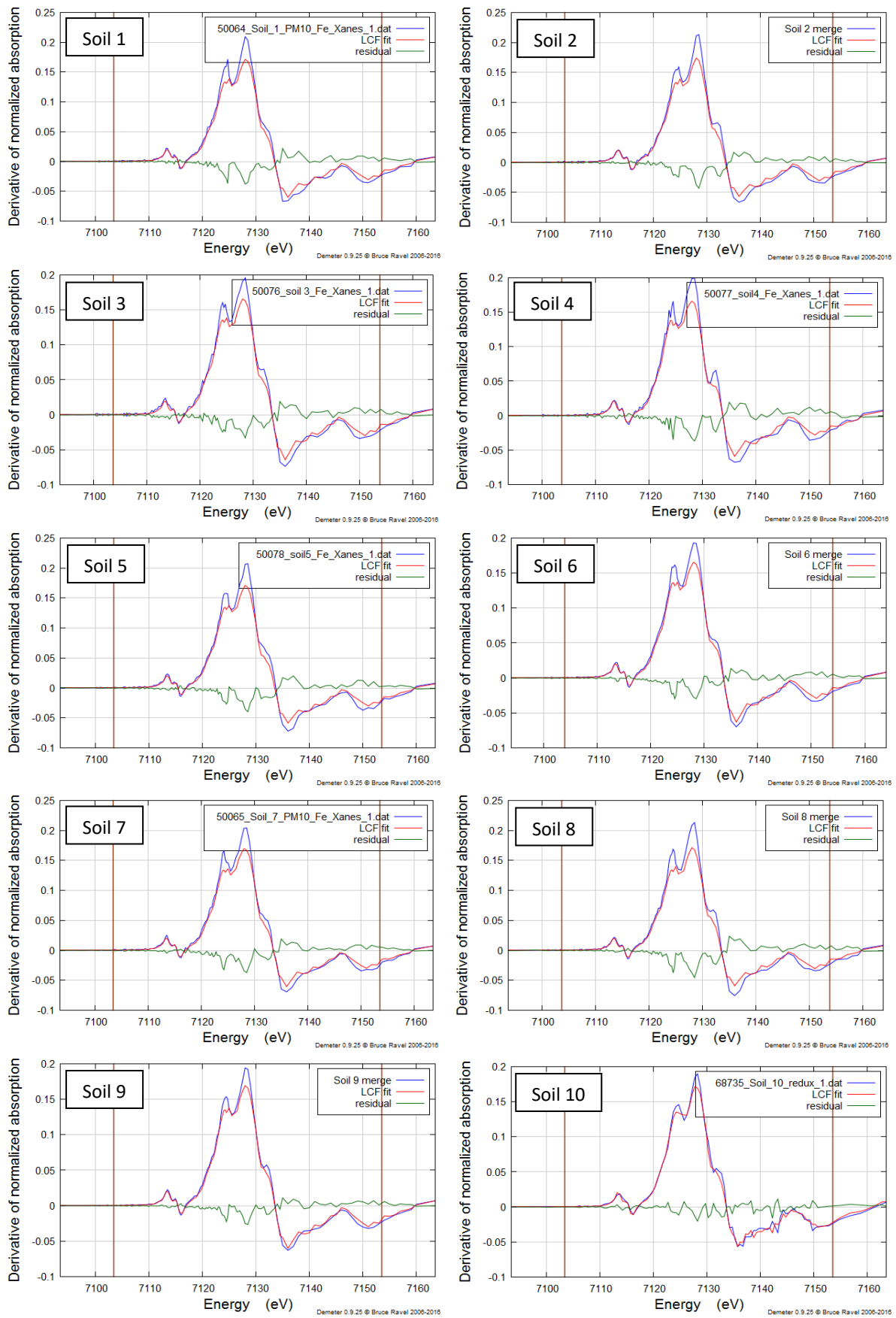


Figure 43 Linear Combination Fits of soil samples collected from northeast Libya, with the sample spectrum in blue, the best fit combination of standards in red, and the difference at each point represented as a residual line in green. The brown lines indicate the fitted range.

Deviations from the best fit of available standards, as seen in figure 43, show some consistency across all of the Libyan soil samples. While the pre-edge regions fit well across the board, implying that the Fe(II):Fe(III) ratio is accurately determined, differences in intensity at around 7124, 7128 and 7133 eV indicate that at least one Fe species is not represented by the standards. Soil in the region has an average organic matter content of <4% (Hegazy, et al., 2011) so organically bound iron is unlikely to be significant and the available mineral iron standards should be sufficient to describe it.

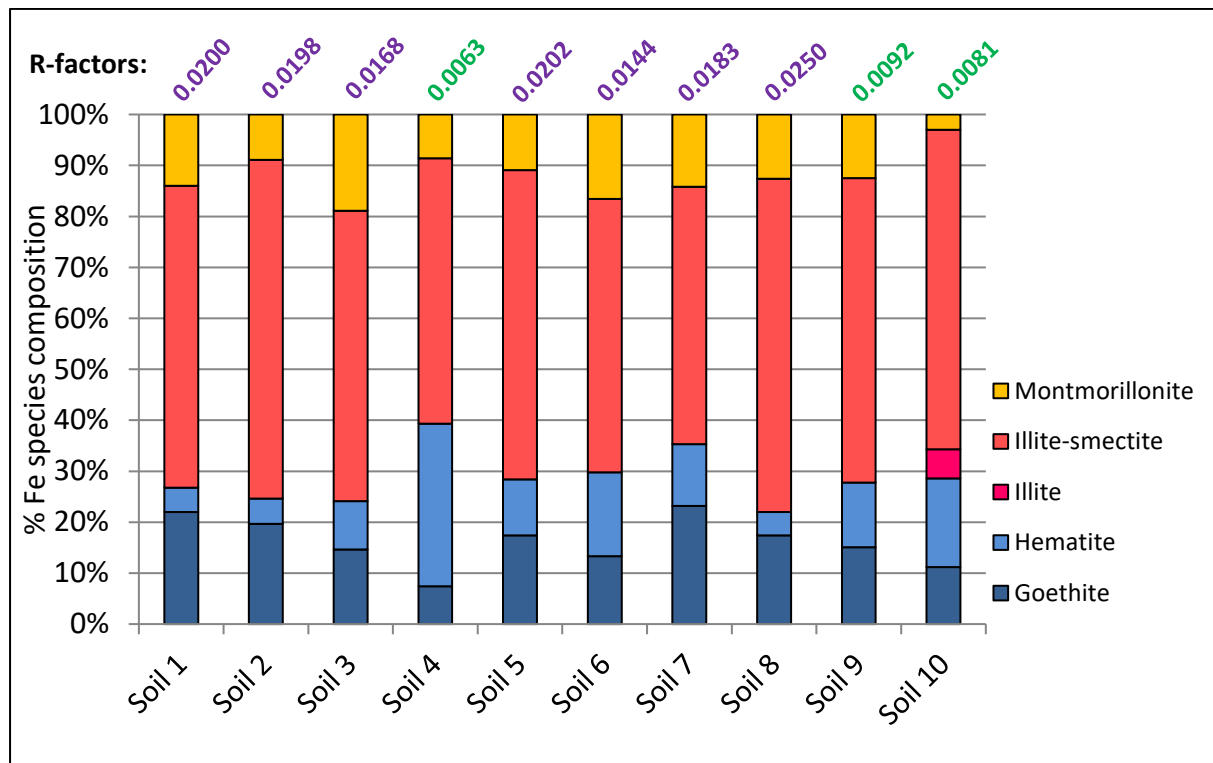


Figure 44 Iron speciation in Libya soil samples according to Athena LCF

Figure 44 shows that the identifiable iron species in the Libyan soil samples break down similarly across all of the samples, with the majority of the resident Fe present within illite-smectite clay and 25-35% of total Fe as common iron oxides.

### 3.9 Soil Samples: Bodélé Depression

Bodélé soil samples were collected from a variety of environs from sand dunes to river banks (see table 3) by Prof. Charlie Bristow. The Bodélé depression in Chad was formed from a desiccated paleolake, and the erosion of the soft diatomite lake bed is presently the world's largest source of windborne mineral dust (Bristow, et al., 2009) (Koren, et al., 2006). Previous analysis of samples from the Bodélé depression (Shi, et al., 2011) has found unusually low concentrations of iron compared to other regions, but there is still sufficient iron to generate XANES spectra with low noise.

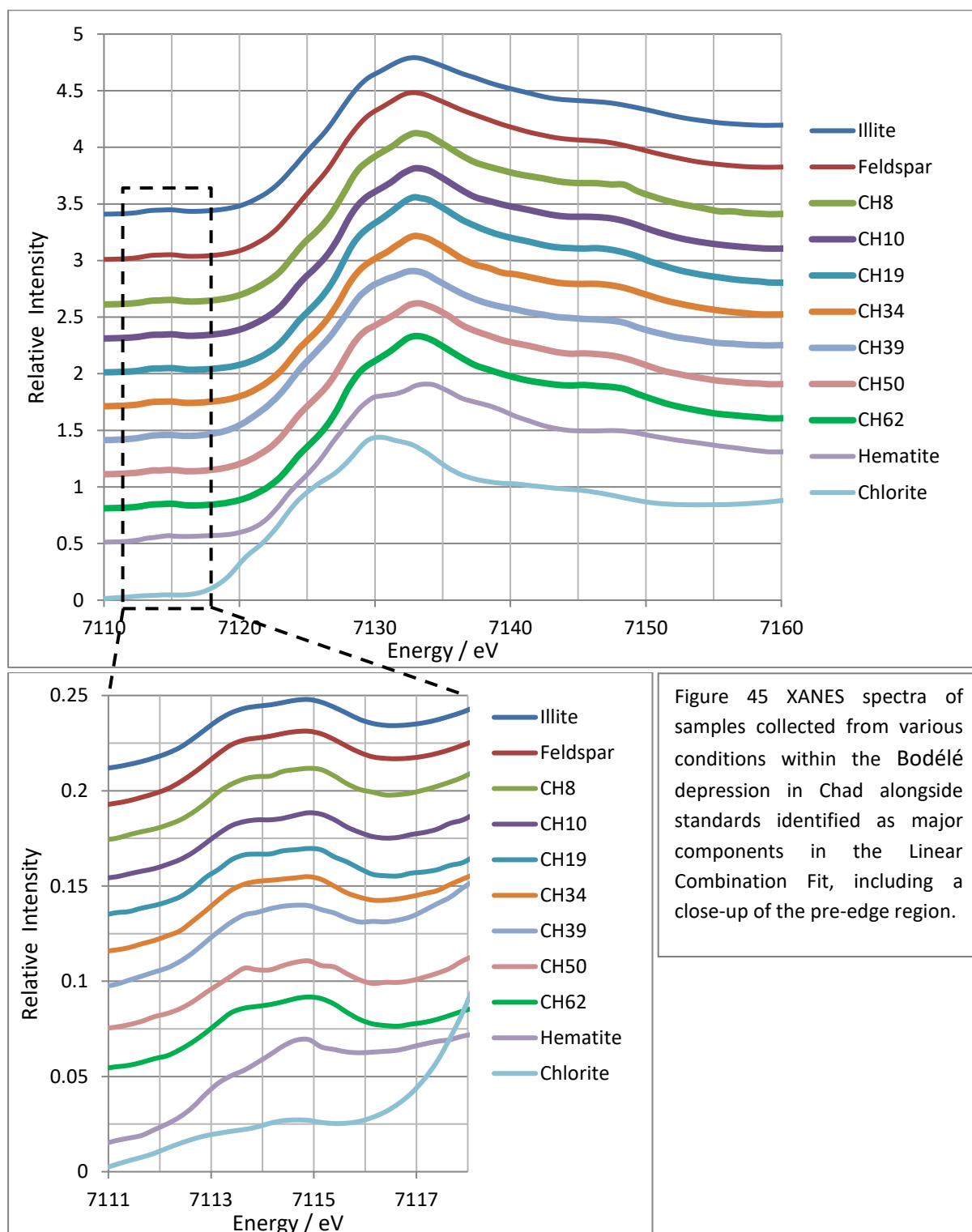


Figure 45 XANES spectra of samples collected from various conditions within the Bodélé depression in Chad alongside standards identified as major components in the Linear Combination Fit, including a close-up of the pre-edge region.

Examination of the pre-edge regions of the Bodélé samples in figure 45 indicates that the samples are all Fe(III) rich, which excludes siderite ( $\text{FeCO}_3$ ), a common authigenic mineral found in paleolake sediments (Felder, et al., 2006) as a major component of total iron.

The pre-edge regions of the linear combination fits in figure 46 show that the Fe(II):Fe(III) ratio of the samples is in line with those of the applied standards. Figure 47 shows that illite-smectite is the closest fit to the Fe species present in most of the Bodélé samples with an Fe(II):Fe(III) ratio of 1:9.

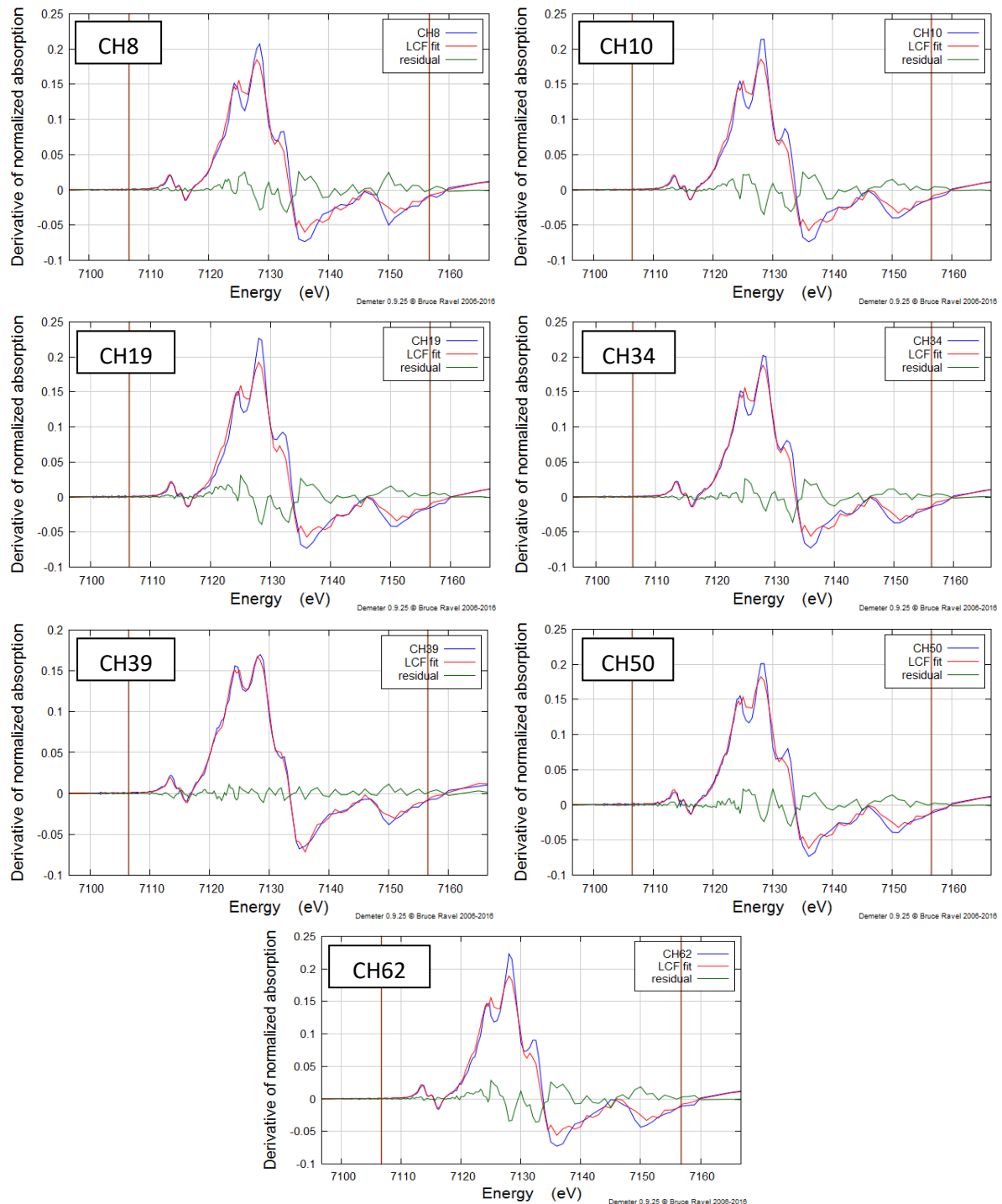


Figure 46 Linear Combination Fits of soil samples collected from the Bodélé depression, Chad, with the sample spectrum in blue, the best fit combination of standards in red, and the difference at each point represented as a residual line in green. The brown lines indicate the fitted range.

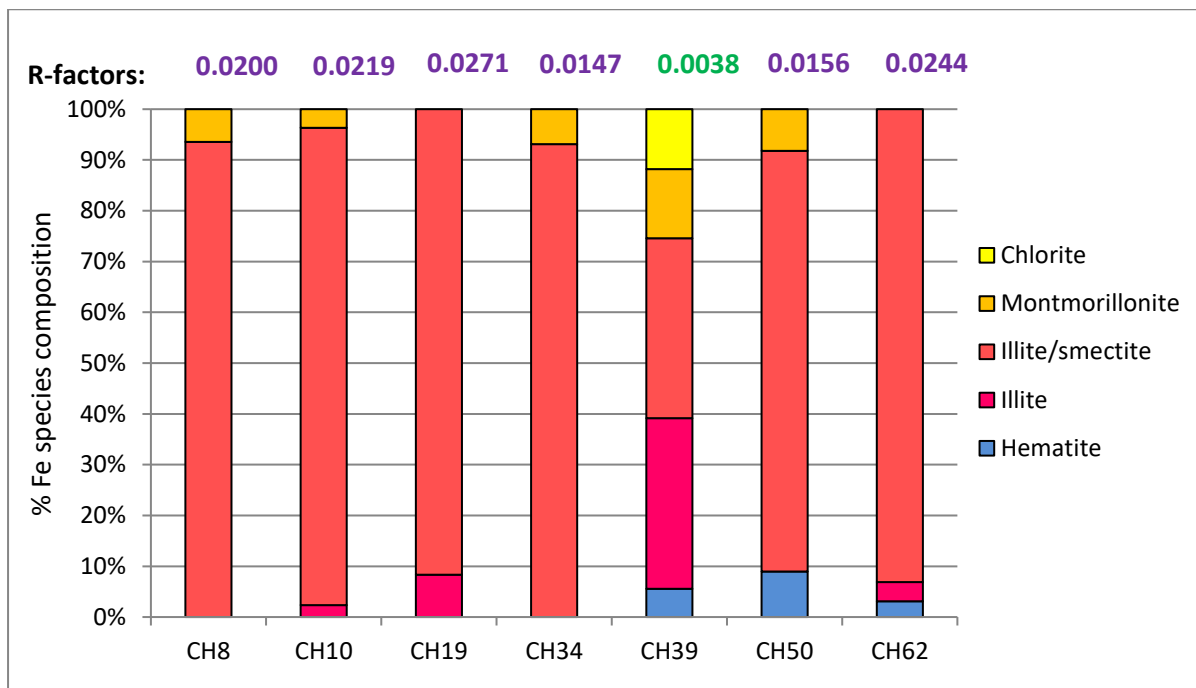


Figure 47 Iron speciation in Bodélé depression soil samples according to Athena LCF

Deviation from the best fit of standards occurs at every major peak in the derived spectra in every sample with the exception of CH39, as shown in figure 46. Combined with the concerning reported R-factors for these samples, the report of illite-smectite can best be described as a close resemblance to the iron-bearing minerals in Bodélé soil rather than a positive identification. Only sample CH39, mudstone from the Angama delta, fits the available standards well and shows that ~95% of iron is bound within clay particles and is not readily bioavailable.

### 3.10 Natural mineral sample overview

XANES can at best be described as a semi-quantitative technique with regard to the speciation of natural mineral samples. The comparison of potential iron solubility based on XANES report of speciation to measured solubility in mineral dust shown in figure 19 shows reasonably good agreement with results  $\pm 10\%$  of each other. By comparison, samples from the Bodélé depression whose best linear combination fits indicate little even sparingly soluble iron across the board, while chemical extraction (Shi, et al., 2012) found around 20% dithionite extractable species (most commonly goethite and hematite) in samples from the same locations.

This contrast between the two sample sets illustrates the requirements for accurate XANES fitting, namely the need for an abroad range of appropriate standards informed by earlier processing by techniques that do not require synchrotron radiation such as sequential extraction and/or XRD.

### 3.11 Ship emitted particles

While ship emissions are a small contribution to the global aerosol budget, generating 1.2-1.6 Tg/yr compared to >1000 Tg/yr for mineral dust (Corbett & Koehler, 2003) (Han, et al., 2012), the iron present in ship emissions is likely to be in more soluble forms (Schroth, et al., 2009) (Ito, 2013). The heavy residual oil used as fuel by large ships is higher in sulfur than other liquid fuels, which has led to legal restrictions on its use in busy shipping lanes as an ongoing public health concern (European Commission, 2016). Particulate emissions from burning heavy oil are sulfate-rich (Mueller, et al., 2011) and sulfate-rich plumes are more likely to form iron (III) sulfate (Oakes, et al., 2012), which is highly water soluble and thus readily bioavailable. Existing studies on Fe speciation in oil fly ash from power stations have found that iron (III) sulfate is the dominant form of Fe (Schroth, et al., 2009).

The samples in table 4 represent the first emissions collected directly from ship stacks and analysed with synchrotron radiation, allowing both speciation proportionation by XANES and XRF mapping of elements. One sample, CB116P, was collected directly from the funnel of a Norwegian research ship by a group led by Dr Jana Moldanová (Moldanova, et al., 2009). The sample was collected on filters via a commercial dilution system attached directly to the ship's stack. An XRF map was generated to examine the content and distribution of transition metals across the filter (figure 48).

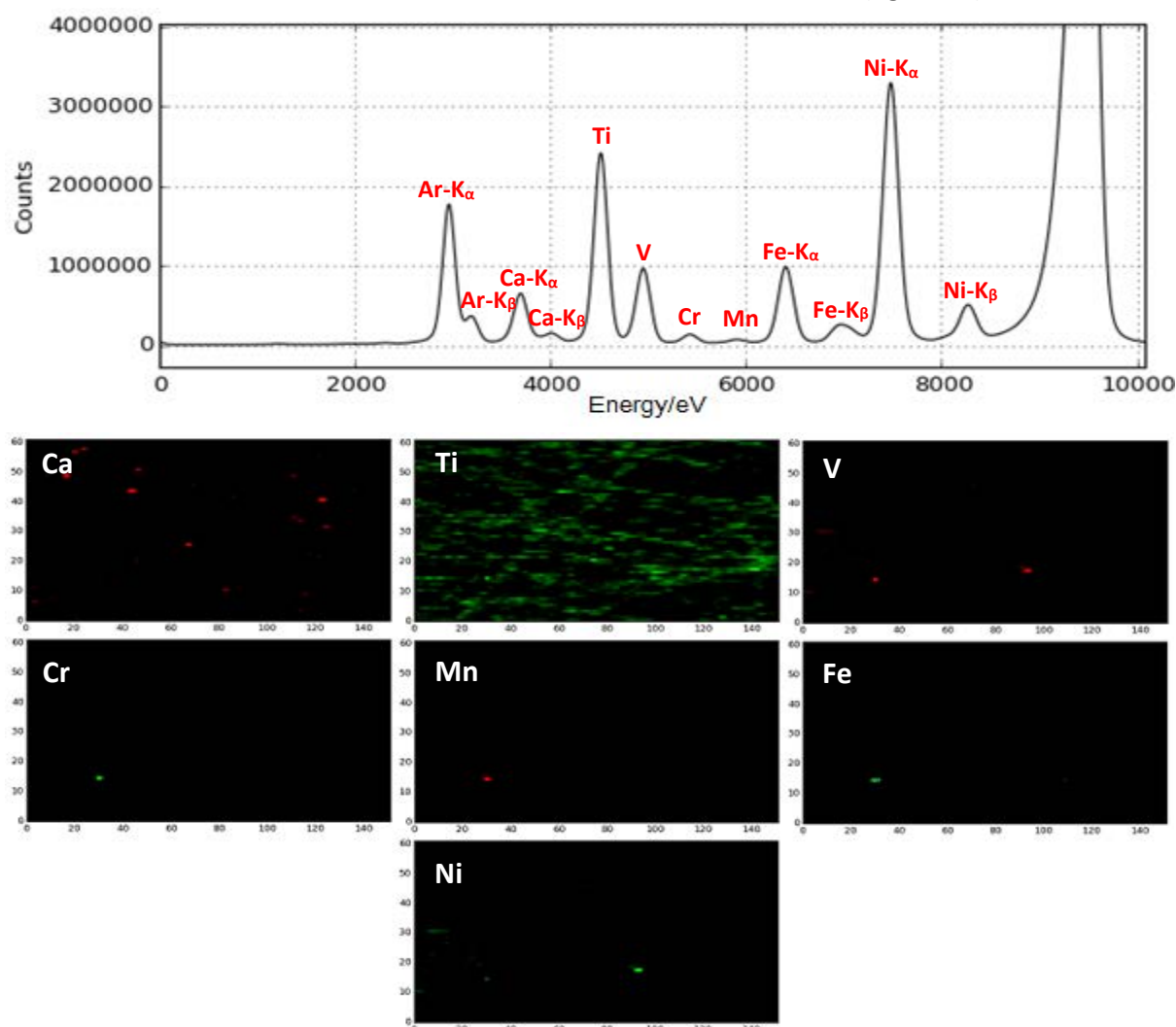


Figure 48 XRF spectrum and 450 x 600  $\mu\text{m}$  elemental maps of particulate sample collected directly from the chimney of a Norwegian research vessel

The hotspot in the bottom left appears to account for the majority of the iron, manganese and chromium signals in the mapped region as well as a significant proportion of the nickel and vanadium. The XRF spectrum agrees with the mass spectroscopy results taken from the emissions soon after sampling (Moldanova, et al., 2009) apart from the strong reading for titanium. The distribution of titanium appears to line up with the fibres of the filter, which implies that some or all of the titanium signal comes from white pigment in the filter itself rather than emissions.

A further XRF spectrum was collected from the sample provided by fellow PhD student Chao Zhang, from a Chinese research vessel (figure 49). Although the vessel asked not to be identified, the sample was provided specifically for this research and will not feature in Mr Zhang's own thesis. The I18 beamline was adjusted to 7200 eV to avoid fluorescence of cobalt that might interfere with the  $K_{\beta}$  peak of iron.

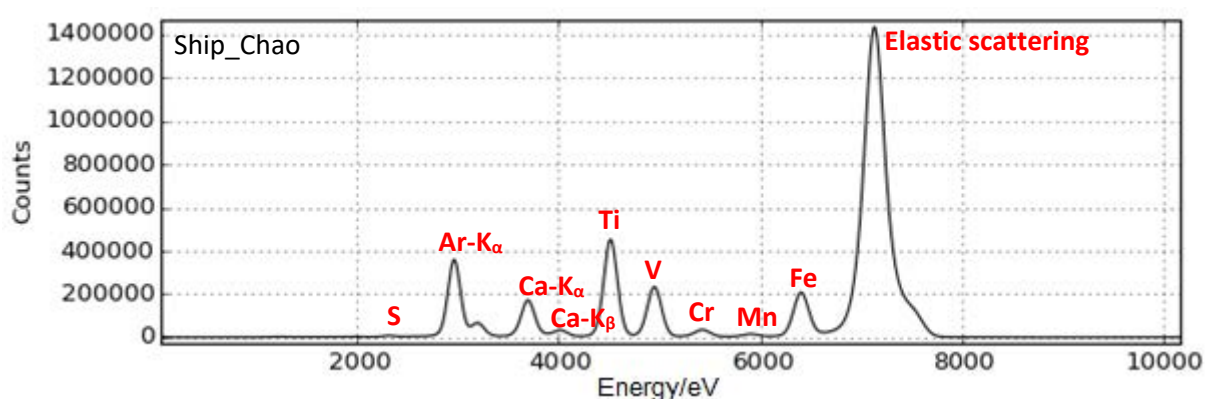


Figure 49 XRF spectra of ship emissions collected by Chao Zhang in China

The identity and proportion of metals in the ship\_chao sample is similar to CB116P. Again, the titanium signal is unlikely to be representative of the emitted particles due to the use of titanium as a white pigment in the filters.

Due to the low iron content of many of the samples, resulting in noisy XANES spectra as seen in figure 50, measures were taken to concentrate the poly\_3 sample which was found in initial scans to generate a particularly weak spectrum. The “poly” samples were collected from the same research vessel burning heavy fuel oil in an Emission Control Zone off the coast of Sweden (Moldanová, et al., 2013), where both fuel and emissions were found to be rich in sulfur. The poly\_3 sample was placed in a container of ethanol and sonicated to remove as much solid material as possible from the filter. The ethanol suspension was evaporated to dryness and the solid particulates were resuspended in methanol and applied to Kapton tape as a more concentrated spot. While the XANES spectrum in figure 50 still shows some noise, the poly\_3 spectrum is smoother than the poly\_4 which was left as solid particles on its filter.

As shown in figure 50, the spectrum of a “hotspot” area of the CB116P filter is similar to that of an area with a less intense iron signal, which suggests that the iron present in the hotspot is a concentrated spot of particulate fuel exhaust rather than a fragment of refined metal from engine wear.

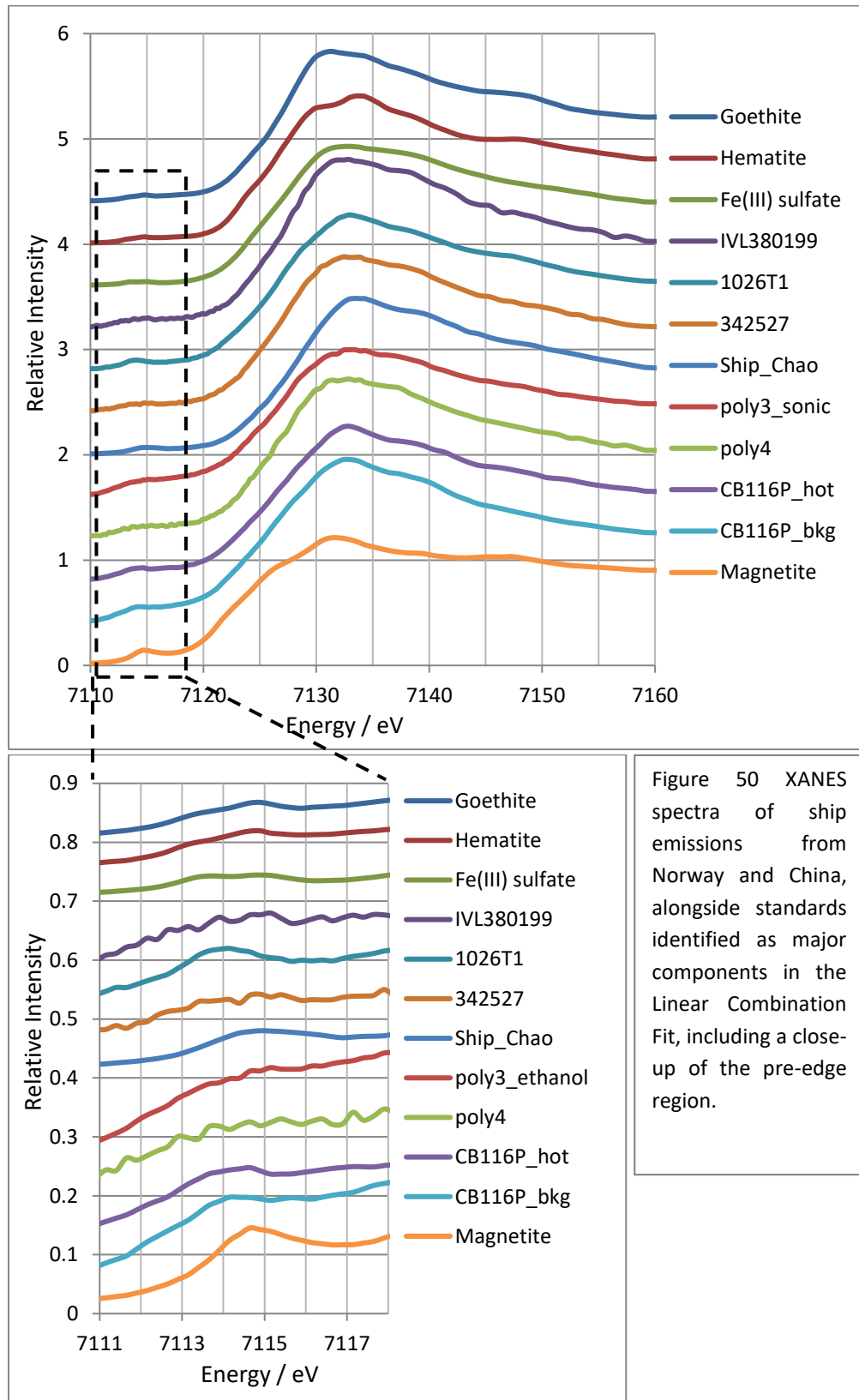


Figure 50 XANES spectra of ship emissions from Norway and China, alongside standards identified as major components in the Linear Combination Fit, including a close-up of the pre-edge region.

All of the sample spectra apart from the poly3 & poly4 samples show a distinct shoulder at around 7140 eV, in common with the spectrum of iron (III) sulfate. Examining the pre-edge regions reveals that some samples, in particular 1026T and CB116P, have centroids shifted towards 7114 eV, implying a significant proportion of Fe(II) among the iron in the exhaust. A high Fe(II) : Fe(III) ratio is unexpected because of the highly oxidising conditions inside a ship's engine, although Fe(II)-rich magnetite has been detected in residual oil fly ash (Chen, et al., 2004) (Flanders, 1994).

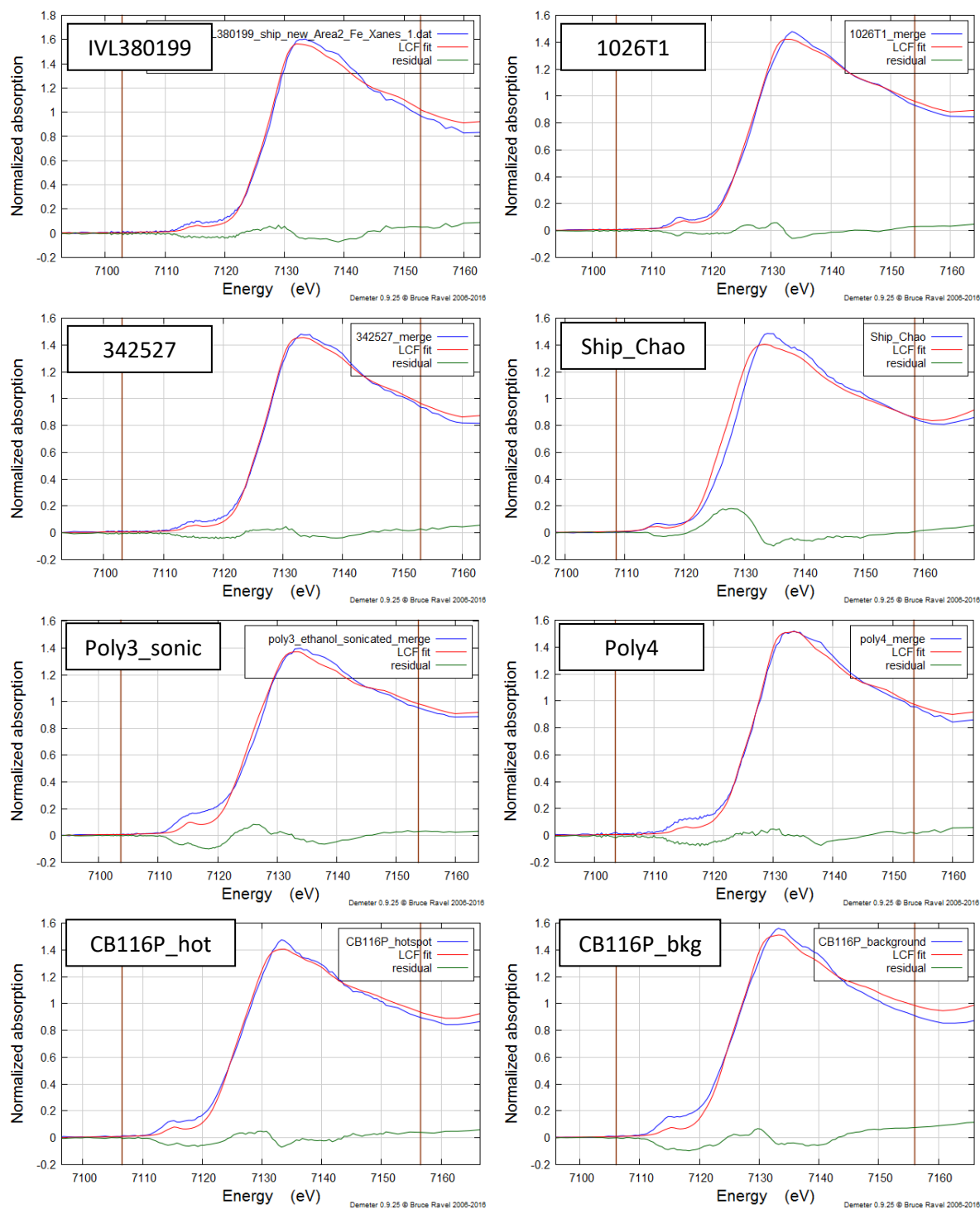


Figure 51 Linear combination fits of all ship emission samples, with the sample spectrum in blue, the best fit combination of standards in red, and the difference at each point represented as a residual line in green. The brown lines indicate the fitted range.

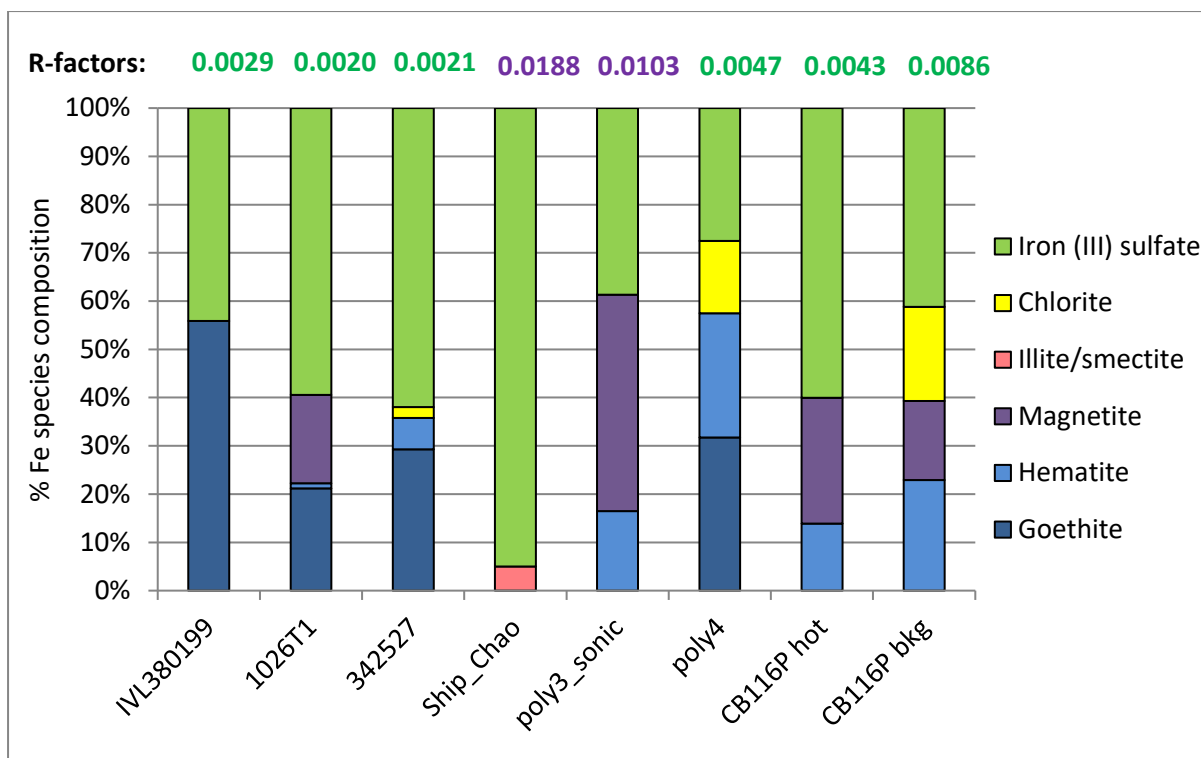


Figure 52 Iron speciation in ship emission samples according to Athena LCF of normalised spectra

The results of linear combination fitting (figure 52) line up with existing literature on oil fly ash (Chen, et al., 2004) (Schroth, et al., 2009) with iron (III) sulfate appearing as a major constituent of the iron in each sample, alongside common combustion products magnetite and hematite. From the fits in figure 51, the gaps between the pre-edge peaks of samples and best-fits are mostly a matter of intensity rather than position and could be interpreted as artefacts of Athena's normalisation of the weak sample signals as much as unrepresentative speciation.

The exceptions are samples 1026T1 which exhibits a pre-edge centroid shifted more towards the Fe(II) region than the best fit of standards allows, and ship\_Chao that exhibits a spectrum shape close to that of pure iron (III) sulfate but shifted slightly to higher energy. The sample spectrum does not show any issues with energy shift or post-edge positioning that might cause an error in fitting, so the poor fit implies at least one other Fe(III) species is present in the sample that is not represented by the available standards.

These results indicate that a substantial fraction of the iron found in particulate emissions from ships burning heavy fuel oil is present as highly water soluble ferric sulfate, similar to the fly ash of oil fired power stations (Schroth, et al., 2009) and in line with the predicted speciation previously applied to the IMPACT atmosphere-ocean model (Ito, 2013) which assigns high Fe solubility to ship emissions. The proportion of ferric sulfate to less soluble iron species like magnetite and goethite varies widely between sources, most likely determined by fuel quality and engine type. Thus, total iron content will not necessarily be an indicator of available iron content. Future measurements will be further complicated by the presence of particles of engine wear in particulate samples that are also Fe-rich.

### 3.12 Particles from Biomass Burning

Particulates generated by biomass burning are a known source of bioavailable nitrogen (Lobert, et al., 1990), but as a source of iron it is still poorly understood. Measurements of iron solubility in biomass ash varies from as little as 2% of total iron (Guieu, et al., 2005), to 5-15% (Fu, et al., 2014) (Holly, et al., 2016) or as much as 18% (Bowie, et al., 2009). A group working under Dr Adewale Taiwo at the University of Agriculture in Abeokuta, Nigeria collected multiple samples of biomass ash from different sets of conditions, from controlled agricultural burning to forest fires, along with collections from lab-based burning.

XRF maps were produced to compare the concentration and distribution of elements across samples collected in the field against those collected in a controlled environment.

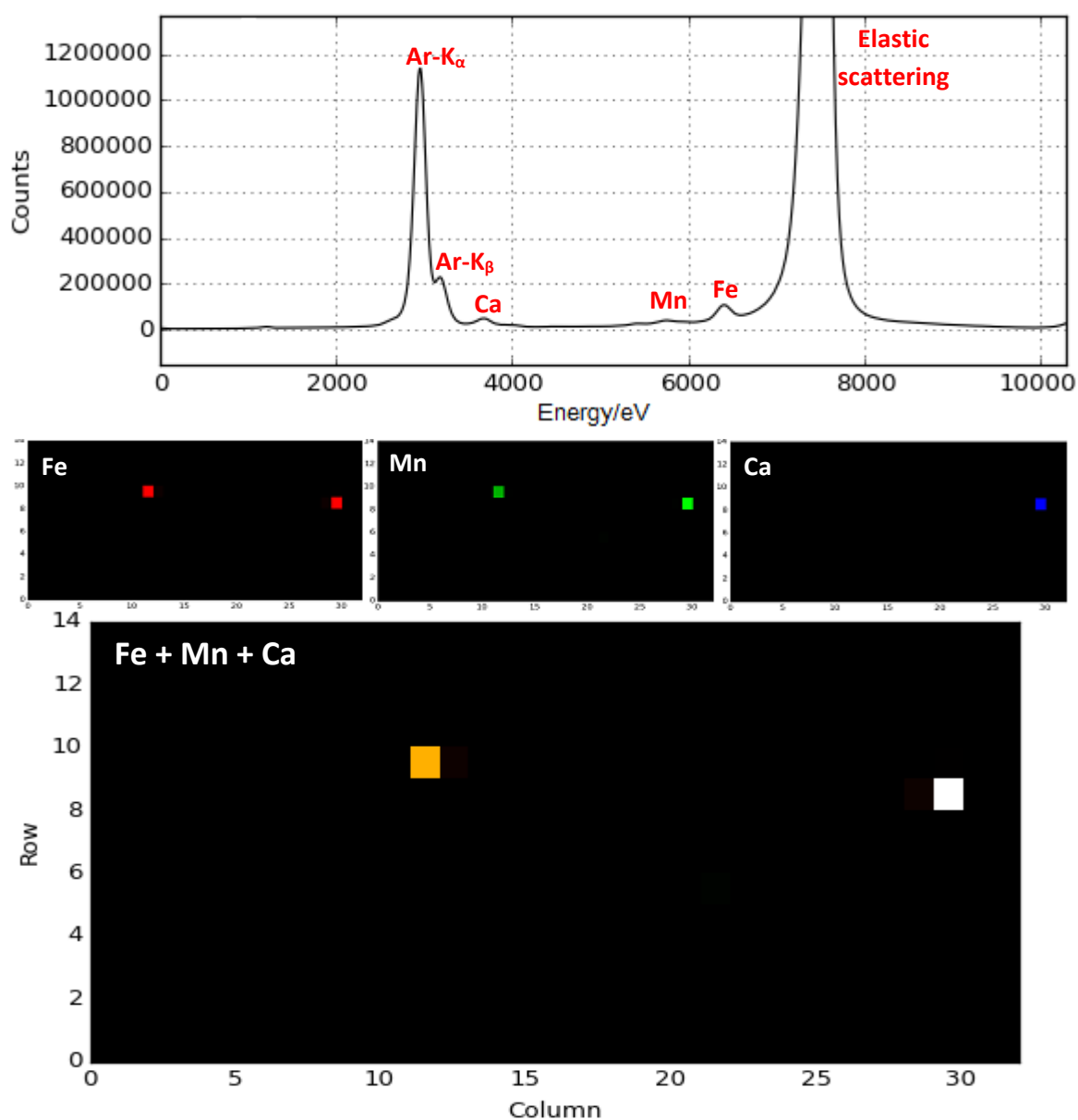


Figure 53 XRF spectrum and 640 x 280  $\mu\text{m}$  map of ash collected from flaming cornstalks in laboratory conditions. PyMCA can overlay up to 3 different element maps, combining the preselected colours in the manner of coloured light- red and green overlapping appears yellow, red and blue appear magenta, green and blue appear cyan and if all three elements are present in the same 20 x 20  $\mu\text{m}$  region, they appear in white.

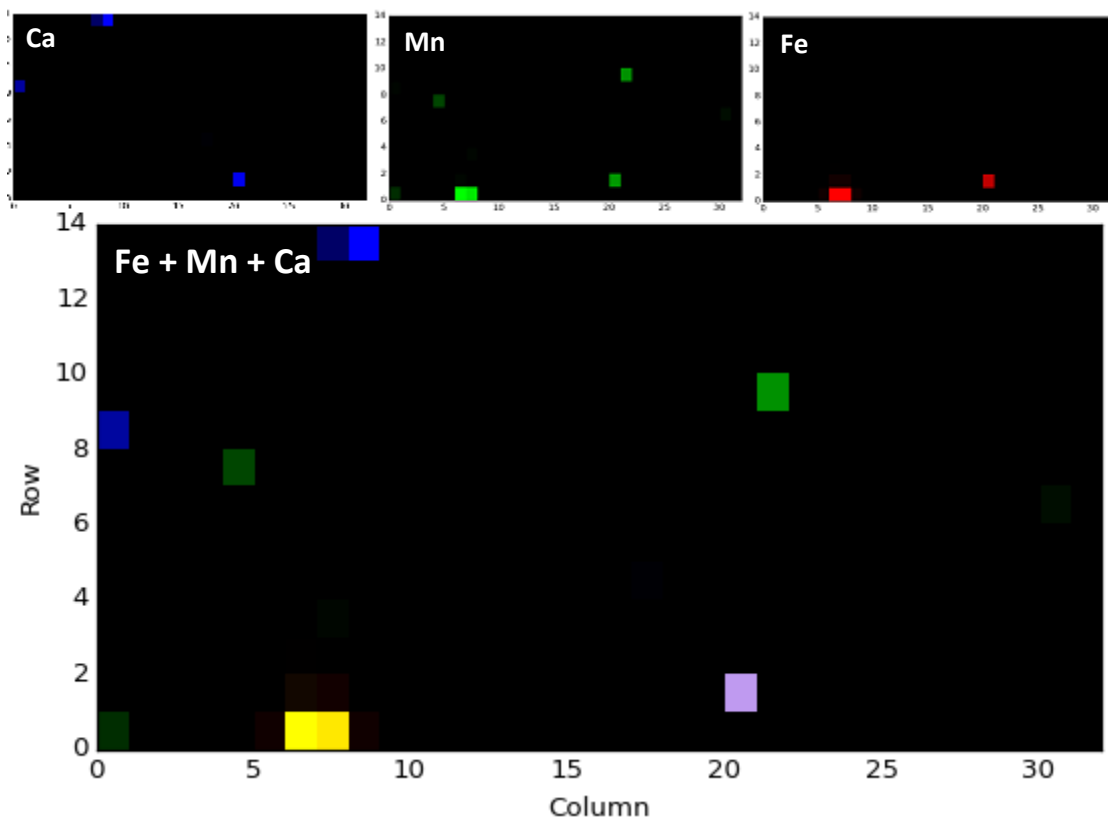
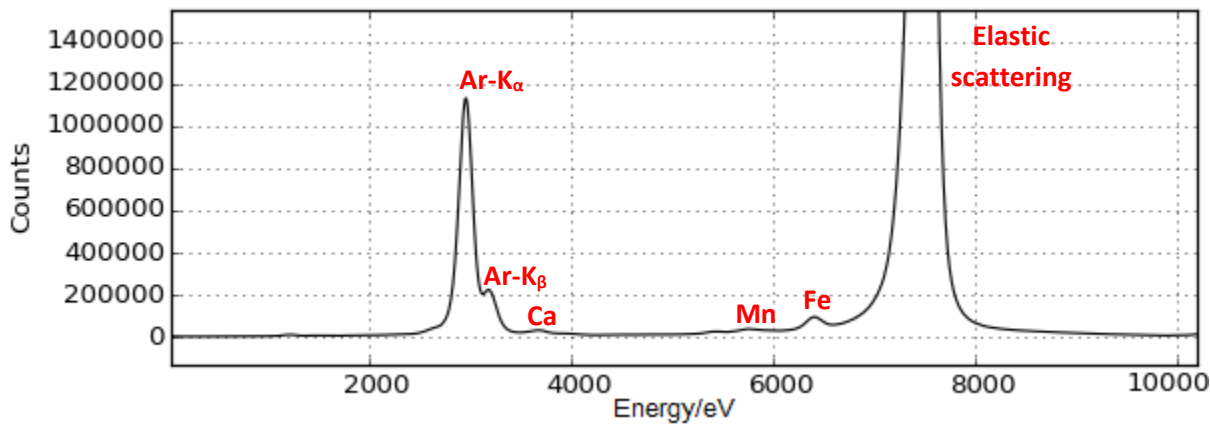


Figure 54 XRF spectrum and 640 x 280  $\mu\text{m}$  element map from a second site on the "flaming cornstalk" lab-based sample filter

Figures 53 and 54 show that the only detectable metals in one of the lab-based samples are confined to a small number of hotspots <20 to  $\sim$ 40  $\mu\text{m}$  in size. The sample filter is coated in dark material that is assumed to be mostly black carbon, which is not detectable by the XRF setup. The sample did not contain enough iron to generate a XANES spectrum.

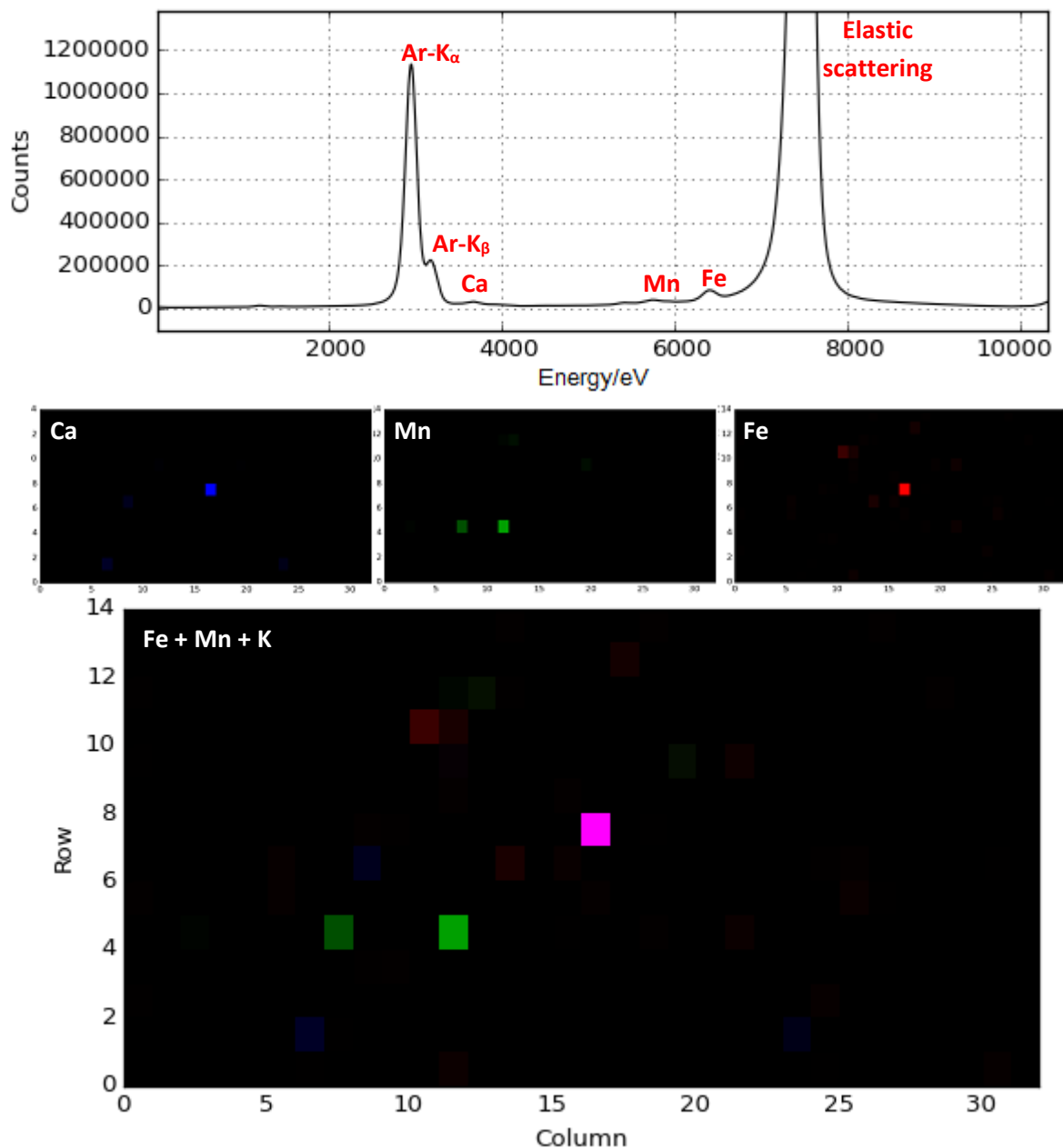


Figure 55 XRF spectrum and 640 x 280  $\mu\text{m}$  element map of smouldering cornstalk sample collected under laboratory conditions

Figure 55 shows the distribution of metals in ash collected from burnt cornstalk samples once the flames have been extinguished. Distribution of metals is wider than in the ash from the flaming samples with less overlap in hotspots, but overall concentration are still low and again there was insufficient iron to generate a usable XANES spectrum.

Biomass ash samples taken from field sites, as illustrated in figures 48 and 49, show more detectable metals and greatly elevated iron concentrations over the lab-based samples. As with the lab-based samples, field-based samples followed a pattern of potassium and calcium (present in corn silage at 9000 and 2500 ppm respectively, all values from (Troeh & Thompson, 2005)) appearing evenly distributed across the XRF maps while iron (90 ppm), manganese (60 ppm) and titanium (trace) are found overlapping on metal-rich hotspots.

All of the field-based samples contained enough iron to generate XANES spectra.

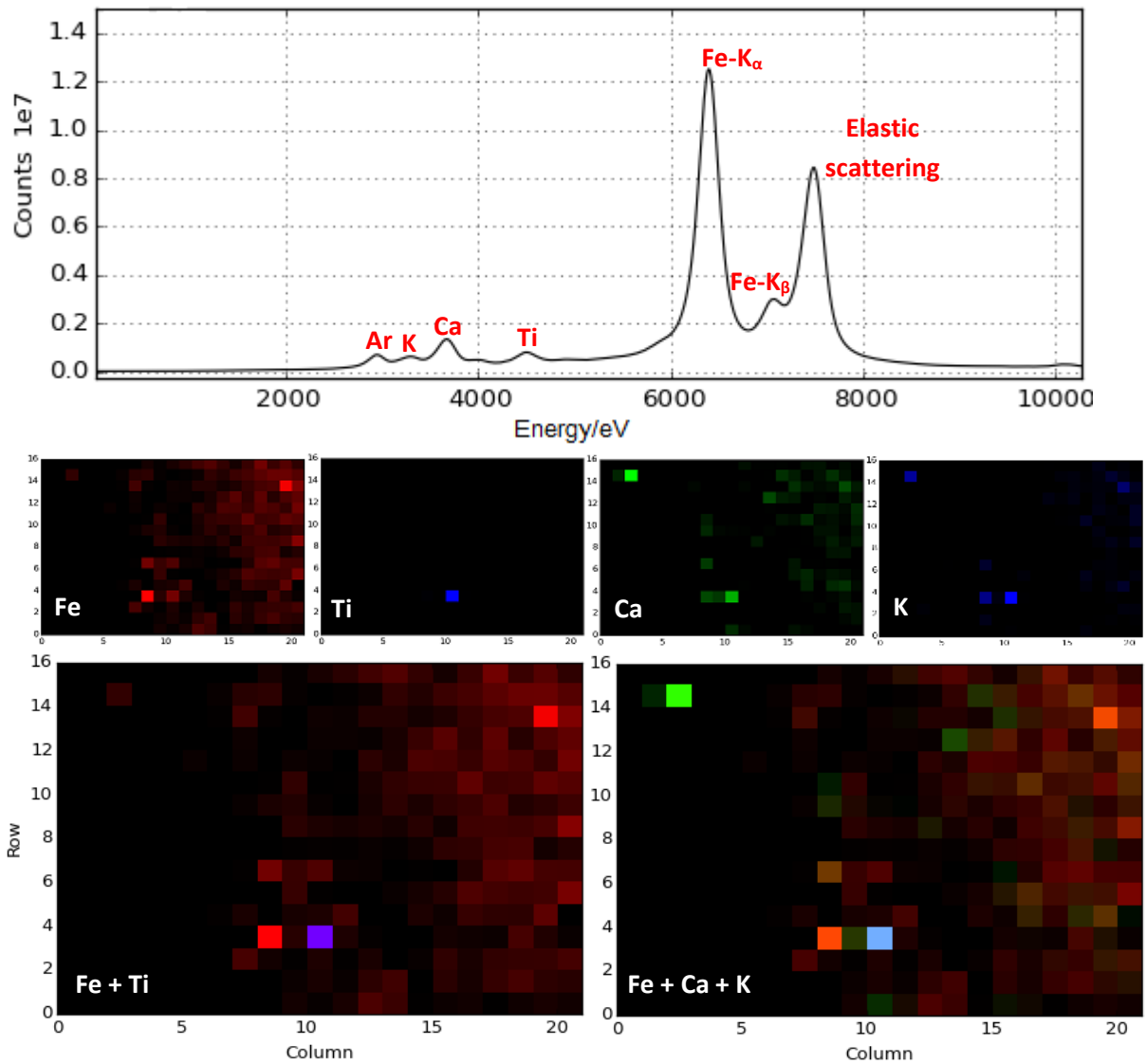


Figure 48 XRF spectrum and 420 x 320  $\mu\text{m}$  elemental maps of field biomass ash sample ZB5

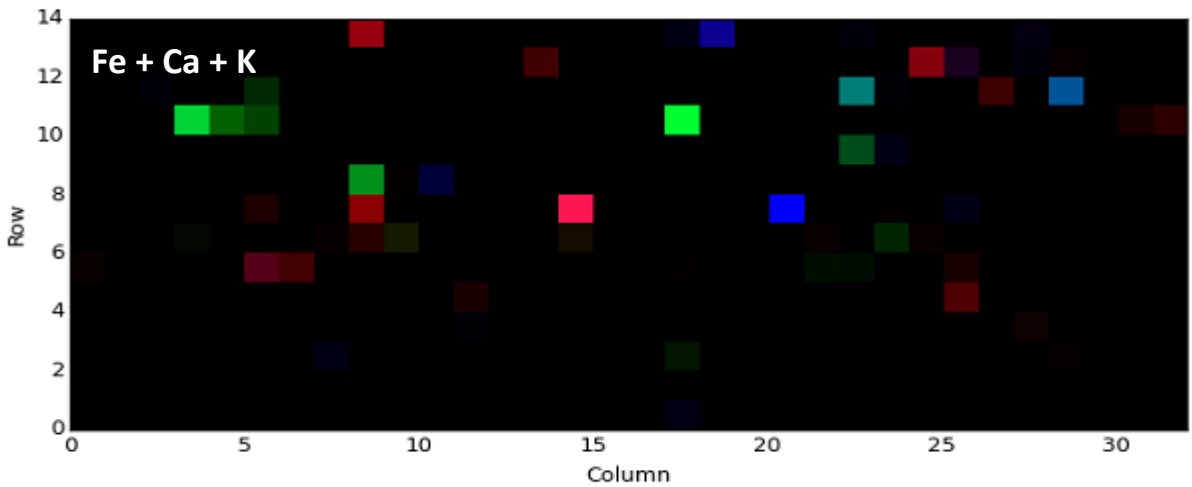
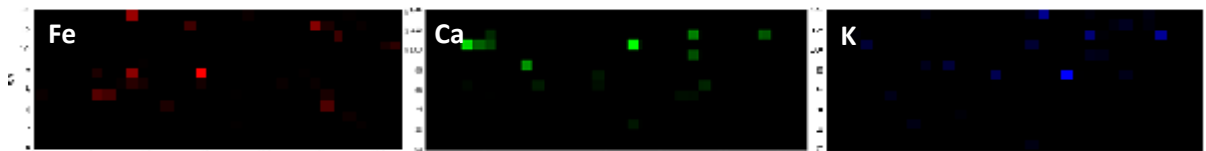
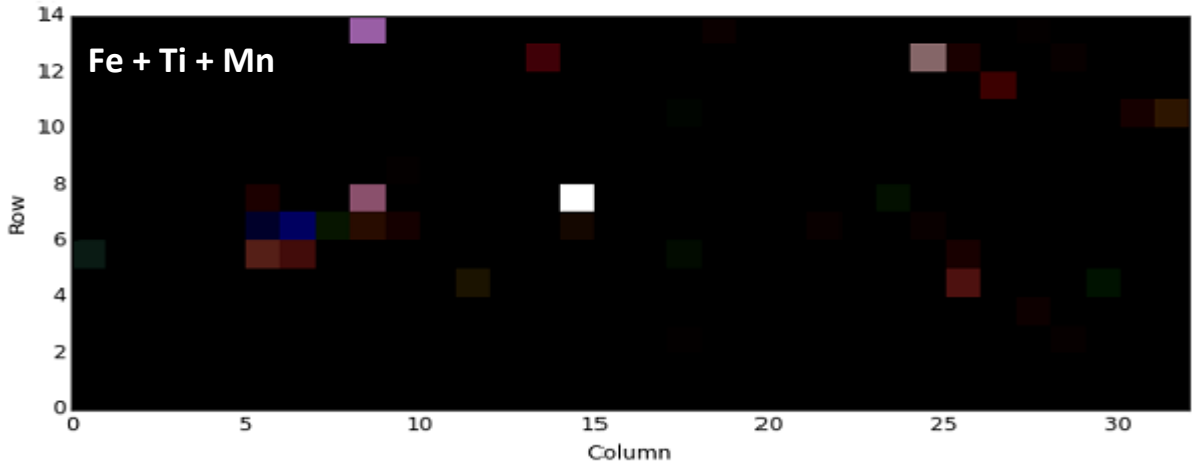
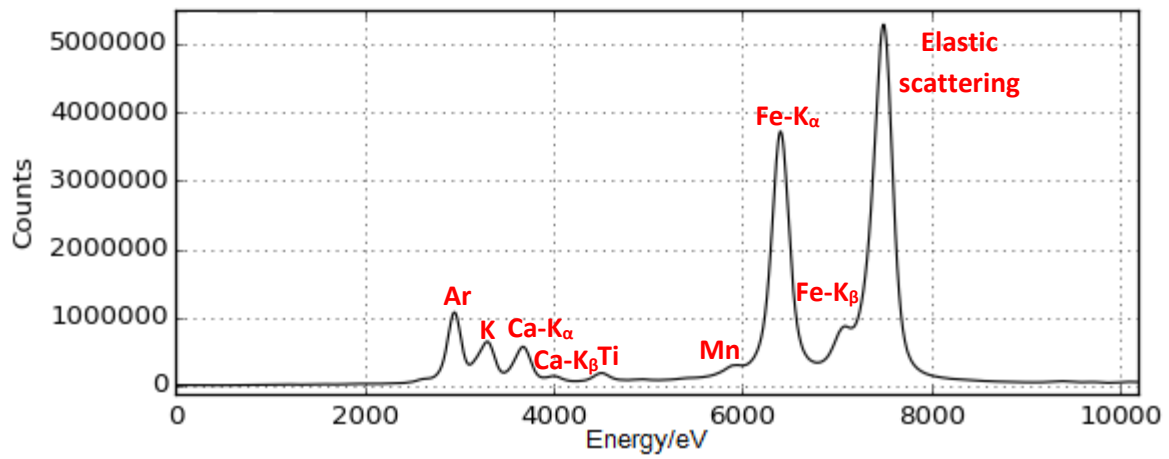


Figure 57 XRF spectrum and 640 x 280  $\mu\text{m}$  elemental maps of field biomass ash sample ZB15, with iron overlaid with other prominent transition metals (top) and alkali & alkali earth metals (bottom).

Figure 58 shows the contrast between two 20 x 20  $\mu\text{m}$  regions of a single field sample filter, identified in a preliminary scan as a representative “background” area and an iron-rich hotspot. The proportion of metals in both sites is similar, and the “hotspot” site contains ~65% more iron than the background ( $6.2 \times 10^7$  counts vs  $3.76 \times 10^7$  counts). This indicates that iron is still present between the hotspots, rather than confined to them exclusively.

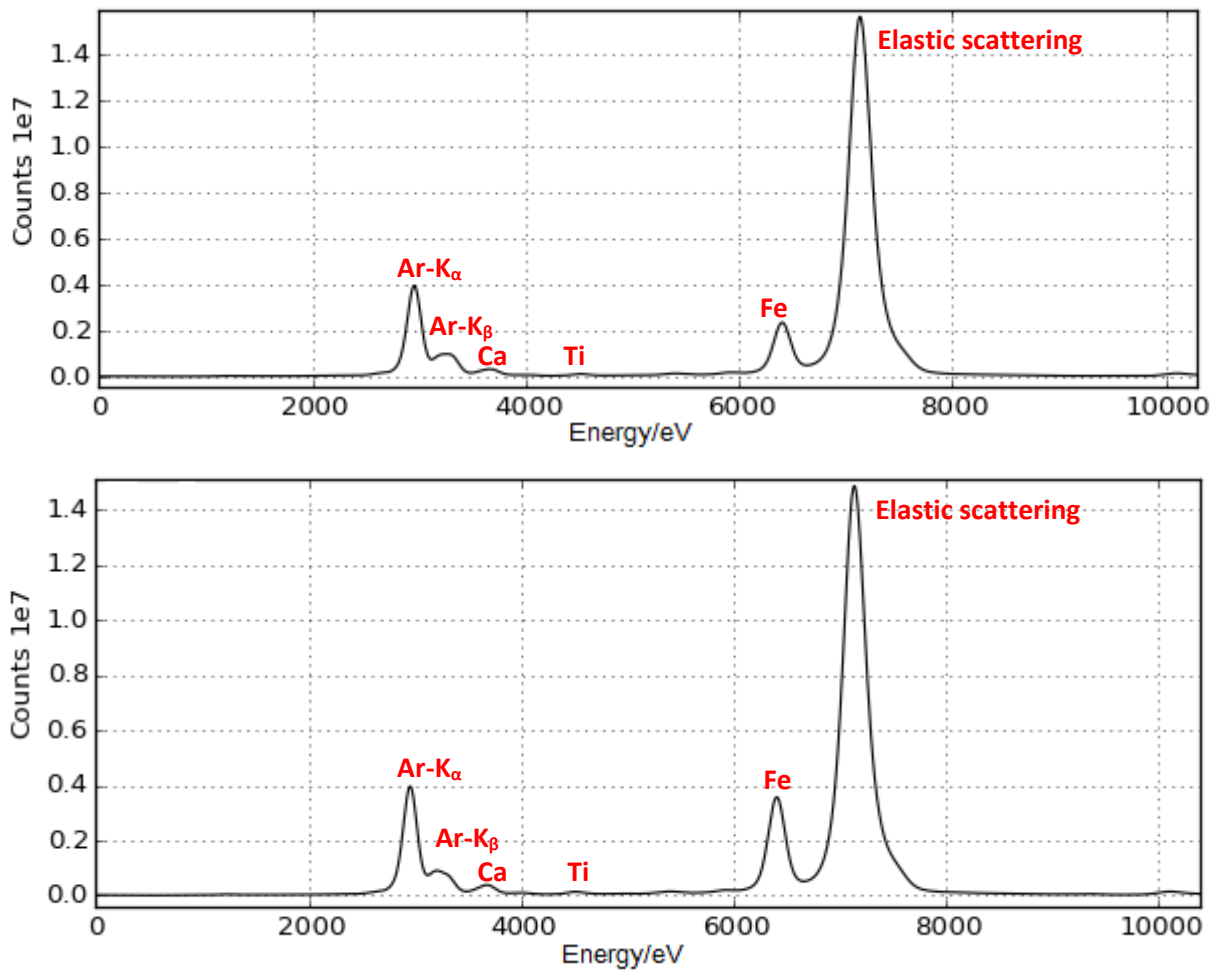


Figure 58 XRF spectra of regions of field biomass ash sample ZS5 identified as "background" and "hotspot" regions for iron by preliminary low resolution XRF scan

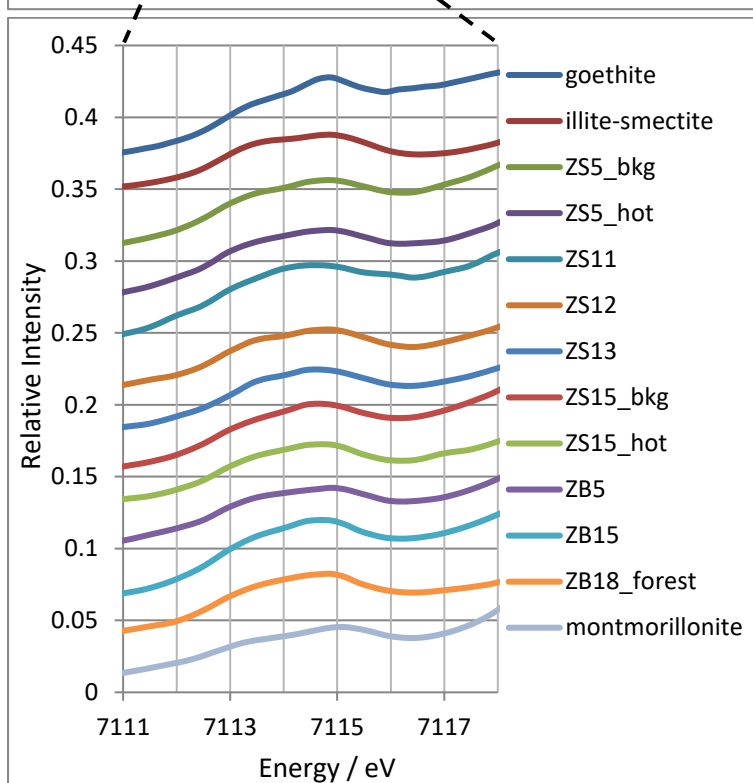
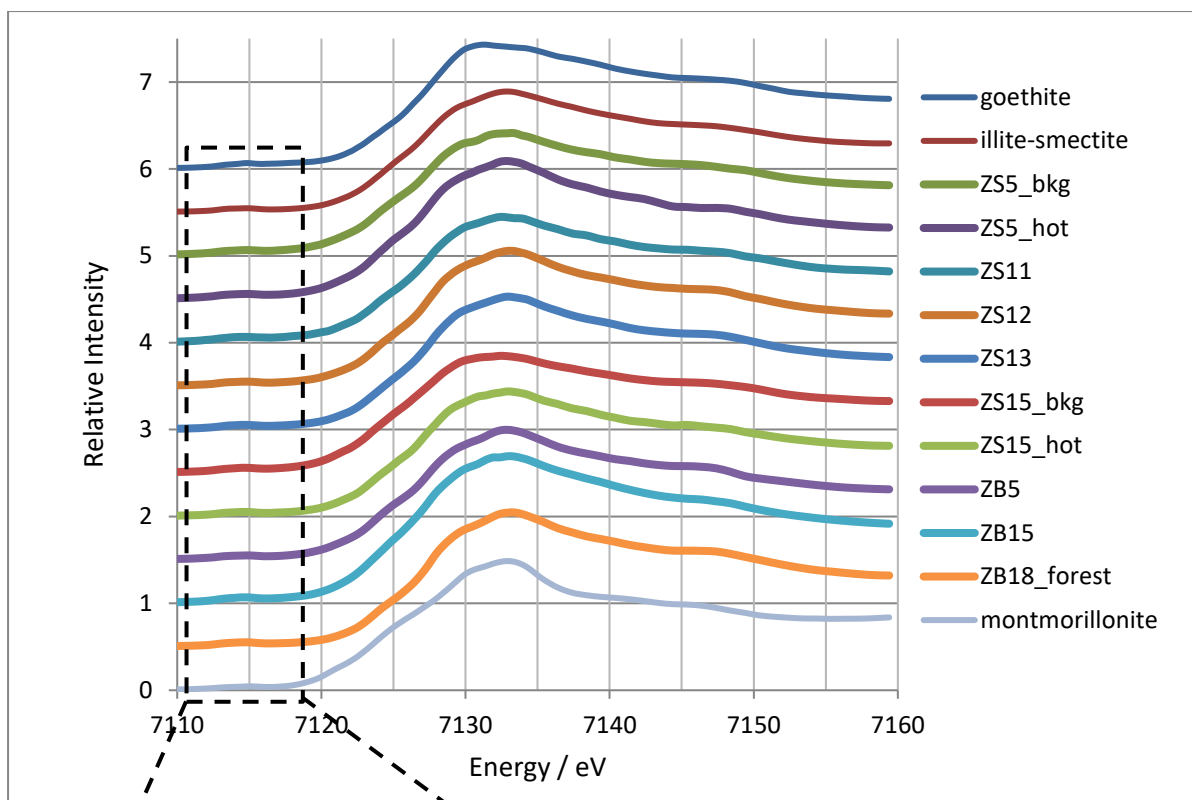


Figure 51 XANES spectra of ash from natural and agricultural biomass burning events in Nigeria, alongside standards identified as major components in the Linear Combination Fit, including a close-up of the pre-edge region.

XANES spectra were generated for “hotspot” and “background” regions of both the ZS5 and ZS15 samples, which show subtle differences in their spectra indicating differences in iron speciation. In particular, the peak at 7133 eV is more pronounced in the hotspots than in the backgrounds, potentially indicating a higher proportion of iron present in species such as illite-smectite. Pre-edge centroid positions denote Fe(III)-rich character across the board, apart from samples ZS11 and ZB15 whose centroids are displaced towards 7114.5 eV.

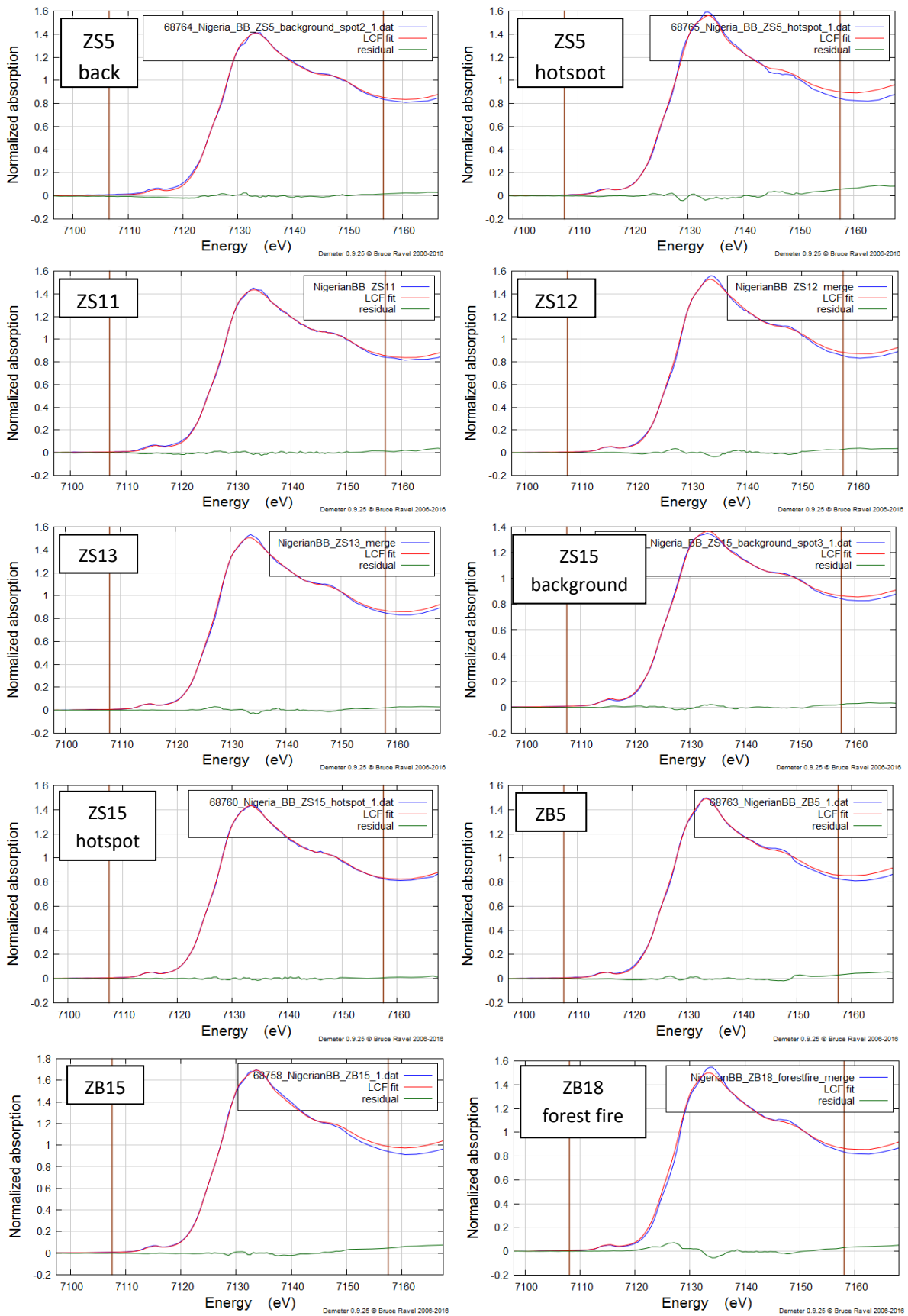


Figure 52 Linear combination fits of the normalised spectra of Nigerian ash samples from biomass burning, with the sample spectrum in blue, the best fit combination of standards in red, and the difference at each point represented as a residual line in green. The brown lines indicate the fitted range.

The linear combination fits presented in figure 52 are among the closest fits generated by any of the samples analysed in this set. According to the LCF results in figure 53, most of the iron in each ash sample is present as Fe(III) rich clays and common iron oxides, with any Fe(II) species accounted for by small quantities of magnetite (explaining the shift in ZS11's pre-edge centroid) or chlorite.

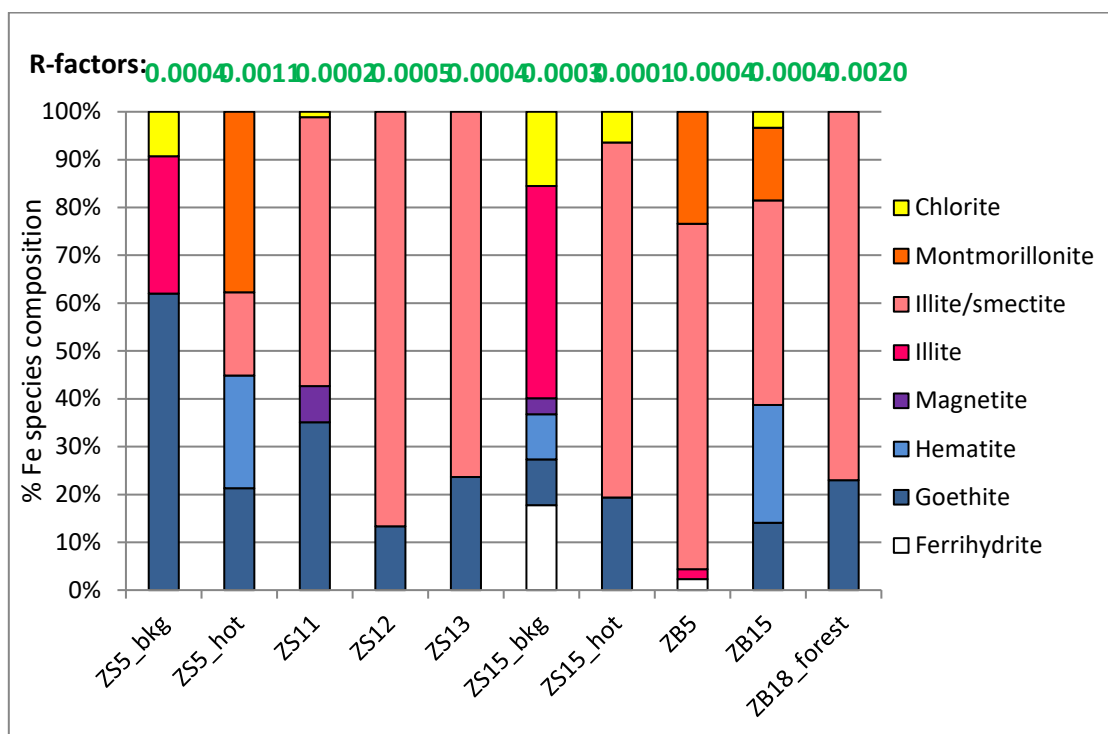


Figure 53 Iron speciation in Nigerian biomass burning samples according to Athena LCF

The identity and ratio of the iron species identified by the LCF resemble the results accumulated from the mineral dust and dust-based aerosol analyses in sections 3.3 – 3.6. This implies that the majority of the detectable iron in ash from biomass burning is in fact mineral dust carried into the air by the heat of the combustion process. Collecting mineral dust samples for analysis from the same regions prior to planned agricultural burning would help to verify this hypothesis.

The stated detection limit of the I18 beamline's XRF is  $\leq 10$  ppm, and the lack of detectable Fe outside of hotspots with speciation similar to mineral dust suggests that Fe generated directly from burning biomass constitutes a very minor component of the resulting fly ash, and that determining speciation within the ash will require the collection of larger quantities of material from biomass samples burned in a laboratory environment to minimise dust contamination.

## 4. Summary and future work

Standard Intercomparison has shown that the XANES technique struggles to differentiate between different minerals that hold iron in similar configurations, such as illite and feldspar which both contain iron mostly in octahedral lattices surrounded by oxide and hydroxide groups. As the sequential extraction versus XANES comparisons demonstrated, however, XANES analysis can be used to make reasonable predictions about the availability of iron in mineral samples.

Experiments with standard addition to samples of known composition demonstrated that XANES can plot changes in speciation across a series of samples, but individual spectra can vary in their fitting accuracy and ferrihydrite in particular is difficult to quantify.

With regard to environmental samples, XANES analysis and fitting was generally successful, although fittings would be improved with access to a wider range of standard spectra. Multiple iron standards including iron pyrite, several oxides and silicates, and a series of iron oxides with progressively rising Fe(II):Fe(III) ratios were recently generated on the B18 beamline at Diamond and have been shared with this research group. Prior to presenting this work for publication, all samples will be reanalysed with the expanded array of standards.

Combustion particulate samples known to contain a small proportion of iron tended to yield spectra that were harder to fit to standards and in several cases had insufficient material to generate a XANES spectrum at all. Care should be taken with future samples to ensure heavier material loading onto filters, or material should be removed from filters and concentrated as spots to increase the depth of material.

Future ship emission samples collected simultaneously, both directly from the funnel and from downwind collection points might improve understanding of the magnitude of sources of error from external dust sources or engine wear. Another issue raised by the XRF map of CB116P is the presence of titanium in the fibres of the sample filter. Titanium dioxide is a popular white pigment and its presence renders the titanium readings on the XRF spectrum useless for examining the content in the ash and raises concern about other metal contamination in unused filters. The type of filter used to collect ash from CB116P should be avoided in future studies.

Analysis of the speciation of ash from biomass burning in Nigeria indicates that most or all of the detectable iron is derived from mineral dust mobilised into the air by the heat of combustion and carried with the ash. This interpretation explains why the ash generated by burning biomass in a laboratory setting contains comparatively little iron and offers a possible explanation for the large differences in iron solubility found across biomass ash samples from different geographical sources. Further collection and analysis of mineral dust samples from areas scheduled to undergo agricultural burning, to compare against iron speciation in the resulting ash, as well as collecting larger samples of burnt biomass under controlled conditions, would provide support for this hypothesis. Further research using chemical extraction and ICP detection would inform how large the samples would have to be.

XANES fitting would be improved by expanding the range of standards. Some like iron oxalate would be useful due to its reactivity prevalence in natural systems (Mangiante, et al., 2017) but attempt to produce standard spectra in the I18 beamline ended in failure as the compound degraded in the path

of the beam. A major iron mineral species that would benefit the existing set of standards is lepidocrocite, a common product of iron corrosion (Jaén & Iglesias, 2016) that is often found in both natural (Hoffmann, et al., 1996) and anthropogenic (Salma, et al., 2009) aerosols. A sample of synthetic lepidocrocite should be included in any future beamline sessions at Diamond by this research group.

## Works Cited

Allen, A. G. et al., 2010. Influence of intensive agriculture on dry deposition of aerosol nutrients. *Journal of Brazillian Chemical Society*, Volume 21.

Avila, A., M.Alarcón & I.Queralt, 1998. The chemical composition of dust transported in red rains - its contribution to the biogeochemical cycle of a holm oak forest in Catalonia (Spain). *Atmospheric Environment*, 32(2), pp. 179-191.

Balestrini, R., Galli, L. & Tartari, G., 2000. Wet and dry atmospheric deposition at prealpine and alpine sites in northern Italy. *Atmospheric Environment*, 34(9), pp. 1455-1470.

Bianconi, A., 1980. Surface x-ray absorption spectroscopy: surface EXAFS and surface XANES. *Applications of Surface Science*, Volume 6, pp. 392-418.

Bianconi, A., Dell'Araccia, M., Durham, P. J. & Pendry, J. B., 1982. Multiple-scattering resonances and structural effects in the x-ray absorption near-edge spectra of Fe II and Fe III hexacyanide complexes. *Phys Ref*, 26(12), pp. 6502-6508.

Bowie, A. R. et al., 2009. Biogeochemical iron budgets of the Southern Ocean south of Australia: Decoupling of iron and nutrient cycles in the subantarctic zone by summertime supply. *Global Biogeochemical Cycles*, Volume 23, p. GB4034.

Bristow, C. S., Drake, N. & Armitage, S., 2009. Deflation in the dustiest place on Earth: the Bodélé Depression, Chad. *Geomorphology*, Volume 105, pp. 50-58.

Buck, K. N., Lohan, M. C. & Berger, C. J. M., 2007. Dissolved iron speciation in two distinct river plumes and an estuary: Implications for riverine iron supply. *Limnology & Oceanography*, 52(2), pp. 842-855.

Chadwick, O. A. et al., 1999. Changing sources of nutrients during four million years of ecosystem development. *Nature*, Volume 397, pp. 491-497.

Chantler, C. T. et al., 2005. *X-ray Form Factor, Attenuation and Scattering Tables (version 2.1)*. [Online]  
Available at: <http://physics.nist.gov/ffast>  
[Accessed 14 3 2018].

Chao, T. T. & Zhou, L., 1982. Extraction Techniques for Selective Dissolution of Amorphous Iron Oxides from Soils and Sediments. *Soil Science Society of America Journal*, 47(2), pp. 225-232.

Chen, Y., Shah, N., Huggins, F. E. & Huffman, G. P., 2004. Investigation of the microcharacteristics of PM2.5 in residual oil fly ash by analytical transmission electron microscopy. *Environmental Science & Technology*, Volume 38, pp. 6553-6560.

- Clay Minerals Society, 2017. *Source Clays*. [Online]  
Available at: <http://www.clays.org/Sourceclays.html>  
[Accessed 13 05 2017].
- Corbett, J. J. & Koehler, H. W., 2003. Updated emissions from ocean shipping. *Journal of Geophysical Research: Atmospheres*, 108(D20).
- Croot, P. L. & Johansson, M., 1999. Determination of Iron Speciation by Cathodic Stripping Voltammetry in Seawater Using the Competing Ligand 2-(2-Thiazolylazo)-p-cresol (TAC). *Electroanalysis*, 12(8), pp. 565-576.
- Diaz-Moreno, S., Chandler, C. T. & Newville, M., 2017. *International Workshop on Improving Data Quality in XAFS Spectroscopy*. Harwell, Oxfordshire, Diamond Light Source.
- Dyar, M. D. et al., 2001. *Fe<sup>3+</sup> and Fe<sup>2+</sup> iron in feldspar: Calibration and interpretation of XANES spectra*, South Hadley, MA: Mount Holyoke College.
- Edwards, A. M., Platt, T. & Sathyendranath, S., 2004. The high-nutrient, low-chlorophyll regime of the ocean: limits on biomass and nitrate before and after iron enrichment. *Ecological Modelling*, 171(1-2), pp. 103-125.
- European Commission, 2016. *Air pollutants from maritime transport*. [Online]  
Available at: <http://ec.europa.eu/environment/air/transport/ships.htm>  
[Accessed 05 09 2017].
- Felder, Marita, Gaupp & Reinhard, 2006. The  $\delta^{13}\text{C}$  and  $\delta^{18}\text{O}$  signatures of siderite – a tool to discriminate mixis patterns in ancient lakes. *Zeitschrift der Deutschen Gesellschaft für Geowissenschaften*, 157(3), pp. 387-410.
- Fishwick, M. P. et al., 2014. The impact of changing surface ocean conditions on the dissolution of aerosol iron. *Global Biogeochemical Cycles*, 28(11), pp. 1235-1250.
- Flanders, P. J., 1994. Collection, measurement, and analysis of airborne magnetic particulates from pollution in the environment (invited). *Journal of Applied Physics*, Volume 75, pp. 5931-5936.
- Formenti, P. et al., 2014. Dominance of goethite over hematite in iron oxides of mineral dust from Western Africa: Quantitative partitioning by X-ray absorption spectroscopy. *Journal of Geophysical Research: Atmospheres*, 119(22), pp. 12740-12754.
- Formenti, P. et al., 2008. Regional variability of the composition of mineral dust from western Africa: Results from the AMMA SOP0/DABEX and DODO field campaigns. *Journal of Geophysical Research*, Volume 113.
- Fu, H. B. et al., 2014. Fractional iron solubility of aerosol particles enhanced by biomass burning and ship emission in Shanghai, East China. *Science of the Total Environment*, Volume 481, pp. 377-391.
- George, G. N. & Pickering, I. J., 2006. *Synchrotron X-ray Absorption Spectroscopy*, Stanford, CA: Stanford Synchrotron Radiation Lightsource.

Guieu, C., Bonnet, S. & Wagener, T., 2005. Biomass burning as a source of dissolved iron to the open sea?. *Geophysical Research Letters*, Volume 32, p. L19608.

Han, Q. et al., 2012. Global estimates of mineral dust aerosol iron and aluminum solubility that account for particle size using diffusion-controlled and surface-area-controlled approximations. *Global Biogeochemical Cycles*, 26(2), p. GB2038.

Hegazy, A. K., Boulos, L., Kabieli, H. F. & Sharashy, O. S., 2011. Vegetation and Species Altitudinal Distribution in Al-Jabal Al-Akhdar Landscape, Libya. *Pakistan Journal of Botany*, 43(4), pp. 1885-1898.

Herut, B. et al., 2016. The Potential Impact of Saharan Dust and Polluted Aerosols on Microbial Populations in the East Mediterranean Sea, an Overview of a Mesocosm Experimental Approach. *Frontiers in Marine Science*, Volume 15.

Hicks, L. J., 2015. *X-ray spectroscopy and electron microscopy of planetary materials*. Leicester: University of Leicester.

Hirayama, H., 2000. *Tutorials for electron/gamma Monte Carlo: building blocks and applications*. Lisbon, Portugal, International Conference on the Monte Carlo 2000, Advanced Monte Carlo on Radiation Physics, Particle Transport Simulation and Applications.

Hoffmann, P. et al., 1996. Speciation of iron in atmospheric aerosol samples. *Journal of Aerosol Science*, 27(2), pp. 325-337.

Holly, V. et al., 2016. Dry season aerosol iron solubility in tropical northern Australia. *Atmospheric Chemistry and Physics*, Volume 16, pp. 12829-12848.

Ingall, E. D. et al., 2013. Role of biogenic silica in the removal of iron from the Antarctic seas. *Nature Communications*, Volume 4, p. Article 1981.

Ito, A., 2013. Global modelling study of potentially bioavailable iron input from shipboard aerosol sources to the ocean. *Global Biogeochemical Cycles*, Volume 27, pp. 1-10.

Ito, A. & Shi, Z., 2016. Delivery of anthropogenic bioavailable iron from mineral dust and combustion aerosols to the ocean. *Atmospheric Chemistry and Physics*, Volume 16, pp. 85-99.

Jaén, J. A. & Iglesias, J., 2016. *Corrosion study of steels exposed over five years to the humid tropical atmosphere of Panama*. Panama City, Panama, 15th Latin American Conference on the Applications of the Mössbauer Effect.

Jenkins, R., Manne, R., Robin, R. & Senemaud, C., 1991. *Nomenclature System for X-ray Spectroscopy*, s.l.: IUPAC.

Johnson, J. H. & Cardile, C. M., 1987. Iron substitution in montmorillonite, illite & glauconite by <sup>57</sup>Fe Mössbauer spectroscopy. *Clays and Clay Minerals*, 35(3), pp. 170-176.

Journet, E., Desboeufs, K. V., Caquineau, S. & Colin, J.-L., 2008. Mineralogy as a critical factor of dust iron solubility. *Geophysical Research Letters*, Volume 35, p. L07805.

Kelly, S. D., Hesterberg, D. & Ravel, B., 2008. Analysis of soils and minerals using x-ray absorption spectroscopy. In: A. L. Ulery & L. R. Drees, eds. *Methods of Soil Analysis*. Madison, WI: Soil Society of America, pp. 367-463.

Koren, I. et al., 2006. The Bodélé depression: a single spot in the Sahara that provides most of the mineral dust to the Amazon forest. *Environmental Research Letters*, 1(1), p. 014005.

Leslie, B. W., Hammond, D. E., Berelson, W. M. & Lund, S. P., 1990. Diagenesis in anoxic sediments from the California continental borderland and its influence on iron, sulfur and magnetite behaviour. *Journal of Geophysical Research*, 95(B4), pp. 4453-4470.

Li, W. et al., 2012. Haze particles over a coal-burning region in the China Loess Plateau in winter: Three flight missions in December 2010. *Journal of Geophysical Research*, 117(D12), p. D12306.

Li, W. et al., 2017. Air pollution-aerosol interactions produce more bioavailable iron for ocean ecosystems. *Science Advances*, Volume 3, p. e1601749.

Lobert, J. M., Scharffe, D. H., Hao, W. M. & Crutzen, P. J., 1990. Importance of biomass burning in the atmospheric budgets of nitrogen-containing gases. *Letters to Nature*, Volume 346, pp. 552-554.

Longo, A. F. et al., 2016. Influence of Atmospheric Processes on the Solubility and Composition of Iron in Saharan Dust. *Environmental Science & Technology*, Volume 50, pp. 6912-6920.

Majestic, B. J., Schauer, J. J. & Shafer, M. M., 2007. Application of synchrotron radiation for measurement of iron red-ox speciation in atmospherically processed aerosols. *Atmospheric Chemistry & Physics*, Volume 7, pp. 2475-2487.

Mangiante, D. M. et al., 2017. Mechanism of Ferric Oxalate photolysis. *ACS Earth Space Chemistry*, 1(5), pp. 270-276.

Moldanova, J. et al., 2009. Characterisation of particulate matter and gaseous emissions from a large ship diesel engine. *Atmospheric Environment*, Volume 43, pp. 2632-2641.

Moldanová, J. et al., 2013. Physical and chemical characterisation of PM emissions from two ships operating in European Control Areas. *Atmospheric Measurement Techniques*, Volume 6, pp. 3577-3596.

Mueller, D. et al., 2011. Ships, ports and particulate air pollution - an analysis of recent studies. *Journal of Occupational Medicine and Toxicology*, 6(31).

Nenes, A. et al., 2011. Atmospheric acidification of mineral aerosols: a source of bioavailable phosphorus for the oceans. *Atmospheric Chemistry and Physics*, Volume 11, pp. 6265-6272.

Nenes, A. et al., 2011. Atmospheric Acidification of Mineral Aerosols: a source of bioavailable phosphorus for the oceans. *Atmospheric Chemistry & Physics*, Volume 11, pp. 6265-6272.

Nodwell, L. M. & Price, N. M., 2001. Direct use of inorganic colloidal iron by marine mixotrophic phytoplankton. *Limnology and Oceanography*, 46(4), pp. 765-777.

- Oakes, M. et al., 2012. Iron solubility related to particle sulfur content in source emission and ambient fine particles. *Environmental Science & Technology*, Volume 46, pp. 6637-6644.
- Oakes, M. et al., 2012. Characterization of iron speciation in urban and rural single particles using XANES spectroscopy and micro X-ray fluorescence measurements: investigating the relationship between speciation and fractional iron solubility. *Atmospheric Chemistry and Physics*, Volume 12, pp. 745-756.
- Pan, Y., Brown, A. & Brydson, R., 2006. Electron Beam Damage Studies on 6-line Ferrihydrite. *Journal of Physics: Conference Series*, Volume 26, pp. 46-49.
- Peak, D. & Regier, T., 2012. Direct Observation of Tetrahedrally Coordinated Fe(III) in Ferrihydrite. *Environmental Science & Technology*, 46(6), pp. 3163-3168.
- Pitchford, J. W. & Brindley, J., 1999. Iron limitation, grazing pressure and oceanic high nutrient-low chlorophyll (HNLC) regions. *Journal of Plankton Research*, 21(3), pp. 525-547.
- Poulton, S. W. & Canfield, D. E., 2005. Development of a sequential extraction procedure for iron: implications for iron partitioning in continentally derived particulates. *Chemical Geology*, 214(3-4), pp. 209-221.
- Randall, C. R. et al., 1995. X-ray Absorption Pre-Edge Studies of High-Spin Iron(II) Complexes. *Inorganic Chemistry*, Volume 34, pp. 1036-1039.
- Ravel, B., 2015. *Athena: A User's Guide*. [Online]  
Available at: <https://bruceravel.github.io/demeter/aug/index.html>  
[Accessed 25 April 2017].
- Rich, H. W. & Morel, F. M. M., 1990. Availability of well-defined iron colloids to the marine diatom *thalassiosira weissflogii*. *Limnology and Oceanography*, 35(3), pp. 652-662.
- Roe, A. L. et al., 1984. X-ray Absorption Spectroscopy of Iron-Tyrosinate Proteins. *Journal of American Chemical Society*, Volume 106, pp. 1676-1681.
- Salma, I. et al., 2009. Properties and sources of individual particles and some chemical species in the aerosol of a metropolitan underground railway station. *Atmospheric Environment*, 43(22-23), pp. 3460-3466.
- Schroth, A. W., Crusius, J., Sholkovitz, E. R. & Bostick, B. C., 2009. Iron solubility driven by speciation in dust sources to the ocean. *Nature Geoscience*, Volume 2, pp. 337-340.
- Schulze, D. G., 1980. Identification of Soil Iron Oxide Minerals by Differential X-ray Diffraction. *Soil Science Society of America Journal*, 45(2), pp. 437-440.
- Shi, Z. et al., 2011. Iron dissolution kinetics of mineral dust at low pH during simulated atmospheric processing. *Atmospheric Chemistry & Physics*, Volume 11, pp. 995-1007.
- Shi, Z. et al., 2011. Influence of chemical weathering and aging of iron oxides on the potential iron solubility of Saharan dust during simulated atmospheric processing. *Global Biogeochemical Cycles*, 25(2), p. GB2010.

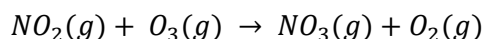
- Shi, Z., Krom, M. D., Bonneville, S. & Benning, L. G., 2015. Atmospheric processing outside clouds increases soluble iron in mineral dust. *Environmental Science & Technology*, 49(3), pp. 1472-1477.
- Shi, Z. et al., 2012. Impacts on iron solubility in the mineral dust by processes in the source region and atmosphere: A review. *Aeolian Research*, Volume 5, pp. 21-42.
- Shi, Z., Shao, L., Jones, T. P. & Lu, S., 2005. Microscopy & mineralogy of airborne particles collected during severe dust storm episodes in Beijing, China. *Journal of Geophysical Research*, Volume 110, p. D01303.
- Siebecker, M., 2016. *A practical workshop on EXAFS shell fitting for environmental samples*, Newark, DE: Delaware Environmental Institute.
- Stockdale, A. et al., 2016. Understanding the nature of atmospheric and acid processing of mineral dusts in supplying bioavailable phosphorus to the oceans. *Proceedings of the National Academy of Sciences*, 113(51), pp. 14639-14644.
- Takahashi, Y., Higashi, M., Furukawa, T. & Mitsunobu, S., 2011. Change of iron species and iron solubility in Asian dust during the long-range transport from western China to Japan. *Atmospheric Chemistry & Physics*, Volume 11, pp. 11237-11252.
- Tessier, A., Campbell, P. G. C. & Bisson, M., 1979. Sequential Extraction Procedure for the Speciation of Particulate Trace Metals. *Analytical Chemistry*, 51(7), pp. 844-851.
- Troeh, F. R. & Thompson, L. M., 2005. *Soils and Soil Fertility*. 6th ed. New York: Oxford University Press.
- Usher, C. R., Michel, A. E. & Grassian, V. E., 2003. Reactions on Mineral Dust. *Chemical Reviews*, 103(12), p. 4883-4940.
- Visser, F. et al., 2003. The role of the reactivity and content of iron of aerosol dust on growth rates of two antarctic diatom species. *Journal of phycology*, 39(6), pp. 1085-1094.
- Wang, R. et al., 2015. Sources, transport and deposition of iron in the global atmosphere. *Atmospheric Chemistry and Physics*, Volume 15, pp. 6247-6270.
- Weaver, C. E. & Pollard, L. D., 1973. Relations of Composition to Structure. In: C. E. Weaver & L. D. Pollard, eds. *The Chemistry of Clay Minerals*. Amsterdam: Elsevier, pp. 173-184.
- Wells, M. L., Zorkin, N. G. & Lewis, A. G., 1983. The role of colloid chemistry in providing a source of iron in phytoplankton. *Journal of Marine Research*, Volume 16, pp. 731-746.
- Westre, T. E. et al., 1997. A multiplet analysis of Fe K-edge 1s-3d pre-edge features of iron complexes. *Journal of American Chemical Society*, Volume 119, pp. 6297-6314.
- Wilke, M. et al., 2001. Oxidation state and coordination of Fe in minerals: an Fe K-XANES spectroscopic study. *American Mineralogist*, Volume 86, pp. 714-730.

## Chapter 2 Analysis of chloride in particles produced from a model diesel engine

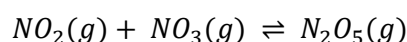
### 1. Introduction

#### 1.1 Tropospheric importance of chloride

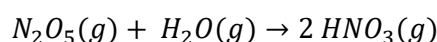
Mineral chloride in aerosol particles plays an important role in air quality, both as an oxidant in its own right and by its interactions with  $\text{NO}_x$  (Mielke, et al., 2011).  $\text{NO}_2$  produced mainly by internal combustion vehicle emissions (Annamalai & Puri, 2007) interacts with peroxy radicals in the atmosphere to produce tropospheric ozone (Wang, et al., 1998), which generates  $\text{NO}_3$ :



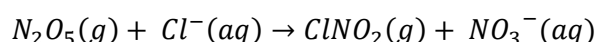
which reacts with further  $\text{NO}_2$  to generate  $\text{N}_2\text{O}_5$ :



$\text{N}_2\text{O}_5$  is unreactive in the atmosphere compared to other  $\text{NO}_x$  species, but it can form nitric acid through interaction with water vapour on the surface of aerosol particles (Aldener, et al., 2006) (Wayne, 2006):



However, in the presence of aerosol droplets containing chloride salts,  $\text{N}_2\text{O}_5$  can also react to form nitryl chloride:



In addition to blocking the reaction pathway that leads to nocturnal  $\text{NO}_x$  depletion, nitryl chloride has a longer atmospheric lifetime than  $\text{N}_2\text{O}_5$  and, when photolysed, releases chlorine radicals:



These radicals promote the photochemical production of tropospheric ozone which impacts local animal and plant life (Osthoff, et al., 2008) (Ainsworth, 2008).

#### 1.2 Sources of tropospheric chloride

Major sources of natural atmospheric mineral chloride include sea salt aerosols, volcanic activity, (Graedel & Keene, 1995) mineral dust and aerosols generated by freshwater bodies (Abuduwaili, et al., 2008). Major anthropogenic sources include coal and biomass burning, incineration and emissions from industries that employ chlorinated solvents (Moreno, et al., 2013) (Querol, et al., 2001). Relative contributions from these sources vary substantially by geography (Thornton, et al., 2010) (McCulloch, et al., 1999).

Source apportionment studies across cities that identify traffic emissions as a distinct source of particulates and analyse elemental composition (Wang, et al., 2016) (Zhang, et al., 2013) (Friend, et al., 2011) (Querol, et al., 2001) report finding chloride among the emissions, but concentrations vary and some samples find no Cl at all (e.g. (Friend, et al., 2011) figure 5). Friend et al's analysis indicates the presence of chlorine in fine particulates from one specific traffic source ("motor vehicle 1"). Chlorine is not found consistently in any other source in Brisbane during the survey period except in sea salt aerosols. The group makes note that this site was located closer to a motorway, where a greater concentration of large diesel vehicles such as trucks and vans would be expected. It is also noted that the site where the "motor vehicle 2" emissions were collected was exposed to wind from

the direction of a train yard, which would also be expected to contain diesel fumes albeit from different engine setups.

This research was commissioned on the strength of data generated from an XRF spectrum of a particulate sample from the exhaust of a model diesel engine which was collected along with three others by personnel from the Public Health department at the University of Birmingham and analysed in the SUL-X beamline at the ANKA synchrotron at KIT. The spectrum (figure 1) showed an unexpected and prominent chlorine peak representing a significant release of chlorine or chloride-rich material from the engine.

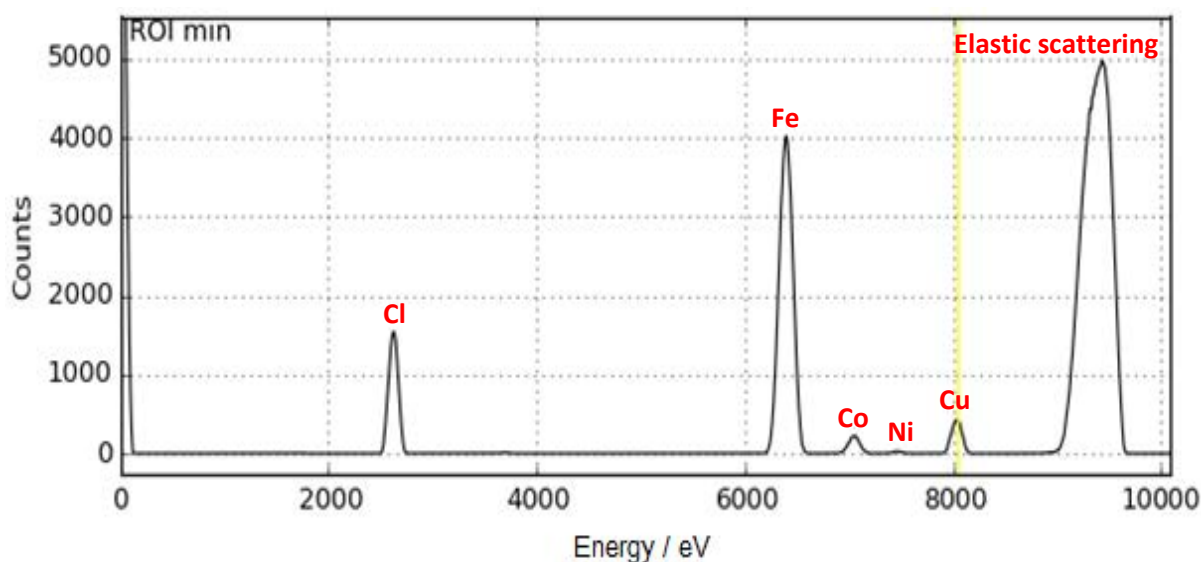


Figure 4 XRF spectrum of diesel particulate emissions sample D3

The question remains regarding the source of chloride within diesel emissions. A patent application was filed by Matthew Fairlie in 1939 (Fairlie, 1939) stating that calcium phenyl stearate is used in conventional engine lubricants to improve the shear strength of the resulting films. However, at temperatures above 240°C, the surfactant breaks down and forms calcium chloride that causes wear on engine components. Fairlie's patent states that chlorination of the surfactant to calcium chlorophenyl stearate improves its thermal stability significantly, in testing up to 350°C. Carboxylate salts became unpopular due to their corrosive effects on susceptible engine components, particularly bearings (Anon., 1977) and were phased out and replaced with salicylates and alkyl-substituted sulfonic acids in 1977.

Modern diesel engine lubricants employ zinc dithiophosphate (ZDDP) or related phosphate compounds (Jaye, et al., 2008) as surfactants to help remove contamination from engines and prevent wear. The range of common lubricant additives used in modifying the viscosity of engine oils is covered in (Carvalho, et al., 2010) and includes "polymeric hydrocarbons, ester containing polymers and modified polymers". Said modified polymers contain nitrogen-rich groups (amines, pyridines, imidazoles etc) and contain no reference to chlorinated compounds. This leaves the fuel itself as the most likely source of chlorinated compounds, and compounds such as chloroacetophenone are known to be added to diesel fuel as additives, although they are not detectable in waste streams (Gong, et al., 2003).

## 2. Methods and Materials

### 2.1 Sample collection

Four particulate matter samples were collected from separate runs of a model Euro 5 diesel engine supplied by Jaguar Land Rover Ltd and operated by the Mechanical Engineering department at the University of Birmingham. The engine ran on ultra-low sulphur (<10ppm) diesel fuel. Fully synthetic Halfords SW30 lubricating oil was used exclusively in the engine. All particulate matter was collected on Millipore Isopore™ polycarbonate membrane filters with 0.2 µm pore size. The greatest number of particulates produced by diesel vehicle engines are known to be in the 0.1 – 0.2 µm diameter range (Kleeman, et al., 2000) but this fraction could not be retained. The high flow rate of the model engine exhaust prohibited the use of filters with a finer pore size.

### 2.2 Synchrotron analysis

Samples and standards were analysed using x-ray absorbance near edge structure (XANES) and x-ray fluorescence (XRF) mapping on the SUL-X beamline at the ANKA synchrotron in Karlsruhe, Germany in November 2014. Representative areas were cut from the filters and loaded into the beamline hutch across bands of Kapton tape. Readings were collected in the fluorescence mode with a Gresham 7 element Si(Li) detector. Due to the low energy of the K-edge transition in chlorine and the potential for photons to be absorbed by the air between sample and detector, all measurements had to be performed in a chamber that was evacuated to  $2 \times 10^{-5}$  mbar.

The following standards were run in the same beamline in April 2015 by Dr *Jörg Göttlicher*:

- Ammonium chloride (Sigma Aldrich)
- Sodium chloride (Fisher Scientific)
- Potassium chloride (VWR International)
- Magnesium chloride anhydrous (Sigma Aldrich)
- Magnesium chloride hexahydrate (VWR International)
- Calcium chloride anhydrous (Sigma-Aldrich)
- Calcium chloride dihydrate (Sigma-Aldrich)

Due to the logistical difficulties of transferring hygroscopic anhydrous compounds to Kapton tape and moving the sample plate to the beamline without substantial water uptake from the air occurring, the validity of the anhydrous spectra cannot be guaranteed. Similarly, evacuation of the chamber may have caused partial dehydration of the hydrated salts prior to analysis.

### 2.3 Scanning Electron Microscopy with Energy Dispersive X-ray Spectroscopy (SEM-EDX)

SEM-EDX was carried out in August 2015 at the University of Birmingham in the Metallurgy and Materials building under the direction of Dr Paul Stanley. All measurements were collected on a Philips XL30 ESEM-FEG using the bundled software. The detector was run in back scattered mode, causing heavier elements to appear darker on the readout.

### 2.4 Software

XANES spectra were handled using Athena v0.9.25, part of the Demeter software package for handling XAFS data by Bruce Ravel. XRF data were handled using PyMCA v5.1.1.

### 3. Results

#### 3.1 X-ray Absorbance Near Edge Structure (XANES) comparisons

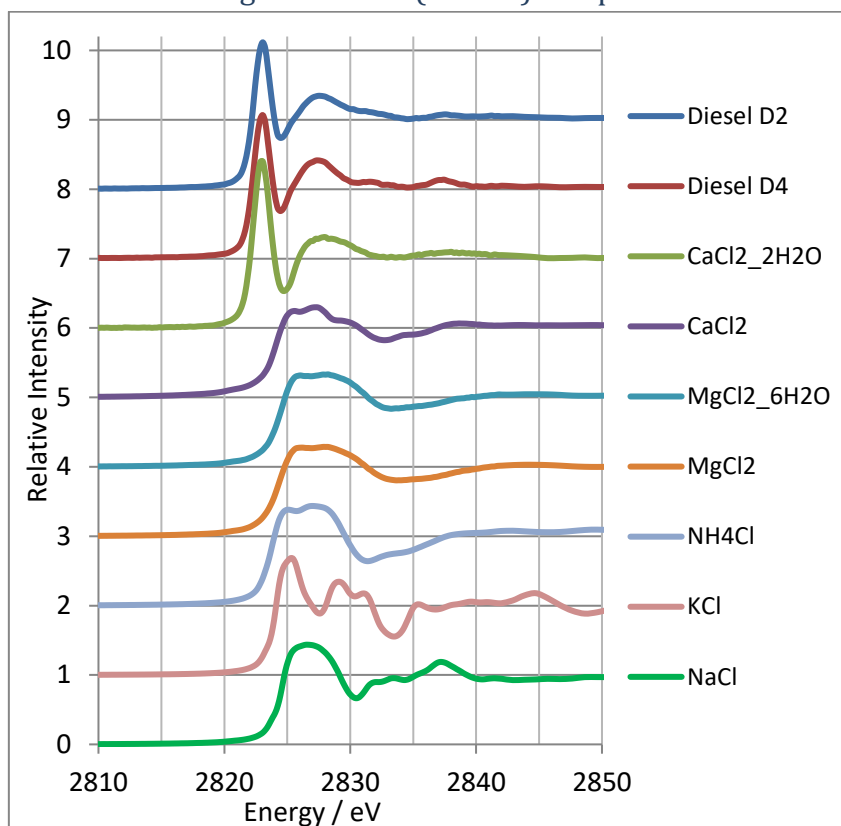


Figure 5 Cl K-edge XANES spectra of ammonium, alkali and alkali earth metal chlorides collected by Dr Joerg Goettlicher at ANKA in 2015 from samples sent from the University of Birmingham, contrasted against diesel particulate emission samples D2 and D4

The XANES spectra generated by two diesel emission particulate samples (figure 2) appear to bear a strong resemblance to the calcium chloride dihydrate standard, particularly with regard to the prominent white line (Meitzner, et al., 1992) at 2823 eV and the broad peak at 2827 eV. The small trough at 2830 eV and distinctive peak at 2837 eV also implies a minor contribution from sodium chloride. However, the spectrum of calcium chloride dihydrate does not resemble the spectrum recorded in literature (Zhu, et al., 2010) figure 1, reproduced in figure 3 for comparison purposes).

The literature spectra were recorded in the BL-9A beamline at the Photon Factory in Tsukuba, Japan which prevents signal loss from air by examining lighter elements in a helium environment (KEK-PF, 2014) rather than by evacuating the chamber. Comparison of the spectra of anhydrous and hydrated magnesium chloride suggests that the hydrated standard was dehydrated by the evacuation process. The calcium chloride dihydrate standard spectrum recorded in SUL-X does not match the literature, nor does it match the spectrum of anhydrous calcium chloride which does compare well to the literature. The calcium chloride dihydrate spectrum collected in SUL-X is thus considered unreliable and cannot be used as a reference.

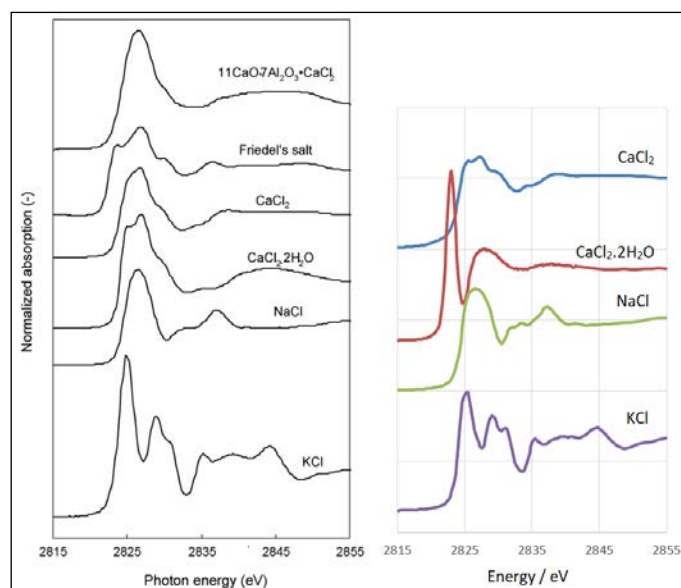


Figure 6 Comparison of mineral chloride salt XANES spectra collected by (Zhu, et al., 2010) (left) and those collected by Dr Goettlicher at ANKA in 2015 (right)

Comparison against a wider range of mineral chlorides by the same research group (Zhu, et al., 2008) shows no strong resemblance to the diesel emissions spectra. The distinctive white line at 2823 eV is also found in chlorinated organic compounds like chlorophenol, nitrobenzene and polyvinyl chloride (PVC) (Fujimori, et al., 2010), which implies that the majority of the chlorine present in the diesel particulate emissions is bonded to organic molecules.

### 3.2 Scanning Electron Microscopy with Energy Dispersive X-ray Spectroscopy (SEM-EDX)

SEM-EDX was carried out on the remaining fragments of diesel particulate sample filters left over from the examination at ANKA. Sites were selected based on the lightness of the region, since the system was configured in back scattering mode causing heavy elements like iron to appear as dark grey patches while lighter elements such as aluminium, silicon and chlorine appear as light grey or white patches. An example region is shown in figure 4. The detection range was 0 – 8 KeV, meaning that any element heavier than cobalt could not be detected.

Elemental compositions (excluding carbon) of the various sites are presented in figure 5. The light spots are most commonly iron oxide, silica, other metal oxides beyond the detection range of the equipment, or organic compounds with oxygen-containing groups. Chlorine is rarely found in the samples in sufficiently high concentration to register on the detector, which implies that the chlorine detected in the XANES spectra is mostly diffuse rather than constrained in hot spots, although a small number of hotspots do exist.

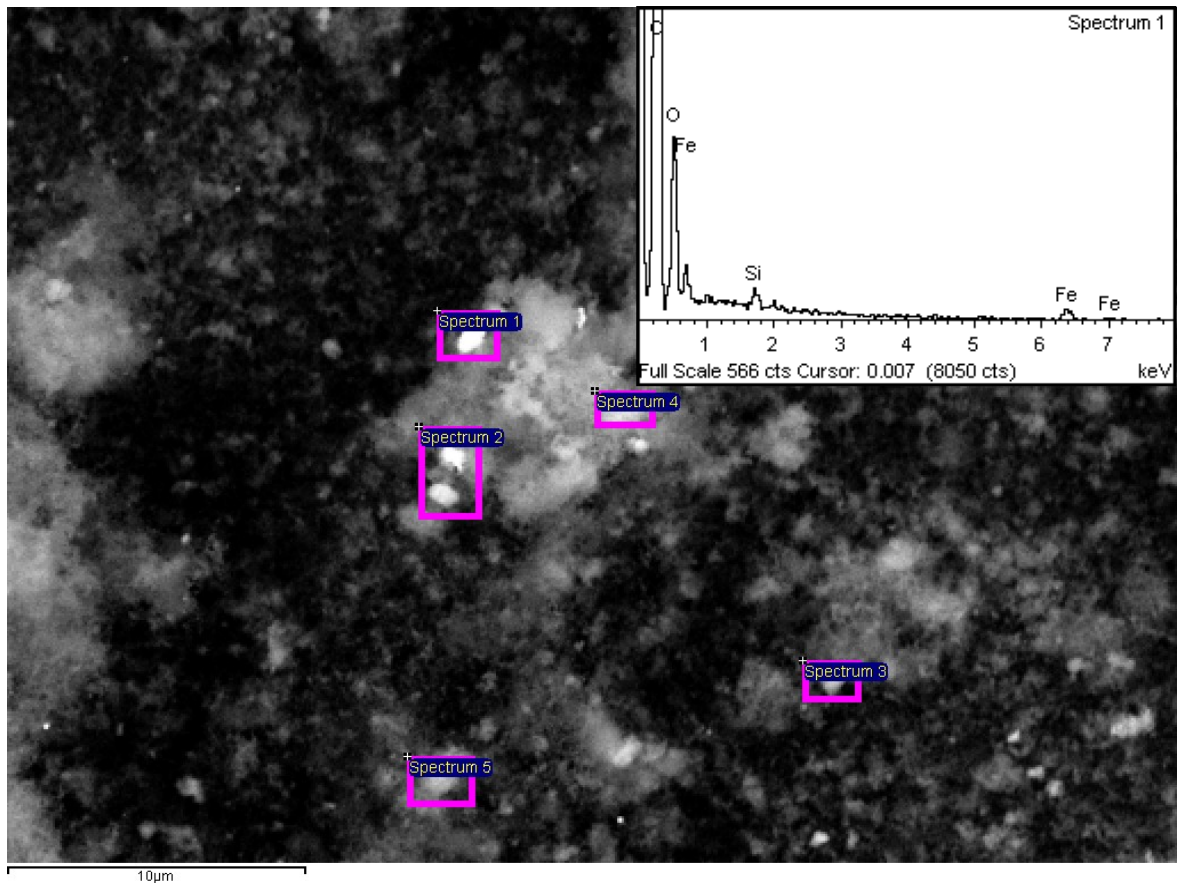


Figure 7 A 40 x 40 um region of diesel particulate sample D3, including regions rich in light elements from which elemental compositions were reported. Inset: the elemental composition of the "Spectrum 1" spot

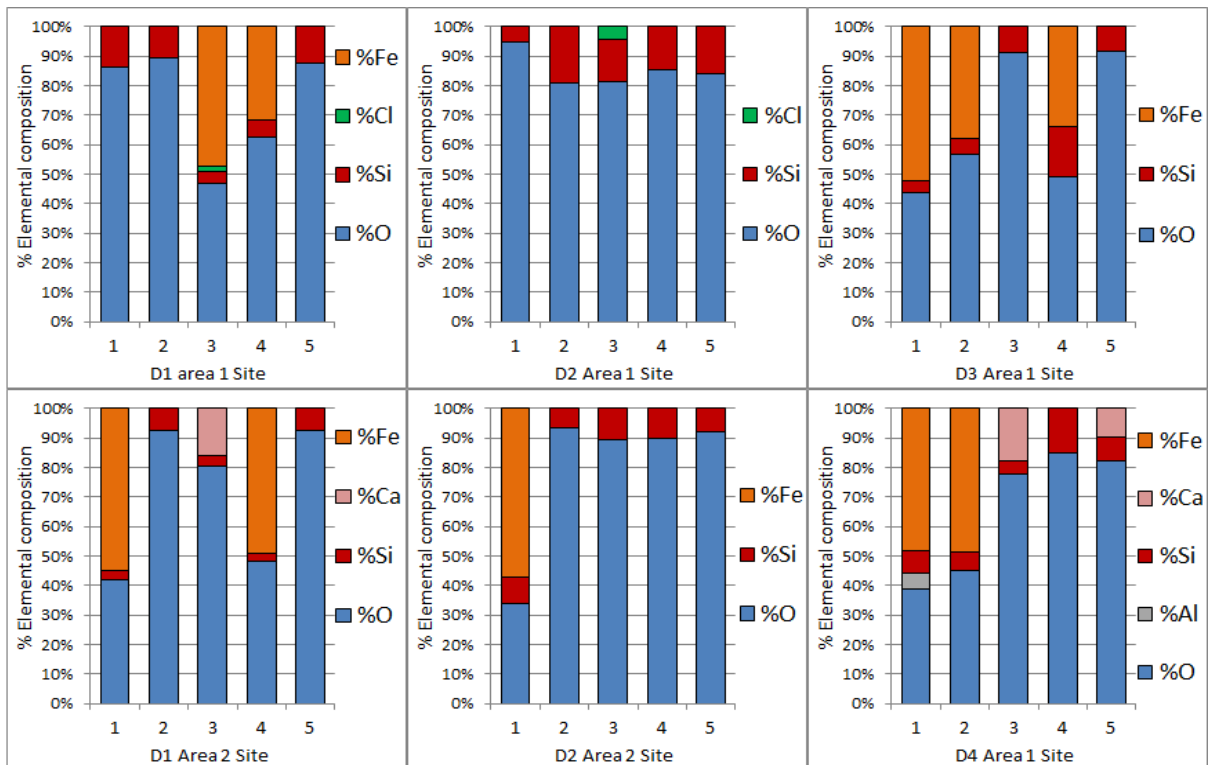


Figure 8 Elemental composition of bright spots found on SEM-EDX maps of diesel particulate samples, excluding carbon. D1-D4 pertains to the different sample filters, while Area refers to the numbered bright spot selected as shown in figure 4

### 3.3 X-Ray Fluorescence Map

Figure 6 shows that the distribution of chlorine and copper in the observed section of one diesel particulate emission sample is diffuse and evenly distributed. The dark patches visible on the filter  $\sim 250 \mu\text{m}$  apart match the grille on which the filter was mounted in the model engine exhaust stream. Figure 7 shows that the iron and cobalt readings also overlap, implying that the visible particulates are composed of refined alloy from engine wear. Figure 8 shows that iron and cobalt are distinct from the copper, and the small nickel signal does not overlap with that of any other element.

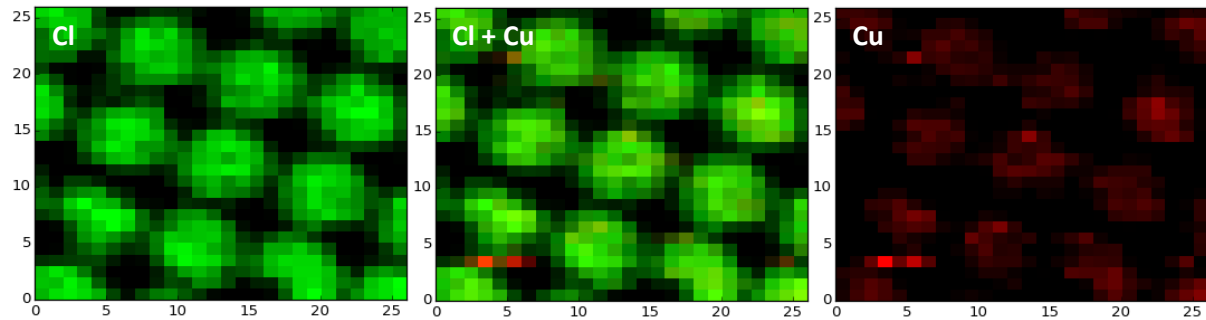


Figure 9 XRF maps of chlorine (left) and copper (right) distribution across a 1 x 1 mm section of diesel emission sample filter D3, along with an overlay of both elements (centre)

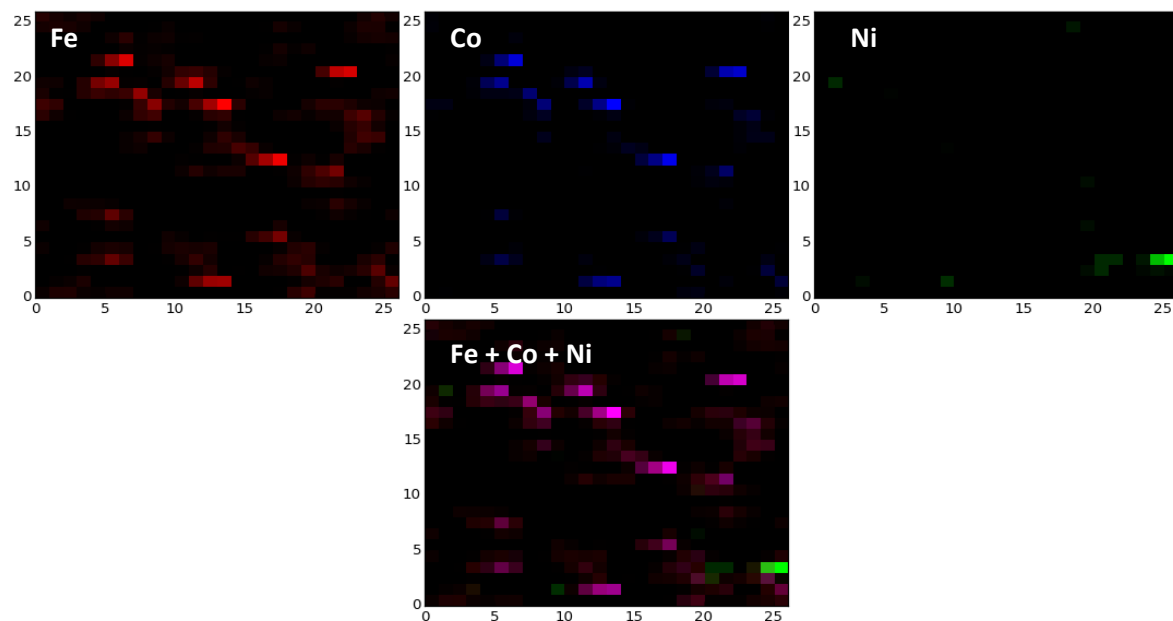


Figure 10 XRF maps of iron (top left), cobalt (top middle) and nickel (top right) distribution across a 1 x 1 mm section of diesel emission sample filter D3, along with an overlay of all three elements (bottom middle)

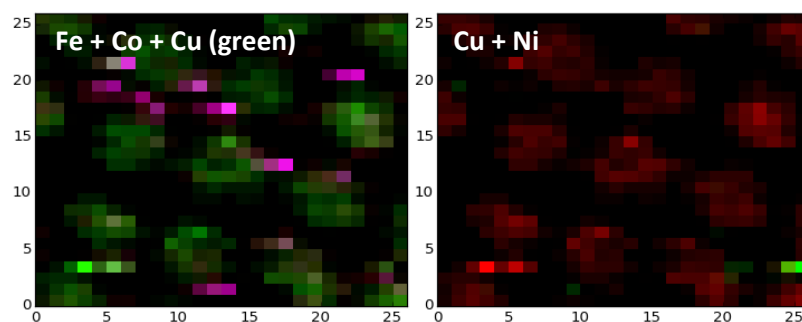


Figure 11 Overlaid XRF maps of iron, cobalt and copper (left) and copper and nickel (right)

Figure 8 emphasises the difference in relative concentrations of chlorine and copper illustrated in the maps, with chlorine exhibiting 3.3x the fluorescence signal of copper.

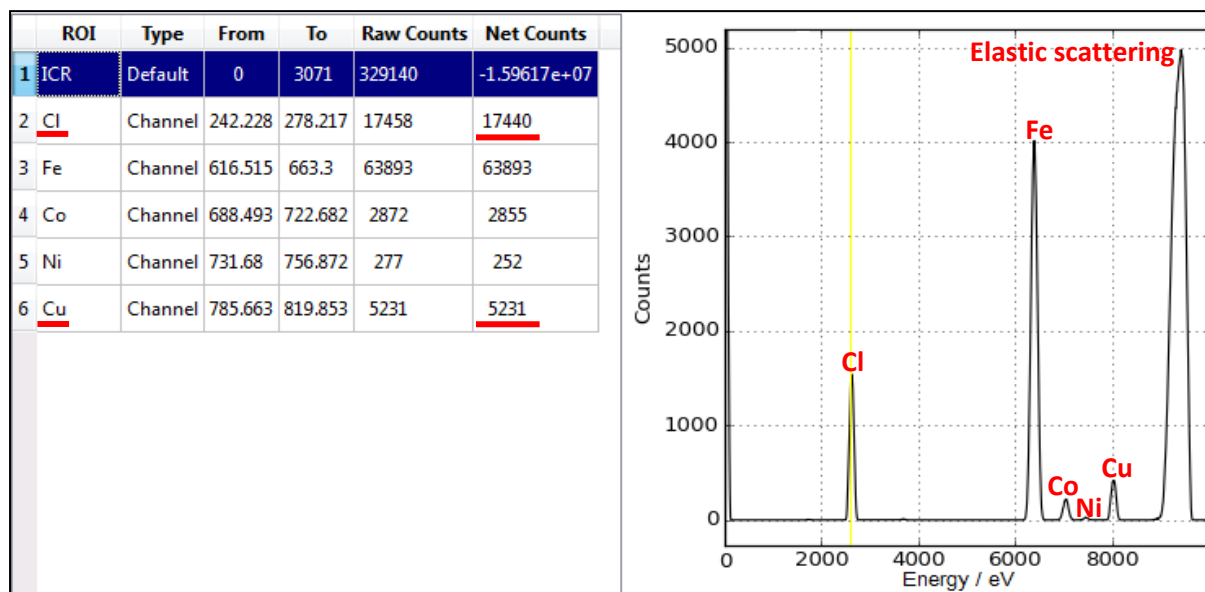


Figure 12 XRF spectrum and counts of detected elements in D3 diesel emission sample

The even distribution of Cu and Cl across the filter might be indicative of contamination, but an XRF spectrum of a blank polycarbonate filter (figure 9) shows no detectable quantities of either element, while a map of particulates from biomass burning (figure 10) on a polycarbonate filter shows a different distribution. These scans were taken at the same time in the same sample holder, and imply that the source of Cu and Cl in the diesel emission sample is the engine rather than external contamination. However, this cannot be confirmed due to the small number of samples and the removal of the model engine.

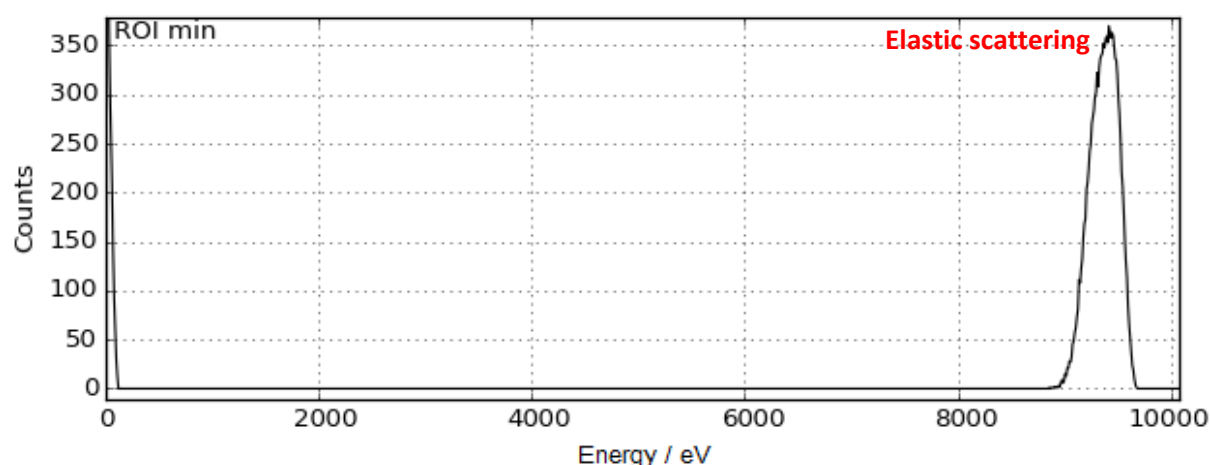


Figure 13 XRF spectrum of a blank polycarbonate filter. The filter is composed of carbon, hydrogen and oxygen and the installed detector does not detect elements lighter than sodium, so the spectrum appears blank apart from the elastic scattering peak at 9500 eV

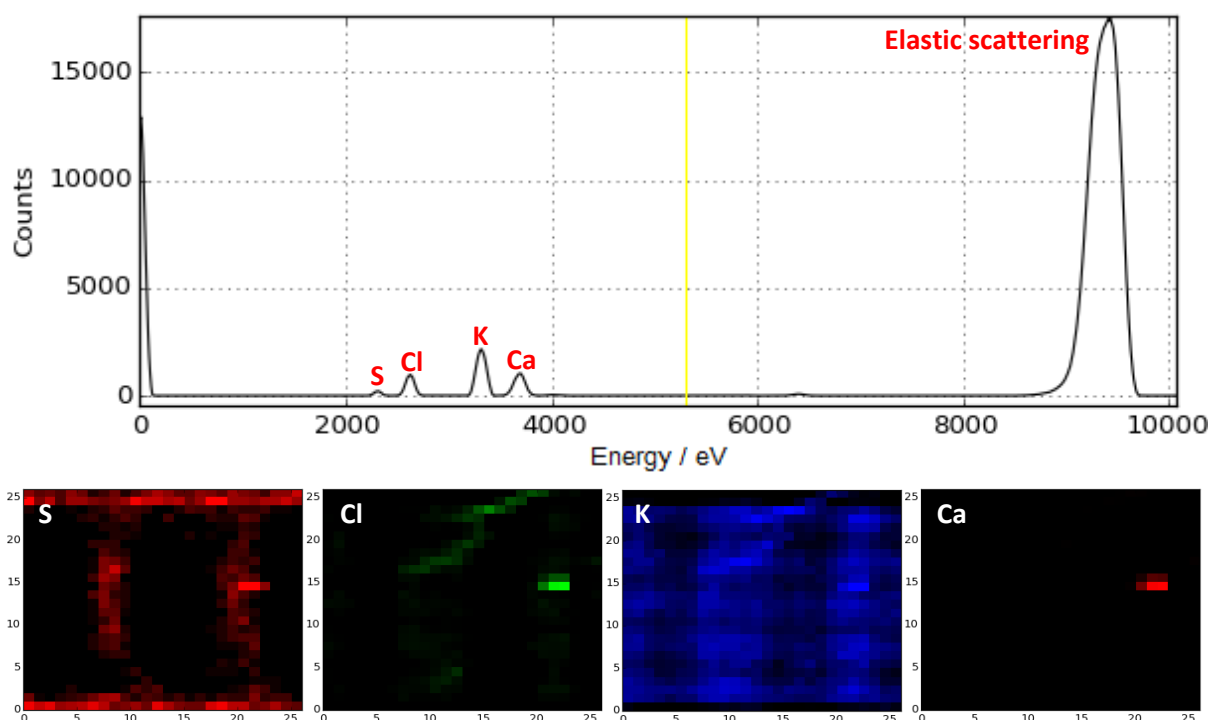


Figure 14 XRF spectrum and element maps of a sample from agricultural biomass burning collected in China. While some chlorine is detected, the sample shows a different concentration and distribution of Cl from the diesel emission sample, and no detectable copper.

#### 4. Discussion

An analysis of 10 different diesel fuels, and three different lubricating oils, all with different chlorine/chloride concentrations (Dyke, et al., 2007) found that the formation of chlorinated organic compounds in the exhaust was driven primarily by the content of the fuel. No discernible correlation was found between the chlorine concentration in lubricating oil and the exhaust.

Catalysts represent another potential source of chlorine compounds. (Johnson, 2008) Magnesium chloride is an effective storage material for urea, which functions as a selective reduction catalyst (SCR) employed to reduce  $\text{NO}_x$  emissions in modern diesel engines (Johnson, 2008).

Alkali metal chlorides in copper molybdate, tungstate or vanadate matrices were found to be effective catalytic surfaces for supporting the oxidation of diesel soot due to the formation of volatile copper chlorides on their surfaces (Kruse, et al., 1998). Copper and chromium oxides in conjunction with potassium chloride were also shown to be effective at oxidising combustion products from diesel fuel (Wang & Haynes, 2003). More recent literature (Liu, et al., 2011) (Laroo, et al., 2013) refer to the popularity of copper zeolites (aluminosilicate clay particles with high isomorphous substitution and a high copper content) as particulate filters and active surfaces for the urea SCR to operate on. Both papers express concern that these catalysts may also facilitate the formation of polychlorinated dioxins and furans, although neither group reported any detectable release.

Copper oxidation catalysts are poisoned by the presence of chlorine, as volatile copper chlorides with a low Tamman's temperature (the temperature at which the atoms in a solid become mobile and reactive) are generated, forming a layer of material on the metal surface (Twigg & Spenser, 2003) (Argyle & Bartholomew, 2015). This layer is lost from the catalyst when it undergoes regeneration and thus enters the exhaust stream, and potentially represents a significant, albeit intermittent, source of

chlorine to the exhaust stream. The XRF maps generated by the D3 sample may represent an example of this phenomenon, but a single sample is not sufficient to draw such conclusions from.

## 5. Summary and further work

This series of experiments provides information on the distribution and speciation of chlorine in diesel particulate emissions from a model Euro-5 diesel engine. SEM-EDX shows that the chlorine content of the particulates is evenly distributed across the filter with no particular hotspots, and this is supported by the more sensitive XRF mapping apparatus. XRF mapping also shows that the chlorine distribution overlaps with that of copper, implying that the chlorine is present as copper chloride. However, the relative concentrations of copper and chlorine reported by the XRF spectrum show that copper chloride can only account for ~60% of the total chlorine, and the Cl XANES spectrum more closely resembles the spectra of chlorinated organic compounds.

The dehydrating effect of evacuation on the mineral chloride standards in SUL-X imply that the setup is less suitable than the helium atmosphere employed for low-energy x-ray measurement employed at other synchrotrons like DIAMOND or the Photon Factory, and the possibility that evacuation has altered the composition and thus the XANES spectra of the diesel particulate samples cannot be ruled out. Further XANES analysis of fresh samples in a helium environment would provide clarity, however the model Euro-5 engine at the University of Birmingham was replaced with a Euro-6 model provided by the manufacturer in February 2015 and thus no further samples can be collected under the same conditions for direct comparison.

Samples from the model Euro-6 engine are currently undergoing organic analysis via two dimensional gas chromatography (2DGC) (unpublished) and the group has reported tentative findings of chlorinated organic compounds in the vapour phase. The composition of the oxidation catalyst is under examination at time of writing.

Copper chloride is known to function as a catalytic surface for the chlorination of unsaturated organic molecules (Arcoya, et al., 1982) (Taylor, et al., 2000) which may be more of an issue with vehicles burning biodiesel which contain more unsaturated compounds in their emission (Price, et al., 2017). Further experimentation burning diesel fuels in the presence of copper chloride might yield results that inform future real engine testing for chlorinated exhaust products. Collection of particulate samples from the surface of the catalyst prior to regeneration has the potential to yield further information on whether chlorinated organics are formed on the catalyst surface or separately during combustion.

## Works Cited

- Abuduwaiti, J., Gabchenko, M. V. & Junrong, X., 2008. Eolian transport of salts-A case study in the area of Lake Ebinur (Xianjiang, Northwest China). *Journal of Arid Environments*, 72(10), pp. 1843-1852.
- Ainsworth, E. A., 2008. Rice production in a changing climate: a meta-analysis of responses to elevated carbon dioxide and elevated ozone concentration. *Global Change Biology*, Volume 14, pp. 1-9.
- Aldener, M. et al., 2006. Reactivity and loss mechanisms of NO<sub>3</sub> and N<sub>2</sub>O<sub>5</sub> in a polluted marine environment: results from in situ measurements during New England air quality study 2002. *Journal of Geophysical Research*, Volume 111, p. D23S73.
- Annamalai, K. & Puri, I. K., 2007. NO<sub>x</sub> sources and production mechanisms. In: *Combustion Science & Engineering*. Boca Raton; FL: CRC Press, pp. 755-765.
- Anon., 1977. Additives, lubricants. In: *Encyclopedia of Chemical Processing and Design: Volume 2 - Additives to Alpha-olefins*. New York: Marcel Dekker Inc, p. 79.
- Arcoya, A., Cortes, A. & Seoane, X. L., 1982. Optimization of copper chloride based catalysts for ethylene oxohydrochlorination. *The Canadian Journal of Chemical Engineering*, 60(1), pp. 55-60.
- Argyle, M. D. & Bartholomew, C. H., 2015. Heterogeneous Catalyst Deactivation and Regeneration: A Review. *Catalysts*, Volume 5, pp. 145-269.
- Carvalho, M. J. S. d., Seidl, P. R., Belchior, C. R. P. & Sodre, J. R., 2010. Lubricant viscosity and viscosity improver additive effects on diesel fuel economy. *Tribology International*, pp. 2298-2302.
- Dyke, P. H., Sutton, M., Wood, D. & Marshall, J., 2007. Investigations on the effect of chlorine in lubricating oil and the presence of a diesel oxidation catalyst on PCDD/F releases from an internal combustion engine. *Chemosphere*, Volume 67, pp. 1275-1286.
- Fairlie, M., 1939. USA, Patent No. 2239953 A.
- Friend, A. J., Ayoko, G. A., Stelcer, E. & Cohen, D., 2011. Source apportionment of PM<sub>2.5</sub> at two receptor sites in Brisbane, Australia. *Environmental Chemistry*, 8(6), pp. 569-580.
- Fujimori, T., Tanino, Y., Takaoka, M. & Morisawa, S., 2010. Chlorination mechanism of carbon during dioxin formation using Cl-K near-edge x-ray absorption fine structure. *Analytical Sciences*, Volume 26, pp. 1119-1126.
- Gong, R., Hochmuth, M. & Weatherburn, D. C., 2003. *Polycyclic Aromatic Hydrocarbons and Diesel Particulates*. Wellington, New Zealand, Australian Transport Research Forum.
- Graedel, T. E. & Keene, W. C., 1995. Tropospheric budget of reactive chlorine. *Global Biogeochemical Cycles*, 9(1), pp. 47-77.
- Jaye, C., Woicik, J. & Fischer, D. A., 2008. Enhancement of Engine Oil Wear and Friction Control Performance through Titanium Additive Chemistry. *Tribology Transactions*, pp. 324-331.

- Johnson, T. V., 2008. Review of Diesel emissions and control. *International Journal Engine Research*, pp. 275-285.
- KEK-PF, 2014. *BL-9A : High-intensity and low-energy XAFS*. [Online] Available at: [http://pfwww.kek.jp/users\\_info/station\\_spec/xafsbl/9a/bl9a.html](http://pfwww.kek.jp/users_info/station_spec/xafsbl/9a/bl9a.html) [Accessed 21 09 2017].
- Kleeman, M. J., Schauer, J. J. & Cass, G. R., 2000. Size and composition distribution of fine particulate matter emitted from motor vehicles. *Environmental Science & Technology*, 34(7), pp. 1132-1142.
- Kruse, N., Frennet, A. & Bastin, J.-M., 1998. *Catalysis and Automotive Pollution Control IV*. Eastbourne: Elsevier.
- Laroo, C., Schenk, C., Sanchez, J. & McDonald, J., 2013. Emissions of PCDD/Fs, PCBs, and PAHs from a Modern Diesel Engine Equipped with Selective Catalytic Reduction Filters. *SAE International Journal of engines*, 45(15), pp. 1311-1339.
- Liu, Z. G. et al., 2011. Investigation of PCDD/F emissions from mobile source diesel engines: impact of copper zeolite SCR catalysts and exhaust aftertreatment configurations.. *Environmental Science & Technology*, pp. 2965-72.
- McCulloch, A. et al., 1999. Global emissions of hydrogen chloride and chloromethane from coal combustion, incineration and industrial activities: reactive chlorine emissions inventory. *Journal of Geophysical Research*, 104(D7), pp. 8391-8403.
- Meitzner, G., Via, G. H., Lytle, F. W. & Sinfelt, J. H., 1992. Analysis of X-ray Absorption Edge Data on Metal Catalysts. *Journal of Physical Chemistry*, 96(12), pp. 4960-4964.
- Mielke, L. H., Furgeson, A. & Osthoff, H. D., 2011. Observation of ClNO<sub>2</sub> in a mid-continental urban environment. *Environmental Science & Technology*, Volume 45, pp. 8889-8896.
- Moreno, T. et al., 2013. Daily and hourly sourcing of metallic and mineral dust in urban air contaminated by traffic and coal-burning emissions. *Atmospheric Environment*, Volume 68, pp. 33-44.
- Osthoff, H. D. et al., 2008. High levels of nitryl chloride in the polluted subtropical marine boundary layer. *Nature Geoscience*, Volume 1, pp. 324-328.
- Price, D. J. et al., 2017. More unsaturated, cooking-type hydrocarbon-like organic diesel particle emissions from renewable diesel compared to ultra low sulfur diesel in at-sea operations of a research vessel. *Aerosol Science and Technology*, 51(2), pp. 135-146.
- Querol, X. et al., 2001. Monitoring of PM<sub>10</sub> and PM<sub>2.5</sub> around primary particulate anthropogenic emission sources. *Atmospheric Environment*, Volume 35, pp. 845-858.
- Querol, X. et al., 2001. PM<sub>10</sub> and PM<sub>2.5</sub> source apportionment in the Barcelona metropolitan area, Catalonia, Spain. *Atmospheric Environment*, Volume 35, pp. 6407-6419.
- Taylor, P. H. et al., 2000. Copper-catalyzed chlorination and condensation of acetylene and dichloroacetylene. *Chemosphere*, 40(12), pp. 1297-1303.

- Thornton, J. A. et al., 2010. A large atomic chlorine source inferred from mid-continental reactive nitrogen chemistry. *Nature Letters*, Volume 464, pp. 271-275.
- Twig, M. V. & Spenser, M. C., 2003. Deactivation of copper metal catalysts for methanol decomposition, methanol steam reforming and methanol synthesis. *Topics on Catalysis*, 22(3-4), pp. 191-203.
- Wang, S. & Haynes, B. S., 2003. Catalytic combustion of soot and metal oxides and their supported metal chlorides. *Catalysis Communications*, 4(11), pp. 591-596.
- Wang, Y., Logan, J. A. & Jacob, D. J., 1998. Global simulation of tropospheric O<sub>3</sub>-NO<sub>x</sub>-hydrocarbon chemistry. *Journal of Geophysical Research*, 103(D9), pp. 10727-10755.
- Wang, Z. et al., 2016. Analysis of chemical characteristics of PM<sub>2.5</sub> in Beijing over a 1 year period. *Journal of Atmospheric Chemistry*, 73(4), pp. 407-425.
- Wayne, R. P., 2006. 4.4 Influence of Trace Constituents. In: *Chemistry of Atmospheres - Third Edition*. Oxford: Oxford University Press, pp. 177 - 247.
- Zhang, R. et al., 2013. Chemical characterization and source apportionment of PM<sub>2.5</sub> in Beijing: a seasonal perspective. *Atmospheric Chemistry and Physics*, Volume 13, pp. 7053-7074.
- Zhu, F. et al., 2010. Chlorides behavior in raw fly ash washing experiments. *Journal of Hazardous Materials*, 178(1-3), pp. 547-552.
- Zhu, F. et al., 2008. Chloride chemical form in various types of fly ash. *Environmental Science & Technology*, 42(11), pp. 3932-3937.

## Chapter 3 Atmospheric Processing of iron in Coal Fly Ash

### 1. Introduction

Iron is most common limiting nutrient in high nutrient, low chlorophyll (HNLC) regions where microbial populations are not as developed as one would expect from the abundance of other nutrients like N and P (Meskhidze, et al., 2005) (Siefert, et al., 1994).

The Redfield Ratio, first defined by A. C. Redfield et al (Redfield, et al., 1963) and later refined by Claudia Benitez-Nelson (Benitez-Nelson, 2000) defines the ratio of macronutrients found in marine microbiota. The ratio of carbon to nitrogen to phosphorus required for growth was originally quantified at 106:16:1 but is now estimated to be closer to 117:14:1. On the same scale, the ratio of iron is around 0.001 (Martin, 1990) (Raynor-Canham & Flynn, 2010).

Near-surface seawater has a positive redox potential of +200 to +600 mV, and a pH of around 8 (Cooper, 1937) (Edgington, et al., 1967) (Liss, et al., 1973) (Hansen, 1999). Iron is oxidised to Fe(III) at redox potential above +160 mV at pH 8 (Siggs, 2000). Fe(III) is exceptionally insoluble in water at the pH of seawater (figure 1).

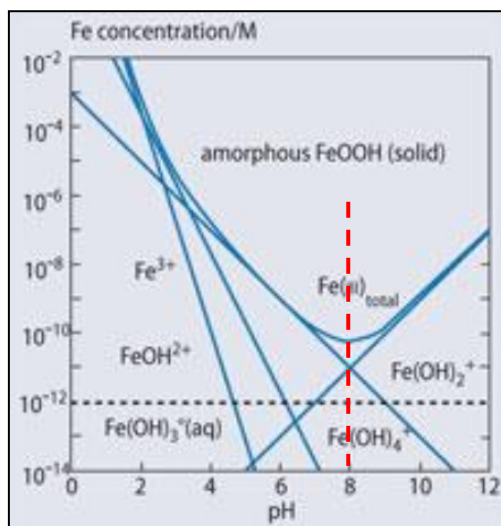


Figure 15 Log concentration vs pH of iron in seawater, from *The Biogeochemistry of iron in seawater* (Turner & Hunter, 2002). The background concentration of uncharged Fe(OH)<sub>3</sub> is depicted with the black dotted line, while the average pH of seawater is highlighted with a red dotted line

Historically, iron was thought to be available in relatively high concentrations in seawater until the primary source was discovered to be contamination from research vessels (Broecker & Peng, 1982). Improved sampling techniques have minimised this contamination (Worsfold, et al., 2014) and modern fluorescence-based techniques (Bowie, et al., 1998) have allowed for accurate determination of iron concentrations in natural seawater, which is generally 0.05 – 2 nanomoles per litre (Achterberg, et al., 2001).

Estimates of global iron deposition from the Earth's surface to the oceans range from 8.4 to 13.3 Tg/yr, with contributions from coal combustion estimated at between 0.16 and 0.455 Tg/yr based on rates of consumption and distribution of emission control devices such as scrubbers and electrostatic precipitators (Wang, et al., 2015) (Ito, 2013). Contributions from extra-terrestrial sources may be considerable but are not included in current models due to the high uncertainty in rates of global

deposition (Plane, et al., 2015). These estimates state that coal combustion contributes 1.2 – 5.4% of total iron deposition, but the bioavailability of the iron in coal fly ash (CFA) is predicted to be greater due to iron being present in combustion products as more soluble species (Chen, et al., 2012) (Oakes, et al., 2012) (Mahowald, et al., 2009) (Schroth, et al., 2009). The solubility of iron in coal fly ash should be further enhanced by atmospheric processing, where strong oxidising agents like ozone, NO<sub>x</sub> and SO<sub>2</sub> react with the particles to render the resident iron more available (Li, et al., 2017) (Wang, et al., 2012) (Desboeufs, et al., 2001) as it has been shown to in mineral dust (Shi, et al., 2015) (Shi, et al., 2011) (Solmon, et al., 2009).

This series of experiments examines samples of CFA collected by the electrostatic precipitators on three different power plants from Wales, Poland and China. The ≤ 10 μm fraction (representing ~23% of all coal power plant emissions (Wang, et al., 2015)) was selected due to its mobility in the atmosphere and high surface area to mass ratio. In addition to elemental composition, iron availability in each sample was tested by selective extraction of the most soluble species. Samples were subjected to simulated atmospheric processing in a controlled environment with fixed concentrations of NO<sub>x</sub>, SO<sub>x</sub> and ozone with and without contributions from photochemistry, after which further solubility studies were carried out to determine changes in metal availability as well as nitrate and sulfate uptake. Attempts were made to classify the speciation of iron in the CFA samples using selective chemical extraction and XANES using synchrotron radiation.

## 2. Methods and materials

### 2.1 Coal Fly Ash samples:

The Polish “Krakow” ash was collected from a flue trap in the Elektrociepłownia Kraków facility burning bituminous coal in 2008.

The “Aberthaw” ash was collected from a flue trap in the Aberthaw B power station in Wales burning anthracite in 2010.

The “China” ash was supplied by Shandong University in 2010. It was collected from a flue trap in a local power station burning bituminous coal which has asked not to be identified.

### 2.2 PM10 separation:

PM10 fractions were collected from each sample using a resuspension apparatus (figure 2) that uses nitrogen gas to push samples through settling plates to remove larger particles. Particles were driven through the system by an intermittent flow of nitrogen gas at 0.4 bar, controlled by a manually operated ball valve. Samples were collected on pre-weighed 47 mm 0.2 µm pore size Isopore™ polycarbonate filter papers by Millipore, installed in a cartridge and pulled towards the filter by a reciprocating air pump pulling through a flow meter at 50 L/min. Switching the pump on and off at such a high flow rate tended to destroy the filter papers, so prior to shut down after sample collector the flow meter was restricted to <5 L/min. At all times the filter papers were handled with plastic forceps in order to avoid contamination with metal tools.

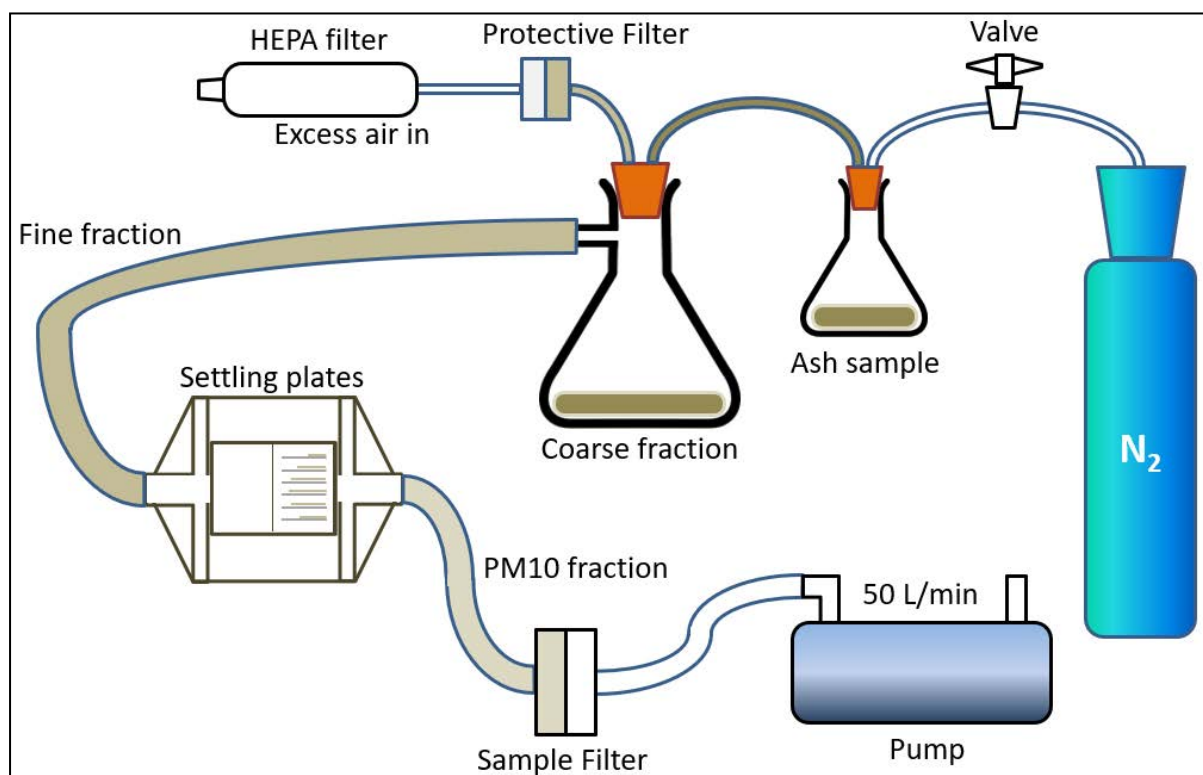


Figure 2 Dust resuspension apparatus

To collect PM10, the sample was placed in a 500ml conical flask sealed with a rubber stopper with 6mm diameter inlet and outlet plastic tubing, with joints composed of rubberised plastic tubing. A barbed reducer on the inlet line increased the pressure of the inflowing nitrogen by reducing the line

diameter to 1mm. The outlet fed into a 1L Buchner flask with two inlets- one carrying air and ash from the first flask and the other carrying clean air via a HEPA filter to avoid pressure gradients. The filter was protected from ash intrusion upon reversal of flow by the nitrogen line by a quartz filter paper that was replaced when the sample was changed. The Buchner flask's sidearm was connected to a specially constructed PTFE settling chamber where the samples passed into a 60 x 55 x 55 mm antechamber followed by a bank of 33 mm settling plates where the remaining >10 µm particles settled out of the flow. The remaining particles were carried onto a filter paper, which was removed and placed in a 90 mm petri dish to be re-weighed to determine the mass of collected material.

Particle size was confirmed by examination of lightly coated filters under a Kyow Medilux-12 light microscope with an XLi USB camera attachment. The resulting images are shown in figure 3.

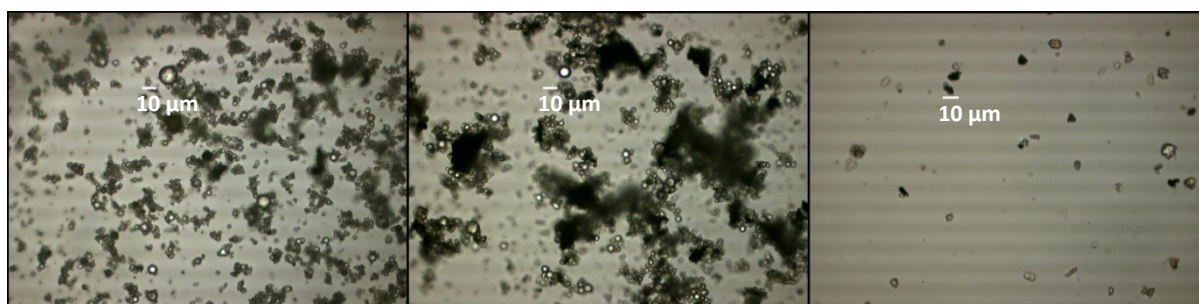


Figure 3 Microscope images of PM10 fraction of ash separated by the resuspension apparatus, from Krakow (left), Aberthaw (centre) and Shandong (right)

### 2.3 Selective extraction of soluble iron by ammonium acetate at pH 4.7

After processing, sample filter papers were placed in fresh 50 ml sample tubes along with 10 ml of ammonium acetate buffer solution at pH 4.7 (Dean, 2003) (Müller & Seiler, 1999). Ammonium acetate brings exchangeable and non-crystalline iron into solution, although the effectiveness of acetate as a chelating agent also promotes the dissolution of relatively insoluble Fe(II) species like siderite (iron (II) carbonate) (Bénézech, et al., 2009) so the results were contrasted against ascorbate extraction (section 2.4) to quantify the siderite content. Sample tubes were set on a Stuart SB3 rotary mixer at 15 rpm for 90 minutes. After mixing, the solutions were filtered through Pall 32 mm Acrodisc syringe filters with 0.2 µm Supor membranes into fresh sample tubes which can be stored with no significant changes in soluble iron concentration anticipated.

### 2.4 Ascorbate extraction of exchangeable iron

Ascorbate extraction is a common method of quantifying readily soluble and exchangeable iron in solid samples (Gleyzes, et al., 2002) (Kostka & III, 1994). Ascorbate extractant was prepared in deoxygenated deionised water, prepared by bubbling nitrogen gas through deionised water for 120 minutes.

The conventional method of preparing ascorbate extractant requires 50 g/L of sodium citrate. Due to the lack of commercially available sodium citrate above 98% purity, citric acid was used as a substitute. The pH of the extractant solution was adjusted to 7.5 with sodium hydroxide. The extractant solution was prepared using:

- 300 ml deoxygenated, deionised water
- 15 g sodium hydrogen carbonate (Sigma Aldrich)
- 11.25 g citric acid (Honeywell Fluka TraceSELECT)
- 3 g ascorbic acid (Fluka Analytical TraceSELECT)
- 36 ml 0.1 M sodium hydroxide (Sigma Aldrich)

5 mg CFA samples were placed in fresh 15 ml sample tubes along with 5 ml of ascorbate extractant. Sample tubes were set on a Stuart SB3 rotary mixer at 15 rpm for 90 minutes. After mixing, the solutions were filtered through Pall 32 mm Acrodisc syringe filters with 0.2  $\mu\text{m}$  Supor membranes into fresh sample tubes prior to colorimetric analysis.

## 2.5 Timed dissolution

Samples of Aberthaw and Shandong ash were suspended in dilute acid and mixed over an extended period of time to monitor the rate of dissolution of iron and other elements of biological relevance (see section 2.7). The dissolution matrix was set up to approximate the conditions surrounding cloud condensation nuclei: acidic, rich in ammonium sulfate and containing natural organic chelating agents such as oxalate (Pöschl, 2005) (Chen, et al., 2012) (Chen & Grassian, 2013). For each CFA sample (Krakow ash was not available during this period), two solutions were prepared:

- Two beakers containing magnetic stirrers and 200 ml of dilute HCl (Sigma Aldrich), one at pH 2 and one at pH 3
- 5.4 mg sodium oxalate (Fisher Scientific) added to each beaker, leading to a concentration of 200  $\mu\text{M}$
- 26.4 g ammonium sulfate (Sigma Aldrich) added to each beaker, leading to a concentration of 1 M

The beakers were covered in foil to avoid photochemical effects and placed on magnetic stirring plates. Once the plates were turned on, 6 mg of ash was added to each beaker- a material concentration of 30 mg/L. Samples were collected in disposable 1ml plastic syringes and passed through disposable Whatman 0.02  $\mu\text{m}$  syringe filters into 1.5 ml Eppendorf centrifuge tubes for storage at fixed time intervals: 2.5 min, 10 min, 60 min, 24 hours, and 7 days after each ash sample was added. Samples were analysed for iron content by colorimetry and multiple elements by ICP-MS.

## 2.6 Colorimetric determination of soluble iron

The soluble iron content of samples was quantified by ferrozine colorimetry, using the following reagents:

- Romil-SpA Super Purity HCl diluted to 0.1M (pH 1)
- 0.01M Fluka Analytical TraceSELECT ascorbic acid
- 0.01M Sigma Aldrich BioXtra 3-(2-Pyridyl)-5,6-diphenyl-1,2,4-triazine-*p,p'*-disulfonic acid monosodium salt hydrate (ferrozine) in 0.1M ammonium acetate solution
- A concentrated ammonium acetate buffer solution containing 7.3M Fisher Scientific trace metals grade ammonium hydroxide and 5.22M Fluka Analytical TraceSELECT glacial acetic acid

Aliquots from the filtered samples were acidified using 100  $\mu\text{L}$  pH 1 HCl, reduced with 100  $\mu\text{L}$  ascorbic acid solution, complexed with 100  $\mu\text{L}$  ferrozine and stabilised after 30 minutes with 100  $\mu\text{L}$  of concentrated buffer solution. Standards were generated from pH 2 HCl stock solutions of AAS grade Fe diluted using the appropriate matrix and previously documented reagents. Samples and standards were analysed by a Cary50 UV-VIS spectrophotometer, scanning the wavelength range from 540 to 720 nm. Measurements were based on the absorbance reading at 562 nm, minus the reading at 700 nm which is considered the background for each sample.

## 2.7 Multi-element analysis by Inductively Coupled Plasma Mass Spectrometer (ICP-MS)

The Perkin Elmer® NexION 300X ICP-MS with SimulScan™ dual stage detector requires that all samples be loaded in 2%  $\text{HNO}_3$ . All samples were prepared using 0.8 ml of sample in 9.2 ml of 2.2%  $\text{HNO}_3$ . Standards and blanks were prepared in 2%  $\text{HNO}_3$  containing 0.8 ml of the appropriate sample matrix. The system was set up to quantify seven elements:

- Iron (limiting nutrient (Jickells, et al., 2005))
- Aluminium (phytotoxic in high concentrations (Lindemann, et al., 1990))
- Copper (inhibits photosynthesis in algae (Melis, et al., 2000))
- Manganese (essential micronutrient for photosynthesis (Livorness & Smith, 1982))
- Selenium (essential for algal enzymes, low toxic threshold (Vitova, et al., 2015))
- Lead (toxic heavy metal)
- Arsenic (toxic heavy metal with soluble oxyanion at positive redox potential (Masscheleyn, et al., 1991))

Al and Fe standards were prepared in the range of 5 – 500 ppb, while other elements were expected to be lower in concentration and were prepared in the 0.5 – 50 ppb range.

## 2.8 Simulated Atmospheric Processing

All gas cylinders were supplied by BOC. Gases were supplied to the chamber from three cylinders:

50L compressed air

50L nitrogen with 10ppm  $\text{SO}_2$

20L nitrogen with 50ppm  $\text{NO}_2$

via four Brooks Instruments mass flow controllers (two 58505 units and two GF040 units). The air flow was split into two lines- one of which was passed through a bubbler to raise RH while the other line was passed through a Pen-Ray®3SC-9 Light source with 185nm lamp to generate ozone. Gas was supplied to the chamber in the following ratio:

300  $\text{cm}^3/\text{min}$  air (bubbler line) with high RH

100  $\text{cm}^3/\text{min}$  air (ozone generator line) with ozone

100  $\text{cm}^3/\text{min}$  nitrogen/ $\text{SO}_2$

25  $\text{cm}^3/\text{min}$  nitrogen/ $\text{NO}_2$

The average concentration delivered to the system for  $\text{SO}_2$  is therefore  $100/525 \times 10 = 1.9$  ppm, and for  $\text{NO}_2$  is  $25/525 \times 50 = 2.4$  ppm.

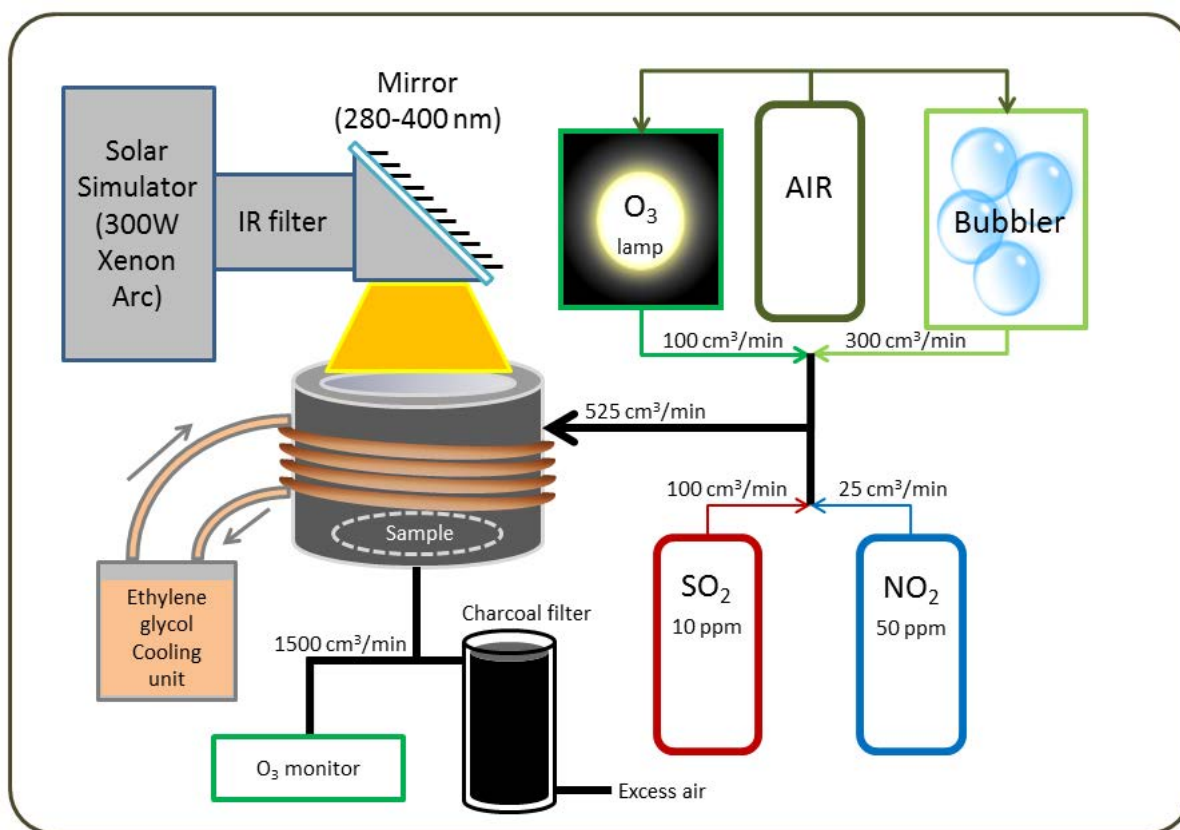


Figure 4 Schematic of the simulated atmospheric processing chamber

Since ozone is known to interact rapidly with  $\text{NO}_2$  in the atmosphere, the ozone concentration throughout the system was monitored by connecting an InDevR 2B Ozone Monitor (model 205) to the chamber outlet, with an additional air inlet since the monitor pump draws at a rate of 1.5 L/min. The monitor reported an average  $\text{O}_3$  content of 4.65 ppm in the outflow, equivalent to 13.3 ppm in the chamber.

To simulate daytime conditions, a L.O.T. Oriel 300W xenon-arc lamp in a 200-500W LSH302 housing was positioned next to the chamber. A mirror designed to reflect light in the 280 – 400 nm region delivered lamp light directly into the top of the chamber where the samples were positioned during exposure. The chamber was sealed with a 90 mm diameter 2 mm thick quartz window by UQG optics with ~90% transmittance at the near-UV range. For “light” exposures the lamp was run at 225W.

Readings collected with a Sensirion SHT/75 Temperature/Relative Humidity (RH) probe inside the chamber showed that use of the solar simulator lamp raised the temperature inside the chamber by around 5°C with a corresponding drop in RH. Since high relative humidity is a prerequisite for the majority of metal solubilisation reactions considered in atmospheric processing (Usher, et al., 2003) the readings from “light” processed samples cannot be considered representative and are included for completeness and to highlight any changes that occur in metal solubility without high RH. Samples that were processed with the solar simulator lamp without temperature/RH control are appropriately marked.

## 2.9 Metal analysis of processed ash by Inductively Coupled Plasma Optical Emission Spectroscopy (ICP-OES)

Samples of ash that had undergone simulated atmospheric processing were compared against untreated (raw) ash by analysing ammonium acetate extracts in a Perkin Elmer® Optima 8000 ICP-OES. 5 ml samples were mixed with 5 ml of 4% HNO<sub>3</sub> in order to match the pH requirements of the apparatus. This work was carried out prior to elemental composition determination by XRF, and prior to modification of the processing chamber to prevent drying of particles during processing with the solar simulator lamp.

Six elements were analysed during the run. Aluminium, copper and arsenic (also analysed in timed dissolution samples by ICP-MS), vanadium (essential for pigment synthesis in algae (Butler & Carter-Franklin, 2004)) and cobalt (essential component of several enzymes in algae (Croft, et al., 2006)) were also quantified in addition to iron.

## 2.10 ICP-OES versus ICP-MS

Inductively coupled plasma devices represent a step up from older atomic absorption spectrophotometer (AAS) devices in quantifying specific elements in solution. The main advantage of ICP-OES is that the 6000°C argon flame in the atomisation chamber causes samples to emit photons with spectral lines corresponding to the specific elements they contain. The atomised sample emitting photons due to the extreme high temperature rather than absorbing them as in an AAS setup means that an ICP does not require element-specific light sources for detection, and a single ICP setup can detect multiple elements using pre-configured photomultiplier tubes with no need to change the device configuration. The Optima 8000 ICP-OES can detect up to 12 different elements in a single run. The main limiting factor for OES observation is that spectral lines for some elements can overlap and minor emission lines from elements that represent major components of the sample can obscure major emission lines from minor components. To check for interference, multiple emission lines can be selected for a single element with significantly higher readings at a specific wavelength providing evidence of overlap. The downside of this check is that it limits the number of elements that can be detected per run.

ICP-MS devices drive atomised samples down a mass spectrometer quadrupole instead of passing them over photomultiplier tubes and determine elemental composition and concentration by mass: charge ratio rather than spectral photon emission. While MS devices have lower detection limits (<0.1 ppb versus 5 – 50 ppb for OES devices, depending on element) they can also suffer from interferences that are hard to compensate for. For example, it is difficult to measure arsenic in samples prepared in hydrochloric acid because As has an atomic weight of 75, and so does <sup>35</sup>Cl bonded temporarily to argon by the heat of the plasma. In this series of experiments, the processed ash samples were run in the ICP-OES because the ICP-MS had not yet been installed in the department.

## 2.11 Water-soluble cations by ion chromatography

Raw and processed ash samples on 47 mm polycarbonate filter papers (0.2 µm pore size) were placed in 50 ml sample tubes along with 10 ml deionised water. Sample mass was close to 10 mg so that sample concentration was close to 1 g/L. All samples were shaken for 90 minutes on a Stuart SB3 rotary mixer at 15 rpm. After mixing, the solutions were filtered through Pall 32 mm Acrodisk syringe

filters with 0.2 µm Supor membranes into fresh 15 ml sample tubes prior to analysis by ion chromatography.

Samples were divided for separate cation and anion quantification. Cation standards were prepared in the 0.5 – 10 ppm range with sodium, potassium, magnesium and calcium chloride from Sigma Aldrich. Anion standards were prepared in the 0.5 – 10 ppm range with sodium chloride, nitrite, nitrate, silfute, sulfate and phosphate, again all from Sigma Aldrich. Cation concentrations were determined using a Dionex DX500 ion chromatogram with a Thermo Scientific IonPac™ CS12A column, while anions were determined on a Dionex ICS2100 with an IonPac™ AS11HC column with an AG11HC guard column. Two Krakow ash samples were lost from the cation data set due to a leak and a pressure fault in the IC column.

## 2.12 Temperature moderation and humidity maintenance in processing chamber

The ambient temperature in the lab was fixed at 22°C. In order to maintain similar internal temperatures during “light” and “dark” exposures, the sample chamber was wrapped in 6mm internal diameter copper piping which carried ethylene glycol from a Julabo F32 cooler unit. The temperature of the chamber was monitored with a Sensirion SHT/75 temperature/RH probe while ethylene glycol was pumped through at varying temperatures. An ethylene glycol temperature of 5°C was found to yield a chamber temperature of 22°C while the solar simulator lamp was shining through the quartz window.

To further enhance RH inside the chamber for the duration of processing runs, the stainless steel grill on which the sample filters sit was spotted with deionised water prior to each sample being loaded.

## 2.13 Elemental Composition by X-Ray Fluorescence

X-ray Fluorescence was carried out on a Bruker S8 Tiger Wavelength Dispersive XRF with a 3KW rhodium tube source. Samples were installed in the autosampler as 500 mg of loose powder in Chemplex Industries FunnelShape SpectraMicro XRF sample cups, with the powder contained by a layer of 2.5 µm pre-cut thin-film Mylar. The Quant-Express software packaged with the device includes an “Oil 2 µm Mylar” add-on that compensates for the loss of signal from the Mylar layer in the output. Mylar is known to contain impurities in the ppm range of calcium, phosphorus, antimony, iron and zinc.

Reading from a 75 µm sample containing 50 mg/g of iron + 2.5 µm Mylar layer with either 0 or 999ppm, 0 or 1 mg/g of iron:

- No Fe impurity:  $((75 \times 50) + (2.5 \times 0) / 77.5) = 48.39$  mg/g before software modification
- Maximum Fe impurity:  $((75 \times 50) + (2.5 \times 0.999) / 77.5) = 48.42$  mg/g

The maximum possible addition to the iron signal from the Mylar layer is +0.03 mg/g or 0.062% for a sample containing 5% iron by weight. The contribution to the iron signal from Mylar is not considered significant.

XRF detected fluorescence signals equivalent to 37 - 41% of the total mass of the samples. This is within the expected range for XRF analysis of coal fly ash, with the remaining ~60% of the sample mass taken up by oxygen (Tiwari, et al., 2014) (Santoso, et al., 2016).

## 2.14 X-ray Absorbance Near Edge Structure (XANES)

Raw and processed CFA samples were analysed by XANES in the Sul-X beamline at the ANKA synchrotron at KIT, Karlsruhe, Germany. Readings were collected from samples on filters placed on Kapton tape. Readings were collected in the fluorescence mode with a Gresham 7 element Si(Li) detector. Beamline emission was set to 9.5 KeV.

## 2.15 XANES standards

The following iron-containing minerals were run as standards for Linear Combination Fitting of the coal fly ash samples. XANES spectra of the clay standards (illite, illite-smectite, montmorillonite and chlorite) were provided by Dr Angela Milne from the University of Plymouth. The spectra of siderite, pyrite and epidote were provided by Dr Konstantin Ignatyev, beamline operator at Diamond Light Source, Harwell.

Standard	Repeating unit	Crystal structure	% Fe	%Fe(II)	%Fe(III)
Goethite	$\alpha\text{-FeOOH}$	Dipyramidal	62.9%	0%	100%
Hematite	$\alpha\text{-Fe}_2\text{O}_3$	Rhombohedral	69.9%	0%	100%
Magnetite	$\text{Fe}_3\text{O}_4$	Hexoctahedral	77.7%	33%	67%
Ferrihydrite	$\text{Fe}_2\text{O}_3 \cdot \frac{1}{2}\text{H}_2\text{O}$	Di-hexagonal pyramidal	66.2%	0%	100%
Iron(II) sulfate heptahydrate	$\text{FeSO}_4 \cdot 7\text{H}_2\text{O}$	Monoclinic	20.1%	100%	0%
Siderite	$\text{FeCO}_3$	Trigonal hexagonal scalenohedral	62.1	100%	0%
Pyrite	$\text{FeS}_2$	Isometric diploidal	46.6%	100%	0%
Iron(III) sulfate	$\text{Fe}_2(\text{SO}_4)_3$	Trigonal hexagonal scalenohedral	27.9%	0%	100%
Illite	$(\text{Al}, \text{Mg}, \text{Fe})_2(\text{Si}, \text{Al})_4\text{O}_{10}[(\text{OH})_2, (\text{H}_2\text{O})]$	2:1 layer clay	5.5%	7.7%	92.3%
Illite-smectite mixed layer	(Layers of Illite & Montmorillonite)	2:1 layer clay	0.9%	9.1%	90.9%
Montmorillonite	$(\text{Na}, \text{Ca})_{1/3}(\text{Al}, \text{Mg})_2(\text{Si}_4\text{O}_{10})(\text{OH})_2 \cdot n\text{H}_2\text{O}$	2:1 layer clay	2.6%	9.6%	90.4%
Chlorite	$(\text{Mg}, \text{Fe})_3(\text{Si}, \text{Al})_4\text{O}_{10}(\text{OH})_2 \cdot (\text{Mg}, \text{Fe})_3(\text{OH})_6$	2:1 layer phyllosilicate	34.8%	53.5%	46.5%
Epidote	$\text{Ca}_2\text{Fe}_{2.25}\text{Al}_{0.75}(\text{SiO}_4)_3(\text{OH})$	Monoclinic prismatic	24.2%	0%	100%
Feldspar	$\text{KAlSi}_3\text{O}_8$	Monoclinic (tetrahedral Fe)	0.2%	0%	100%

### 3. Results

#### 3.1 Elemental composition

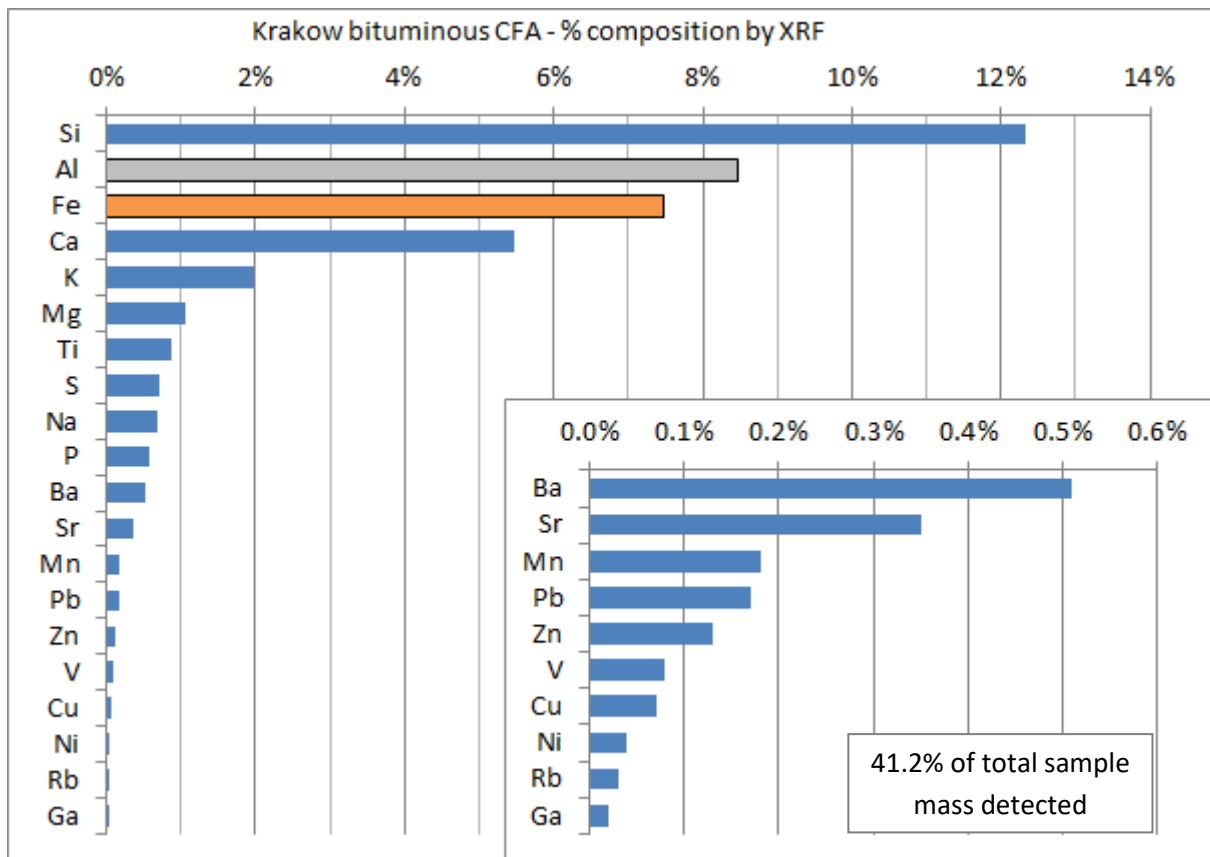


Figure 5 Elemental composition of a 500 mg sample of bituminous coal CFA from Krakow, including a close-up of the concentrations of minor elements representing  $\leq 0.5\%$  of the sample by mass

Notable features of the Krakow ash sample:

- Krakow CFA has the highest Fe content and lowest Al content of all the ash samples analysed, at 7.5% and 8.5% respectively
- Has the highest calcium content at 5.5%
- No detectable arsenic or selenium, implying total content of  $< 0.01\%$
- Contains  $\sim 0.7\%$  sulfur

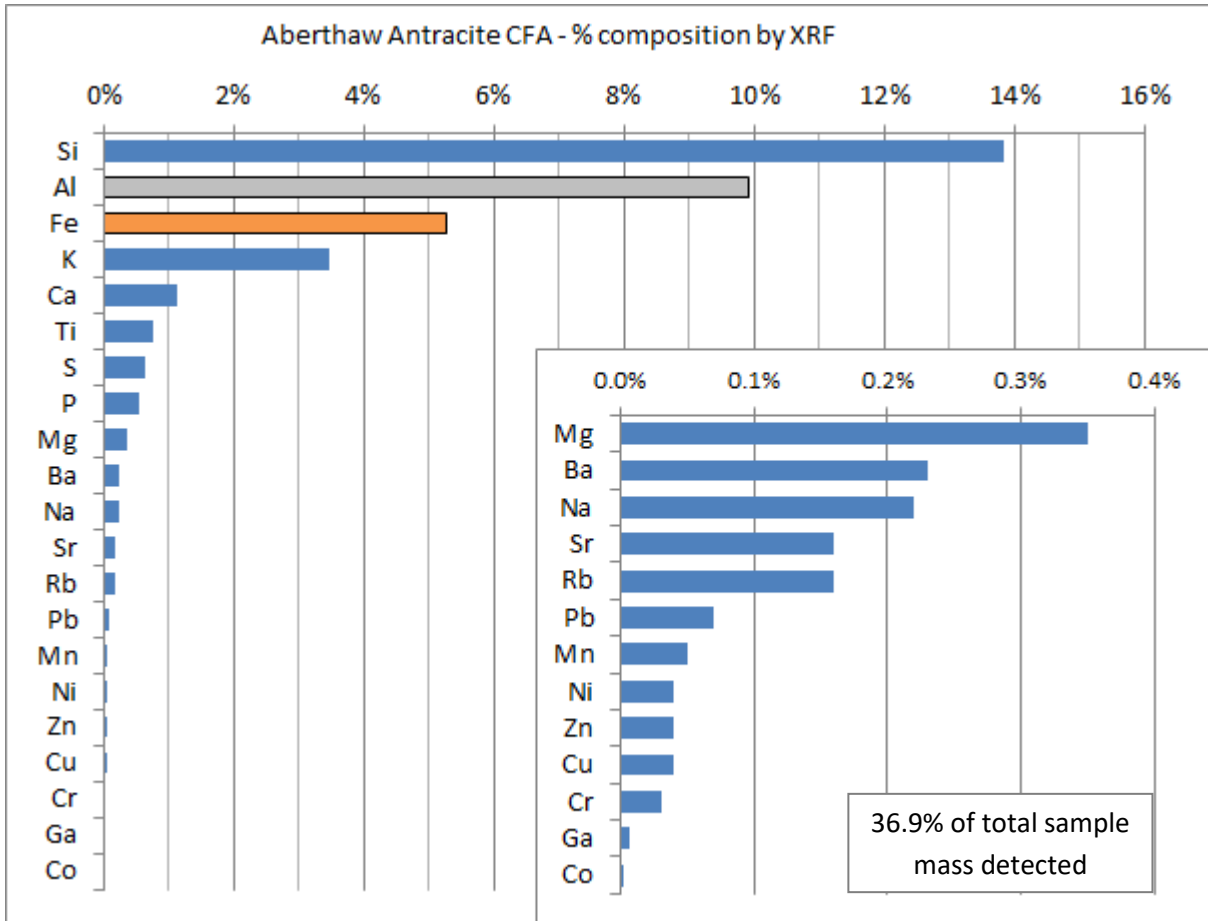


Figure 6 Elemental composition of a 500 mg sample of anthracite coal CFA from Aberthaw, Wales, including a close-up of the concentrations of minor elements representing  $\leq 0.5\%$  of the sample by mass

Notable features of the Aberthaw ash sample:

- Aberthaw CFA has a roughly 2:1 ratio of Al to Fe, at 9.9% and 5.2% respectively
- Lowest calcium concentration at 1.2%
- Contains no detectable arsenic or selenium, implying maximum content of  $<0.01\%$

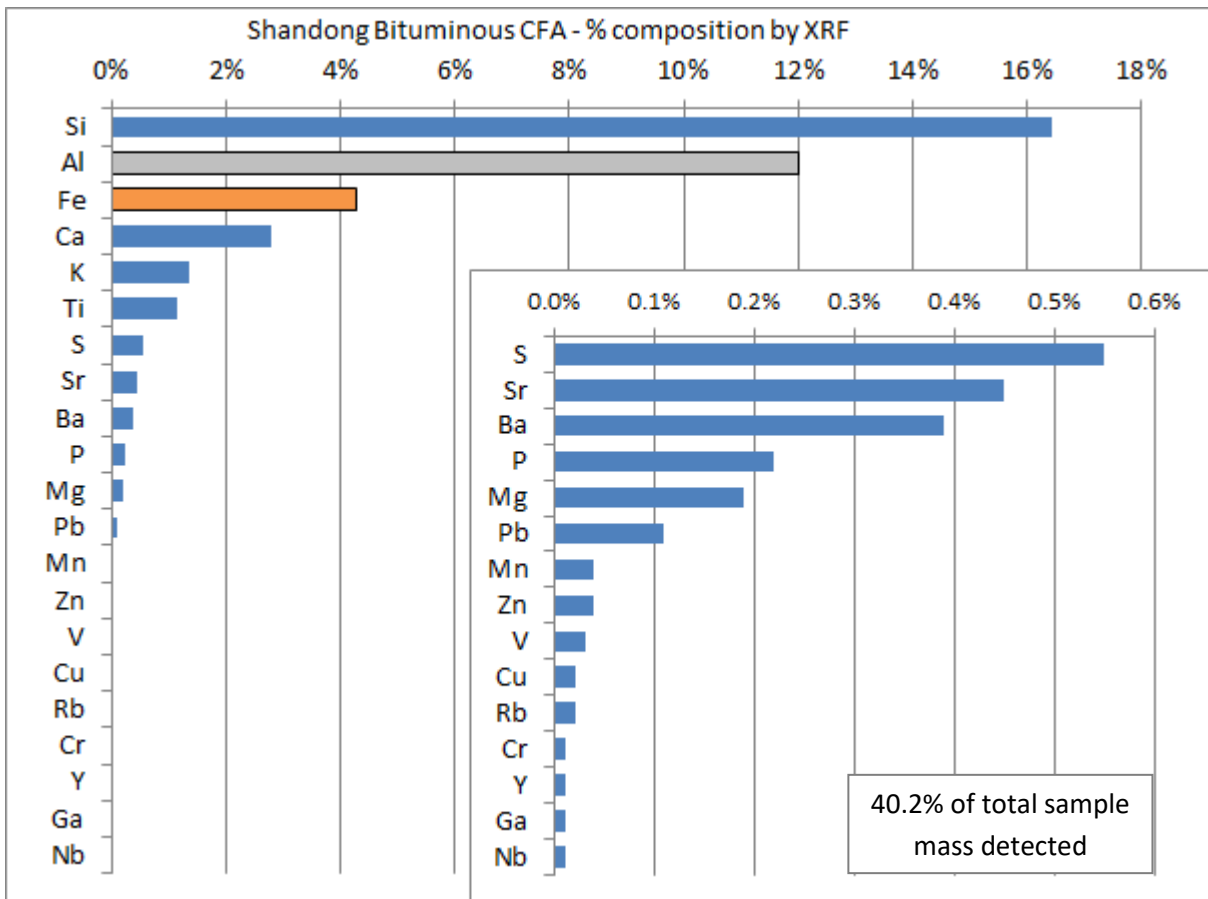


Figure 7 Elemental composition of a 500 mg sample of CFA provided by Shandong University, including a close-up of the concentrations of minor elements representing  $\leq 0.5\%$  of the sample by mass

Notable features of the ash sample provided by Shandong University:

- Sample contains the highest Al : Fe ratio at almost 3:1, containing 12% and 4.2% respectively
- Contains 2.8% calcium, half the amount present in the Krakow ash
- Contains no detectable arsenic or selenium, implying maximum content of  $<0.01\%$

### 3.2 Oxalate-promoted acid dissolution – ICP-MS analysis

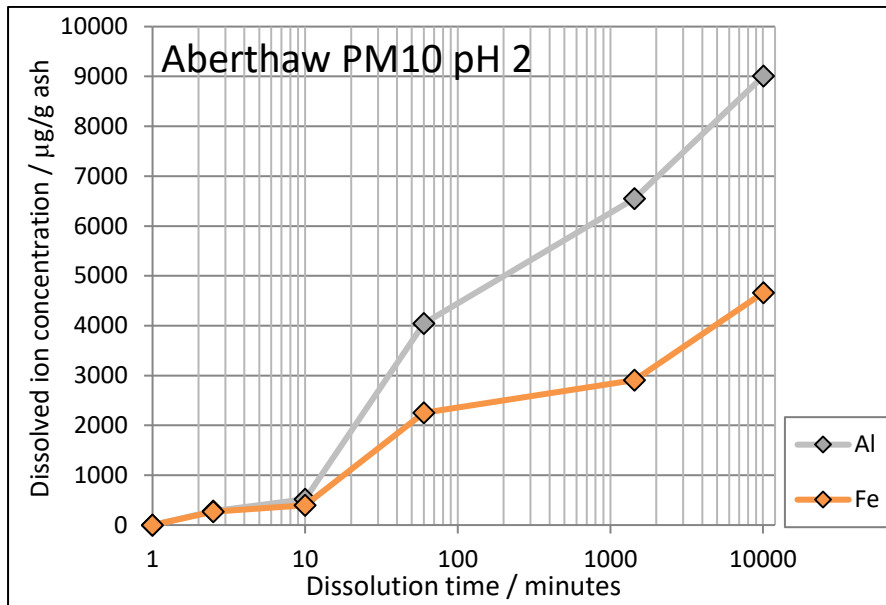


Figure 8a: 200 µM oxalate-promoted dissolution of common metals in 30 mg/L Aberthaw PM10 CFA in HCl at pH 2 over 7 days (10080 minutes).

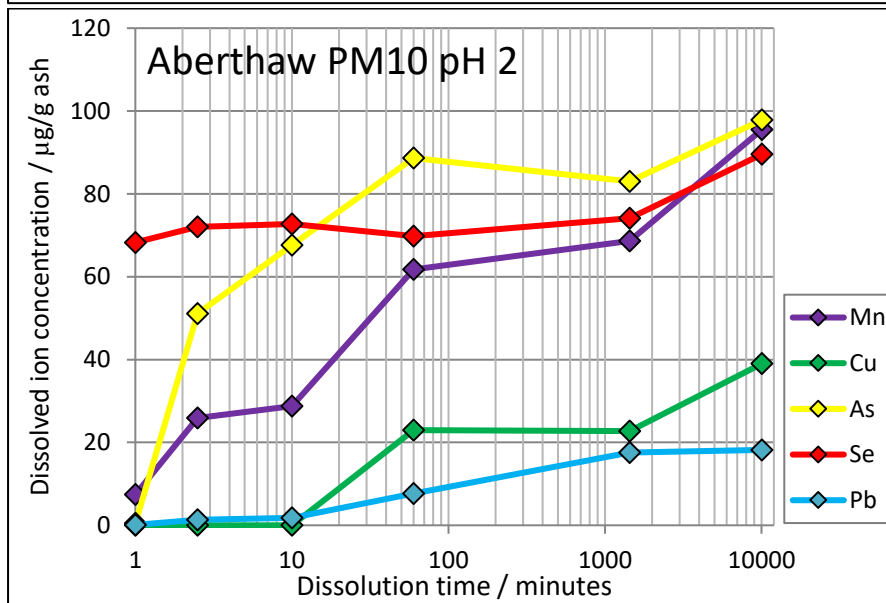


Figure 8b: 200 µM oxalate-promoted dissolution of minor metals and arsenic in 30 mg/L Aberthaw PM10 CFA in HCl at pH 2 over 7 days (10080 minutes).

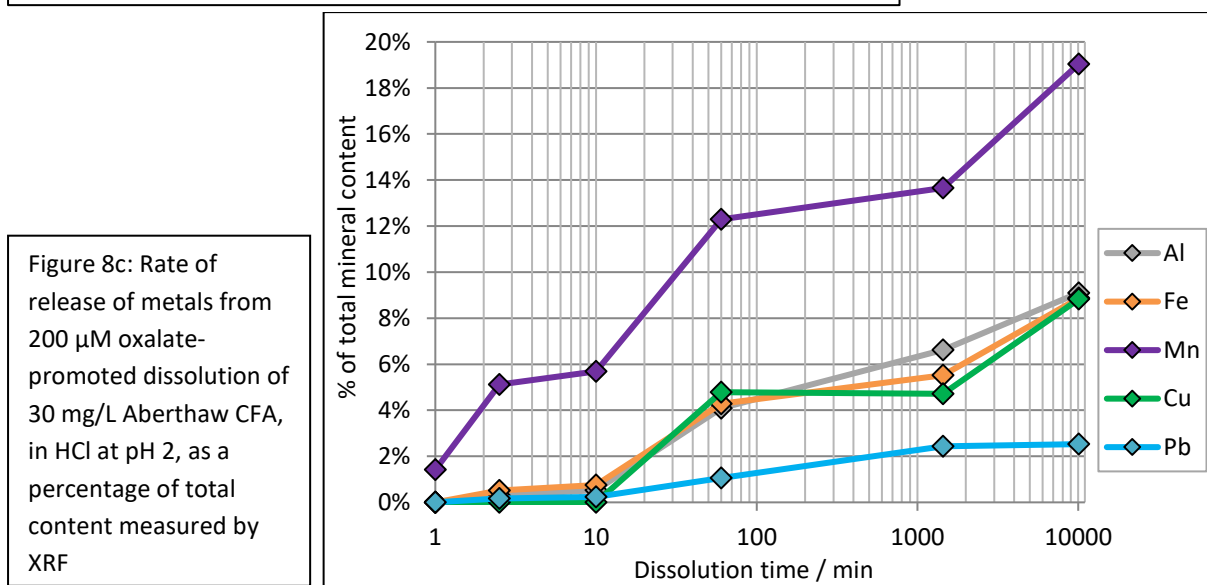


Figure 8c: Rate of release of metals from 200 µM oxalate-promoted dissolution of 30 mg/L Aberthaw CFA, in HCl at pH 2, as a percentage of total content measured by XRF

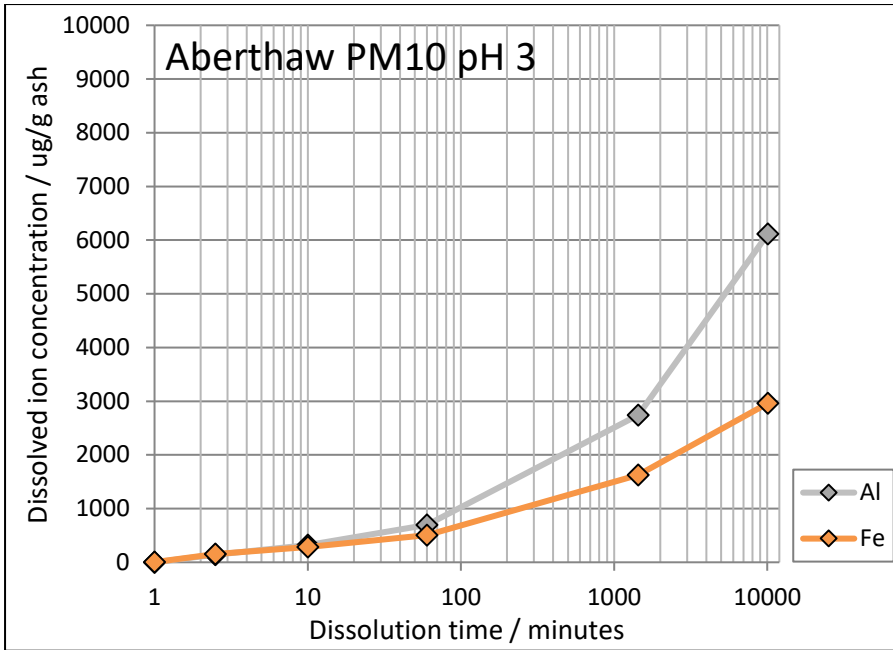


Figure 9a: 200 μM oxalate-promoted dissolution of common metals in 30 mg/L Aberthaw PM10 CFA in HCl at pH 3 over 7 days (10080 minutes).

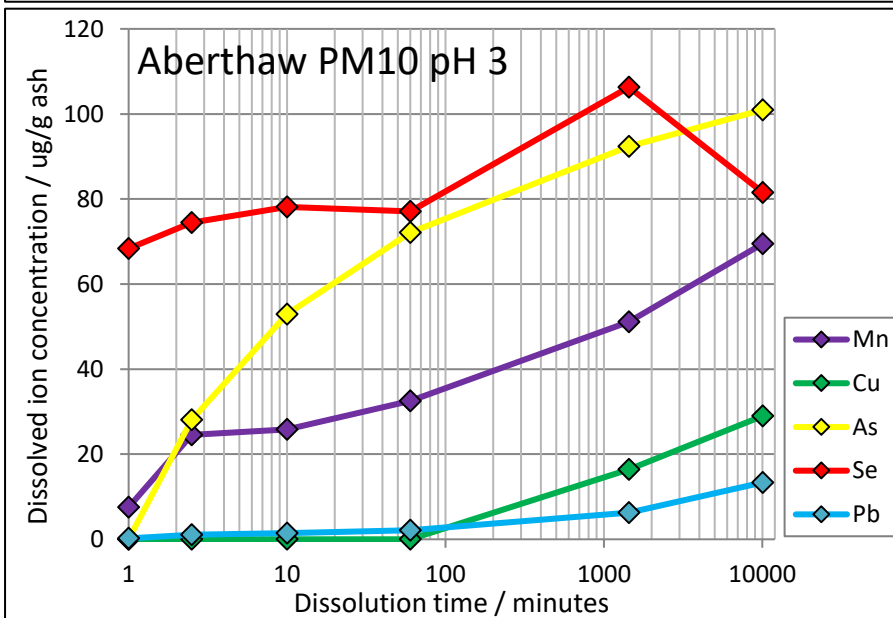


Figure 9b: 200 μM oxalate-promoted dissolution of minor metals and arsenic in 30 mg/L Aberthaw PM10 CFA in HCl at pH 3 over 7 days (10080 minutes).

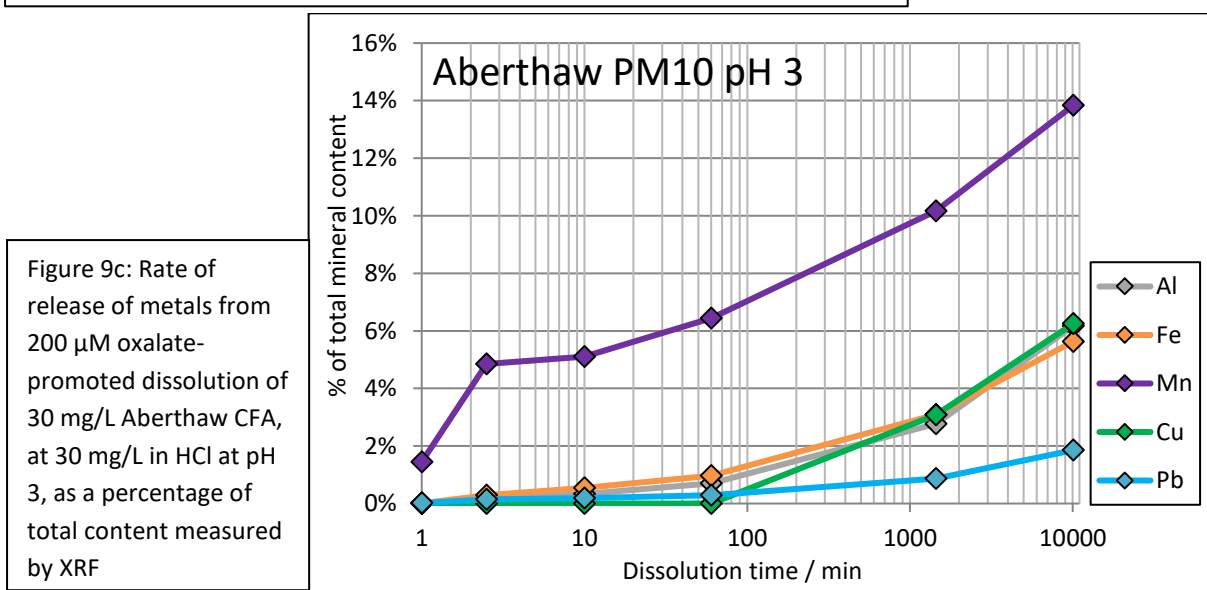


Figure 9c: Rate of release of metals from 200 μM oxalate-promoted dissolution of 30 mg/L Aberthaw CFA, at 30 mg/L in HCl at pH 3, as a percentage of total content measured by XRF

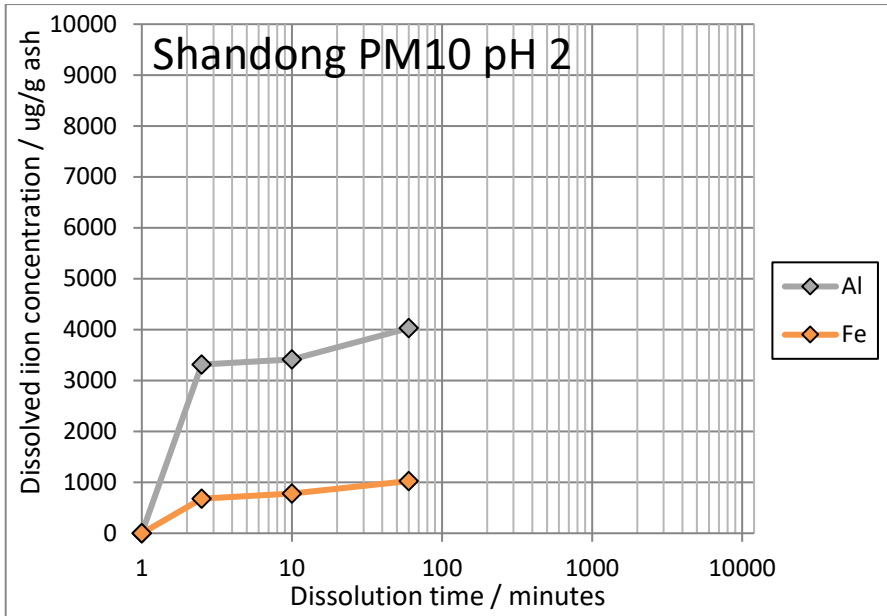


Figure 10a: 200  $\mu$ M oxalate-promoted dissolution of common metals in PM10 CFA provided by Shandong University, at 30 mg/L in HCl at pH 2 over 7 days (10080 minutes).

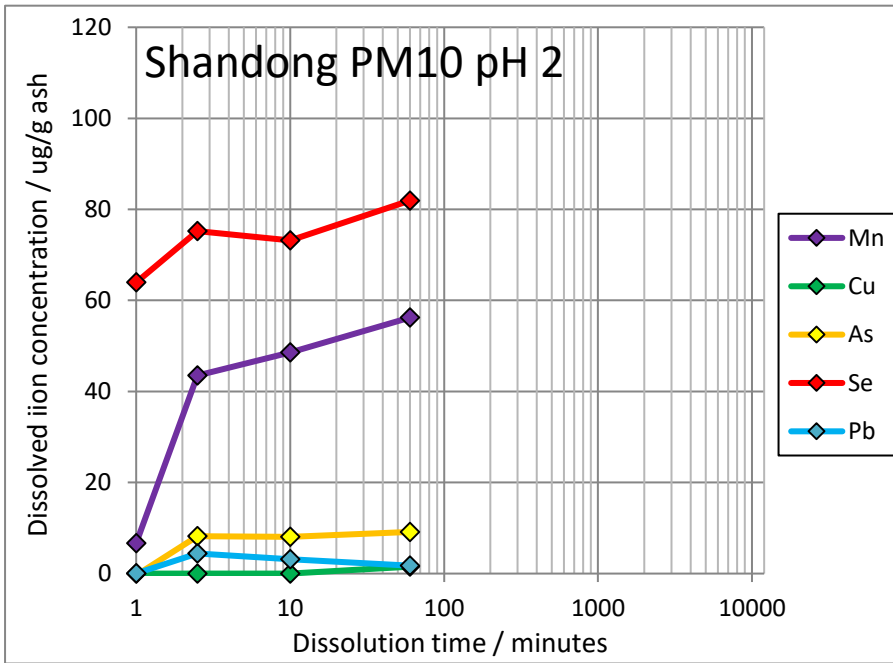


Figure 10b: 200  $\mu$ M oxalate-promoted dissolution of minor metals and arsenic in PM10 CFA in PM10 CFA provided by Shandong University, at 30 mg/L in HCl at pH 2 over 7 days (10080 minutes).

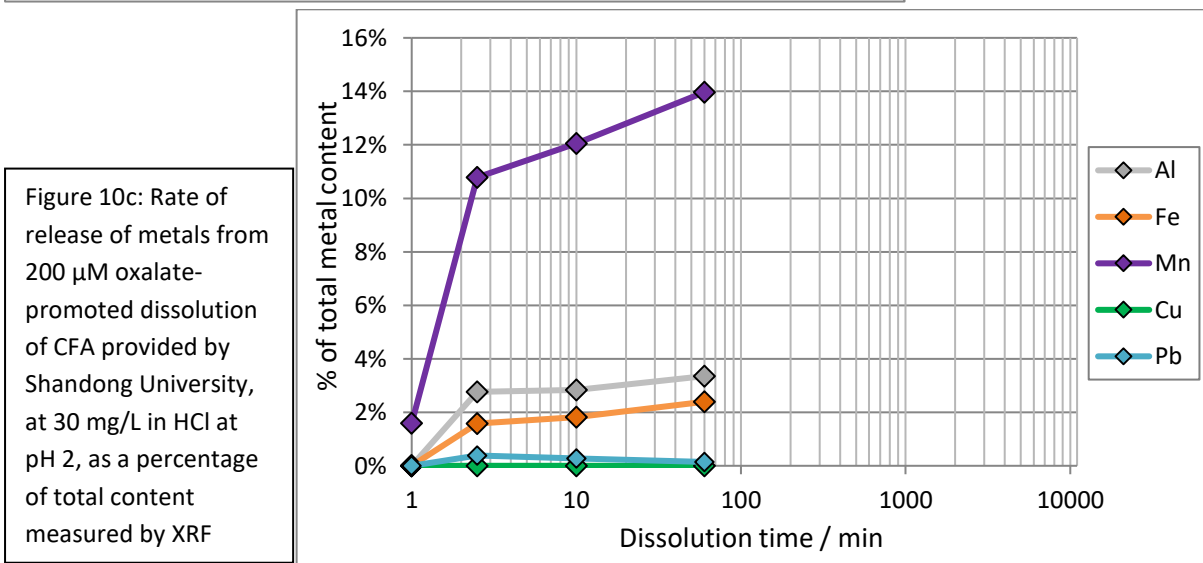


Figure 10c: Rate of release of metals from 200  $\mu$ M oxalate-promoted dissolution of CFA provided by Shandong University, at 30 mg/L in HCl at pH 2, as a percentage of total content measured by XRF

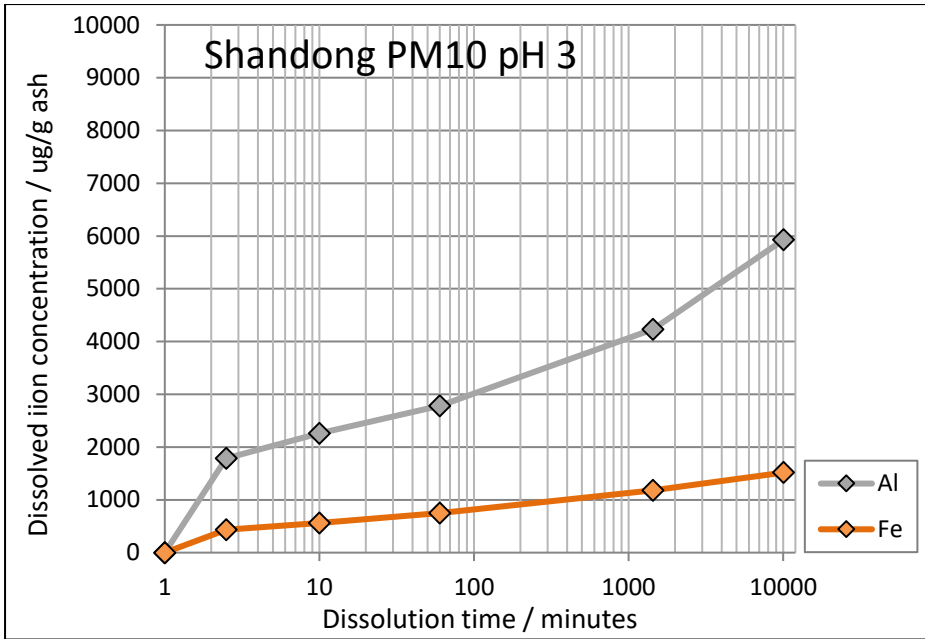


Figure 11a: 200  $\mu$ M oxalate-promoted dissolution of common metals in PM10 CFA provided by Shandong University, at 30 mg/L in HCl at pH 3 over 7 days (10080 minutes).

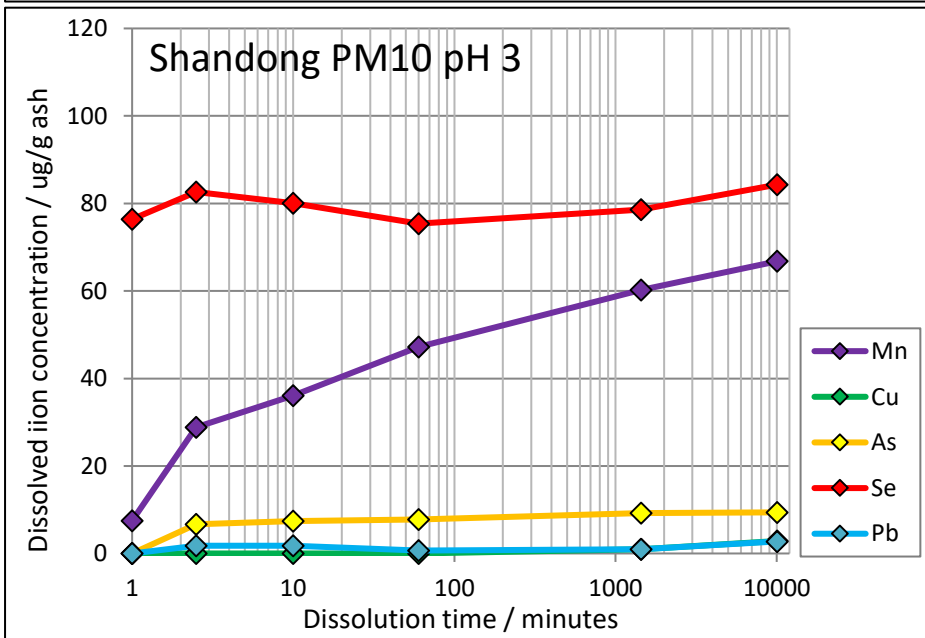


Figure 11b: 200  $\mu$ M oxalate-promoted dissolution of minor metals and arsenic in PM10 CFA provided by Shandong University, at 30 mg/L in HCl at pH 3 over 7 days (10080 minutes).

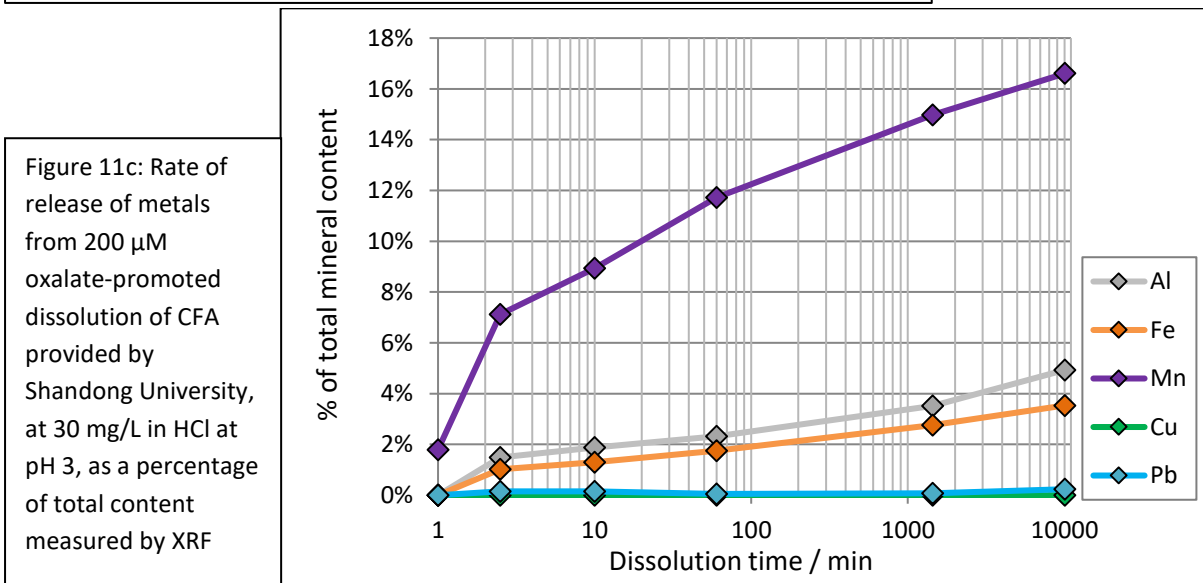


Figure 11c: Rate of release of metals from 200  $\mu$ M oxalate-promoted dissolution of CFA provided by Shandong University, at 30 mg/L in HCl at pH 3, as a percentage of total content measured by XRF

### Dissolution observations:

- The 24 hour and 7 day solution samples from Shandong ash dissolved in pH 2 HCl were lost prior to analysis due to insecure capping of the sample tubes after dilution with 2% HNO<sub>3</sub>. This series of experiments is being repeated along with a wider range of solution conditions (see section 5) in order to generate a more complete set of data.
- At pH 2 and pH 3, the dissolution rate of iron and aluminium is similar and proportional to the total content of each element.
- Manganese is the most readily soluble transition metal among those analysed.
- Despite being so low in total content as to be undetectable by XRF in either ash, arsenic is found to be readily released into solution at low pH. If resident As is 100% soluble after 7 days under the conditions described in section 2.5, then Aberthaw ash contains ~100ppm As and ash from Shandong University ~9ppm.
- Copper is as readily soluble in Aberthaw as iron and aluminium, but almost no copper is dissolved from Shandong ash during the observed periods.
- Lead is more readily dissolved in the Aberthaw ash than in the Shandong ash despite having a lower lead concentration. This may indicate that both lead and copper are present as less soluble mineral species in the Shandong ash, or that the Shandong ash has greater buffering capacity.

### 3.3 Readily soluble iron quantification

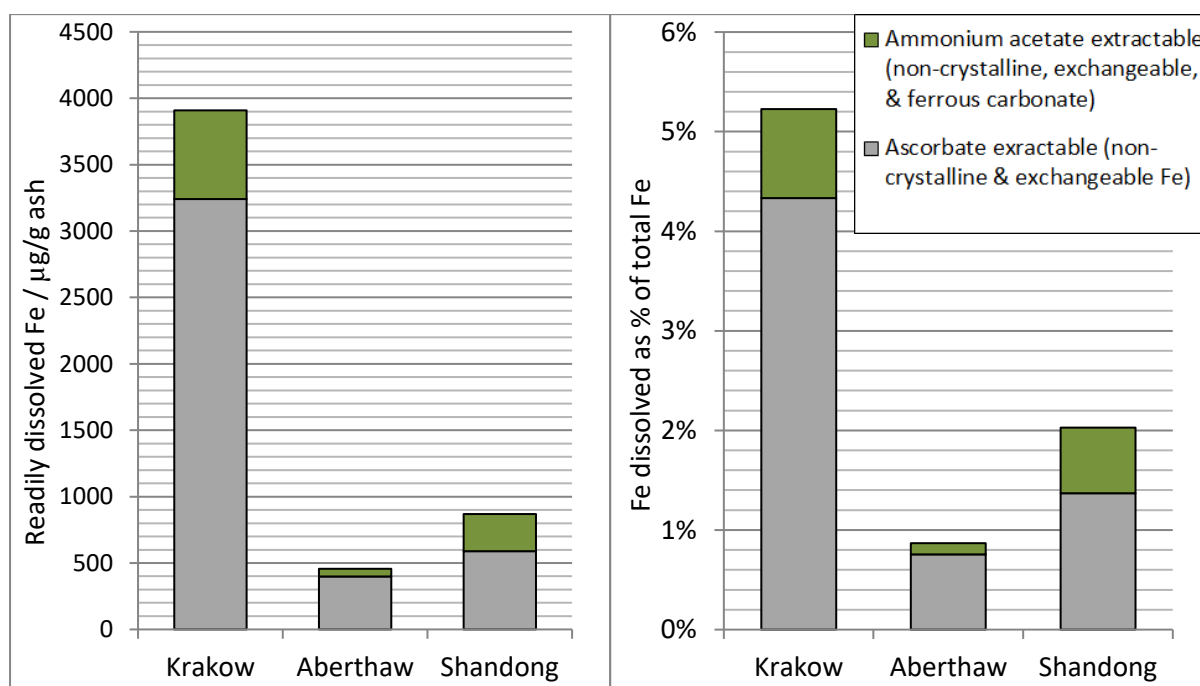


Figure 12 Comparison of exchangeable & non-crystalline iron in each coal fly ash sample based on 90 minute extractions with ascorbate extractant at pH 8 and ammonium acetate at pH 4.7, per gram of material (left) and as a percentage of total Fe measured by XRF (right).

### 3.4 Initial atmospheric processing

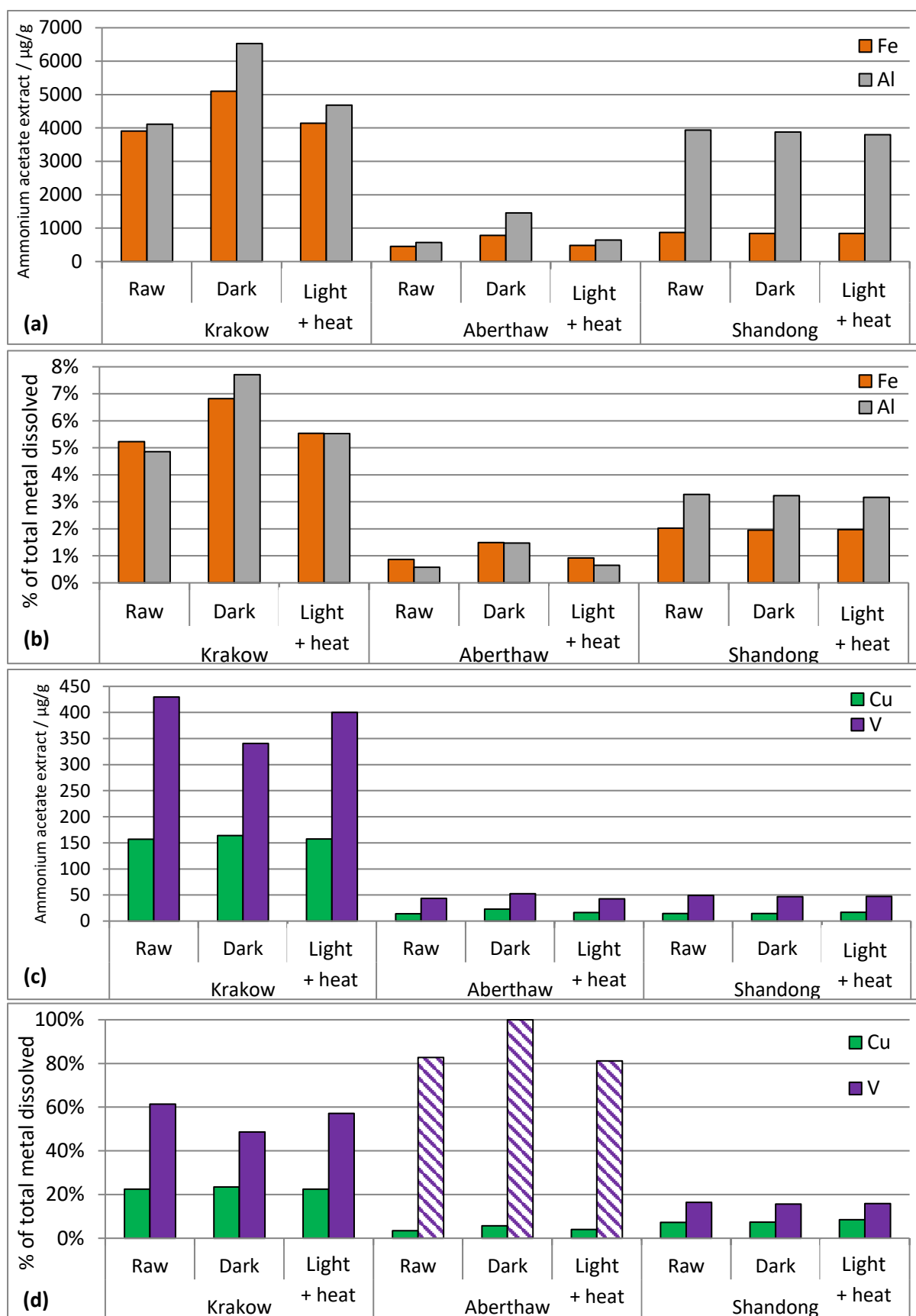


Figure 13 Changes in transition metal solubility in response to simulated atmospheric processing. These samples were processed prior to temperature/RH stability modifications to the processing chamber.

### 3.5 Water soluble ion content

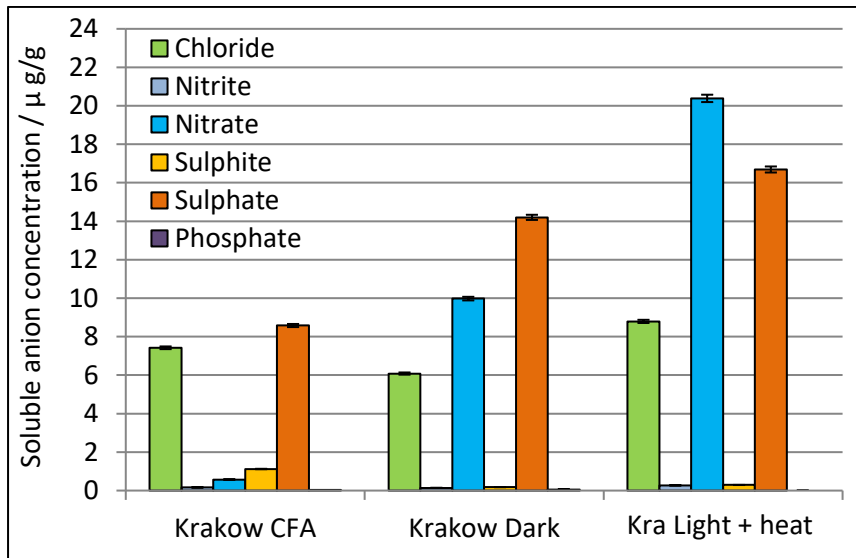


Figure 14 Water soluble anion concentrations in raw and processed CFA from Krakow.

Figure 15 Water soluble anion concentrations in raw and processed CFA from Aberthaw.

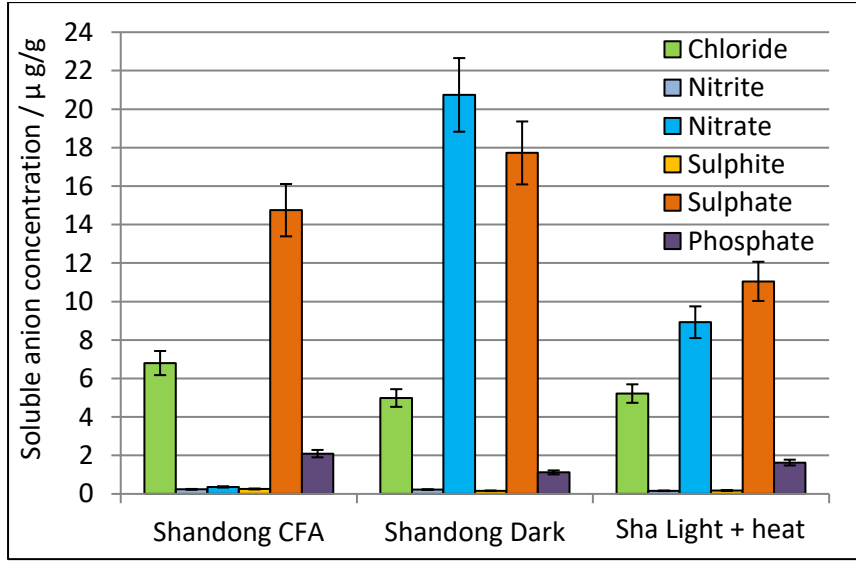
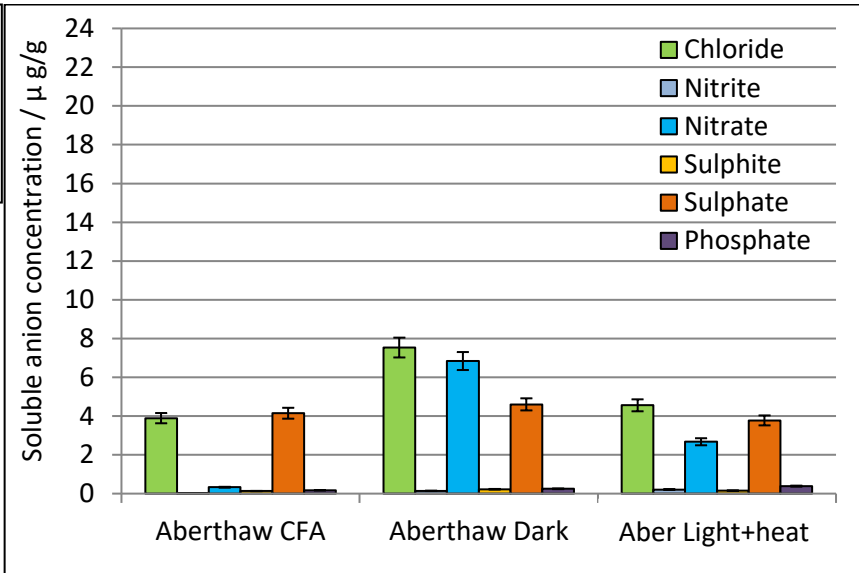


Figure 16 Water soluble anion concentrations in raw and processed CFA supplied by Shandong University.

\*These samples were processed prior to temperature/RH stability modifications to the processing chamber

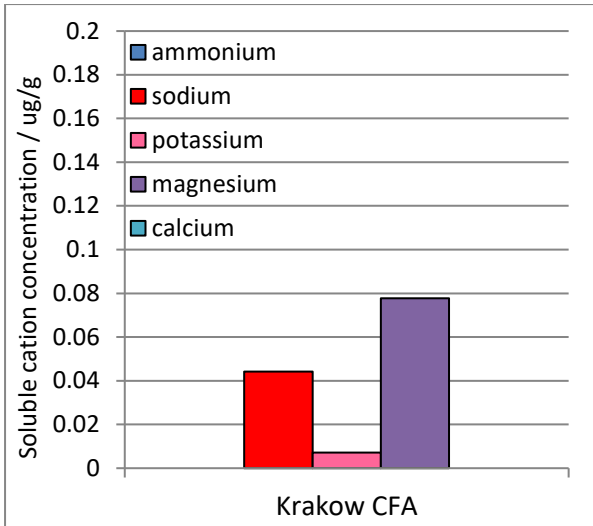


Figure 17 Water soluble cation concentrations in raw CFA from Krakow. The processed samples were lost due to a leak in the system.

Figure 18 Water soluble cation concentrations in raw and processed CFA from Aberthaw.

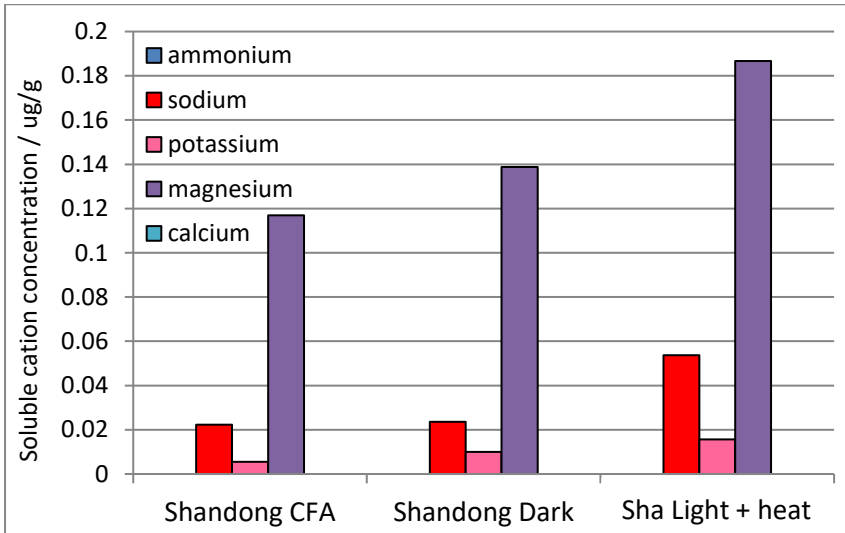
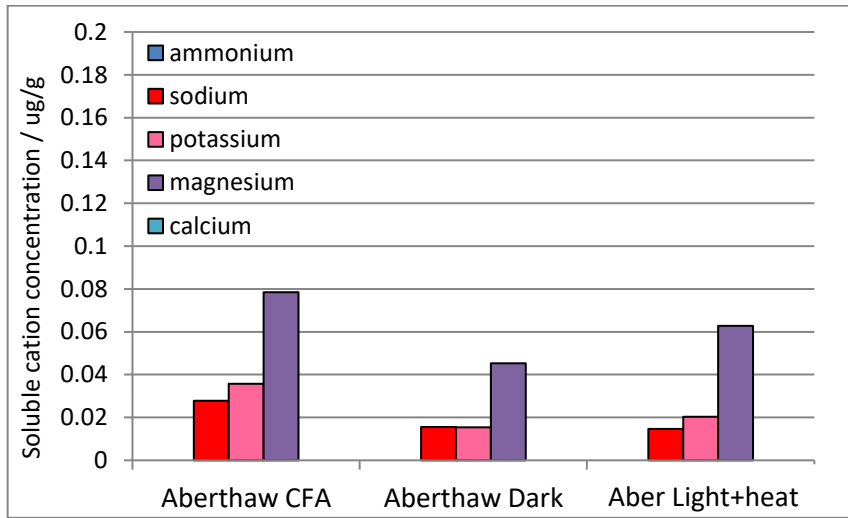


Figure 19 Water soluble cation concentrations in raw and processed CFA supplied by Shandong University.

These samples were processed prior to temperature/RH stability modifications to the processing chamber

### 3.6 X-ray Absorbance Near Edge Structure

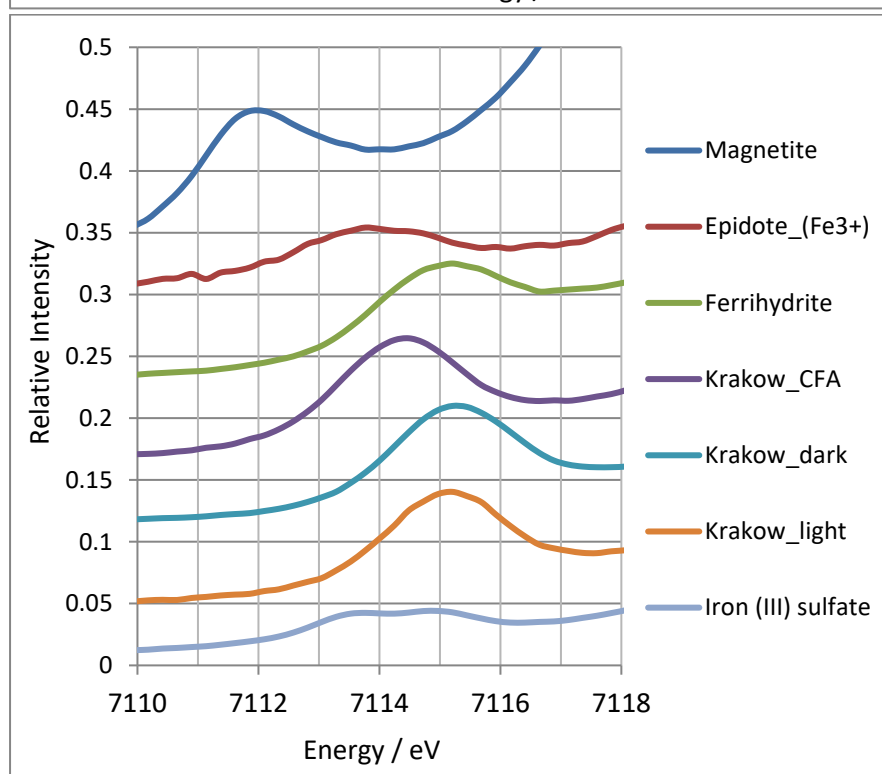
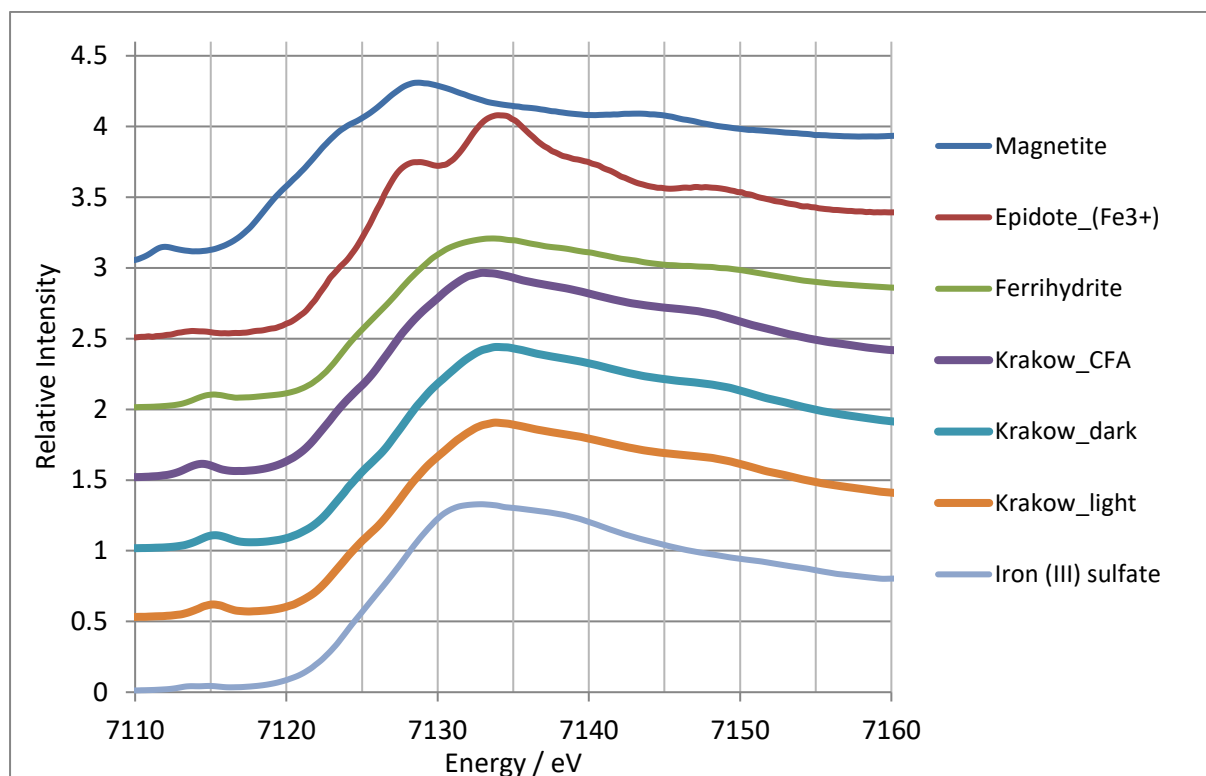


Figure 20 XANES spectra of raw and processed CFA samples from Krakow, alongside standards identified as major components in the Linear Combination Fit, including a close-up of the pre-edge region.

Spectra are manually separated by 0.5 relative intensity units for clarity and ease of comparison. Pre-edge close-ups are separated by 0.05 intensity units.

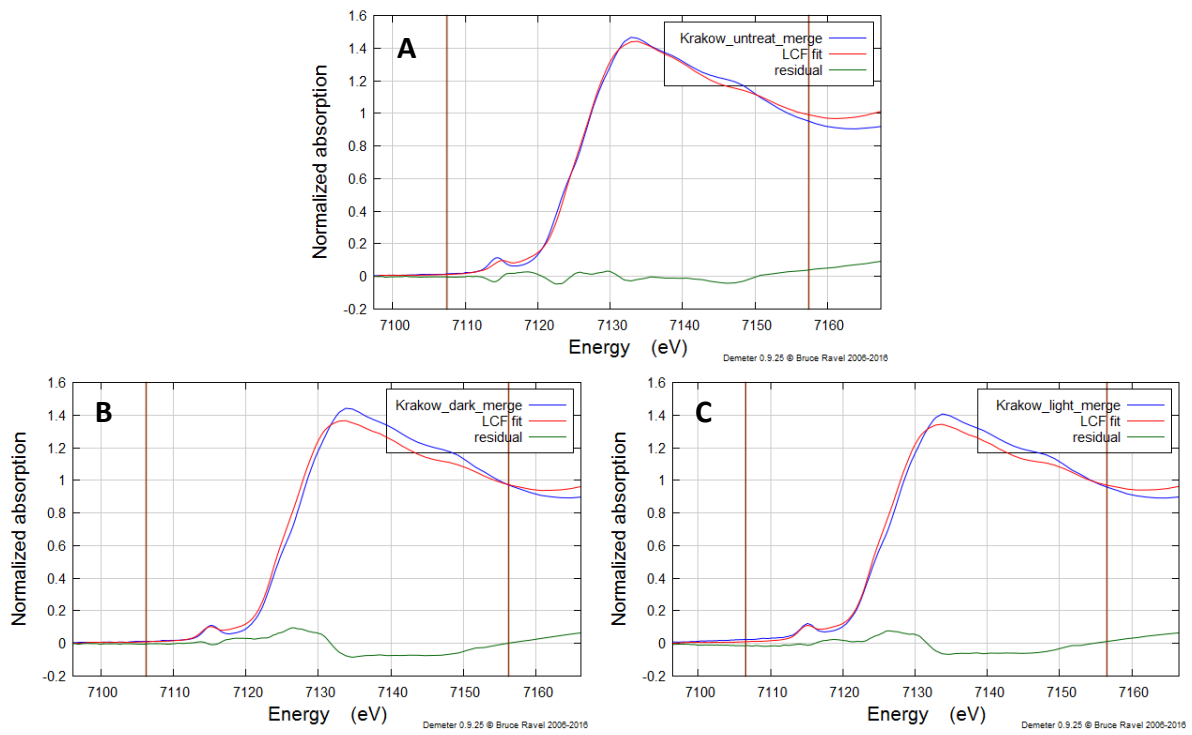
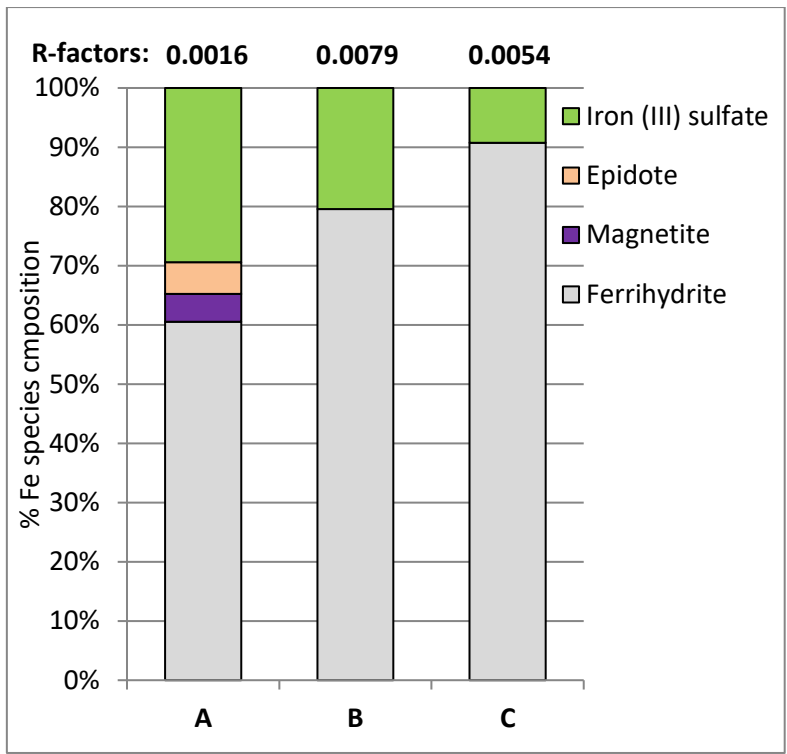


Figure 21 XANES linear combination fit results including quantification of identifiable species, for Krakow coal fly ash (A), and samples exposed to simulated atmospheric processing for 60 minutes in the dark (B) and under exposure to a 300W solar simulator lamp prior to temperature/RH stabilisation (C)

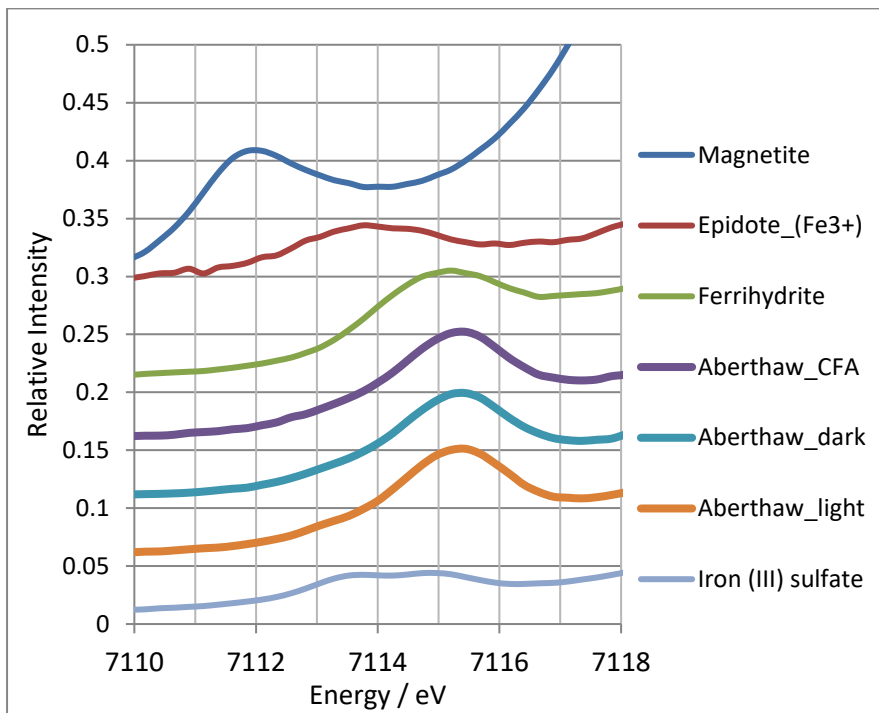
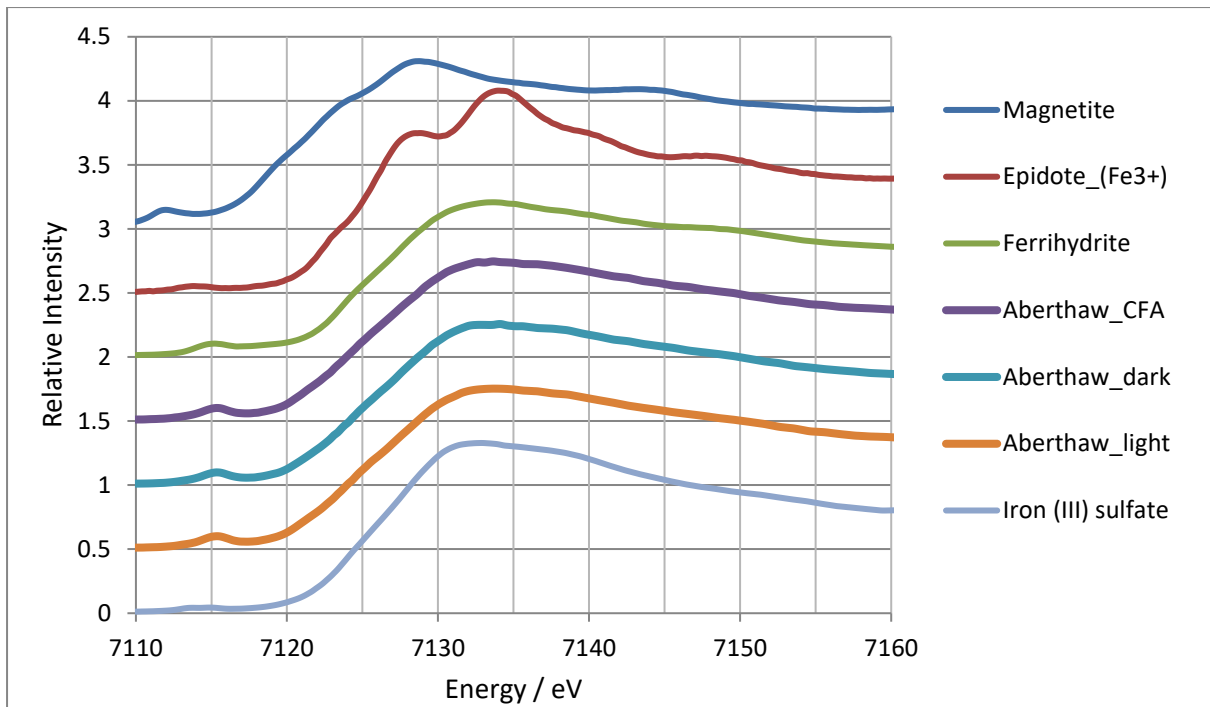


Figure 22 XANES spectra of raw and processed CFA samples from Aberthaw, alongside standards identified as major components in the Linear Combination Fit, including a close-up of the pre-edge region.

Spectra are manually separated by 0.5 relative intensity units for clarity and ease of comparison. Pre-edge close-ups are separated by 0.05 intensity units.

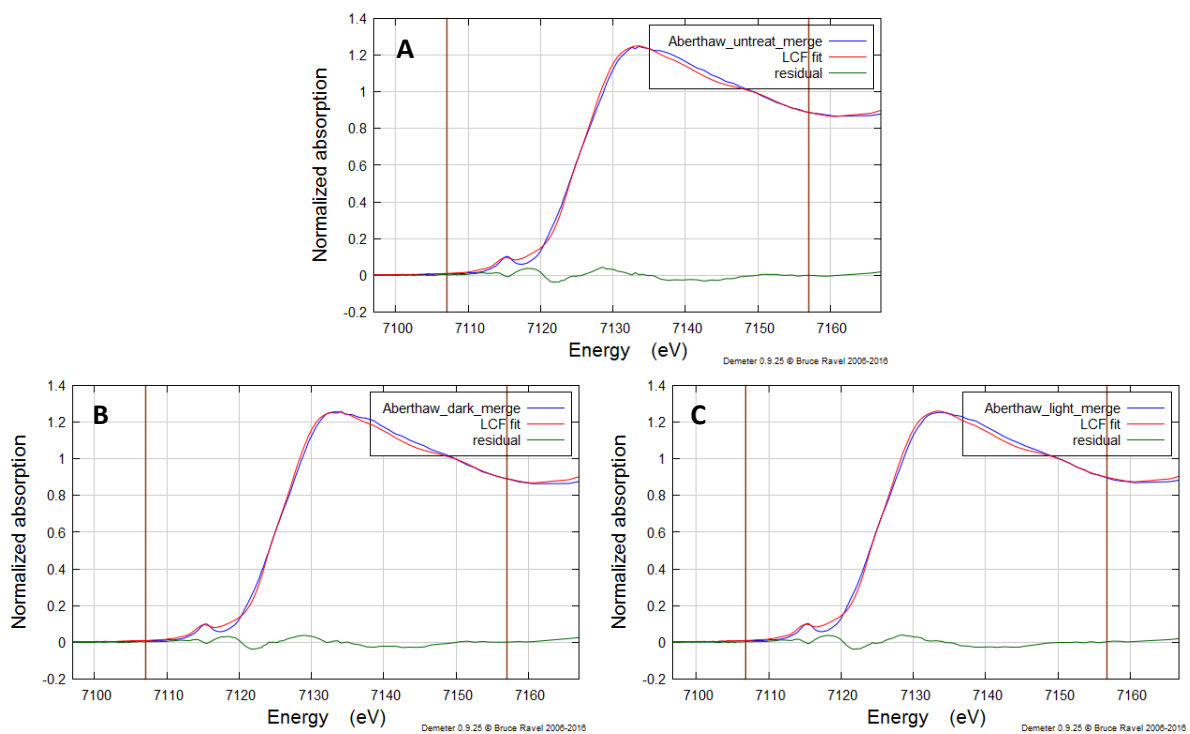
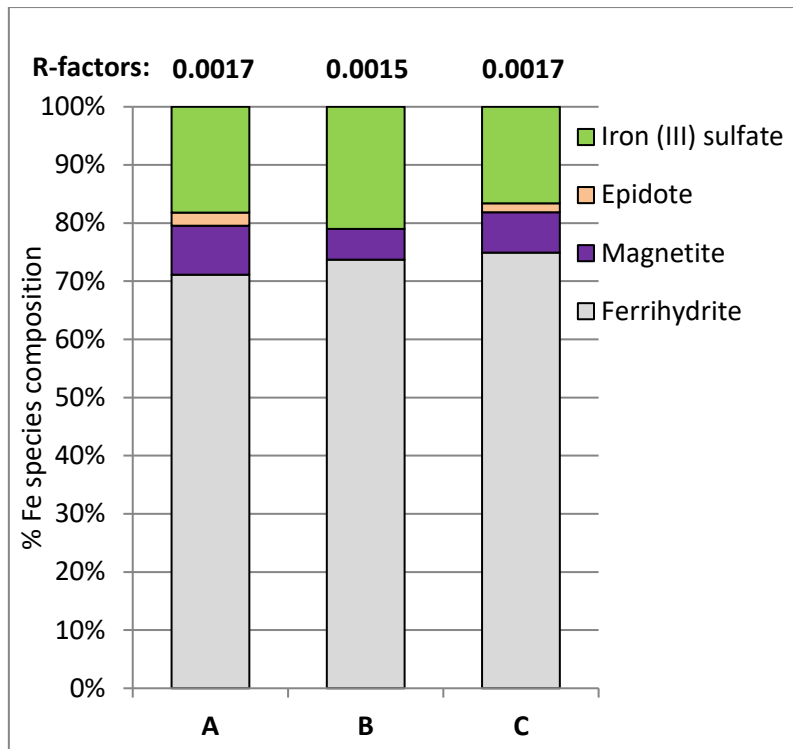


Figure 23 XANES linear combination fit results including quantification of identifiable species, for Krakow coal fly ash (A), and samples exposed to simulated atmospheric processing for 60 minutes in the dark (B) and under exposure to a 300W solar simulator lamp prior to temperature/RH stabilisation (C)

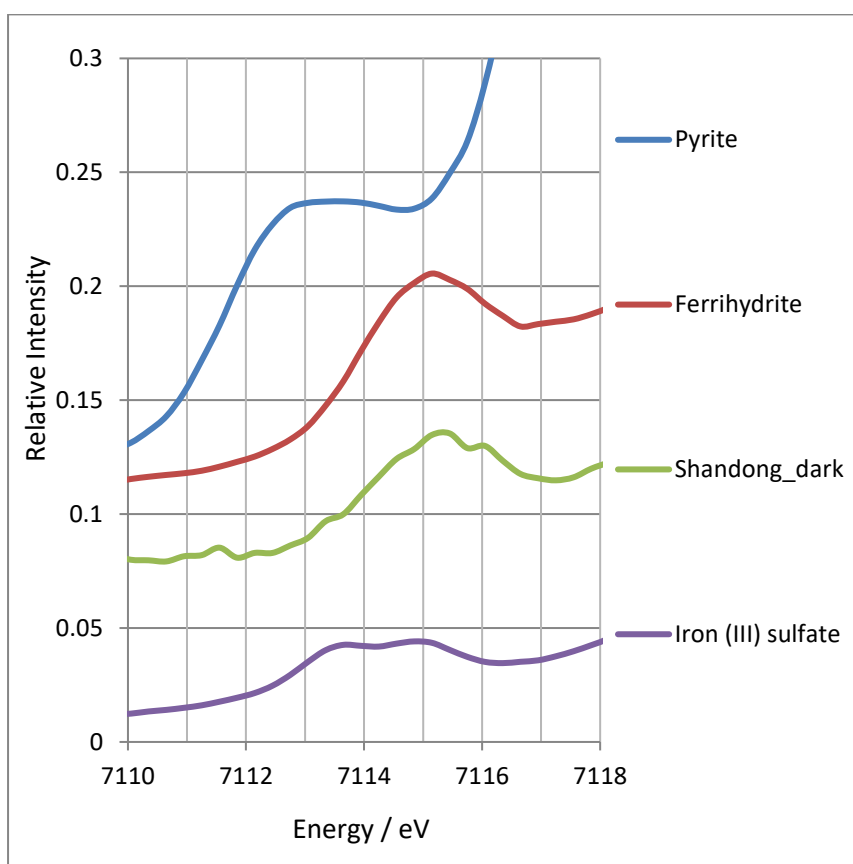
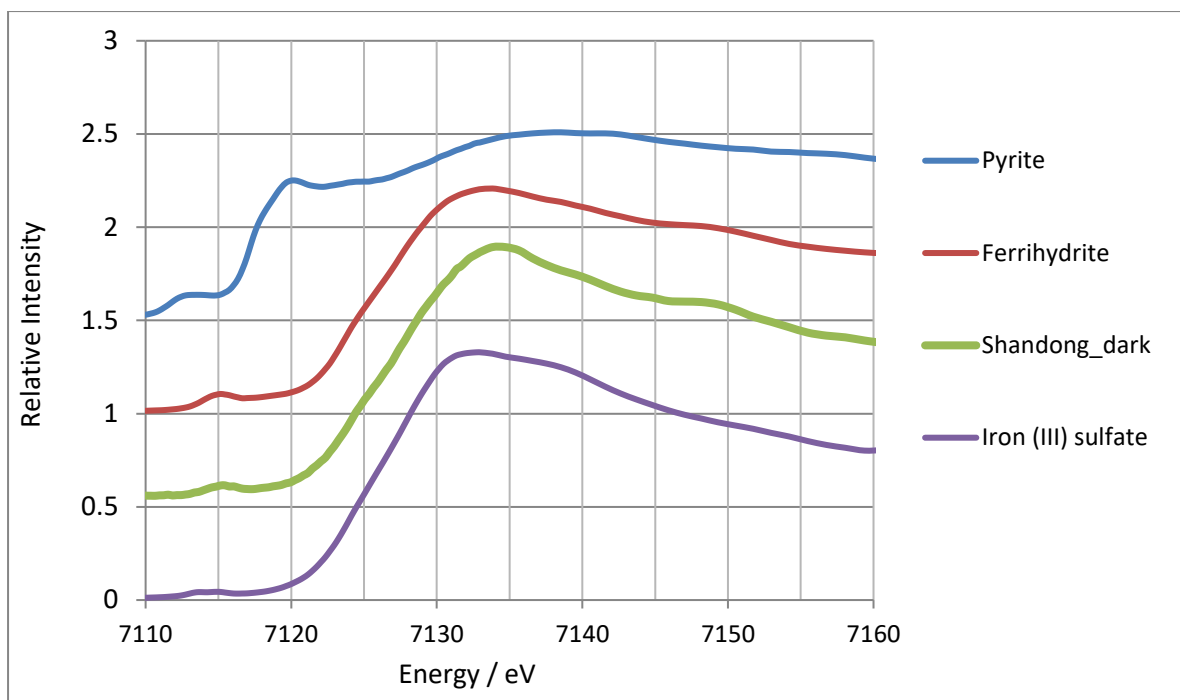


Figure 24 XANES spectra of one processed sample of CFA provided by Shandong University, alongside standards identified as major components in the Linear Combination Fit, including a close-up of the pre-edge region.

Spectra are manually separated by 0.5 relative intensity units for clarity and ease of comparison. Pre-edge close-ups are separated by 0.05 intensity units.

The raw and “light” processed samples from Shandong did not produce viable spectra. This was a result of selecting too thick a shield on the x-ray detector, which blocked so much of the Fe signal that there were insufficient photons to build up a XANES spectrum.

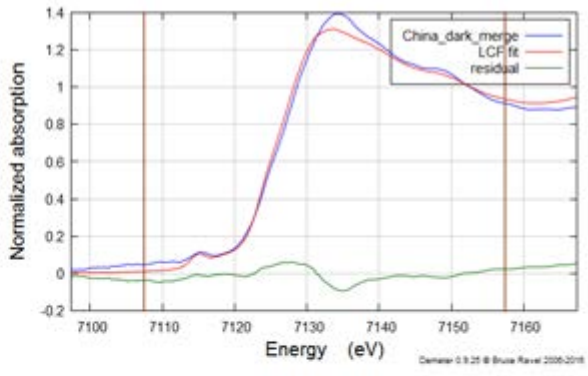
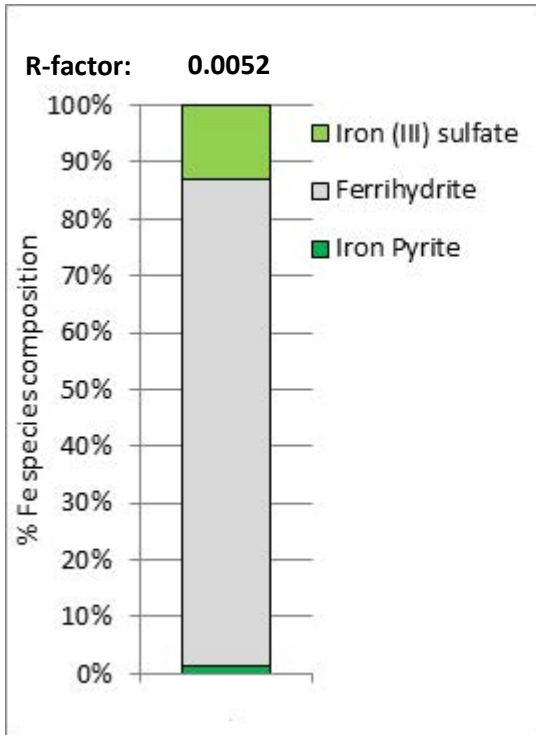


Figure 25 XANES linear combination fit including quantification of identifiable species for coal fly ash provided by Shandong University. Only the sample exposed to simulated atmospheric processing under dark conditions generated a viable XANES spectrum.

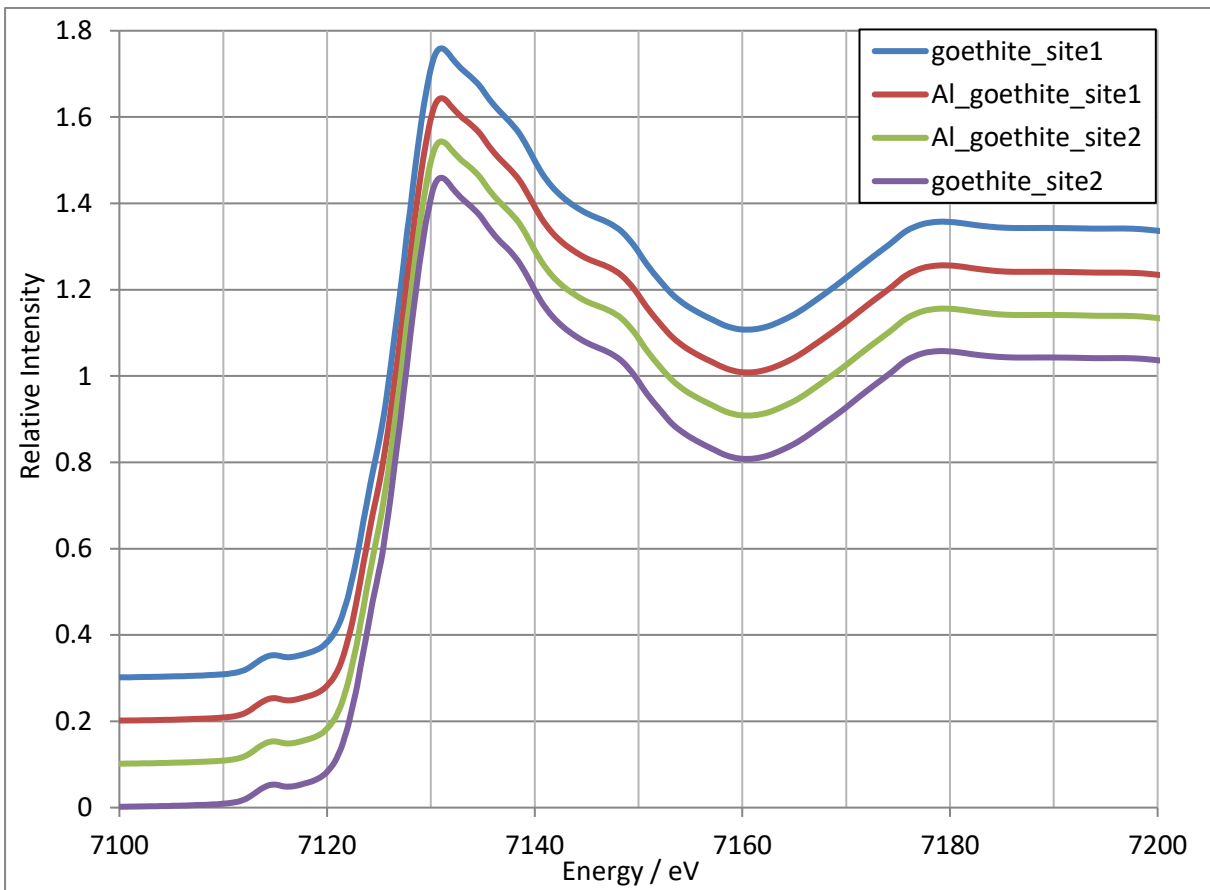


Figure 26 Comparison of XANES spectra of pure synthetic goethite and 5% Al-substituted goethite

### 3.7 Simulated Atmospheric Processing with Temperature/RH stabilisation

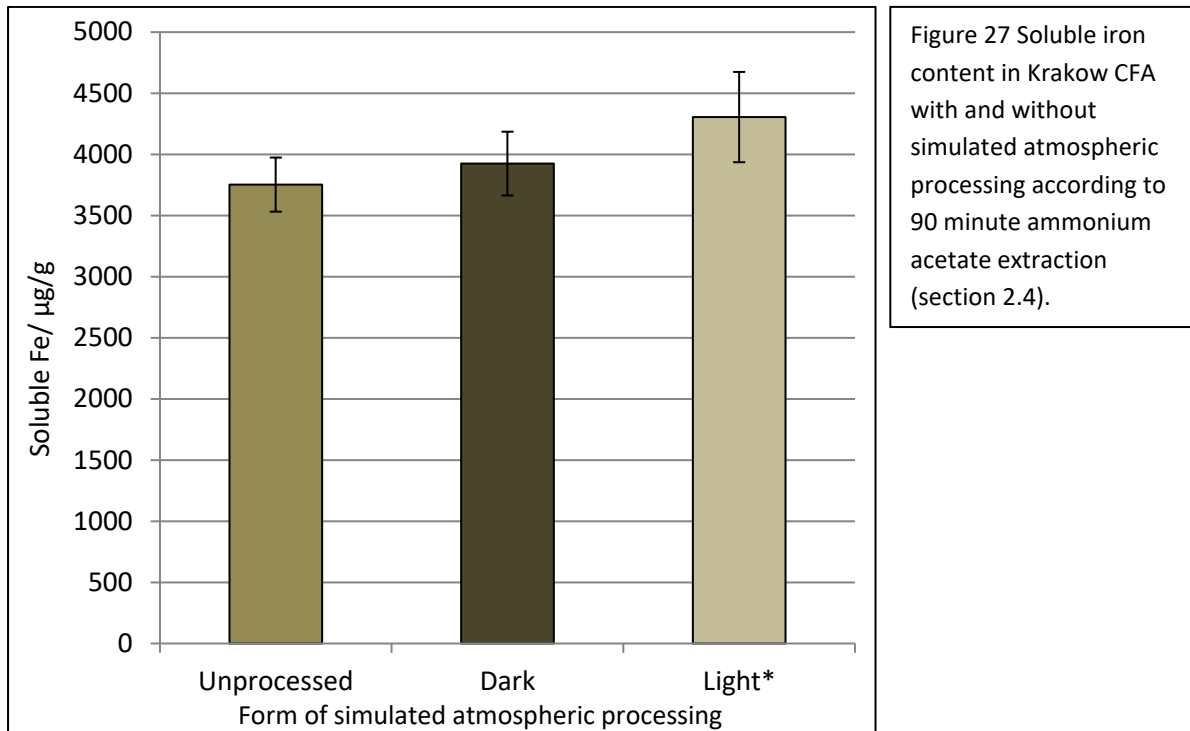


Figure 28 Soluble iron content in Aberthaw CFA with and without simulated atmospheric processing according to 90 minute ammonium acetate extraction (section 2.4).

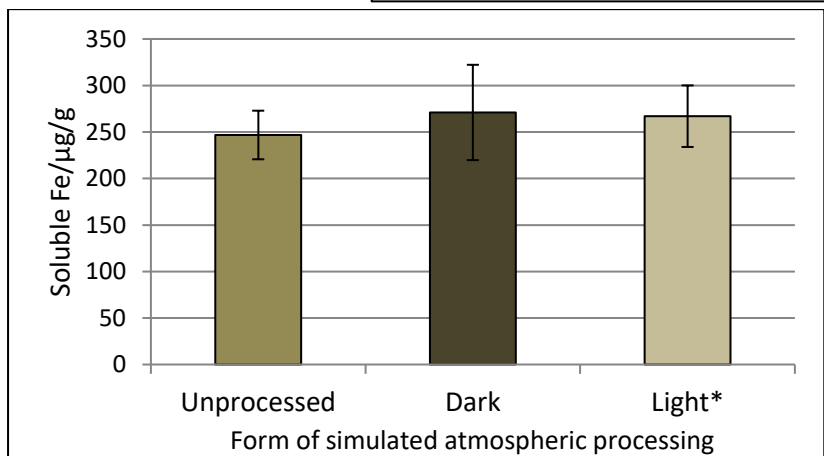
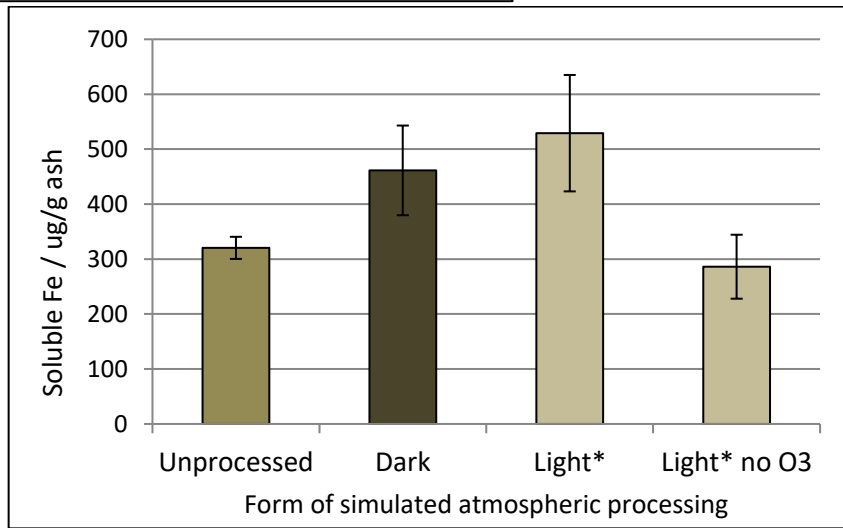


Figure 29 Soluble iron content in CFA provided by Shandong University with and without simulated atmospheric processing according to 90 minute ammonium acetate extraction (section 2.4).

\*The samples processed with simulated sunlight (Light) were processed with the temperature/ RH stability modifications to the processing chamber.

## 4. Discussion

### 4.1 Oxalate-promoted timed dissolution

Selenium contamination was a problem for all results in this sample set. Bottle blanks (blank samples containing only 2% HNO<sub>3</sub>, handled with the same containers as samples) showed an average of 4 ppb of selenium, equivalent to ~18 µg/g dissolved from samples. Sample blanks (collected prior to the addition of ash to the beakers in section 2.5) are placed in figures 8 – 11 at 1 minute dissolution time since a log graph cannot display zero. Selenium concentrations in the sample blanks are found to be equivalent to 60 – 75 µg/g across all sample sets, with the concentration never rising significantly over time. Combined with the lack of a selenium signal in any of the XRF spectra in figures 5 – 7, this implies that selenium is not present in significant quantities within the ash samples and simply has a high background.

Manganese is also found in the blanks at concentrations equivalent to ~7 µg/g in all sample sets, but the presence of manganese in the XRF spectrum and increasing solution concentration over time shows that it is released from the ash as well as being present in the reagents as a contaminant.

Arsenic was not present in any ash sample in sufficiently high concentration to register on the XRF spectra in figures 5 – 7 despite being within the device's detection range and being found in all of the solutions. Aberthaw ash in particular releases close to 100 µg/g of As into solution within 1 hour at pH 2 (figure 8b) and within 7 days at pH 3 (figure 9b). Conditions within natural seawater tend to rapidly immobilise arsenic (Johnston, et al., 2010) (Burke, et al., 2013) so ocean regions are unlikely to be affected, but As-rich ash may be a concern for downwind agricultural land.

The ash provided by Shandong University is shown to contain ~50% more lead by weight (figure 7) than ash from Aberthaw B (figure 6), but the lead is found to be more readily soluble in the Aberthaw ash, releasing ~2% of total Pb into solution after 7 days even at pH 3 (figure 9c) compared to less than 1% from the Shandong ash (figure 11c). Rate of release at pH 2 is not directly comparable after 1 hour due to the aforementioned loss of the later Shandong pH 2 samples, but at the 1 hour mark Aberthaw ash had released ~1% of its total Pb compared to < 0.3% from the Shandong sample.

Iron and copper follow a similar pattern: while Aberthaw ash (figure 6) contains twice as much copper and 20% more iron than ash from Shandong (figure 7), Shandong ash releases almost none of its Cu into solution, less than 4% of its total Fe after 7 days (figure 11a) at pH 3 compared to more than 6% of both Fe and Cu leaching into solution from the Aberthaw ash (figure 9a) in the same time. Only 2.4% of total Fe is released from the Shandong ash after 1 hour at pH 2 (figure 10a) compared to >4% from Aberthaw ash at the same acid concentration (figure 8a). By contrast, Shandong ash contains ~20% more aluminium per gram (figure 7) than Aberthaw ash (figure 6) and dissolution rates are roughly similar (figures 8a & 10a, 9a & 11a).

### 4.2 Exchangeable & non-crystalline iron and siderite – ascorbate vs ammonium acetate extraction

The results illustrated in figure 12 stand in contrast to the results of oxalate-promoted acid dissolution discussed in the previous section- while the higher pH and less strongly binding organic ligands would lead to predictions of slower Fe mobilisation, the ammonium acetate extractant mobilises iron at

roughly the same rate as HCl/oxalate at pH 3 (~1% from Aberthaw ash (figure 9c) and ~2% from Shandong (figure 11c) after 60 minutes) due to the added contribution from the breakdown of  $\text{FeCO}_3$ .

Figure 12 also facilitates the first direct comparison of available iron in the Krakow ash compared to the other two types. The Krakow ash contains ~40% more total Fe (figure 5) than the Aberthaw, but releases more than five times as much Fe in a 90 minute extraction. The Krakow ash contains a similar proportion of  $\text{FeCO}_3$  to the ash provided by Shandong University at 0.8% and 0.7% respectively, but more than three times the exchangeable/non-crystalline Fe.

#### 4.3 Initial Simulated Atmospheric Processing – transition metal solubility enhancement

Figure 13 plots the concentrations of various ionic species in the three ash types, in solution after ammonium acetate extraction and analysed by ICP-OES, while figures 14 – 19 plot the concentrations of various water soluble ionic species analysed by ion chromatography. The untreated “raw” ash samples were contrasted against samples exposed to  $\text{SO}_2$ ,  $\text{NO}_2$  and ozone under high humidity conditions with no light source (Dark) and under exposure to the solar simulator lamp (Light). This sample set was prepared before the issue of the lamp heating and drying the processing chamber was resolved, so Light and Dark results cannot be directly compared. Light results are included to illustrate the necessity of high RH for acid processing to occur.

Six elements were analysed as stated in section 2.9. However, due to high detection limits for the particular elements and low solution concentrations, no soluble arsenic or cobalt was detected in any of the samples. Vanadium is significant for the Aberthaw ash, because 40 – 50 ppm was detected in the ammonium acetate extract despite the XRF failing to detect any. In the absence of other information, the highest solution concentration found in any Aberthaw sample (the Dark / high RH processed sample) is assumed to represent 100% of the vanadium content to allow for comparison with the unprocessed sample.

The three ash types respond to simulated atmospheric processing to varying degrees. The ash from Shandong University does not appear to be affected at all, with Raw and processed samples releasing similar concentrations of iron, aluminium, copper and vanadium, within  $\pm 5\%$ . The Aberthaw ash, by contrast, releases 50% more iron and copper, and more than double the concentration of aluminium into solution after processing. Krakow ash shows some response to processing, releasing 30% more iron and 50% more aluminium into solution, while copper and vanadium concentrations are unaffected. As with iron and aluminium, copper in the Krakow sample is significantly more common in exchangeable/readily soluble forms than in the other ash types. In both the Krakow and Aberthaw ash, “Light” processing does not significantly increase metal solubility, demonstrating the necessity of high RH for the reactions to occur on the particle surfaces.

#### 4.4 Initial Simulated Atmospheric Processing – ion chromatography of water leachate

Figures 14 – 19 cover the results of deionised water extraction of common ionic species. The unprocessed Krakow ash (figure 14) was the only sample containing measurable quantities of nitrite and sulfite, indicating that the ash is not fully oxidised. These oxidisable anionic species are not found in either of the processed samples, presumably due to the exposure to ozone. The Krakow ash takes up significant amounts of exchangeable nitrate and sulfate during atmospheric processing with high RH and no photochemical enhancement (Dark), but despite showing no signs of enhanced transition

metal solubility under illuminated conditions with lower RH (Light), the Krakow ash takes up more  $\text{SO}_4^{2-}$  and twice as much  $\text{NO}_3^-$ . Krakow ash contains ~5.5% calcium, which if present as calcium carbonate is known to form gypsum during atmospheric processing (Solmon, et al., 2009) (Ito & Feng, 2010) (Rastogi & Sarin, 2006). This provides an explanation for the uptake of  $\text{SO}_4^{2-}$ , although some of the increased  $\text{SO}_4^{2-}$  concentration is accounted for by the oxidation of  $\text{SO}_3^{2-}$  by ozone. The greater  $\text{NO}_3^-$  concentration under “Light” conditions suggests that temperature is a more important factor in  $\text{NO}_3^-$  uptake in Krakow ash than RH.

By contrast, Aberthaw ash (figure 15) takes up much less  $\text{NO}_3^-$  and shows no measurable change in water soluble  $\text{SO}_4^{2-}$  content.  $\text{NO}_3^-$  uptake is restricted under “Light” conditions, most likely due to the drop in RH limiting the formation of nitric acid on particle surfaces. The negligible change in water soluble  $\text{SO}_4^{2-}$  content reflects the low calcium content (1.1%) in the Aberthaw ash.  $\text{NO}_3^-$  uptake under dark, high RH conditions appears to correspond to a rise in soluble  $\text{Cl}^-$ , suggesting that  $\text{Cl}^-$  is being displaced from particle surfaces by the high concentration of  $\text{NO}_3^-$ .

Despite ash from Shandong University showing no measurable change in metal solubility with atmospheric processing (figure 13), the ash takes up more  $\text{NO}_3^-$  than any other samples in dark, high RH conditions (figure 16). Ash from Shandong is the only sample to release significant quantities of phosphate into solution, which may enhance algal growth in ocean regions deficient in phosphorus as well as iron.

The cation chromatography measurements demonstrate that the alkali and alkali earth metal ions in the ash samples are not present in readily water soluble forms. Calcium is considered an important ion due to the buffering capacity of  $\text{CaCO}_3$  potentially inhibiting acid processing (Stockdale, et al., 2016) and taking up sulfate (Solmon, et al., 2009). Despite the high concentration of calcium in each ash type (5.5% in Krakow (figure 5), 1.1% in Aberthaw (figure 6) and 2.8% in Shandong (figure 7)), no calcium was detectable in any of the water leachate.

Potassium is also common in all three ash types but almost none was found in the leachate. Magnesium is the most available of the cations, but the highest leachate concentration (0.18  $\mu\text{g/g}$  of ash) that occurs in the Shandong ash represents less than 0.1% of the total Mg content by XRF (190 ppm, figure 7). Black carbon is known to have a high cation exchange capacity (Liang, et al., 2006) and with no alternative in the extractant to displace bound cations, little material can be expected to leach out.

#### 4.5 Initial Simulated Atmospheric Processing – X-ray Absorbance Near Edge Structure

The XANES spectra collected from samples of Krakow ash (figure 20) have aspects in common with three standards in particular- the relatively featureless shape of ferrihydrite and iron (III) sulfate, the energy maximum at ~7134 eV of ferrihydrite, the shoulder at ~7148 eV of ferrihydrite and the shoulder at ~7125 eV of magnetite. Close examination of the pre-edge region supports the anion chromatography results covered in section 4.4: while the shape of the pre-edge peak resembles ferrihydrite in all Krakow samples, the peak centroid (Hicks, 2015) in the unprocessed ash is displaced from 7114.5 to 7114.2 eV, indicating a small but significant contribution of reduced Fe(II) to the spectrum. The processed ash appears to be 100% Fe(III) with pre-edge centroids of ~7114.5 eV.

Linear combination fitting of the normalised spectra of unprocessed Krakow ash (figure 21, fit A) indicates that iron in the ash is present as 60% ferrihydrite and 30% iron (III) sulfate, with the remaining 10% composed of magnetite and epidote (an iron-rich clay similar to chlorite). The R-factor suggests that the fit is close but other readings raise issues with this interpretation.

The elemental composition by XRF (figure 5) of Krakow ash is ~7.5% Fe and ~0.7% S by mass, which means that if 100% of the resident S is bonded to Fe as  $\text{Fe}_2(\text{SO}_4)_3$  it can only account for ~11% of the total iron. While XANES results are more likely to be accurate due to more frequent and rigorous calibration of the apparatus, there are also reasons to question the XANES fit. Each XANES spectrum is generated from the merged composite of scans from 3 regions on each sample to minimise the chance of an unrepresentative spectrum. The small downward shift in excitation energy of the pre-edge and near edge peaks in the unprocessed Krakow ash caused by the Fe(II) content implied by the pre-edge centroid position may cause the whole spectrum to resemble ferric sulfate (which in turn resembles ferrihydrite, but with a slightly higher excitation peak at 7131 eV while ferrihydrite's maximum excitation occurs at ~7133 eV) more closely due to its standard spectrum exhibiting a similar near-edge shift, while the true cause of the shift is the presence of an Fe(II) rich species that is not well represented by the available standards.

The much smaller readings for ferric sulfate in the more oxidised, processed Krakow ash samples back up this assumption. However, the Krakow ash only contains ~4% readily soluble iron, which implies that the true ferric sulfate content is even lower and that at least one Fe(III) species or combination of species with similar XANES spectra to ferric sulfate are not represented among the available standards either.

The second issue is the dominance of ferrihydrite in the spectrum, which is best discussed in the wider context of all three ash samples.

The XANES spectra of Aberthaw ash (figure 22) are visually highly similar to ferrihydrite, and the pre-edge centroid position of both processed and unprocessed samples indicate that they are essentially 100% Fe(III). Linear combination fitting (figure 23) again shows very strong fits and reports that the iron in Aberthaw ash is 70-75% ferrihydrite, 7-10% magnetite and ~20% ferric sulfate. There is sufficient sulfur in the Aberthaw ash (figure 6) to produce around 15% ferric sulfate if 100% of the available sulfate is present as  $\text{Fe}_2(\text{SO}_4)_3$ , so again ferric sulfate appears to be slightly over-reported in the fit and may indicate further unidentified species.

The filters coated in ash from Shandong University were too light in material to generate viable XANES spectra for all but one sample- the "dark" sample processed under high RH conditions with no UV light source. Chemical extraction (figure 13) indicates that the iron in the Shandong ash is not significantly altered by atmospheric processing, and the Aberthaw Fe spectra do not show significant changes despite considerable enhancement of iron solubility, so the spectrum in figure 24 can be considered representative of the Fe speciation in the unprocessed ash as well. Although the signal is weak and close examination of the pre-edge region shows significant noise in the spectrum, the Shandong ash is again seen to be effectively 100% Fe(III) and resembles the structure of ferrihydrite barring slightly higher shoulders at 7135 and 7150 eV.

The linear combination fit (figure 25) indicates that Shandong ash is around 85% ferrihydrite, with the remaining 15% appearing as ferric sulfate and a small proportion of iron pyrite. The identification of

iron pyrite may be an artefact of the ash spectrum shoulder at 7150 eV, and the pre-edge position shows no indication of any Fe(II) presence, and thus should not be given credence without further testing.

All of the ash spectra show that the majority of the iron present is in the form of ferrihydrite. Ferrihydrite is a nanocrystalline compound that dissolves readily in water (Yu, et al., 2002) (Kraemer, et al., 2006), but the readily soluble iron content of Krakow ash, the most soluble ash, is only ~5% after 90 minutes (figure 12). In addition, within the high temperature environment of a coal fired power station, ferrihydrite would be expected to undergo dehydration and aggregation/recrystallization as a more stable iron oxide such as hematite (Vu, et al., 2008). However, all of the ash samples are also high in aluminium. Aluminium substitution is known to inhibit the growth of crystalline hematite at high temperatures, causing iron oxides to remain as ferrihydrite (Schwertzmann, et al., 1979). Additionally, Al-substitution is known to reduce the solubility product of ferrihydrite by several orders of magnitude, slowing its rate of dissolution more as the extent of Al-substitution increases (Schwertzmann, 1991).

This correlates with the dissolution experiments carried out on the Aberthaw and Shandong ashes- while the ash from Shandong University contains more exchangeable/non-crystalline iron according to ascorbate and ammonium acetate extraction (figure 12), its higher Al : Fe ratio (3:1, compared to 2:1 in the Aberthaw ash according to XRF in figures 6 & 7) results in slower release of both iron and aluminium into solution (figures 8a – 11a). Krakow ash, with its Al : Fe ratio closer to 1:1, shows more rapid release of iron into solution than the others.

At time of writing, no comparative XANES studies of ferrihydrite with increasing levels of substitution could be found in the literature, but an EXAFS comparison of pure Fe ferrihydrite and ferrihydrite with an Al mole fraction of 0.44 shows that the two produce nearly identical spectra (Adra, et al., 2013). A sample of 5% Al-substituted goethite was taken to ANKA, however, and its XANES spectrum is practically identical to pure goethite even with the larger crystal size (figure 26). This suggests that Al-substituted ferrihydrite would appear in a XANES spectrum as indistinguishable from pure ferrihydrite and the Athena interpretation can be considered valid.

Comparison of ammonium acetate and ascorbate extraction (figure 12) indicates that siderite is present in each of the ash samples, although in all cases it represents less than 1% of the total iron. Such a small proportion would not be distinguishable in a XANES fitting by current methods.

#### 4.6 Simulated atmospheric processing with stabilised temperature / RH

With external cooling to minimise temperature changes and an internal water reservoir to keep RH high throughout the processing runs, the effect of “Dark” and “Light” simulated atmospheric processing on iron solubility in the three ash types could be directly compared. Seven samples were run in each set of conditions to generate a statistically useful spread of results. Krakow ash (figure 27) shows no significant change in iron solubility under exposure to SO<sub>2</sub>, NO<sub>2</sub> and ozone in dark conditions. A t-test in Excel indicated that processing with simulated sunlight does significantly increase iron solubility, albeit only by a marginal ~15%.

Aberthaw ash (figure 28) again shows a significant increase in iron solubility, of ~50% under “Dark” processing conditions and ~70% under “Light”. However, t-testing shows that the two sets of

processed samples are not significantly different from each other, so the influence of photochemistry cannot be considered significant in its own right. Due to a procedural error, three Aberthaw samples were processed without an O<sub>3</sub> source (three further samples were run to complete the data set). These samples were analysed along with the rest and found to be unchanged in terms of iron solubility, indicating that a strong oxidising agent is essential for any significant solubility enhancement along with acidic gases and high humidity.

Ash from Shandong University (figure 29) is again unaffected by simulated atmospheric processing.

## 5. Conclusions and Future Work

This series of experiments indicates that the majority of iron present in coal fly ash is in the form of aluminium-substituted ferrihydrite, and the primary determinant of iron solubility is the ratio of aluminium to iron. Selective extraction reveals that  $\leq 1\%$  of the total iron in the three ash samples analysed was present as siderite. The presence of this and other minor species may make the XANES spectra produced by ash samples difficult to accurately classify and may help to explain the high reported concentrations of iron sulfate which are not reflected in the results of chemical solubility tests.

Lower concentrations of calcium carbonate, which inhibits atmospheric acid processing, explains why iron solubility in Aberthaw ash is significantly affected by processing while Shandong ash is not despite their similar iron content and speciation. The Krakow ash contains the highest calcium content but also the lowest Al : Fe ratio. While it exhibits the highest rate of dissolution of the three ashes, it is relatively unaffected by atmospheric processing and acid buffering by calcium carbonate is the most likely inhibiting factor. Setting up a timed dissolution experiment with the Krakow ash would demonstrate the difference in soluble iron content once the buffering capacity of any resident calcium carbonate is overcome, and early measurements have the potential to confirm or dispute the high concentration of ferric sulfate reported in the XANES linear combination fit.

The simulated atmospheric processing technique has significant potential for further modification to better replicate conditions in a real-world polluted atmosphere. The lowest concentrations of NO<sub>2</sub>, SO<sub>2</sub> and ozone generated by the existing setup are several orders of magnitude above the concentrations found in the atmosphere. This has the potential to generate synergistic effects on the edges of solid particles that could not occur at environmentally representative concentrations (Usher, et al., 2003). Longer term processing of samples with more dilute gas inputs would yield more representative results. This would require a combination of higher flow rates and lower concentrations of NO<sub>2</sub> and SO<sub>2</sub> in the source gases, or abandoning gas mixtures for continual in-line generation of reactive gases similarly to the production of ozone. A significant challenge would come from generating gas concentrations that are both stable and low enough to be representative. On a positive note, accurate detection of NO<sub>x</sub> with computerised logging is available in most air pollution labs so continuous monitoring by researchers during long term exposures would not be necessary.

Additionally, the mirror that directs the light from the solar simulator lamp into the sample chamber to simulate daylight conditions only covers the wavelength range 280 – 400 nm, which does not include wavelengths known to photodegrade nitrogen oxides in daytime (Bayliss & Bucat, 1975). A replacement mirror that reflects a broader range of UV wavelengths would produce more representative conditions.

## Works Cited

- Achterberg, E. P. et al., 2001. Determination of iron in seawater. *Analytical Chimica Acta*, 442(1), pp. 1-14.
- Adra, A. et al., 2013. Arsenic scavenging by aluminium-substituted ferrihydrites in a circumneutral pH river impacted by acid mine drainage. *Environmental Science & Technology*, Volume 47, pp. 12784-12792.
- Bayliss, N. S. & Bucat, R. B., 1975. The photolysis of aqueous nitrate solutions. *Australian journal of chemistry*, 28(9), pp. 1865-1878.
- Bénézech, P., Dandurand, J. L. & Harrichoury, J. C., 2009. Solubility product of siderite (FeCO<sub>3</sub>) as a function of temperature (25-250oC). *Chemical Geology*, Volume 265, pp. 3-12.
- Benitez-Nelson, C. R., 2000. The biogeochemical cycling of phosphorus in marine systems. *Earth-Science Reviews*, 51(1-4), pp. 109-135.
- Bowie, A. R., Achterberg, E. P., Mantoura, R. F. C. & Worsfold, P. J., 1998. Determination of sub-nanomolar levels of iron in seawater using flow injection with chemiluminescence detection. *Analytica Chimica Acta*, Volume 361, pp. 189-200.
- Broecker, W. S. & Peng, T.-S., 1982. Transport of iron and manganese in the sea. In: *Tracers in the Sea*. New York: Lamont-Doherty Geological Observatory, pp. 226-229.
- Burke, I. T. et al., 2013. Behavior of aluminum, arsenic, and vanadium during the neutralization of red mud leachate by HCl, gypsum, or seawater. *Environmental Science & Technology*, Volume 47, pp. 6527-6535.
- Butler, A. & Carter-Franklin, J. N., 2004. The role of vanadium bromoperoxidase in the biosynthesis of halogenated marine natural products. *Natural Product Reports*, Volume 21, pp. 180-188.
- Chen, H. & Grassian, V. H., 2013. Iron dissolution of dust source materials during simulated acidic processing: the effect of sulfuric, acetic and oxalic acids. *Environmental Science and Technology*, 47(18), pp. 10312-10321.
- Chen, H. et al., 2012. Coal fly ash as a source of iron in atmospheric dust. *Environmental Science & Technology*, Volume 46, pp. 2112-2120.
- Cooper, L. H. N., 1937. Oxidation-reduction potential in sea water. *Journal of the Marine Biological Association of the UK*, 22(1), pp. 167-176.
- Croft, M. T., Warren, M. J. & Smith, A. G., 2006. Algae Need Their Vitamins. *Eukaryotic Cell*, 5(8), pp. 1175-1183.
- Dean, J. R., 2003. Selective Extraction Methods. In: *Methods for Environmental Trace Analysis*. Chichester: John Wiley & Sons Ltd, pp. 76-79.
- Desboeufs, K. V., Losno, R. & Colin, J. L., 2001. Factors influencing aerosol solubility during cloud processes. *Atmospheric Environment*, 35(20), pp. 3529-3537.

- Edgington, H. C., Gressingh, L. E., Liebel, B. W. & Roberts, R. M., 1967. *Monitoring and control of seawater composition*, Port Hoeneme, California: U.S. Naval Civil Engineering Laboratory.
- Gleyzes, C., S.Tellier & Astruc, M., 2002. Fractionation studies of trace elements in contaminated soils and sediments: a review of sequential extraction procedures. *TrAC Trends in Analytical Chemistry*, 21(6-7), pp. 451-467.
- Hansen, H. P., 1999. Determination of oxygen. In: K. Grasshoff, K. Kremling & M. Ehrhardt, eds. *Methods of Seawater Analysis*. Weinheim, New York, Chichester, Brisbane, Singapore, Toronto: Wiley, pp. 75-90.
- Hicks, L. J., 2015. *X-ray spectroscopy and electron microscopy of planetary materials*. Leicester: University of Leicester.
- Ito, A., 2013. Global modelling study of potentially bioavailable iron input from shipboard aerosol sources to the ocean. *Global Biogeochemical cycles*, Volume 27, pp. 1-10.
- Ito, A. & Feng, Y., 2010. Role of dust alkalinity in acid mobilization of iron. *Atmospheric Chemistry & Physics*, Volume 10, pp. 9237-9250.
- Jickells, T. D. et al., 2005. Global Iron Connections Between Desert Dust, Ocean Biogeochemistry, and Climate. *Science*, Volume 308, pp. 67-71.
- Johnston, S. G. et al., 2010. Arsenic Mobilization in a Seawater Inundated Acid Sulfate Soil. *Environmental Science & Technology*, Volume 44, pp. 1968-1973.
- Kostka, J. E. & III, G. W. L., 1994. Partitioning and speciation of solid phase iron in saltmarsh sediments. *Geochimica et Cosmochimica Acta*, 58(7), pp. 1701-1710.
- Kraemer, S. M., Crowley, D. E. & Kretzschmar, R., 2006. iron Bearing Minerals and Soluble Iron Species in the Rhizosphere. In: *Advances in Agronomy vol 91*. San Diego, CA: Elsevier, pp. 9-12.
- Liang, B. et al., 2006. Black carbon increases cation exchange capacity in soils. *Soil Science Society of America Journal*, Volume 70, pp. 1719-1730.
- Lindemann, J., Holtkamp, E. & Hermann, R., 1990. The impact of aluminium on green algae isolated from two hydrochemically different headwater streams, Bavaria, Germany. *Environmental Pollution*, 67(1), pp. 61-77.
- Liss, P. S., Herring, J. R. & Goldberg, E. D., 1973. The Iodide/Iodide System in Seawater as a Possible Measure of Redox Potential. *Nature Physical Science*, Volume 242, pp. 108-109.
- Livorness, J. & Smith, T. D., 1982. *The role of manganese in photosynthesis*. Berlin, Springer, pp. 1-44.
- Li, W. et al., 2017. Air pollution-aerosol interactions produce more bioavailable iron for ocean ecosystems. *Science Advances*, Volume 3, p. e1601749.
- Mahowald, N. M. et al., 2009. Atmospheric iron deposition: global distribution, variability, and human perturbations. *Annual Review of Marine Science*, Volume 1, pp. 245-278.

Martin, J. H., 1990. Glacial-interglacial CO<sub>2</sub> change: the iron hypothesis. *Paleoceanography*, 5(1), pp. 1-13.

Masscheleyn, P. H., Delaune, R. D. & Jr, W. H. P., 1991. Effect of redox potential and pH on arsenic speciation and solubility in a contaminated soil. *Environmental Science & Technology*, 25(8), pp. 1414-1419.

Melis, A. et al., 2000. Sustained photobiological hydrogen gas production upon reversible inactivation of oxygen evolution in the green alga *Chlamydomonas reinhardtii*. *Plant Physiology*, 122(1), pp. 127-136.

Meskhidze, N., Chameides, W. L. & Nenes, A., 2005. Dust and pollution: A recipe for enhanced ocean fertilization?. *Journal of Geophysical Research*, 110(D3), pp. 1-23.

Müller, J. & Seiler, K.-P., 1999. Relevance of self-sealing processes in pyrite sinters for heavy metal mobility. In: H. Armannsson, ed. *Geochemistry of the Earth's Surface*. Rotterdam: CRC Press, pp. 211-214.

Oakes, M. et al., 2012. Characterization of iron speciation in urban and rural single particles using XANES spectroscopy and micro x-ray fluorescence measurements: investigating the relationship between speciation and fractional iron solubility. *Atmospheric Chemistry & Physics*, Volume 12, pp. 745-756.

Plane, J. M. C., Feng, W. & Dawkins, E. C. M., 2015. The mesosphere and metals: chemistry and changes. *Chemical Reviews*, Volume 115, pp. 4497-4541.

Pöschl, U., 2005. Atmospheric aerosols: composition, transformation, climate and health effects. *Angewandte Chemie*, Volume 44, pp. 7520-7540.

Rastogi, N. & Sarin, M. M., 2006. Chemistry of aerosols over a semi-arid region: evidence for acid neutralization by mineral dust. *Geophysical Research Letters*, 33(23), p. L23815.

Raynor-Canham, G. & Flynn, C., 2010. *Iron ocean seeding*. [Online] Available at: <https://eic.rsc.org/feature/iron-ocean-seeding/2020176.article> [Accessed 07 04 2017].

Redfield, A. C., Ketchum, B. H. & Richards, F. A., 1963. The influence of organisms on the composition of sea-water. *The Sea*, Volume 2, pp. 26-77.

Santoso, M. et al., 2016. Trace elements and As speciation analysis of fly ash samples from an Indonesian coal power plant by means of neutron activation analysis and synchrotron based techniques. *Journal of Radioanalytical Nuclear Chemistry*, Volume 309, pp. 413-419.

Schroth, A. W., Crusius, J., Sholkovitz, E. R. & Bostick, B. C., 2009. Iron solubility driven by speciation in dust sources to the ocean. *Nature Geoscience*, Volume 2, pp. 337-340.

Schwartzmann, U., 1991. Solubility and dissolution of iron oxides. In: Y. C. & Y. Hadar, ed. *Iron Nutrition and Interaction in Plants*. Jerusalem: Kluwer Academic Publishers, pp. 3-27.

- Schwartzmann, U., Fitzpatrick, R. W., Taylor, R. M. & Lewis, D. G., 1979. The influence of aluminum on iron oxides. Part II. Preparation and properties of Al-substituted hematites. *Clays and Clay Minerals*, 27(2), pp. 105-112.
- Shi, Z. et al., 2011. Influence of chemical weathering and aging of iron oxides on the potential iron solubility of Saharan dust during simulated atmospheric processing. *Global Biogeochemical Cycles*, 25(2).
- Shi, Z., Krom, M. D., Bonneville, S. & Benning, L. G., 2015. Atmospheric processing outside clouds increases soluble iron in mineral dust. *Environmental Science & Technology*, 49(3), pp. 1472-1477.
- Siefert, R. L., Pehkonen, S. O., Erel, Y. & Hoffmann, M. R., 1994. Iron photochemistry of aqueous suspensions of ambient aerosol with added organic acids. *Geochimica et Cosmochimica Acta*, 58(15), pp. 3271-3279.
- Siggs, L., 2000. Redox Potential Measurements in Natural Waters: Significance, Concepts and Problems. In: J. S. e. al, ed. *Redox: Fundamentals, Processes and Applications*. Berlin: Springer Berlin Heidelberg, pp. 1-12.
- Solomon, F., Chuang, P. Y., Meskhidze, N. & Chen, Y., 2009. Acidic processing of mineral dust iron by anthropogenic compounds over the north Pacific Ocean. *Journal of Geophysical Research*, Volume 114, p. D02305.
- Stockdale, A. et al., 2016. Understanding the nature of atmospheric acid processing of mineral dusts in supplying bioavailable phosphorus to the oceans. *PNAS*, 113(51), pp. 14639-14644.
- Tiwari, M. et al., 2014. Elemental Characterization of coal, fly ash, and bottom ash using an energy dispersive X-ray fluorescence technique. *Applied Radiation and Isotopes*, Volume 90, pp. 53-57.
- Turner, D. R. & Hunter, K. A., 2002. *The biogeochemistry of iron in seawater*. New York: Wiley.
- Usher, C. R., Michel, A. E. & Grassian, V. H., 2003. Reactions on mineral dust. *Chemical Reviews*, Volume 103, pp. 4883-4939.
- Vitova, M., Bisova, K., Doucha, J. & Zachleder, V., 2015. Beneficial or toxic effects of selenium on green algae and their application as nutrient supplements or bioremediators. In: A. Prokop, R. K. Bajpai & M. E. Zappi, eds. *Algal Biorefineries v.2*. s.l.:Springer, pp. 315-335.
- Vu, H. P., Shaw, S. & Benning, L. G., 2008. Transformation of ferrihydrite to hematite: an in situ investigation on the kinetics and mechanisms. *Mineralogical Magazine*, 72(1), pp. 217-220.
- Wang, R. et al., 2015. Sources, transport and deposition of iron in the global atmosphere. *Atmospheric Chemistry & Physics*, Volume 15, pp. 6247-6270.
- Wang, X. et al., 2012. The secondary formation of inorganic aerosols in the droplet mode through heterogeneous aqueous reactions under haze conditions. *Atmospheric Environment*, Volume 63, pp. 68-76.
- Worsfold, P. J., Lohan, M. C., Ussher, S. J. & Bowie, A. R., 2014. Determination of dissolved iron in seawater: A historical review. *Marine Chemistry*, Volume 166, pp. 25-35.

Yu, J.-Y., Park, M. & Kim, J., 2002. Solubilities of synthetic schwertmannite and ferrihydrite. *Geochemical Journal*, Volume 36, pp. 119-132.

## Chapter 4 Measurement of the extended refractive index of Green Fluorescent Protein via Fluorescence Lifetime Imaging Microscopy

### 1. Introduction

The fluorescence lifetime of Green Fluorescent Protein (GFP) is known to be directly related to the refractive index (RI) of its surrounding media (Tregidgo, et al., 2008). While changes in solvent viscosity would normally drive changes in fluorescence lifetime by limiting possible energy shifts and shortening lifetime as solution viscosity increases, GFP's "barrel-like" protein structure prevents external solution viscosity from directly influencing the fluorophore (Ormö, et al., 1996) (Suhling, et al., 2002b), leaving optical effects as the only remaining influence.

Previously the group of Suhling et al measured the optical properties of GFP (Suhling, et al., 2001) (Suhling, et al., 2002a) using Time Correlated Single Photon Counting (TSCPC) of bulk solutions in fluorescence cuvettes with 10 mm path length. Suhling et al noted that the natural radiative lifetime (theoretical fluorescence lifetime in the absence of any non-radiative decay mechanisms) can be predicted by the absorption spectrum in accordance with the equation proposed by Strickler & Berg (Strickler & Berg, 1962). Since the absorption spectrum of fluorescent compounds is related to the Refractive Index (RI) due to the polarizability of the surrounding medium (Garcia-Rubio, 1992) (Borst, et al., 2005), they predicted a relationship between the RI of a medium and the inverse of the measured fluorescence lifetime of a fluorophore in a series of samples of GFP in water/glycerol solutions.

Their data demonstrated a linear relationship between the inverse of GFP's fluorescence lifetime and the relative permittivity (RI squared), see Figure 3. Further experiments with other solvent mixtures including water/polyethylene glycol, water/NaCl and water/glucose (Suhling, et al., 2002b) confirmed that the fluorescence lifetime of GFP was influenced by RI rather than solvent viscosity.

Suhling's group exclusively analysed solutions of  $\sim 1 \mu\text{M}$  GFP concentration. In an aerosol droplet, low RH conditions result in solvent evaporation and progressively higher GFP concentrations. Due to the nature of GFP as an indicator for successful gene expression (Chalfie, et al., 1994) (Valdivia, et al., 1996) its optical activity is most commonly monitored within different parts of living cells (Lee, et al., 2007) (Manen, et al., 2008) (Zou, et al., 2005), within various organic solvents or saline solutions (Suhling, et al., 2002a) or in chaotropic (protein unfolding) fixatives (Chalfe & Kain, 2006). Testing under these dry conditions determines GFP's applicability to the role of a probe for remotely monitoring aerosol droplet viscosity (Hosny, et al., 2013).

Constraining small droplets of GFP in a sucrose and water solution in an optical trap allows the adjustment of solvent (water) composition in situ by adjusting the relative humidity (RH) of the surrounding air by varying the ratio of wet or dry airflow. Lowering the RH around a trapped droplet facilitates the measurement of fluorescence lifetime changes under low sucrose:water ratios that cannot be replicated in bulk solutions because of the crystallization of the sucrose solute. Within the optical trap, sucrose water solutions do not crystallize but become glassy under low RH conditions, meaning that the mass transfer of water throughout the droplet continues but at a dramatically reduced rate (Hosny, et al., 2013) (Power, et al., 2013) (Chenyakin, et al., 2017). This series of experiments uses a combination of optical trapping and Fluorescence Lifetime Imaging Microscopy

(FLIM) to measure the fluorescence lifetime of aerosolised droplets of GFP in both water/sucrose solutions and pure GFP/water solutions. Measurement of the lifetime of GFP in sucrose/water aerosol droplets, under very low RH, allows for the RI of GFP to be measured in conditions that were previously unexplored. GFP/water aerosol droplets were analysed under a similarly wide range of RH conditions, both to monitor changes in lifetime that correspond to changes in RI and to directly observe changes in droplet size as a result of hygroscopic properties.

## 2. Methods and Materials

### 2.1 Calculation of RI of sucrose/water solutions under different RH conditions

A sucrose/water medium was selected since its RI and its hygroscopic properties are well defined. Tong et al. (Tong, et al., 2011) measured the refractive indices of a series of aqueous sucrose solutions at varying concentration and hence mass fraction of solute (MFS), as provided in equation (1).

$$n = 0.071w^2 + 0.1358w + 1.3339 \quad (1)$$

where  $n$  = refractive index and  $w$  = mass fraction of solute (MFS)

This formula allows the refractive index of a sucrose solution to be calculated based upon the MFS. The MFS in turn can be calculated for an aerosol droplet from the work of Zobrist et al (Zobrist, et al., 2011) which provides a parameterization for droplet composition at a given RH. The composition of an aqueous aerosol droplet is dependent on water content (the droplet's hygroscopicity) which is determined by RH in equation (2).

$$a_w(T, w) = \frac{(1+aw)}{(1+bw+cw^2)} + (T - T^\theta)(dw + ew^2 + fw^3 + gw^4) \quad (2)$$

Where  $a_w$  = water activity (RH expressed as a fraction rather than a percentage)  $T^\theta = 298.15^\circ\text{C}$ ,  $T = 293.65^\circ\text{C}$ ,  $w$  = mass fraction of solute/MFS (sucrose/water),  $a$ ,  $b$ ,  $c$ ,  $d$ ,  $e$ ,  $f$  and  $g$  are fitting constants.

The small difference between  $T$  and  $T^\theta$  means that the values in red were found to have a negligible ( $<3 \times 10^{-4}$ , compared to the 0.01-0.07 variation between MFS values based on the known error in RH readings) impact on  $a_w$  using values for  $d$ ,  $e$ ,  $f$  &  $g$  supplied by Zobrist et al. Rearranging the relevant section of equation 2 into a quadratic:

$$\begin{aligned} a_w \cdot cw^2 + ((1 + (b \cdot a_w))w + (a_w - 1)) &= 0 \\ a w^2 + b w + c &= 0 \end{aligned}$$

And applying the quadratic formula ( $w = \frac{-b \pm \sqrt{b^2 - 4ac}}{2a}$ ) allows positive and negative values for MFS to be predicted based on measured RH concentration. The positive values were taken to be the correct MFS, and hence the RI of an aqueous sucrose droplet can be predicted from the measured RH of the surrounding air.

### 2.2 Green Fluorescent Protein solutions

A 2.9 mg solid sample of GFP was collected from a stock provided by STFC (see acknowledgements). The molecular weight of GFP is an estimated 27000 g/mol, so dissolving the solid material in 2.00 ml deionised water produced a stock solution of  $\sim 53.7 \mu\text{mol/L}$ . 1 ml of GFP stock was mixed with 1 ml of

deionised water containing 0.3776 g analytical grade sucrose (Sigma Aldrich) to produce a 36  $\mu\text{mol/L}$  GFP solution in 0.375 M sucrose. The concentration of the GFP in the solution is therefore only a minor component of the overall mixture, by both mass concentration and molarity. Hence, the hygroscopicity of the generated droplets will be dependent solely on the sucrose to water ratio.

It is noted that whilst Suhling et al. used lower concentration solutions, their fluorescence measurements were taken from bulk liquid in 1 cm diameter cuvettes as opposed to micron-sized droplets. The corresponding number of fluorophores in the cuvette experiments far exceeds those in the droplets. It was necessary to use higher GFP concentrations in order to generate sufficient photons from a  $\sim 4 \mu\text{m}$  aerosol droplet to take representative fluorescence lifetime measurements.

A further solid sample of 1.4 mg GFP was dissolved in 1.5 ml of deionised water producing an aqueous GFP solution with a concentration of  $\sim 34.6 \mu\text{mol/L}$ . Lower concentration solutions did not produce droplets with sufficient fluorescence for imaging.

## 2.3 Sample delivery

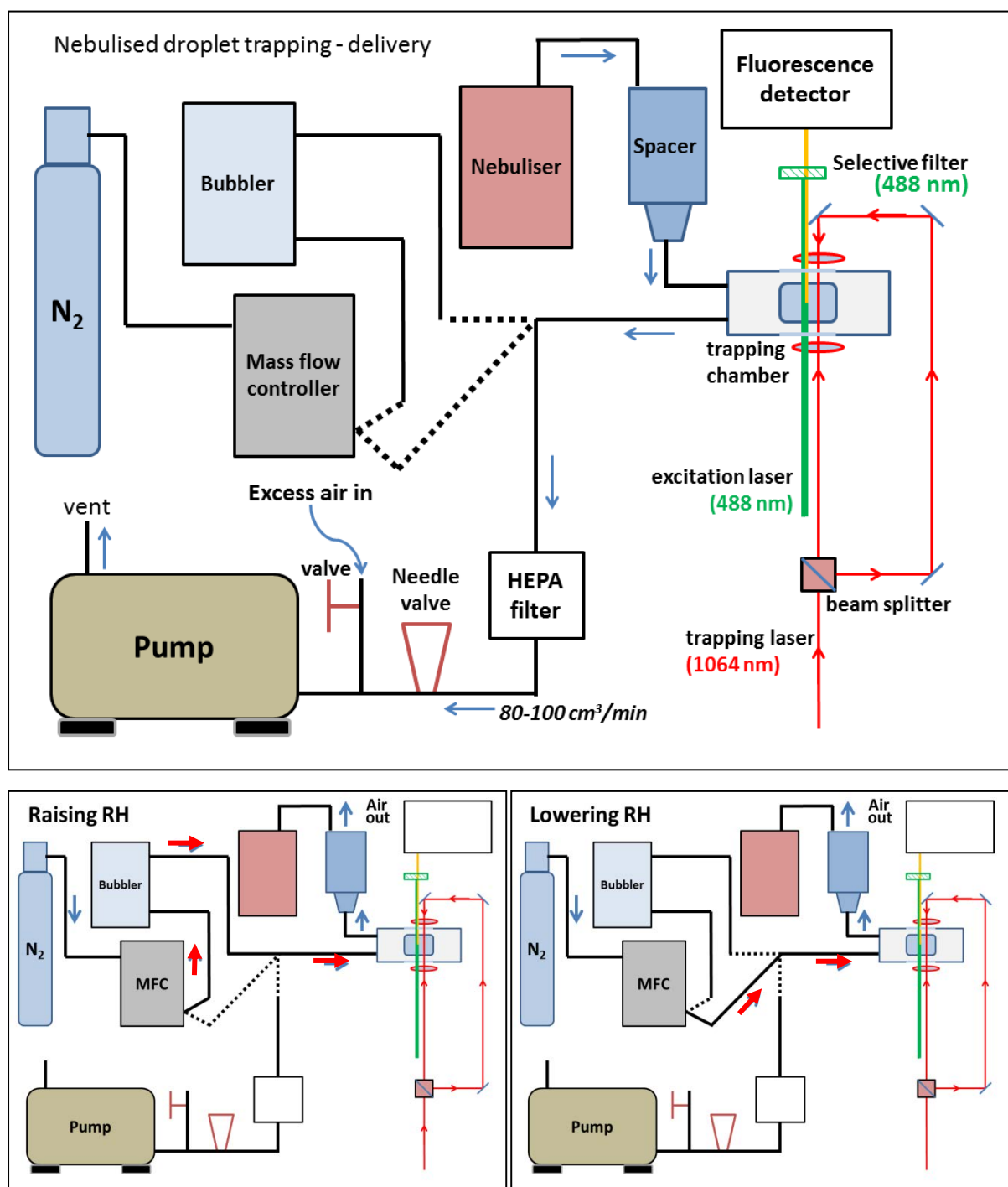


Figure 1. Experimental setup for trapping GFP droplets (top figure), and for raising relative humidity with the bubbler (bottom left) and lowering it with dry nitrogen (bottom right)

GFP solutions were aerosolised by adding  $\sim 1.5$  ml of solution to the reservoir of an Aerosonic Travel Nebulizer (Schill Medical). Droplets were carried into the trapping chamber via a modified Aerochamber Plus spacer (Trudell Medical International) to reduce droplet velocity approaching the chamber and improve the chances of successful trapping. The front baffle inside the mouthpiece of the spacer was removed to allow more droplets to pass through. Average droplets had a diameter of

$\leq 1 \mu\text{m}$ , so trapped droplets were kept in the stream until multiple collisions had occurred and the trapped droplet diameter was  $\sim 5 \mu\text{m}$ . Larger droplets were harder to trap stably and tended to fall out before readings could be taken.

The trapping chamber was a 1 x 2 x 10 cm aluminium cuboid with borosilicate glass panels above and below to admit laser light and similar panels on the sides to allow direct imaging of trapped droplets. Aerosol droplets were pulled through the system by a vacuum pump attached to the chamber outlet. The vacuum pump's pull from the chamber was limited to  $100 \text{ cm}^3/\text{min}$  using a needle valve, as higher flow rates tended to dislodge trapped droplets. An open side line was installed to avoid damaging the pump by restricting air flow. The pump exhaust was connected to the lab extraction vent.

Figure 1 illustrates the delivery system to the trapping chamber, along with the alterations made to the setup to provide RH adjustment. Dry nitrogen gas, from the boil-off from a liquid nitrogen tank, was fed to the chamber at  $100 \text{ cm}^3/\text{min}$  via a mass flow controller (Bronkhorst MV-301) to lower RH. To raise RH, the nitrogen feed was run from the mass flow controller through a water bubbler. Once the desired low RH was reached, the line from the mass flow controller was detached intermittently while the RH was monitored throughout each FLIM measurement. RH was monitored within the chamber with a Sensirion SHT75 temperature-RH probe (manufacturer stated RH uncertainty =  $\pm 1.8\%$  over the range from 10% to 90% (Sensirion AG, 2017)).

## 2.4 Optical trap setup

The first successful attempts at optical levitation occurred using glass spheres in water in 1986 (Ashkin, 1986), but the forces acting upon droplets and particles held stationary by "radiation pressure" were not well understood until six years later (Ashkin, 1992). When a coherent laser beam is focussed inside a sphere of different refractive index to the surrounding media (glass beads in water as in Ashkin et al's early experiments; sucrose-water droplets in air in this case) the change in refractive index alters the path of the laser photons. This change in direction also confers a change in momentum, with an opposite change in momentum occurring at the surface of the sphere.

Photons that reflect from the surface of the sphere rather than refract into it apply an opposing force, but the higher proportion of refracting photons is sufficient to counter the action of gravity on the sphere and hold it aloft, while the balance of forces acting on the sphere drive it towards the centre of the beam and hold it in place. Soon after Dr Ashkin's observations were published, the first counter-propagating dual beam optical trap was demonstrated (Constable, et al., 1993). This setup splits a single laser beam down two optical fibres oriented opposite each other, whose output is balanced to stably hold a particle in the path of the opposing beams. This configuration expanded the range of materials suitable for optical trapping to include very high refractive index solid particles (Horst, et al., 2008) and non-spherical particles, as documented in chapter 5.

The optical trap used in this series of experiments was a counter-propagating dual beam setup similar to the apparatus described by (Rkiouak, et al., 2014) (Tang, et al., 2014), using a 1064 nm Nd:Yag CW laser (Ventus 1064, Laser Quantum) split across a beam splitter and carried to their respective objectives by optical fibres. The top objective was a  $\times 50$  N.A. 0.42 NIR Mplan Apo by Mitutoyo, and the bottom objective was a  $\times 60$  N.A. 1.2 Nikon Apochromat installed in a Nikon Eclipse Ti inverted scanning confocal microscope. Measured laser output from the top objective was 11.4 mW and 9 mW from the bottom objective. The bottom objective employed a water interface with the chamber. The

photodiode power sensor (Thorlabs S120C) was not suitable for water interfaces so the true bottom beam power was assumed to be 30% higher than the measurement in dry air, so the actual bottom objective beam power was around 11.7 mW. The optical trap was positioned 40  $\mu\text{m}$  above the cover slip with a separation of 10  $\mu\text{m}$ .

## 2.5 FLIM & droplet imaging setup

The FLIM and FLIM/optical trap setups were first described in (Fitzgerald, et al., 2016) and (Athanasiadis, et al., 2016) respectively. Fluorescence was achieved with an NKT SuperK EXTREME supercontinuum laser using a prism and a  $488 \pm 10$  nm interference filter to select output to 488 nm to excite the GFP. 488 nm light was blocked with a Comar OG495 selective filter from the fluorescence detector, a cooled high speed PMT: PMC-100-1 by Becker-Hickl GmbH, used as the detector all operated through a B&H SPC150 TCSPC card. A CCD camera was mounted at the side window of the trapping chamber to allow brightfield microscopic imaging of trapped droplets.

Multiple droplets were trapped and scanned at the highest and lowest RH the apparatus could maintain while stably trapping an aerosol, and at regular stages in between. Each fluorescence lifetime reading was collected over 300 seconds to allow sufficient fluorescence intensity to be collected for fluorescence lifetime analysis. The RH was stabilised for  $\sim 1$  minute before beginning fluorescence reading, allowing sufficient time for the droplets to equilibrate to the environmental RH (Tong, et al., 2011)).

## 2.6 Data Processing

Fluorescence lifetime readings were collected using SPCM application software (Becker and Hickl), and results were processed in Tri2 (version 2.8). Each fluorescence measurement was binned by a factor of 8 (17 x 17 pixels) with a threshold of 100 counts per pixel. A bi-exponential Marquadt fit was applied, and a  $X^2$  range of 0.8 – 1.2 was selected before generating a histogram of results. Sample readings from SPCM and Tri2 are shown in figure 2.

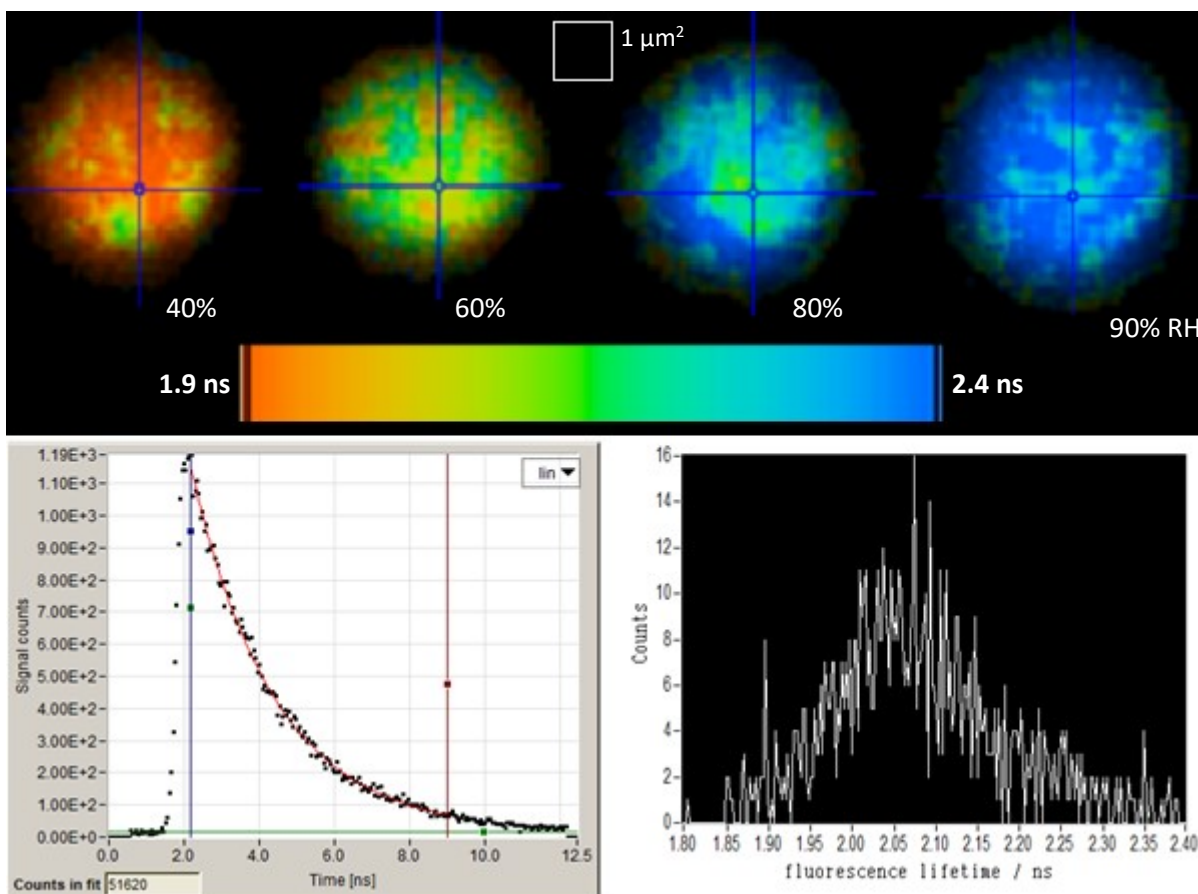


Figure 2 Top: Example fluorescence lifetime images of the same droplet of GFP in sucrose/water at 40, 60, 80 & 90% RH collected by SPCimage. Bottom left: time-resolved data plot of the 40% RH droplet in Tri2. Bottom right: lifetime histogram of the same droplet, with lifetime on the x-axis and number of counts on the y-axis.

SPCimage images were collected by B. Bateman of STFC from this group's data set.

Histograms of the fluorescence lifetime were analysed to obtain the full-width half-maximum (FWHM) of each fluorescence lifetime measurement. The mid-point of the FWHM region was taken to be the average lifetime value, while the upper and lower bounds of the FWHM define the error bars on the y-axis. The error in RI was calculated by defining upper and lower bounds of each RH reading using the known uncertainty in the RH measurements. This error range was applied to the relative permittivity using the Harvard formula for error propagation (Harvard, 2007).

A graticule placed over the brightfield monitor allowed droplet size to be measured and calibrated, and images were handled with the ImageJ processing software (v1.51n).

### 3. Results

#### 3.1 Dependence of inverse fluorescence lifetime on relative permittivity

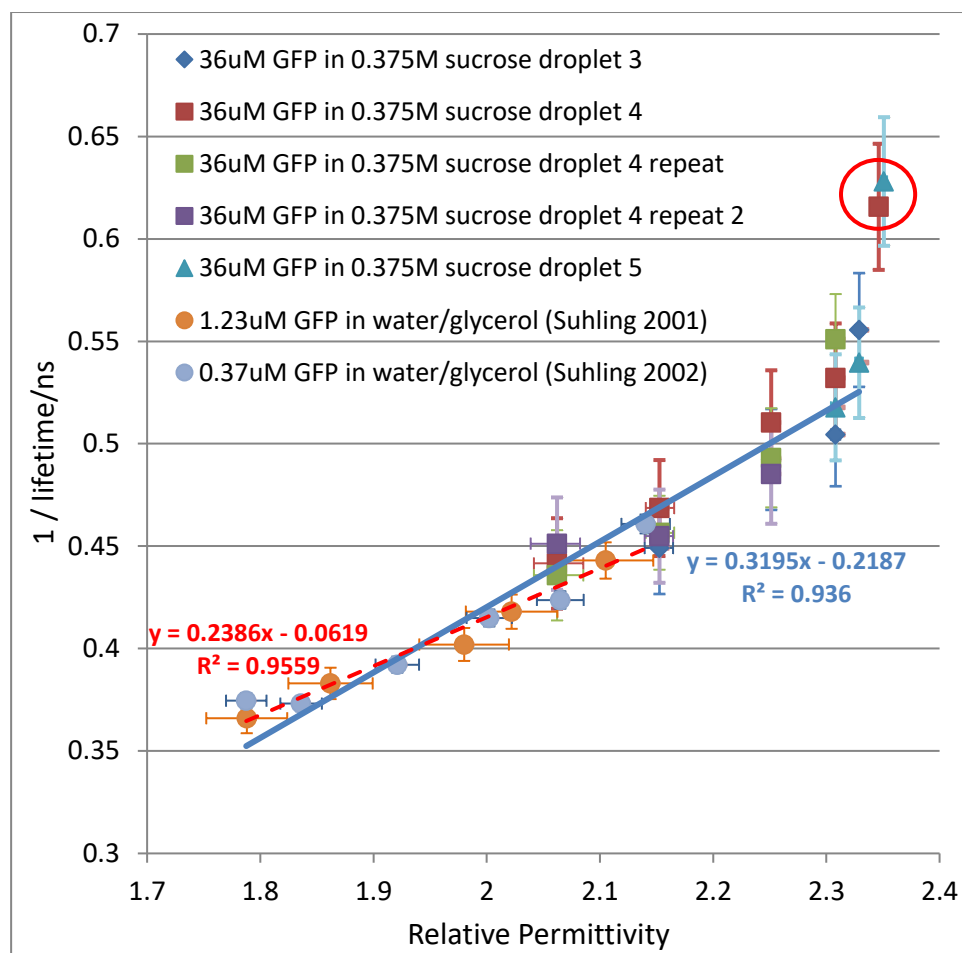


Figure 3 Inverse fluorescence of GFP versus relative permittivity of droplets composed of sucrose/water/GFP. The trendline based on Suhling et al's results alone is shown in red, while the trendline based on all viable readings is in blue. Readings collected at RH below the glass transition point identified by Tong et al are circled in red and excluded from the calculation of the trendline since conditions within the droplet were in flux during detection.

The average fluorescence lifetime of droplets composed of sucrose/water/GFP were measured. In total three droplets were measured with each droplet analysed under multiple RH conditions, thereby resulting in 19 measurements in the RH range 17 - 90% and MFS range of 0.58 – 0.97. The relationship between inverse fluorescence lifetime and relative permittivity is found to be near linear, in the range of relative permittivity of 2.05-2.25, as shown previously by Suhling et al (Suhling, et al., 2002b), see Figure 3.

In the region of overlap of relative permittivities, measured both by this study and by Suhling et al., there is good agreement and all measurements are within the error bars of the other experiments. This study has extended the measurements of relative permittivity beyond 2.14 and up to 2.35 thereby much increasing the measurement region. While the Strickler & Berg formula (Strickler & Berg, 1962) predicts a linear relationship between inverse fluorescence lifetime and relative permittivity, at the highest measured relative permittivities there appears to be a deviation from linearity.

Aerosolised sucrose becomes highly viscous at low RH (Tong, et al., 2011) This transition, according to Tong et al's measurements, takes at least 20 minutes to occur. Due to the instability of particles in the optical trap at low RH (thus high relative permittivity), readings were collected at  $\leq 20\%$  RH as soon as the humidity reading had stabilised but while the particle was still undergoing transition. If these readings are excluded, the remaining readings (including those collected by Suhling et al) correlate linearly in agreement with the Strickler & Berg formula as stated in equation (3).

$$n^2 = 2.9299 \cdot \frac{1}{\tau} - 0.776 \quad (3)$$

$$R^2 = 0.936$$

Where  $\tau$  = fluorescence lifetime and  $n$  = refractive index (RI). The Suhling data alone produces a trendline with a similar  $R^2$  but a significantly different gradient, demonstrating the importance of testing the same material across an expanded range of conditions.

Some heterogeneity is visible in the range of fluorescence lifetime values recorded in the GFP/sucrose droplets shown in figure 2, although the resulting histograms illustrate that the influence over the average lifetime measurement is small. The recorded histograms mostly show a normal distribution of lifetimes with no strong second peaks that would indicate heterogeneous regions within the droplet.

### 3.2 Hygroscopicity and the refractive index of GFP

The results documented in section 3.1, along with the work of Suhling et al., establishes the relationship between RI and GFP fluorescence lifetime. In this section, the RI of GFP/water droplets are calculated from the measured fluorescence lifetimes of the droplets by converting the fluorescence lifetime to refractive index using equation 3.

In total five GFP/water droplets were measured with each droplet being measured at multiple RH conditions, resulting in 15 measurements in the RH range 11-91%. Figure 4a shows the measured RI of the GFP/water droplets versus RH.

The RI of the GFP/water droplets rise with falling RH, as the loss of the water solvent, which has a lower RI index than GFP, causes the droplet to become more concentrated in the solute. The refractive index of pure GFP can thus be estimated by plotting the curve of RI vs RH and measuring the RI value where RH = 0. This value is likely to be an upper limit estimate since GFP (a 27000 Dalton protein) is anticipated to retain some associated water even under dry conditions.

As expected, the refractive index of GFP/water droplets increases as the RH is lowered due to the droplets containing a higher proportion of the solute compared to solvent at low RH. The relationship of the RI of GFP/water droplets appears to be linear with respect to RH over the RH range investigated, with the data quality deteriorating at RH greater than ca. 80%.

Assuming a linear relationship between RI and RH, and extrapolating to an RH of 0% i.e. completely dry air; GFP in isolation is estimated to have an RI of  $1.68 \pm 0.07$ . The error bars are defined by applying the upper and lower bounds of the FWHM of the histogram of each fluorescence lifetime reading.

It is noted that GFP droplets might be expected to follow a hygroscopic growth curve in which the uptake of water becomes more significant at higher RH. This behaviour is observed for simple inorganic and organic aerosol systems e.g. (Pope, et al., 2010) but appears different to GFP. However the tight grouping of lifetime values below 80% RH and especially at <20% RH lend credence to the extrapolated value for GFP RI obtained at 0% RH.

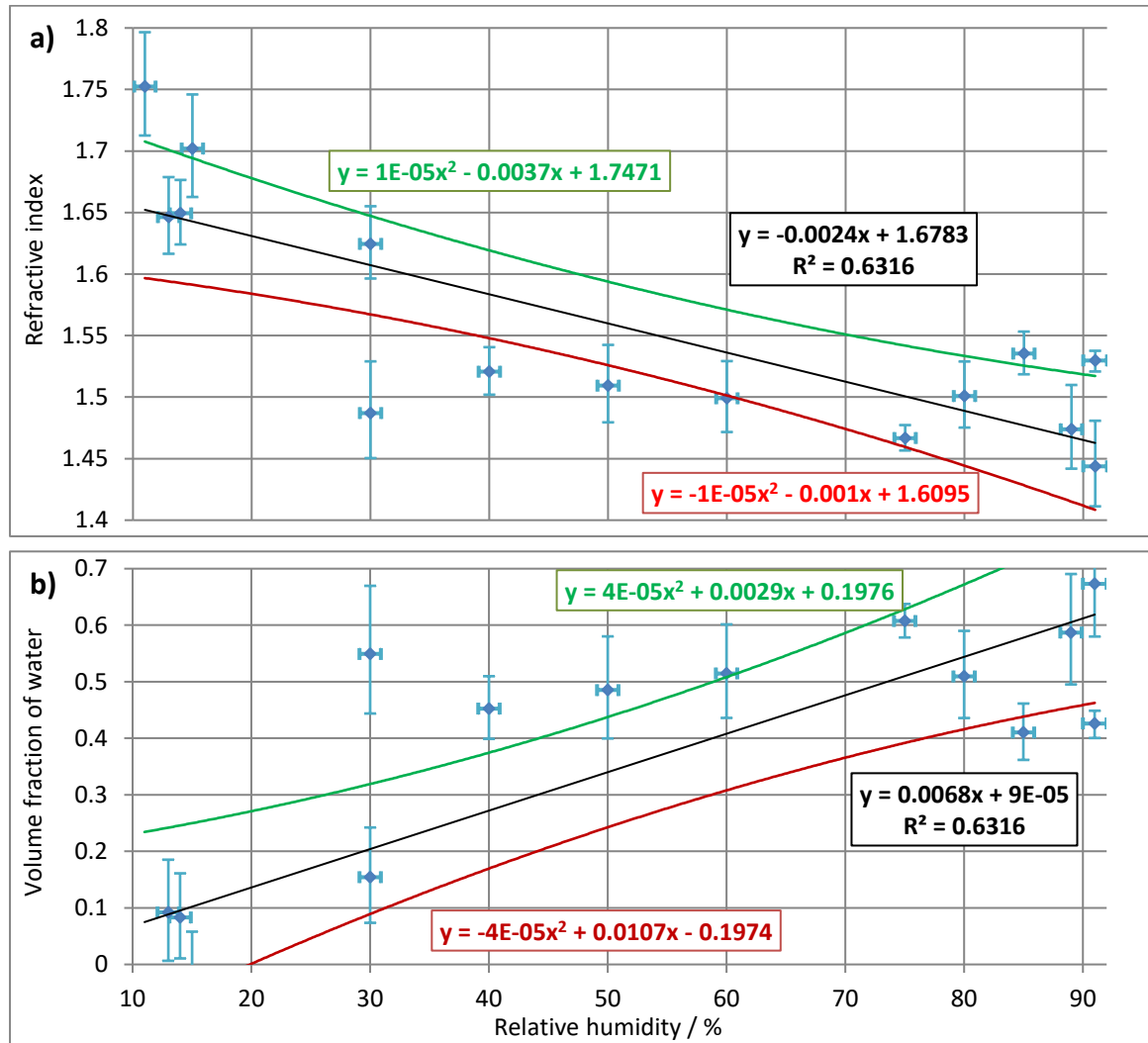


Figure 4 Plot of Refractive Index calculated from RH using equation (4) (a) and volume fraction of water in aqueous GFP droplets (b) at a broad range of relative humidity values. The green and red lines define the upper and lower 95% confidence intervals.

To estimate the water content of GFP particles at different RH, a simple mixing rule was employed using the volume fractions of water and GFP in the droplets, see equation (6). Where  $V_{GFP}$  = volume fraction of GFP at a given RH,  $n_{GFP}$  = refractive index of GFP,  $V_{H2O}$  = volume fraction of water at a given RH,  $n_{H2O}$  = refractive index of water and  $n_{mix}$  = refractive index of droplet at a given RH. Mole fraction is more often employed in mixing rules, but given the large difference in molecular weights between GFP and water (~27000 versus 18 Daltons) volume fraction was deemed to be more representative.

$$n_{mix} = V_{GFP} \cdot n_{GFP} + V_{H2O} \cdot n_{H2O} \quad (4)$$

Since  $V_{GFP} + V_{H2O} = 1$ ,  $V_{H2O}$  can be expressed as  $1 - V_{GFP}$  and the equation can be rearranged into equation (5):

$$V_{GFP} = \frac{n_{mix} - n_{H2O}}{(n_{GFP} - n_{H2O})} \quad (5)$$

This equation allows  $V_{GFP}$  and thus  $V_{H2O}$  to be calculated from known  $n_{H2O}$ ,  $n_{mix}$  values taken from equation (1) (using MFS values calculated from the directly measured RH of droplets), and  $n_{GFP}$  obtained from the formula of the trendline in figure 4a. Figure 4b gives the estimated water content of GFP as a function of RH. The equation of the line shows that from the data  $V_{H2O}$  should be very close to zero at 0% RH, as was determined experimentally.

### 3.3 Droplet volume changes at different RH

In order to check the validity of the plot in figure 4b, brightfield images of the same droplet were examined in ImageJ at high and low RH (figure 5). One image was taken at 17% RH, corresponding to a  $V_{H2O}$  of 0.054 according to a rearrangement of equation (5). The other image was collected at 77% RH corresponding to a  $V_{H2O}$  of 0.246. The volume of GFP alone at 0% RH, or  $V_0$ , is fixed so the total volumes of the droplets under the two conditions are calculated to be:

$$V_{17} = V_0 + \frac{0.054}{0.946} V_0 = 1.057 V_0$$

$$V_{77} = V_0 + \frac{0.246}{0.754} V_0 = 1.326 V_0$$

The brightfield images were collected from a static camera and record the area of the droplets (figure 5). In order to compare areas,  $V_{GFP}$  was fixed at 1 to calculate the droplet radii and thus the areas.

Utilising the upper and lower bounds of the 95% confidence intervals of figure 4b, the areas of the two droplets were found to be  $A_{17} = 1.210 - 1.316$ , and  $A_{77} = 1.329 - 1.480$ . A droplet at 77% RH should therefore have an area 1% to 22% larger than a droplet at 17% RH.

Areas of the brightfield images were approximated by manually defining the region of each image covered by each droplet using the elliptical brush tool in the FIJI 64-bit iteration of ImageJ, v1.51n. Said regions were found to contain 711 (17% RH) and 812 (77% RH) pixels.

$\frac{812}{711} = 1.142$ , meaning that the droplet at 77% RH is approximately **14%** larger in area than the same droplet at 17% RH. This is not inconsistent with the boundaries established by the 95% confidence interval for the  $V_{H2O}$  figures at the respective RH values and lends credence to the volume mixing rule applied in equation (4).

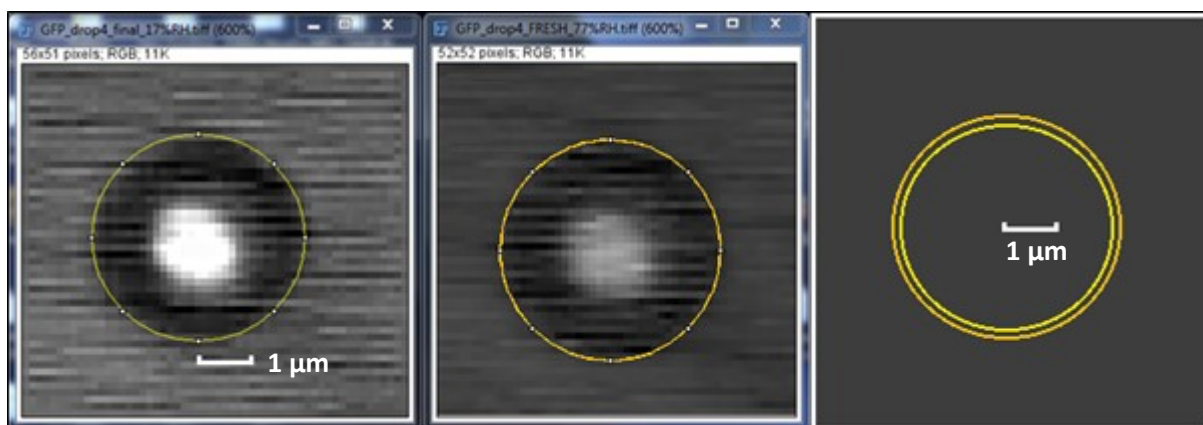


Figure 5 imageJ measurements of the areas of a droplet of GFP at 17% (left) and 77% RH (centre). The droplet areas were defined manually by the “elliptical brush” tool followed by software pixel counting. The droplet areas of the droplet at the 2 RHs are contrasted in the rightmost image.

#### 4. Conclusions

This chapter reports on a series of experiments that investigates optically levitated droplets which are composed of GFP. Droplets contained either GFP mixed with sucrose solution or GFP in deionised water. The results demonstrate that viable fluorescence lifetime measurements can be collected from optically levitated droplets containing GFP at concentrations above  $\sim 35 \mu\text{M}$ .

The refractive indices for said droplets can be reliably calculated based on mass fraction of solute, which in turn can be calculated from the RH measured in situ. The combination of optical trap and fluorescence lifetime imaging allows droplets to be examined at a higher mass fraction of solute than is feasible in a bulk solution. Therefore the fluorescence lifetime of GFP could be collected at high refractive indices using trace amounts of GFP in sucrose/water solutions.

Applying the trendline from the plot of relative permittivity vs the inverse of the measured fluorescence lifetime allowed refractive index values to be obtained directly and thus predicted for GFP in aqueous aerosol droplets down to around 10% RH. Bulk liquid fluorimeter observations by Suhling et al have monitored the RI of GFP at a mass fraction of up to 0.9, while this technique allowed readings to be collected at a GFP mass fraction of  $\sim 0.985$ . Plotting the resulting refractive index values in a humidigram allowed the RI of pure GFP to be estimated at around  $1.68 \pm 0.07$ .

The hygroscopic properties of GFP were observed by measuring brightfield microscope images of aqueous GFP droplets at low and high RH, and verified by comparing the changes in droplet area with those predicted by a volume-based mixing rule. These results show that GFP has the potential to be employed as a probe compound for aerosol droplets. The Refractive Index of pure GFP should be an asset to future researchers examining GFP’s optical properties in solution in high RI media like mowiol, and the FLIM/optical trap setup demonstrates that GFP aerosol solution concentrations can be modified in situ to a high degree of accuracy.

## Works Cited

- Ashkin, A., 1986. Observation of a single-beam gradient force optical trap for dielectric particles. *Optics Letters*, 11(5), pp. 288-290.
- Ashkin, A., 1992. Forces of a single-beam gradient laser trap on a dielectric sphere in the ray optics regime. *Biophysical Journal*, Volume 61, pp. 569-582.
- Athanasiadis, T. et al., 2016. Dynamic viscosity mapping of the oxidation of squalene aerosol particles. *Physical Chemistry Chemical Physics*, 18(44), pp. 30385-30393.
- Borst, J. W., Hink, M. A., Hoek, A. v. & West, A. J. W. G., 2005. Effects of Refractive Index and Viscosity on Fluorescence and Anisotropy Decays of Enhanced Cyan and Yellow Fluorescent Proteins. *Journal of Fluorescence*, 15(2), pp. 153-160.
- Chalfe, M. & Kain, S. R. eds., 2006. Biochemical & Physical Properties of Green Fluorescent Protein. In: *Green Fluorescent Protein: Properties, Applications and Protocols*. Hoboken, NJ: Wiley & Sons, pp. 52-56.
- Chalfie, M. et al., 1994. Green fluorescent protein as a marker for gene expression. *Science*, 263(5148), pp. 802-805.
- Chenyakin, Y. et al., 2017. Diffusion Coefficients of Organic Molecules in Sucrose-water Solutions and Comparison with Stokes-Einstein Predictions. *Atmospheric Chemistry and Physics*, 17(3), pp. 2423-2435.
- Constable, A. et al., 1993. Demonstration of a fiber-optical light-force trap. *Optics Letters*, 18(21), pp. 1867-1869.
- Fitzgerald, C. et al., 2016. Fluorescence lifetime imaging of optically levitated aerosol: A technique to quantitatively map the viscosity of suspended aerosol particles. *Physical Chemistry Chemical Physics*, 18(31), pp. 21710-21719.
- Garcia-Rubio, L. H., 1992. Refractive Index Effects on the Absorption Spectra of Macromolecules. *Macromolecules*, Volume 25, pp. 2608-2613.
- Harvard, 2007. *A Summary of Error Propagation*, Cambridge, MA: Harvard University Department of Physics.
- Höök, M., Li, J., Oba, N. & Snowden, S., 2012. Descriptive and Predictive Growth Curves in Energy System Analysis. *Natural Resources Research*, 20(2), pp. 103-116.
- Horst, A. v. d. et al., 2008. High trapping forces for high-refractive index particles trapped in dynamic arrays of counterpropagating optical tweezers. *Applied Optics*, 47(17), pp. 3196-3202.
- Hosny, N. A. et al., 2013. Fluorescent Lifetime Imaging of Atmospheric Aerosols: A Direct Probe of Aerosol Viscosity. *Faraday Discussions*, Volume 165, pp. 343-356.
- Kuhn, Moscibroda & Wattenhofer, 2005. *On the Locality of Bounded Growth*. Las Vegas, Principles of Distributed Computing.

- Lee, J.-Y. et al., 2007. *Optical properties of green fluorescent proteins and their applications on virus infection*. Munich, Germany, SPIE, Molecular Imaging.
- Manen, H.-J.v. et al., 2008. Refractive index sensing of green fluorescent proteins in living cells using fluorescence lifetime imaging microscopy. *Biophysical Journal*, 94(8), pp. L67-L69.
- Ormö, M. et al., 1996. Crystal Structure of the Aequorea Victoria Green Fluorescent Protein. *Science*, 273(5280), pp. 1392-1395.
- Pope, F. D. et al., 2010. Studies of single aerosol particles containing malonic acid, glutaric acid, and their mixtures with sodium chloride. I. Hygroscopic growth.. *The Journal of Physical Chemistry A*, 114(16), pp. 5335-5341.
- Power, R. M., Simpson, S. H., Reid, J. P. & Hudson, A. J., 2013. The Transition from Liquid to Solid-like Behaviour in Ultrahigh Viscosity Aerosol Particles. *Chemical Science*, 4(6), pp. 2597-2604.
- Rkiouak, et al., 2014. Optical Trapping and Raman Spectroscopy of Solid Particles. *Physical Chemistry Chemical Physics*, pp. 11426-11434.
- Sensirion AG, 2017. *Digital Humidity Sensor SHT7x (RH/T)*. [Online]  
Available at: <https://www.sensirion.com/en/environmental-sensors/humidity-sensors/pintype-digital-humidity-sensors/>  
[Accessed 09 08 2017].
- Strickler, S. J. & Berg, R. A., 1962. relationship between absorption intensity and fluorescence lifetime of molecules. *The Journal of Chemical Physics*, 37(4), pp. 814-820.
- Suhling, et al., 2001. *Influence of the refractive index on EGFP fluorescence lifetimes in mixtures of water and glycerol*. San Jose, CA, SPIE.
- Suhling, K., Davis, D. M. & Phillips, D., 2002b. The Influence of Solvent Viscosity on the Fluorescence Decay and Time-Resolved Anisotropy of Green Fluorescent Protein. *Journal of Fluorescence*, 12(1), pp. 91-95.
- Suhling, K. et al., 2002a. Imaging the Environment of Green Fluorescent Protein. *Biophysical Journal*, 83(6), pp. 3589-3595.
- Tang, et al., 2014. Heterogeneous interactions of SiO<sub>2</sub> with N<sub>2</sub>O<sub>5</sub>: single particle optical levitation-Raman spectroscopy and aerosol flow tube studies. *The Journal of Physical Chemistry*, 118(38), pp. 8817-8827.
- Tong, et al., 2011. Measurements of the timescales for the mass transfer of water in glassy aerosol at low relative humidity and ambient temperature. *Atmospheric Chemistry and Physics*, Volume 11, pp. 4739 - 4754.
- Tregidgo, C., Levitt, J. A. & Suhling, K., 2008. Effect of refractive index on the fluorescence lifetime of green fluorescent protein.. *SPIE*, 3(13).
- Valdivia, R. et al., 1996. Applications for green fluorescent protein (GFP) in the study of host-pathogen interactions.. *Gene*, 173(1), pp. 47-52.

Zobrist, et al., 2011. Ultra-slow water diffusion in aqueous sucrose glasses. *Physical Chemistry Chemical Physics*, Volume 13, pp. 3514 - 3526.

Zou, J. et al., 2005. Expression and optical properties of green fluorescent protein expressed in different cellular environments.. *Journal of Biotechnology*, 119(4), pp. 368-378.

## Chapter 5 Measurement of the Raman spectra and hygroscopicity of four pharmaceutical aerosols as they travel from pressurised metered dose inhalers (pMDI) to a model lung

### 1. Introduction

#### 1.1 Respiratory drugs and drug delivery

Respiratory ailments in the form of asthma and Chronic Obstructive Pulmonary Disease (COPD) are often managed with inhalable drugs. These drugs include beta-2 agonists such as salbutamol and salmeterol, and corticosteroids like fluticasone and ciclesonide.

Salbutamol sulfate and salmeterol xinafoate are both *beta-2 andrenoceptor agonists*, meaning that they target the beta-2 receptors in bronchial muscle cells in a similar manner to adrenaline (Reisine, et al., 1983), forcing calcium out of the cells thus forcing them to relax, and opening the user's airways to allow easier breathing. Salbutamol (Ventalin™, Salamol™) has been a popular treatment for asthma and COPD since 1968 (Icha, 2007), while Salmeterol (Serevent™) was introduced in 1988 as a longer lasting alternative (Ullman & Svedmyr, 1988).

Fluticasone propionate (Flixotide™) is an artificial corticosteroid that assists breathing by reducing inflammation in the lung lining (Harding, 1990). Whilst steroids are useful in managing respiratory conditions, deposition of the drug in the oropharynx suppresses the local immune system, and patients often suffer from mouth and throat infections such as oral candidiasis as a result (Lee, et al., 2012), (Renner, et al., 2012). Fluticasone propionate is also supplied as a combination inhaler with salmeterol xinafoate (Seretide™) due to their complementary modes of action (Woolcock, et al., 1996) (Chapman, et al., 1999) (Calverley, et al., 2003). Pure compounds rather than mixtures were investigated in this study.

Ciclesonide (Alvesco™) is a recently developed inhaled corticosteroid used as a treatment for asthma, hay fever and other respiratory ailments. In order to reduce the mouth and throat infections associated with respiratory steroid application, ciclesonide is designed to be biologically inactive until it interacts with esterase enzymes present in the lung (Mutch, et al., 2007) at which point it is hydrolysed to the active form desisobutyryl-ciclesonide; these enzymes are not found in the oral cavity to the same extent, and hence the potential benefit of reduced oropharyngeal side effects.

Inhalable drugs are predominately administered by nebuliser, dry powder inhaler (DPI) or by pressurised metered dose inhaler (pMDI). Powdered nebulisers have been in use since the 19<sup>th</sup> century (Sanders, 2007), while cheaper and more portable pMDIs were invented in 1955 (Purewal & Grant, 1997). The pMDI is now the most popular device for delivering drugs to the human respiratory system in Great Britain and elsewhere (Lavorini, et al., 2011).

Modern pMDIs contain solid drug particles which are suspended in a liquefied hydrofluoroalkane propellant: most commonly HFA-134a (Cripps, et al., 2000) (Leach, 2005). Other co-solvents such as ethanol or oleic acid can be used depending on the drug (Bell & Newman, 2007). The solvent evaporates within a few milliseconds at ambient temperature upon activation of the pMDI (Stein, 2006), generating a fixed dose, inhalable aerosol of micron-sized solid drug particles travelling at a wide range of planar velocities into the user's trachea and lungs (Crosland, et al., 2009).

## 1.2 Significance of relative humidity and temperature on delivery efficiency

Drugs acting within the respiratory tract are only effective if the particle aerodynamic diameters are in the 1-5 $\mu$ m range since larger particles cannot reach the receptor sites inside the lungs (Labiris & Dolovich, 2003). Hygroscopic particles can increase in size and mass as they collect water from the air (Broday & Georgopoulos, 2001) which means that particles manufactured in the appropriate range when dry may swell to larger than optimal size and higher than optimal mass by the time they pass through the moist air inside the trachea and towards the lungs. While larger particles are less likely to navigate to the regions where they can be absorbed most rapidly, more massive particles have greater momentum, are more likely to impact the back of the throat than pass into the lungs (Mansour, et al., 2016) and their direction of travel is less influenced by the Brownian diffusion processes that would drive them to their intended destination (Tsuda, et al., 2013).

Previous work has shown (Tong, et al., 2014) that salbutamol sulfate deliquesces at around 92% relative humidity (RH). Deliquescence describes the phase change of a crystalline solid to a saturated solution droplet using water collected from the surrounding air. Temperature can affect the RH level required to bring about deliquescence in hygroscopic substances but the effect varies between compounds (Lipasek, et al., 2013). Temperature also has a significant influence over the saturation vapour pressure of air (Lawrence, 2005) so the air inside the lungs at 37°C and near-100% RH contains three times the concentration of water as outside air at similar RH and 20°C (Nave, 2004). However, temperature influences the kinetics of drug dissolution only, rather than the thermodynamic behaviour of solid particles, which remain relatively unchanged, and it is not expected to significantly impact hygroscopic properties.

The rate of deliquescence dictates the rate of adsorption of drugs across lung epithelia, since a given drug cannot be absorbed until it has fully dissolved (Bikiaris, 2011). This lends a time-critical aspect to drug delivery since solid particles in the lungs are removed over time by ejection via the mucociliary escalator in the ciliated regions of the lungs or partition into macrophages in the alveoli (Hardy & Chadwick, 2000) and dissolution appears to be the rate-limiting step for the uptake of inhalable drugs (Bur, et al., 2010). If more of a given drug is removed in these manners before it is fully dissolved, a greater dose must be administered and the resultant side effects such as immunosuppression with corticosteroids (Lee, et al., 2012) and hypokalemia with salbutamol (Hung, et al., 1999) will have greater impacts on patient health.

On the other hand, as mentioned in the previous section rapid deliquescence can lead to an increase in particle size that makes it more difficult for drugs to reach deep into the airways. Finding optimal values for both particle size and hygroscopicity is important for providing patients with the most efficiently delivered treatment with the least side effects, and is the primary motivation for this series of experiments. Additionally, a better understanding of the hygroscopic properties of drug molecules should inform which drugs are likely to be pre-wetted by the wicking effect of water uptake upon inhalation, thus kick starting the dissolution of drug particles upon impactation onto higher respiratory tract surfaces like the epithelium (Brain, et al., 2014).

Investigations are ongoing into the hygroscopic behaviour of drug aerosols delivered by nebuliser e.g. (Haddrell, et al., 2014). However, the popularity of pMDI delivery for bronchodilation medication and the logistical difficulties involved in modelling the pharmacokinetic behaviour of medication inside the lung of a living creature mean that similar studies on pMDI-delivered drugs are justified. DPI

formulations have been shown to be vulnerable to high humidity conditions (Janson, et al., 2016) and the lower particle velocity of DPI inhalations compared to pMDI (Ibrahim, et al., 2015) also implies that high humidity conditions are a concern primarily for DPI devices. However, the sudden change in humidity surrounding drug particles from both types of device upon inhalation mean that changes to particles from pMDIs also merit attention.

It is worth noting that the lung deposition rate of pMDI-delivered material is normally less than 10% (Newman, et al., 1981) and with optimised inhalation technique and additional equipment such as spacers (Dolovich, et al., 1981) (Newman, 1996) maximum possible deposition appears to be around 25% of the total inhaled dose. Since larger particles are more likely to impact or be excluded by the processes discussed above, concern over hygroscopic particle growth is justified.

This series of experiments investigates the use of an optical trap to stably levitate drug aerosols released by popular pMDI devices and Raman spectroscopy to monitor signs of hygroscopic particle growth upon rapid increase in RH. The set up allows for the control of temperature and RH to more closely mimic the conditions inside the human lung than conventional cover slip analysis.

## 2. Methods and Materials

The combination of optical trap, Raman spectroscopy and model lung was first described in Tong et al 2014 (Tong, et al., 2014). The optical trap uses a counter propagating dual beam (CPDB) trap configuration first described by Rkiouak et al. (Rkiouak, et al., 2014) and deployed in several subsequent experiments (Tang, et al., 2014) (Jones, et al., 2015) (Hunt, et al., 2015). This trapping setup is remarkable because it is capable of stably trapping micron-sized solid particles of non-spherical geometry for periods of time up to several hours.

### 2.1 Counter propagating dual beam optical trap

The trapping beams were generated by a 1064 nm Nd:Yag laser (Ventus, Laser Quantum) passed through a beam splitter (Oz optics) and fibre-coupled into two single-mode fibres. Each fibre output was delivered to beam expansion and collimation optics before entering the objective lenses. The laser power at output was 15 mW from the top objective lens and 10 mW through the bottom objective lens (figure 2). The asymmetry in power ensured that trapped particles were driven closer to the optical focus plane of the bottom objective through which the Raman laser is passed, ensuring better focus on the resulting images (Rkiouak, et al., 2014). The foci of the lasers were positioned  $\sim 10$   $\mu\text{m}$  apart, which created a trapping volume large enough to stably hold 1-5 $\mu\text{m}$  particles for long periods. Once all useful observations had been collected from a trapped particle, the particle was allowed to fall under gravity to the cover slip by blocking the 1064 nm trapping beams.

There are several reasons to prefer an optical trap to cover slip analysis. The most significant is that pharmaceutical aerosols are, until they reach the respiratory tract, suspended particles and attempts to recreate their conditions should be as close as possible. Interactions between collecting substrates and water can measurably alter the deliquescence point of hygroscopic particles (Eom, et al., 2014) with surfaces like glass reducing the deliquescence point of sodium chloride by 1.5% compared to a suspended particle. Previous work in our group has also observed changes in particle efflorescence upon a cover slip compared to optical trap. Any particle landing on a cover slip will have part of its surface in contact with the cover slip rather than exposed to the surrounding air (see figure 1), so a

hygroscopic particle will form a water layer beginning with a halo around the contact point with the cover slip rather than across the surface dictated by the particle's geometry and density of hygroscopic sites. The shape of the resulting droplet and rate of adsorption will both be affected by the presence of a cover slip.

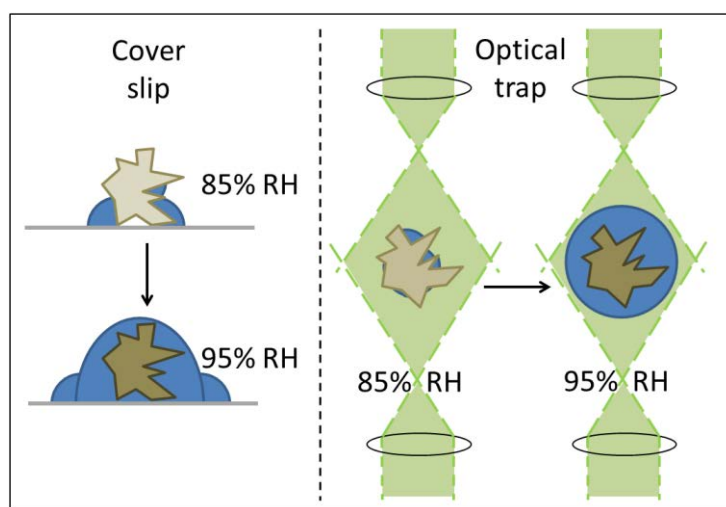


Figure 16. An illustration of the influence of coverslips on the formation of water layers on hygroscopic particles. Optical trapping allows particles to remain suspended as they deliquesce in a manner more representative of particles *in vivo*.

This is especially important in time-critical experiments such as those reported in this paper. Optical trapping represents the best current option for making detailed observations of physical and chemical changes on suspended particles in varying conditions, and yields better resolved Raman spectra than particles observed on a cover slip due to the removal of interfering spectral features associated with the composition of the cover slip. Optical trapping is typically superior for single particle spectroscopy when compared to other single particle levitation techniques, such as electrodynamic balances or acoustic trapping, because the optical setup ensures good alignment between the studied particle and spectroscopic probe (Hargreaves, et al., 2010).

Optical trapping is easiest with spherical or spheroidal particles and droplets due to their symmetry (Ashkin, 1992). While the setup used in this work has demonstrated the capacity to trap non-spherical particles for periods of an hour or longer (Rkiouak, et al., 2014) (Tong, et al., 2014), particles that are closer to spheres are still easier to trap for the same reasons.

## 2.2 Raman Spectroscopy

Raman spectroscopy is a powerful technique for examining the functional groups and intermolecular interactions of substances, requiring very small sample masses and no sample preparation (Hirschfeld & Chase, 1986) (Vankeirsbilck, et al., 2002) and making it ideal for the analysis of micrometer-scale drug particles. Raman spectroscopy has much lower signal-to-noise ratio than competing infrared analysis techniques because of the visible range detection region, and because the scattering wavelengths are separate from those of the excitation laser, so the technique can be effective with very small samples whose absorption would be indistinguishable against a standard FT-IR beam (PerkinElmer Inc, 2008). These experiments use a Raman setup which collects back-scattered photons

along the same path as the excitation laser, but filtering the excitation photons with a RazorEdge dichroic mirror and longpass edge filter combination (SemRock).

Raman scattering was generated using a 514.5nm Ar-ion laser (Innova 300C, Coherent), with a power of 4.3mW measured at the laser focus. Each Raman spectrum was generated by a 30 second exposure to the 514.5nm laser. This is longer than the residence time of particles in the respiratory system but is necessary to generate usable and reproducible spectra. These wavelength and power settings were selected based on previous experiments (Hunt, et al., 2013) as they were found to cause minimal heating of samples over long periods of exposure. Raman scattered light was collected in the region of 540-1830  $\text{cm}^{-1}$ .

Wavelength calibration of the Raman spectrometer was carried out using a cover slip with raised sides containing pure liquid toluene. The spectrum is collected from a focal point within the bulk liquid, away from the surface of the cover slip to avoid interference. The position of spectral peaks for toluene is well characterized and these are used as a reference for wavelength calibration.

### 2.3 Lung-like Environment & Particle Imaging

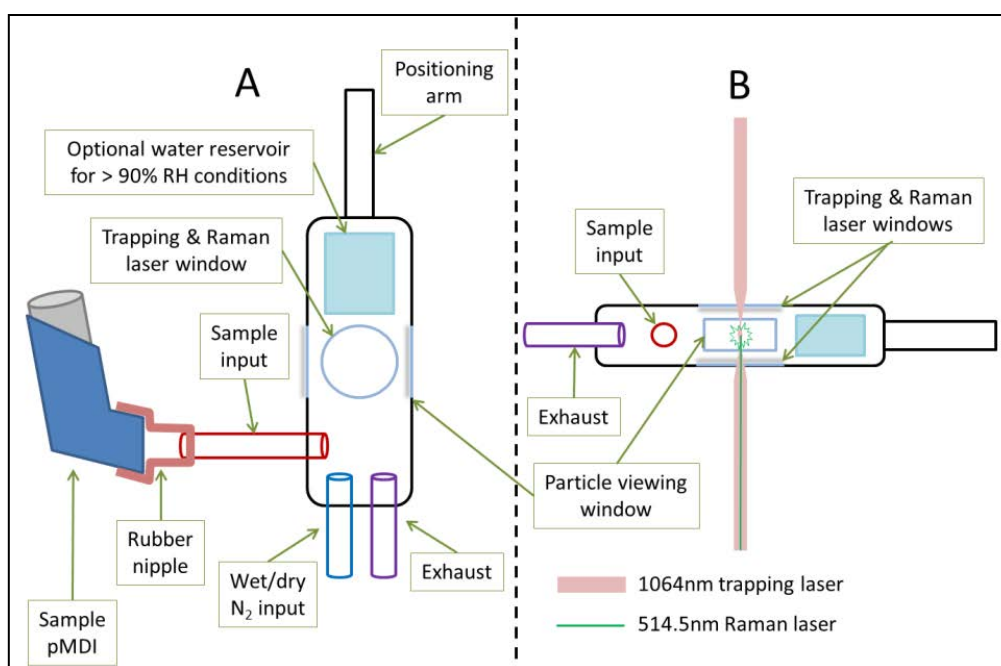


Figure 17 Top-down (A) and side (B) views of the artificial lung chamber (High RH conditions here defined as >93% @ 20°C)

Trapping was carried out in a lung-like environment (figure 2) in an aluminium chamber of internal dimensions approximately 10 x 2 x 1cm, with borosilicate cover slip windows at the top and bottom to admit laser light and also at the sides to observe particles using a Mitutoyo M Plan Apo 20x objective lens connected to a CCD camera (Princeton Instruments, Spec10), opposite an LED source (Comar Optics). A monitor attached to the CCD camera allowed users to observe particles passing around, through and into the optical trap.

RH and temperature were monitored using a Sensirion SHT-75 RH probe with a manufacturer-stated accuracy of  $\pm 1.8\%$  RH and  $\pm 0.3^\circ\text{C}$ . Raman spectra were collected within 3 minutes of reaching the desired RH. This is significantly longer than the 10 seconds recommended by the medical community

for inhalation, holding and exhalation of a pMDI dose but is necessary for adjusting RH accurately and for developing clear and reproducible spectra. RH levels were altered using N<sub>2</sub> gas sourced from boiled off liquid nitrogen, using a flow rate of ~200 cm<sup>3</sup>/min through a Bronkhorst MV-301 mass flow controller. A lower flow rate of 100 cm<sup>3</sup>/min was used for RH adjustment of the Salmeterol particles, since higher flow rates tended to dislodge the particles from the trap for reasons discussed in section 3.3. The input and exhaust ports were located on the same face of the cell in order to generate slow flow conditions around trapped particles and thus minimise turbulence that might dislodge the particle.

The gas was either run into the cell directly (low RH) or passed through a bubbler containing milli-Q grade deionized water before entering the cell (high RH). For very high RH conditions, a water reservoir was added inside the chamber. While the bubbler could provide RH up to ~90%, the reservoir could generate RH as high as 93% at 30°C and up to 98% at 20°C.

Salmeterol xinafoate, fluticasone propionate and ciclesonide were analysed at ambient temperature at high and low RH. Salbutamol sulfate was analysed both at ambient temperature and at more physiologically relevant temperatures by incubation of the microscope environment using Solent Scientific incubator components.

## 2.4 pMDI injection

To dispense the aerosolised drug into the artificial lung chamber, a simple connector was built for the pMDI outlet involving a flexible rubber cap with a rigid 6mm (internal diameter) PTFE tube protruding through it. The tube was connected to a similar tube on the side of the artificial lung by a short length of flexible silicone tubing. The chamber was washed sequentially in deionized water and methanol to minimise potential cross-contamination with other drugs.

The propellant flow within the sample chamber carried material from each pMDI discharge into the path of the trapping beam. Drug particles passing across the side viewing window were illuminated by an LED and observed on a monitor. Scattering of the unfiltered trapping laser from a trapped particle was viewed on the same monitor to indicate the positional stability of the particle.

Based on the stated mass per release of each drug, the density of the solid material (Zhejiang NetSun Co., Ltd., 2010), the assumption that an average particle is solid and has a volume of approximately 10 μm<sup>3</sup>, a single release from each inhaler is estimated to deliver approximately 10<sup>6</sup> to 10<sup>7</sup> particles to the chamber. However, many of these particles are lost by impaction onto the walls of the chamber. A single trapped particle, which is at least 2 μm in diameter, has sufficient material to generate a Raman spectrum.

## 2.5 SEM imaging

Each drug was actuated onto a glass cover slip and coated with 10nm gold particles in a Polaron SC7640 sputter coater. The cover slips were attached to Agar Scientific 25mm double sided sticky carbon tabs prior to imaging on a Philips XL30 ESEM FEG.

## 2.6 Chemical Structures of the asthma drugs investigated

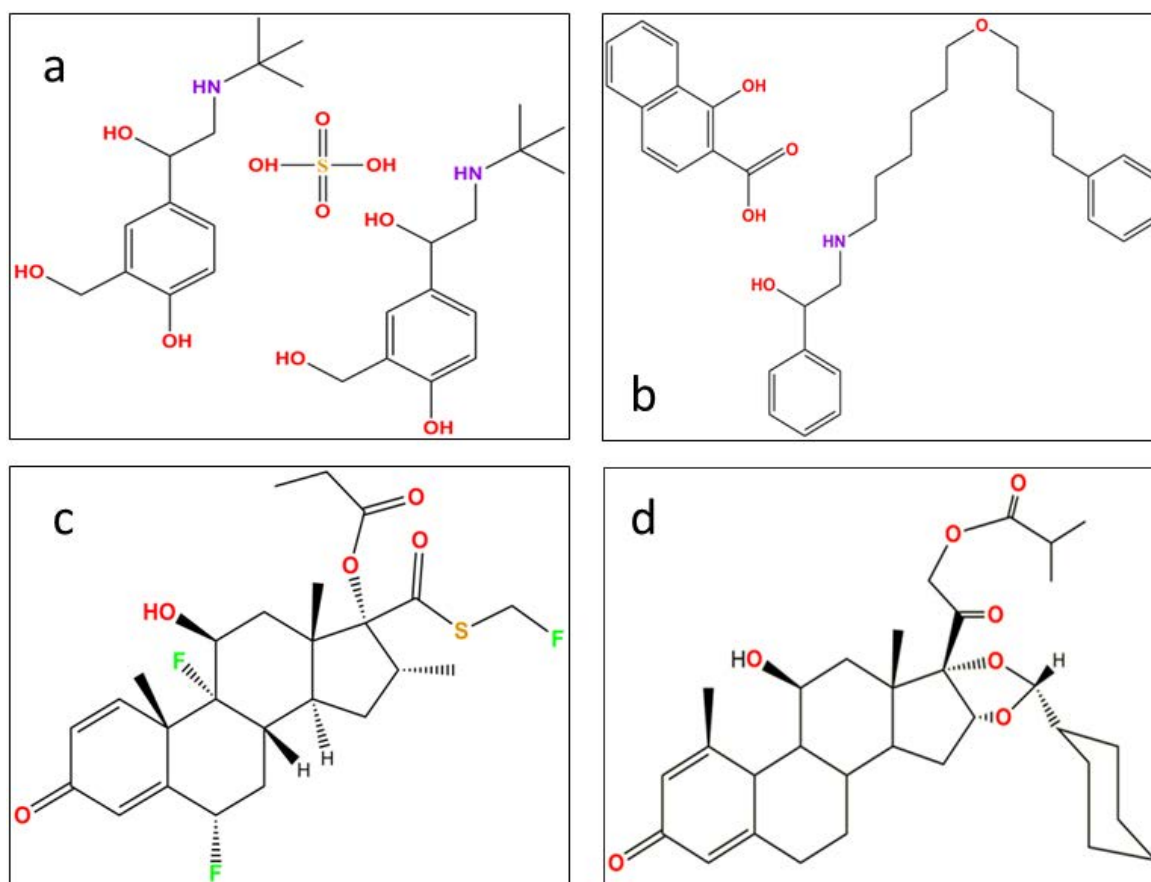


Figure 18 Chemical structures of single molecules of salbutamol sulfate (a), salmeterol xinafoate (b), fluticasone propionate (c), and ciclesonide (d)

Salbutamol sulfate particles were generated from a Salamol brand inhaler by Ivax Chemicals Ltd. Salbutamol sulfate contains several polar groups and no long aliphatic chains, and its hygroscopic character has been documented (Tong, et al., 2014). Salmeterol xinafoate particles were produced from a “Serevent” brand inhaler produced by Cipla Ltd. Salmeterol also contains multiple polar groups but also a long aliphatic chain. Its hygroscopic properties are to be determined.

Fluticasone propionate, generated from a “flixotide” brand inhaler, is manufactured by GlaxoSmithKline, and ciclesonide particles were generated by a “Ciclohaler” brand inhaler also by Cipla Ltd. Ciclesonide is produced under license from Takeda UK Ltd. Fluticasone propionate and ciclesonide are both steroids and as such are relatively hydrophobic and are not expected to show hygroscopic properties.

### 3. Results and Discussion

#### 3.1 Thermodynamic Calculations of Particle Hygroscopicity

Thermodynamic calculations of aerosol particle hygroscopicity were carried out using the Extended Aerosol Inorganics Model (E-AIM) (Clegg, et al., 2001) (Engelhart, et al., 2011) (Ling & Chan, 2008). E-AIM is a thermodynamic model for predicting the water content of aerosol particles at different relative humidities. The model is appropriate for calculating the thermodynamic state of the drug aerosol for a given RH, however, the model does not take into account the time dependent kinetic limitations of water uptake to the particle within the respiratory tract. Within E-AIM, model III is used and the UNIFAC model is chosen to calculate the water activities of the organic fraction of the investigated drugs within the particle at different RH. The UNIFAC model parameterizes the molecular composition of the organic fractions of the investigated drug particle using a combination of structural and functional groups (Wittig, et al., 2003). The calculation of water activities of the sulfate group within salbutamol sulfate is also described by Clegg (Clegg & Brimblecombe, 1998). The type and quantity of UNIFAC parameters chosen to represent the four investigated drugs are provided in Table 1. It is noted in some cases exact matches for molecular composition, using UNIFAC, of the investigated drugs are not possible and in such cases the closest match was used. Standard dissociation constants for the carboxylic acid and amine functional groups were used. The model assumes that both salbutamol sulfate and salmeterol xinafoate dissociate into their respective ions dependent upon their dissociation constants. The formation of solid salts (salbutamol sulfate and salmeterol xinafoate) is disallowed since the activity products of the salts are unknown. Hence the modelled hygroscopicity provides an upper limit estimate.

The output from E-AIM allows for the prediction of the drug molecule hygroscopicity (Clegg, et al., 2001) (Engelhart, et al., 2011) (Ling & Chan, 2008). Figure 4 shows the mass growth factors for the four investigated drugs. Mass growth factor is defined as the mass increase, for a given RH, normalized to the dry mass. It can be seen that Figure 4 predicts two distinct types of interaction. The beta-2 agonists (salbutamol sulfate and salmeterol xinafoate) contain a higher proportion of hydrophilic groups and are thus predicted to be strongly hygroscopic, while the more lipophilic steroids (ciclesonide and fluticasone propionate) are expected to collect little water from the air even under near water saturated conditions. It is noted, that the bulk thermodynamic calculations in E-AIM do not take into account the crystal structure of solid particles which may block access to hydrophilic sites and prevent otherwise hydrophilic molecules from interacting with water in the air. Furthermore, the model runs do not take into account possible deliquescent barriers to water uptake due to the lack of product activity data.

Table 8 UNIFAC parameters used for thermodynamic modelling of the four investigated drugs. Note that the salmeterol xinafoate is modelled as two separate molecules: salmeterol and xinafoate. Also note that the sulphate in salbutamol sulphate is not modelled using UNIFAC hence its omission from the table.

UNIFAC Group	Salmeterol	Xinafoate	Salbutamol	Fluticasone propionate	Ciclesonide
Alkane (CH <sub>3</sub> )	-	-	3	4	3
Alkane (CH <sub>2</sub> )	10	-	1	1	9
Alkane (CH)	1	-	1	4	6
Alkene (CH=CH)	-	-	-	1	1
Alkene (CH=C)	-	-	-	1	1
Aromatic carbon (ACH)	8	6	3	-	-
Aromatic carbon (AC)	4	4	3	-	-
Alcohol (OH)	3	1	3	1	1
Carboxylic acid (COOH)	-	1	-	-	-
Carbonyl (CH <sub>2</sub> CO)	-	-	-	2	2
Ether (CH <sub>2</sub> O)	1	-	-	-	-
Ether (CHO)	-	-	-	-	2
Secondary amine (CH <sub>2</sub> NH)	1	-	1	-	-
Acetate (CH <sub>2</sub> COO)	-	-	-	1	1
Fluoroalkane (CF)	-	-	-	3	-

Ferron's kinetic model (Ferron, 1977), as used in the International Commission on Radiological Protection (ICRP, 1994) provides a parameterization with which to estimate of the time dependent growth of hygroscopic particles. pMDI particles are typically generated in the size range 2 – 5 µm to optimally deliver drugs to the central regions of the lung. The Ferron model suggests that a hygroscopic particle of initial size of 2–5 µm diameter will reach approximately 80–50% of its equilibrium size, respectively, within a typical 2–3 s long inhalation.

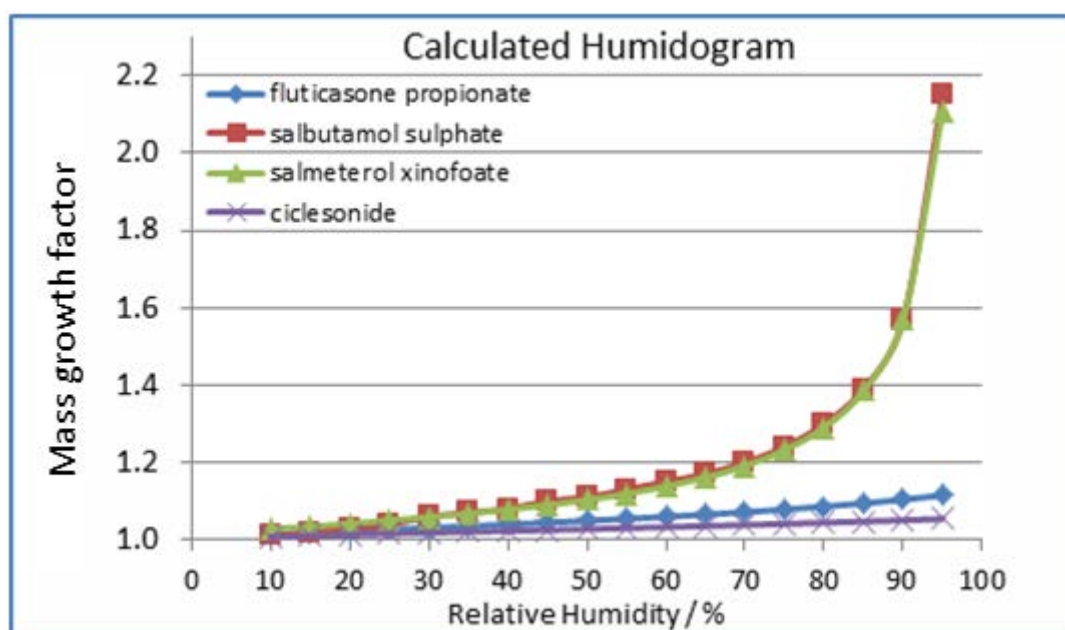


Figure 19 Influence of relative humidity on particle diameter predicted from chemical bonding

### 3.2 Drug Particle Crystallography

The Mercury 3.6 program (Macrae, et al., 2006) was used to simulate the crystal structure of all drugs whose structures had been added to the Cambridge Structural Database run by the Cambridge Crystallographic Data Centre (CCDC, 2015).

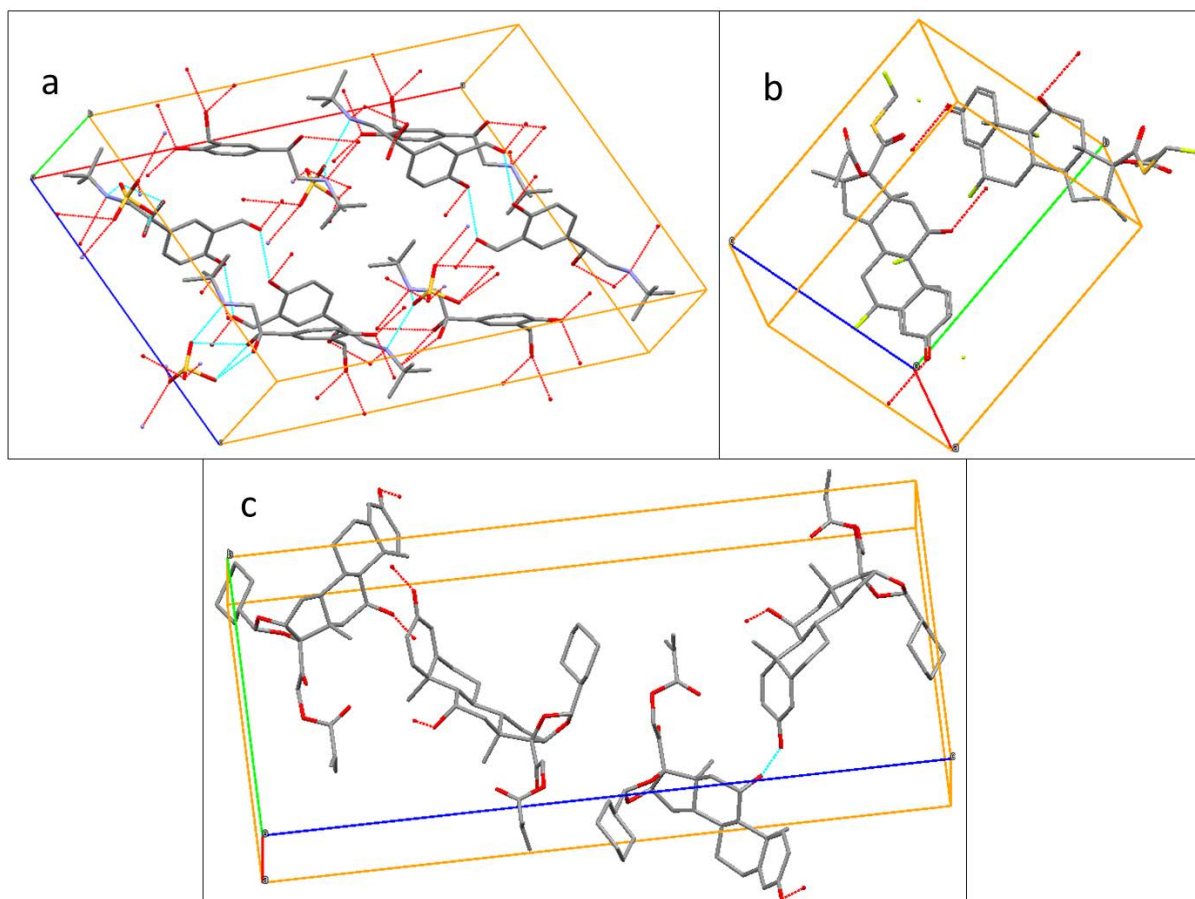


Figure 20 Model unit cells of salbutamol sulfate (a), fluticasone propionate (b), and ciclesonide (c). Salmeterol xinafoate's unit cell was not available at time of writing. Hydrogen bonding within the unit cell is illustrated with a cyan line, while hydrogen bonding external to the unit cell (thus contributing to hygroscopic behaviour) are illustrated with red dotted lines.

The chemical structure of salbutamol sulfate (figure 5a) shows hydrophilic sites across the molecule. The most likely crystal form generated by rapid solvent evaporation in air was first described in 1978 (Leger, et al., 1978), with an 8 molecule unit cell (figure 5a) that shows hydrogen bonding sites on every face. Hygroscopic behaviour is inferred from this structure and has been demonstrated in previous experiments at room temperature (Tong, et al., 2014).

Salmeterol is not found in the Cambridge Structural Database. Solid structures are variously described as either amorphous, or needle-like or plate-like crystals depending on the exact conditions of manufacture (York & Hanna, 1994) (Barjoan & Clotet, 2009). Salmeterol xinafoate is bound together by hydrogen bonding of the  $\delta$ -positive amine group on salmeterol to the  $\delta$ -negative carboxylic acid group on the xinafoic acid. The two groups are expected to cancel their respective charges, leaving few hydrophilic sites open to interaction with water while the particle is in a solid state.

As a steroid, fluticasone is expected to be lipophilic (Lipworth & Jackson, 2000). The structure of fluticasone (figure 5b) does have a number of polar groups. However, the documented crystal structure (Cejka, et al., 2005) describes a plate-like structure with any hydrogen bonding occurring along the plane of growth (figure 5b) resulting in water interaction only along edges, and likely to result in little or no hygroscopic behaviour.

Ciclesonide (figure 5c) is found as either needle-like (Phull, et al., 2012) or needle-like and spherulitic crystals as well as amorphous solids (Feth, et al., 2007) depending on solvent type and evaporation time. Ciclesonide has multiple polar groups but the model unit cell described by Feth et al describes most of the oxygens arranged inside the crystal with the hydrophobic sites facing outward. Limited hydrogen bonding due to the hydroxyl and ketone groups on adjacent molecules have the potential to attract water molecules to crystal faces, but the hydrophobic nature of the rest of the exposed molecule implies that hygroscopic behaviour is unlikely.

### 3.3 SEM imaging and Trapping Logistics

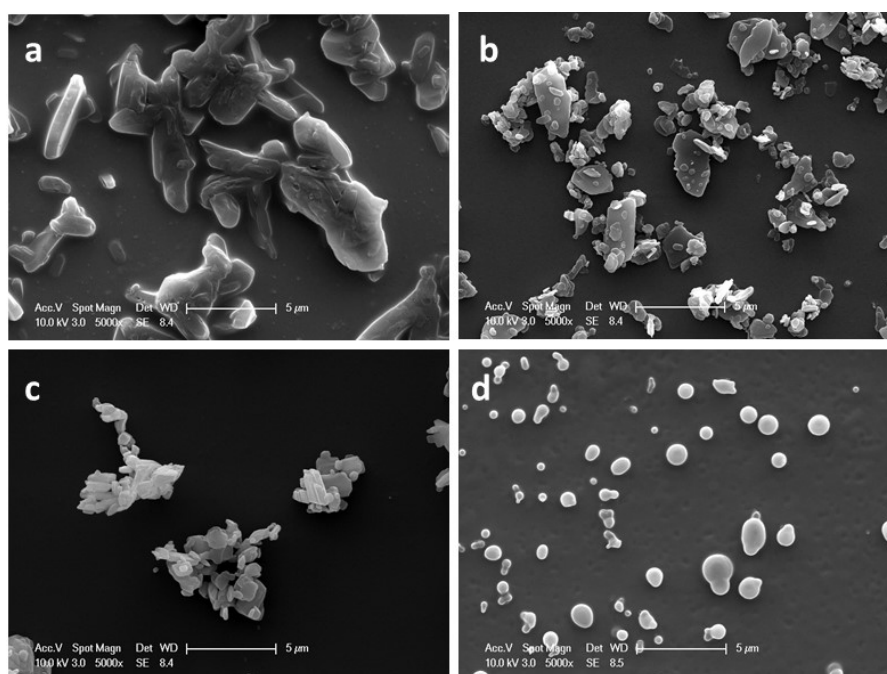


Figure 21 SEM images of: (a) salbutamol sulphate, (b) salmeterol xinafoate, (c) fluticasone propionate & (d) ciclesonide

SEM images of the drug particles were collected under dry conditions in order to determine shape and ease of capture. The likelihood of a particle being successfully caught in the optical trap is dictated by both particle shape and the number of particles generated per release. Salbutamol sulfate had been optically trapped previously on the same apparatus (Tong, et al., 2014). The thick, needle like shape of salbutamol sulfate particles (figure 6a) is well suited to entrapment for reasons detailed in section 2.4, and the 100 µg per release dose of the available inhalers resulted in a successfully suspended particle roughly once for every two releases. Salmeterol xinafoate was significantly harder to trap and retain than the others due to a combination of its low dose (20 µg per release) and flat, platelike aggregate structure (figure 6b). Fluticasone has a similar crystal structure to salmeterol but a much higher dose (250 µg per release) and was more reliably trapped than salbutamol sulfate. Ciclesonide was similar in trapping frequency to fluticasone since its lower dose (160 µg per release) was balanced by a more spherical particle shape (figure 6d).

### 3.4 Raman spectrum changes from hygroscopic properties and additional compounds

Hydrogen bonding with water molecules adjacent to the polar groups of organic molecules expands the range of vibrational energy states that can generate Raman scattering photons. This effect allows water uptake by hygroscopic particles to be monitored by Raman spectroscopy.

All four drugs use hydrofluoroalkane HFA 134a/Norflurane as a propellant. The salbutamol and ciclesonide inhalers also report anhydrous ethanol among their ingredients. Norflurane contains four C-F bonds, each of which generate a distinctive Raman scattering peak at  $1234\text{ cm}^{-1}$ . This peak is not expected to be visible in the Raman spectra of the drug molecules, apart from Fluticasone which has 3 C-F bonds of its own, due to Norflurane's low boiling point ( $-26.5^\circ\text{C}$ , (Lide, 1991)) at atmospheric pressure causing all of the propellant to boil off before readings can be collected. The spectra collected from particles other than fluticasone do not show peaks in the C-F stretching region, which implies that all propellant boils off before the particles are scanned.

### 3.5 Salbutamol sulfate / Salamol™

#### 3.5a Raman spectra and structural information

Each salbutamol molecule contains a single phenol group, two aliphatic hydroxyls and a secondary amine. One molecule of salbutamol contains two ionised salbutamol molecules bound to a single sulfate group. The S=O symmetric stretches on the sulfate show a small but distinctive peak at  $1154\text{ cm}^{-1}$ . The largest peaks in the salbutamol spectrum correspond to -CH wagging at  $656\text{ cm}^{-1}$ , aromatic ring vibration at  $752\text{ cm}^{-1}$ , C-C-O stretches in relation to the aliphatic hydroxyls at  $784\text{ cm}^{-1}$ , asymmetric hydroxyl stretches at  $969$ ,  $977$  and  $1008\text{ cm}^{-1}$ , phenyl ring vibrations at  $1059$  and  $1074\text{ cm}^{-1}$ , a prominent CH stretch at  $1257\text{ cm}^{-1}$  (this bond can be found in figure 3 just above the ring)  $\text{CH}_2$  and  $\text{CHOH}$  vibrations again from the aliphatic hydroxyls at  $1360\text{ cm}^{-1}$ , a broad ring stretching peak around  $1450\text{ cm}^{-1}$  followed by a  $\text{CH}_2\text{-N}$  amine peak at  $1463\text{ cm}^{-1}$ , and finally a strong peak at  $1615\text{ cm}^{-1}$  corresponding to the phenolic C-OH stretch. All of these peaks (figure 7) correspond well with those found in the literature (Ali, et al., 2009).

### 3.5b Impact of RH and Temperature on salbutamol spectra

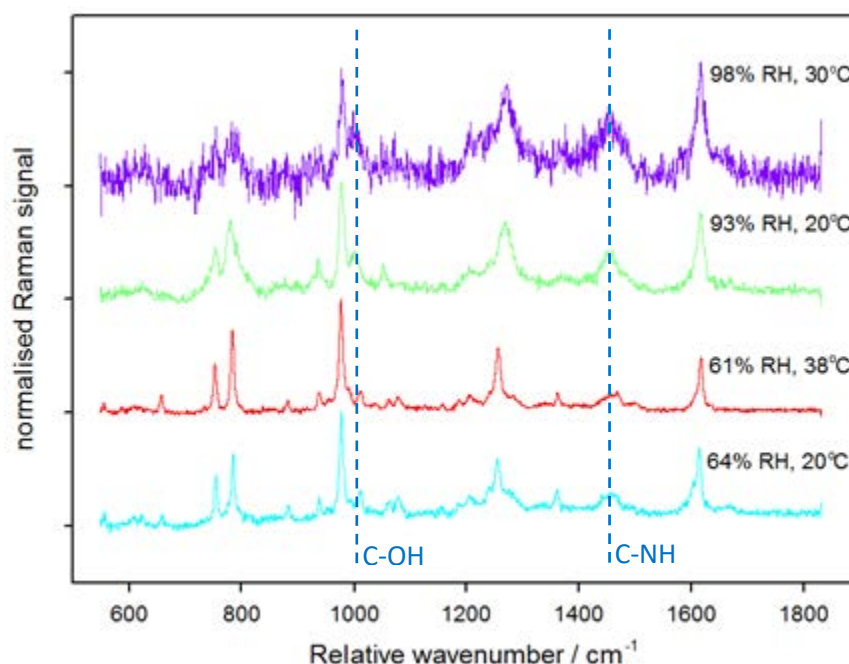


Figure 7 Raman spectra of optically trapped salbutamol sulfate particles at a range of RH and temperatures. Above salbutamol's deliquescence point of 92% RH, peak broadening is visible at the C–OH peak at  $1008\text{cm}^{-1}$  and at the C–NH peak at  $1463\text{cm}^{-1}$ , signifying water interaction with the bonds. Spectra measured at elevated temperatures ( $>20^\circ\text{C}$ ) were taken by Dr Hai-jie Tong's research group.

RH above 92%, the deliquescence point identified by Tong et al (Tong, et al., 2014), could not be maintained at physiological temperature ( $37^\circ\text{C}$ ) with the available equipment, so measurements were taken at  $30^\circ\text{C}$ - the highest temperature at which  $>92\%$  RH could be maintained. The particle trapped at 98% RH and  $30^\circ\text{C}$  was small, hence the poorer signal/noise ratio. The contrast between the relatively dry and relatively wet particles is clear to see as the peaks corresponding to hydrophilic bonds in the wet particles are broader, and some peaks such as the hydroxyl peak at  $1008\text{cm}^{-1}$  and the amine peak at  $1463\text{cm}^{-1}$  are more pronounced.

The spectral traces, recorded at similar RH but under contrasting temperatures, are very similar. Within the temperature range investigated ( $20\text{--}38^\circ\text{C}$ ), there are no observable temperature effects upon particle deliquescence. The deliquescence RH is measured to be ca. 92% RH in agreement with the measurement of Tong et al (Tong, et al., 2014). This implies that the temperature gradient experienced in the trajectory from pMDI to lung is likely to be unimportant in determining particle hygroscopicity; RH is the dominant determinant of particle hygroscopicity.

The modelling results from E-AIM suggested that salbutamol sulfate would show significant hygroscopicity if a deliquescence phase transition occurred. The experimental results confirm this model prediction. The presence of a phase transition and significant water uptake is in line with the high reported solubility of salbutamol sulfate ( $14.1\text{g/L}$ , (Walkowsky & He, 2003). Images were collected of salbutamol particles at low and very high RH but due to a software issue the images were not saved.

## 3.6 Salmeterol xinafoate / Serevent™

### 3.6a Raman spectra and structural information

Salmeterol xinafoate contains several aromatic rings, an ether group, a benzoic acid and a secondary amine. Benzoic acid is distinct from both aromatic rings and carboxylic acids due to the increased conjugation (Kwon, et al., 1994) and shows distinctive peaks in the solid state at  $1627\text{ cm}^{-1}$ ,  $994\text{ cm}^{-1}$  and  $788\text{ cm}^{-1}$ . These peaks are all present in our spectra (figure 8). Ring stretches are clearly visible at  $1580\text{-}1616\text{ cm}^{-1}$ ,  $1400\text{-}1420\text{ cm}^{-1}$  (the multiple strong peaks denoting ring stretches shifted by the various adjacent functional groups) and symmetric ring stretches are visible at  $1000\text{-}1028\text{ cm}^{-1}$ ,  $1215$  and  $1257\text{ cm}^{-1}$ . A strong amine vibration peak is visible at  $1204\text{ cm}^{-1}$ . A sharp peak at  $730\text{ cm}^{-1}$  corresponds to rotational peaks from  $\text{CH}_2$  groups, as would be expected by a molecule with a long aliphatic chain like salmeterol. The ether group can be identified by small peaks at  $554$  and  $1145\text{ cm}^{-1}$ . These spectra correspond well with previously published, well-defined Raman spectra (Ali, et al., 2008a).

Repeated exposure to the Raman laser caused some fluorescence effects in salmeterol xinafoate particles, so each spectrum had to be recorded on a freshly captured particle. The Raman laser was blocked except during the collection of spectra in order to minimise the effect. The fluorescence activity that occurs in salmeterol xinafoate after prolonged exposure to the Raman laser may possibly be avoided in future experiments by using a longer excitation wavelength.

### 3.6b Impact of RH on salmeterol spectra

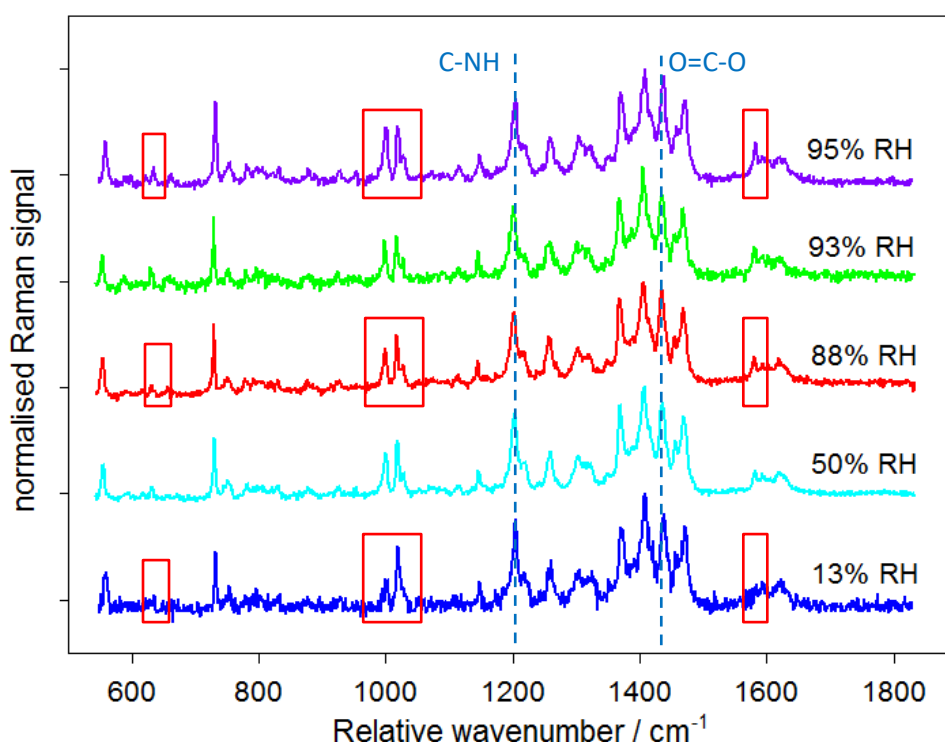


Figure 8 Raman spectra of salmeterol xinafoate at a range of RH values. Even at 95% RH, the amine vibrational peak at  $1204\text{ cm}^{-1}$  and carboxylic acid stretching peak at  $1420\text{ cm}^{-1}$  do not show signs of broadening, contrary to the predicted behaviour modelled by E-AIM. Intensity changes on the aromatic ring stretches at different RH are highlighted in red.

According to the Raman spectra collected in figure 8, salmeterol xinafoate does not demonstrate any visible broadening around peaks corresponding to either salmeterol's amine group or the carboxylic acid group on its xinafoic acid partner upon RH enhancement. This suggests that the salt does not undergo a deliquescent phase transition. The modelling results from E-AIM suggested that salmeterol xinafoate would show significant hygroscopicity if a deliquescence phase transition occurred. The observed lack of deliquescence is in line with the low predicted solubility of salmeterol xinafoate (22.6 mg/L according to ALOGPS (Tetko, 2001)).

The hygroscopic behaviour of salmeterol xinafoate, as predicted by E-AIM, may be limited by the steric hindrance of the hydrophilic sites by hydrophobic structures arranged around them in solid crystals. The relative enhancement of peaks corresponding to aromatic ring stretches at 650, 1000 and 1580  $\text{cm}^{-1}$  imply some interaction with water around some or all of the aromatic rings in salmeterol xinafoate at >88% RH. Most likely, the presence of the hydroxyl and carboxylate groups on the aromatic xinafoate section of the drug enhances water interaction.

### 3.7 Fluticasone propionate / Flixotide

#### 3.7a Raman spectra and structural information

Fluticasone contains several distinctive bonding types that would be expected to yield distinctive peaks in any resulting Raman spectra: a phenone, an ester, a thioether and three C-F bonds across the molecule. Fluticasone has been imaged by Raman spectroscopy previously and its spectra interpreted in depth (Ali, et al., 2008b) (Rogueda, et al., 2011) (Theophilus, et al., 2006) (Wang, et al., 2014), which provides useful references for the spectra generated here.

The raw fluticasone propionate spectra contained a very sharp and strong peak at 640 - 650  $\text{cm}^{-1}$ . This peak was not observed in other spectra in the literature. We believe this peak to be an artefact caused by second harmonic resonance effect from the 1064 nm trapping laser. Confirmation of the spectral artefact was achieved by measuring spectra of fluticasone propionate recorded on the cover slip without the trapping laser present. These spectra did not contain the peak. We have removed this artificial peak from the spectra shown in Figure 9.

The strongest peak in the spectrum of fluticasone is the C=O vibration at 1659 $\text{cm}^{-1}$ , followed by the –CH<sub>3</sub> symmetric stretch (there are 4 –CH<sub>3</sub> groups in Fluticasone) at 1606 $\text{cm}^{-1}$ . –CH<sub>2</sub> and –CH stretches occur at around 1380 and 1330  $\text{cm}^{-1}$  respectively and highly distinctive C-F and S-C-F bands occur at 1234 $\text{cm}^{-1}$  and 1022 $\text{cm}^{-1}$ . Fluticasone is the only compound among the samples that contains a C-F bond, and generated the only spectra showing C-F stretching peaks. This implies that that in all samples the Norflurane propellant had fully evaporated prior to analysis. The phenone group registers as an OOH/CCH aromatic deformation peak at 888 $\text{cm}^{-1}$ . A small C-H wagging peak can be seen at around 700 $\text{cm}^{-1}$ .

### 3.7b Impact of RH on fluticasone spectra

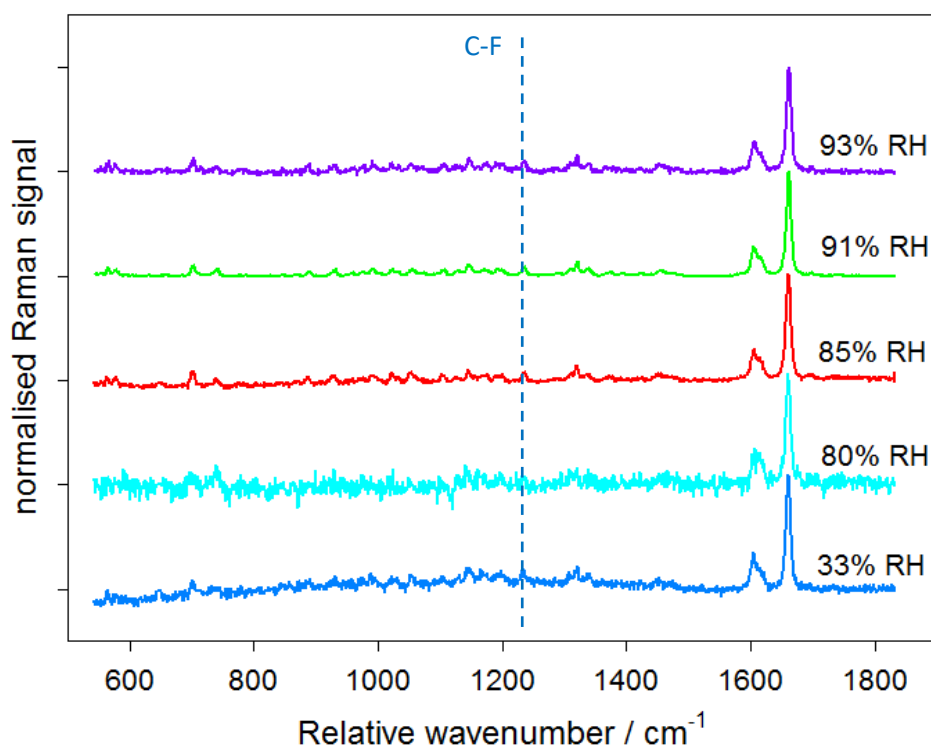


Figure 9 Raman spectra of fluticasone propionate at a range of RH values. The C-F stretching peak at  $888\text{ cm}^{-1}$  is present in this spectrum but not the others, confirming that the Norflurane propellant discussed in section 3.4 has boiled off

The spectrum collected at 80% RH was from a small particle- around  $1\mu\text{m}$  in diameter. This accounts for the greater noise in the signals. Otherwise, no peaks are displaced or strongly deformed by the rise in relative humidity. Fluticasone shows no signs of hygroscopic behaviour, in agreement with the results from E-AIM. Water solubility is low ( $11.4\text{ mg/L}$ ) as predicted by ALOGPS (Tetko, 2001).

## 3.8 Ciclesonide / Alvesco™

### 3.8a Raman spectra and structural information

Ciclesonide (Feth, et al., 2008) has a diverse selection of functional groups, which generates a complicated Raman spectrum. The largest peak at  $1654\text{cm}^{-1}$  (figure 10) represents the stretching vibration of an  $\alpha$ ,  $\beta$ -unsaturated carbonyl, while the adjacent peak at  $1601\text{cm}^{-1}$  shows the neighbouring C=C bond. Ciclesonide contains four  $-\text{CH}_3$  groups and this corresponds to another large, broad peak at  $1443\text{cm}^{-1}$ . The three ether bonds generate another large peak at  $1112\text{cm}^{-1}$ , and the single ester linkage appears at  $1242\text{cm}^{-1}$ . Ciclesonide has a single hydroxyl group attached to a six-membered saturated ring, and a matching “cyclic alcohol” stretch appears at  $1029\text{cm}^{-1}$ . The C-C stretches of the two saturated six-membered rings are found at  $963\text{cm}^{-1}$ . Multiple small peaks around  $800\text{-}900\text{cm}^{-1}$  represent ring deformation in the phenol group adjacent to the saturated rings. Another region of small peaks around  $1330\text{cm}^{-1}$  corresponds to the various symmetric and antisymmetric stretches of the isopropyl group.

### 3.8b Impact of RH and Temperature on Ciclesonide Spectra

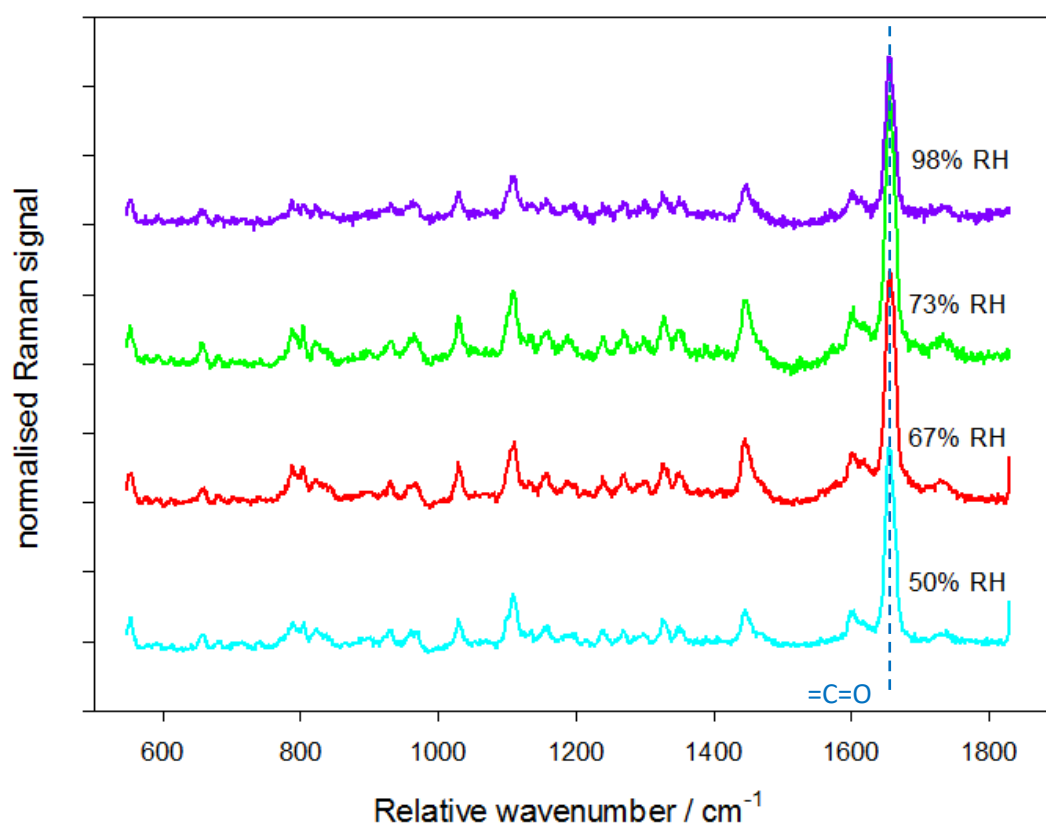


Figure 10 Raman spectra of ciclesonide at a range of RH values. The spectra show no signs of hygroscopic behaviour at up to 98% RH.

As a steroid, ciclesonide is not very hydrophilic and does not contain many polar groups. The crystal structure shows very little opportunity for water uptake on surfaces, and E-AIM predicts that ciclesonide has the lowest hygroscopic potential of any of the drugs analysed. Calculated water solubility is also the lowest of all the drugs (1.57mg/L, (Tetko, 2001)). It would not be expected to show hygroscopic behaviour, and no such behaviour was observed in the Raman spectra compiled in figure 10.

### 3.9 Specific advantages and limitations of procedure to drug delivery

The advantages of this setup and analytical technique to the examination of inhalable drugs do merit some discussion in addition to the general benefits of optical trapping over cover slip analysis documented in section 2.1. The current setup can monitor particle size with an external camera as well as directly monitoring water interactions with hydrophilic functional groups on particles by examining the Raman spectrum. On-board RH monitoring can determine deliquescence points for new drugs, or verify those of existing drugs, to a high degree of accuracy, factoring in the crystal structures of particles as well as their chemical structure in a manner that is difficult to reproduce with software modelling alone.

The main limitation of the technique is the length of time required to collect each Raman spectrum. Since deliquescence occurs faster than the thirty seconds required for the 514nm setup to generate a useful spectrum from a 2  $\mu\text{m}$  particle, the event cannot be monitored in real time with the existing

apparatus. Also, photosensitive compounds like salmeterol xinafoate have to be regularly replaced due to photodegradation of particle surfaces which negates the advantage of being able to observe a specific particle before and after deliquescence. This issue may be avoided by employing a longer wavelength of Raman laser, although this will require either a much more intense source or a longer exposure time to produce viable spectra.

#### 4. Conclusions

This series of experiments has demonstrated a viable technique for examining individual particles of inhalable drugs supplied by pMDIs. With little modification, such as by attaching a vacuum pump to the outlet port of the sample chamber, this experimental setup may also be used to examine single particles from Dry Powder Inhalation devices.

The Raman spectra of four optically trapped drug particles (salbutamol sulfate, salmeterol xinafoate, fluticasone propionate and ciclesonide) were measured within a model lung. The model lung allowed for modification of local RH to test the drugs for hygroscopic behaviour, while the optical trap eliminated any surface effects from water droplets forming around a solid particle on a cover slip. Raman spectroscopy allowed for the direct observation of the hydrogen bonding with water in hydrophilic groups, where the broadening of peaks indicates hygroscopicity.

Spectral peak broadening was observed in salbutamol sulfate particles above their deliquescence point at 92% RH, at room temperature and more physiologically relevant temperatures, while spectra remained similar to dry particles at lower RH regardless of temperature within the observed range. Salmeterol xinafoate shows some spectral changes to the intensities of the peaks corresponding to its aromatic rings, but does not show any changes to the more hydrophilic functional groups which is interpreted as no deliquescence at RH up to 95%. Fluticasone propionate and ciclesonide show no hygroscopic properties at all, as would be expected with their lipophilic composition, low water solubility and the modelled particle growth factors generated using the E-AIM model.

## Works Cited

- Ali, Edwards, Kendrick & Scowen, 2008b. Vibrational spectroscopic study of fluticasone propionate. *Biomolecular Spectroscopy*, pp. 244-247.
- Ali, Edwards, Kendrick & Scowen, 2009. Vibrational spectroscopic study of salbutamol hemisulphate. *Drug Testing and Analysis*, pp. 51-56.
- Ali, et al., 2008a. Vibrational spectroscopic characterisation of salmeterol xinafoate polymorphs and a preliminary investigation of their transformation using simultaneous in situ portable Raman spectroscopy and differential scanning calorimetry. *Analytica Chimica Acta*, pp. 103-112.
- Ashkin, 1992. Forces of a single-beam gradient laser trap on a dielectric sphere in the ray optics regime. *Biophysical Journal*, pp. 569-582.
- Barjoan & Clotet, 2009. Spain, Patent No. EP2127641A1.
- Bell & Newman, 2007. The rejuvenated pressurised metered dose inhaler. *Expert Opinion on Drug Delivery*, pp. 215-234.
- Bikiaris, 2011. Solid dispersions, Part I: recent evolutions and future opportunities in manufacturing methods for dissolution rate enhancement of poorly water-soluble drugs. *Expert Opinion on Drug Delivery*, pp. 1501-1519.
- Bloxham, Eicher-Lorka, J. & Niaura, 2002. The C-S bond in ethylthiols: a study of the characteristic Raman vibrational Spectral Band. *Chemija*, 13(4), pp. 190-193.
- Brain, Kreyling & Godleski, 2014. Inhalation Toxicology. In: Wallace & Kruger, eds. *Hayes' Principles and Methods of Toxicology, Sixth Edition*. Boca Raton, FL: CRC Press, pp. 1402-1414.
- Brodoy & Georgopoulos, 2001. Growth and Deposition of Hygroscopic Particulate Matter in the Human Lungs. *Aerosol Science and Technology*, p. 144-159.
- Bur, Huwer, Muys & Lehr, 2010. Drug Transport Across Pulmonary Epithelial Cell Monolayers: Effects of Particle Size, Apical Liquid Volume, and Deposition Technique. *Journal of Aerosol Medicine and Pulmonary Drug Delivery*, 3(23), pp. 119-127.
- Calverley, et al., 2003. Combined salmeterol and fluticasone in the treatment of chronic obstructive pulmonary disease: a randomised controlled trial. *The Lancet*, pp. 449-456.
- CCDC, 2015. *WebCSD v1.1.1*. [Online]  
Available at: <http://webcsd.cds.rsc.org/index.php>  
[Accessed 10 11 2015].
- Cejka, Kratochvil & Jegorov, 2005. Crystal Structure of Fluticasone Propionate, C<sub>25</sub>H<sub>31</sub>F<sub>3</sub>O<sub>5</sub>S. *Zeitschrift für Kristallographie - New Crystal Structures*, pp. 143-144.
- Chapman, et al., 1999. Salmeterol and fluticasone propionate (50/250 microg) administered via combination Diskus inhaler: as effective as when given via separate Diskus inhalers.. *Canadian Respiratory Journal: Journal of the Canadian Thoracic Society*, pp. 45-51.

- Clark, 1994. Medical Aerosol Inhalers: Past, Present, and Future. *Aerosol Science & Technology*, pp. 374-391.
- Clegg & Brimblecombe, 1998. A thermodynamic model of the system  $H^+ - NH_4^+ - Na^+ - SO_4^{2-} - NO_3^- - Cl^- - H_2O$  at 298.15 K. *The Journal of Physical Chemistry*, 12(102), pp. 2155 - 2171.
- Clegg, Seinfeld & Brimblecombe, 2001. Thermodynamic modelling of aqueous aerosols containing electrolytes and dissolved organic compounds. *Journal of Aerosol Science*, Issue 32, pp. 713-738.
- Coates, 2000. Interpretation of Infrared Spectra, A Practical Approach. In: *Encyclopedia of Analytical Chemistry*. Chichester: John Wiley & Sons Ltd, pp. 10815-10837.
- Cripps, Riebe, Schulze & Woodhouse, 2000. Pharmaceutical transition to non-CFC pressurized metered dose inhalers. *Respiratory Medicine*, 94(2), pp. S3-S9.
- Crosland, Johnson & Matida, 2009. Characterization of the spray velocities from a pressurized metered-dose inhaler. *Journal of Aerosol Medicine and Pulmonary Drug Delivery*, pp. 85-97.
- Delgado, Chou, Silver & Crain, 2003. Nebulizers vs metered-dose inhalers with spacers for bronchodilator therapy to treat wheezing in children aged 2 to 24 months in a pediatric emergency department.. *Archives of Pediatric and Adolescent Medicine*, pp. 76-80.
- Dodson, et al., 2011. Photophysical and photochemical properties of the pharmaceutical compound salbutamol in aqueous solutions. *Chemosphere*, pp. 1513-1523.
- Dolovich, Ruffin, Roberts & Newhouse, 1981. Optimal delivery of aerosols from metered dose inhalers. *Chest*, 80(6), pp. 911-915.
- Engelhart, et al., 2011. Water content of aged aerosol. *Atmospheric Chemistry & Physics*, Issue 11, pp. 911-920.
- Eom, et al., 2014. Influence of collecting substrates on the characterization of hygroscopic properties of inorganic aerosol particles.. *Analytical Chemistry*, 4(86), pp. 2648-2656.
- Ferron, 1977. The size of soluble aerosol particles as a function of the humidity of the air. Application to the human respiratory tract. *Journal of Aerosol Science*, Volume 8, pp. 251-277.
- Feth, et al., 2008. USA, Patent No. US20100120737 A1.
- Feth, et al., 2007. Physicochemical, Crystallographic, Thermal, and Spectroscopic Behavior of Crystalline and X-ray Amorphous Ciclesonide. *Pharmaceutics, Preformulation and Drug Delivery*, pp. 3765-3780.
- Haddrell, et al., 2014. Dynamics of aerosol size during inhalation: Hygroscopic growth of commercial nebulizer formulations. *International Journal of Pharmaceutics*, pp. 50-61.
- Harding, 1990. The human pharmacology of fluticasone propionate. *Respiratory Medicine*, pp. 25-29.
- Hardy & Chadwick, 2000. Sustained Release Drug Delivery to the Lungs. *Clinical Pharmacokinetics*, pp. 1-4.

- Hargreaves, et al., 2010. Measurements of the Equilibrium Size of Supersaturated Aqueous Sodium Chloride Droplets at Low Relative Humidity Using Aerosol Optical Tweezers and an Electrodynamic Balance. *The Journal of Physical Chemistry*, pp. 1806-1815.
- Hirschfeld & Chase, 1986. FT-Raman Spectroscopy: Development and Justification. *Applied Spectroscopy*, 08 January, pp. 133-137.
- Huang, et al., 2003. Near-infrared Raman spectroscopy for optical diagnosis of lung cancer. *International Journal of Cancer*, pp. 1047-1052.
- Hung, Chu, Wang & Yang, 1999. Hypoalkaemia and salbutamol therapy in asthma. *Pediatric Pulmonology*, pp. 27-31.
- Hunt, Ward & King, 2013. Laser heating of sulfuric acid droplets held in air by Raman tweezers. *RSC Advances*, pp. 19448-19454.
- Hunt, Ward & King, 2015. Heterogeneous oxidation of nitrite anion by gas phase ozone in an aqueous droplet levitated by laser tweezers (optical trap): is there any evidence for enhanced surface reaction?. *Physical Chemistry Chemical Physics*, pp. 2734-2741.
- Ibrahim, Verma & Garcia-Contreras, 2015. Inhalation drug delivery devices: technology update. *Medical Devices (Auckland)*, Volume 8, pp. 131-139.
- Icha, 2007. Ventolin remains a breath of fresh air for asthma sufferers, after 40 years. *The Pharmaceutical Journal*, p. 404.
- ICRP, 1994. *Ann. ICRP 24 (1-3) publication 66: Human Respiratory Tract Model for Radiological Protection*, s.l.: Elsevier Health Sciences.
- Janson, et al., 2016. Difference in resistance to humidity between commonly used dry powder inhalers: an in vitro study. *npj Primary Care Respiratory Medicine*, Issue 23, p. 16053.
- Jones, King & Ward, 2015. Atmospherically relevant core-shell aerosol studied using optical trapping and Mie scattering. *Chemical Communications*, pp. 4914-4917.
- Kwon, et al., 1994. Vibrational Spectroscopic Investigation of Benzoic Acid Adsorbed on Silver. *Journal of Physical Chemistry*, pp. 8481-8487.
- Labiris & Dolovich, 2003. Pulmonary drug delivery. Part I: Physiological factors affecting therapeutic effectiveness of aerosolized medications. *Journal of Clinical Pharmacology*, p. 588-599.
- Lavorini, et al., 2011. Retail sales of inhalation devices in European countries: So much for a global policy. *Respiratory Medicine*, pp. 1099-1103.
- Lawrence, 2005. The relationship between relative humidity and the dew point temperature in moist air: A simple conversion and applications. *Bulletin of the American Meteorological Society*, pp. 225-233.
- Leach, 2005. The CFC to HFA Transition and Its Impact on Pulmonary Drug Development. *Respiratory Care*, 50(9), pp. 1201-1208.

- Lee, et al., 2012. The Efficacy of Immediate Diet for Reducing Local Adverse Events of Inhaled Corticosteroid: A Pilot Study. *Tuberculosis and Respiratory Diseases*, pp. 93-99.
- Leger, Goursolle & Gadret, 1978. Structure Cristalline du Sulfate de Salbutamol [tert-Butylamino-2 (Hydroxy-4 hydromethyl-3 phenyl)-1 Ethanol.1/2H<sub>2</sub>SO<sub>4</sub>]. *Acta Crystallographica Section B*, pp. 1203-1208.
- Lide, 1991. *CRC Handbook of Chemistry and Physics*. Boca Raton, FL: CRC Press.
- Ling & Chan, 2008. Partial crystallization and deliquescence of particles containing ammonium sulfate and dicarboxylic acids. *Journal of Geophysical Research*, 113(14), pp. 1-15.
- Lipasek, et al., 2013. Effect of Temperature on the Deliquescence Properties of Food Ingredients and Blends. *Journal of Agricultural and Food Chemistry*, pp. 9241-9250.
- Lipworth & Jackson, 2000. Safety of Inhaled & Intranasal Corticosteroids Lessons for the New Millennium. *Drug Safety*, 1(23), pp. 11-33.
- Macrae, et al., 2006. Mercury: visualization and analysis of crystal structures. *Journal of Applied Crystallography*, Volume 39, pp. 453-457.
- Mansour, et al., 2016. 11.4 Particle deposition in the airways. In: Hillary & Park, eds. *Drug Delivery: Fundamentals and Applications, Second Edition*. Boca Raton, FL: CRC Press.
- Mutch, et al., 2007. The role of esterases in the metabolism of ciclesonide to desisobutyryl-ciclesonide in human tissue. *Biochemical Pharmacology*, pp. 1657-1664.
- Nave, 2004. *Saturated Vapor Pressure, Density for Water*. [Online]  
Available at: <http://hyperphysics.phy-astr.gsu.edu/HBASE/Kinetic/watvap.html#c1>  
[Accessed 6th August 2014].
- Newman, N., 1996. Effect of add-on devices for aerosol drug delivery: Deposition studies and clinical aspects. *Journal of Aerosol Medicine: Deposition, clearance and effects in the lung*, 9(1), pp. 55-70.
- Newman, et al., 1981. Deposition of pressurised aerosols in the human respiratory tract. *Thorax*, Volume 36, pp. 52-55.
- Pandya, Berawala, Khatri & Mehta, 2010. Spectrofluorimetric estimation of salbutamol sulphate in different dosage forms by formation of inclusion complex with  $\beta$ -cyclodextrin. *Pharmaceutical Methods*, pp. 49-53.
- PerkinElmer Inc, 2008. *Advantages of Raman Spectroscopy when Analysing Materials through Glass or Polymer Containers and in Aqueous Solution*. [Online]  
Available at:  
[http://www.perkinelmer.co.uk/CMSResources/Images/APP\\_RamanAnalysisThrougGlassPolymerAqueous.pdf](http://www.perkinelmer.co.uk/CMSResources/Images/APP_RamanAnalysisThrougGlassPolymerAqueous.pdf)  
[Accessed 07 August 2014].
- Phull, Rao & Kankan, 2012. United States of America, Patent No. US 8158780 B2.

- Purewal & Grant, 1997. *Metered Dose Inhaler Technology (Illustrated ed.)*. s.l.:Informa Health Care.
- Reisine, Heisler, Hook & Axelrod, 1983. Activation of beta 2-adrenergic receptors on mouse anterior pituitary tumor cells increases cyclic adenosine 3':5'-monophosphate synthesis and adrenocorticotropin release. *The Journal of Neuroscience*, pp. 725-732.
- Renner, Mueller & Shephard, 2012. Environmental and non-infectious factors in the aetiology of pharyngitis (sore throat). *Inflammation Research*, pp. 1041-1052.
- Rkiouak, et al., 2014. Optical trapping and Raman spectroscopy of solid particles. *Physical Chemistry Chemical Physics*, pp. 11426-11434.
- Rogueda, et al., 2011. Particle synergy and aerosol performance in non-aqueous liquid of two combinations metered dose inhalation formulations: An AFM and Raman investigation. *Journal of Colloid and Interface Science*, pp. 649-655.
- Sanders, 2007. Inhalation therapy: an historical review. *Primary Care Respiratory Journal*, pp. 71-81.
- Sauer, Hofkens & Enderlein, 2011. *Handbook of Fluorescence Spectroscopy and Imaging*. Weinheim: WILEY-VCH Verlag GmbH.
- Stein, M., 2006. The Relative Influence of Atomization and Evaporation on Metered Dose Inhaler Drug Delivery Efficiency. *Aerosol Science and Technology*, Issue 40, pp. 335-347.
- Tang, et al., 2014. Heterogeneous interaction of SiO<sub>2</sub> with N<sub>2</sub>O<sub>5</sub>: single particle optical levitation-Raman spectroscopy and aerosol flow tube studies. *The Journal of Physical Chemistry*, pp. 8817-8827.
- Tetko, 2001. *ALOGPS*. [Online]  
Available at: <http://www.vcclab.org/lab/alogps/>  
[Accessed 21 10 2016].
- Theophilus, et al., 2006. Co-deposition of salmeterol and fluticasone propionate by a combination inhaler. *International Journal of Pharmaceuticals*, pp. 14-22.
- Tong, et al., 2014. Rapid interrogation of the physical and chemical characteristics of salbutamol sulphate aerosol from a pressurised metered-dose inhaler (pMDI). *Chemical Communications*, pp. 15499-15502.
- Tsuda, Henry & Butler, 2013. Particle transport and deposition: basic physics of particle kinetics. *Comprehensive Physiology*, Volume 4, pp. 1437-1471.
- Ullman & Svedmyr, 1988. Salmeterol, a new long acting inhaled beta 2 adrenoceptor agonist: comparison with salbutamol in adult asthmatic patients. *Thorax*, pp. 674-678.
- UNEP, 1987. *The Montreal Protocol on substances that deplete the ozone layer.*, Nairobi: UNEP.
- Vankeirsbilck, et al., 2002. Applications of Raman spectroscopy in pharmaceutical analysis. *TrAC Trends in Analytical Chemistry*, pp. 869-877.

- Walkowsky & He, 2003. *Handbook of aqueous solubility data*. 1st ed. Boca Raton, FL: CRC Press.
- Wang, et al., 2014. Low-frequency shift dispersive Raman spectroscopy for the analysis of respirable dosage forms. *International Journal of Pharmaceutics*, Issue 469, pp. 197-205.
- Wittig, Lohmann & Gmehling, 2003. Vapor–Liquid Equilibria by UNIFAC Group Contribution. 6. Revision and Extension. *Industrial & Engineering Chemical Research*, 42(1), pp. 183 - 188.
- Woolcock, Lundback, Ringdal & Jacques, 1996. Comparison of addition of salmeterol to inhaled steroids with doubling of the dose of inhaled steroids.. *American Journal of Respiratory and Critical Care Medicine*, pp. 1481-1488.
- York & Hanna, 1994. United States of America, Patent No. US5795594 A.
- Zhejiang NetSun Co., Ltd., 2010. *ChemNet.com - Global Chemical Network*. [Online] Available at: <http://www.chemnet.com/cas/> [Accessed 21 09 2015].

## Overall Summary

The preceding work has demonstrated the viability of a series of modern analytical techniques, alongside more established procedures, applied to increasing the collective understanding of the chemistry of aerosol particles in different controlled atmospheric conditions.

XANES was found to be a reliable semi-quantitative technique for estimating the Fe solubility of mineral aerosol samples based on best fits of the observed speciation, with some reservations. As with any analytical technique the quality of the fit is dependent on the quality of the range of standards. Selecting standards appropriate to the Fe species most likely to be present in samples is essential and thus prior knowledge of the sample geology through chemical extraction and/or XRD is advantageous to any attempt at analysis. Furthermore, a solid understanding of the beamline environment is crucial to predicting the complications that can arise from placing samples and standards in such a place. The dehydration of hydrated chloride salts and presently unexplained changes in standard spectra, seen in chapter 2, stand as prime examples of said complications.

Additionally, iron oxalate was considered for use as a standard for determining the effects of natural atmospheric organic ligands on dust and haze samples, but the energy of the beamline caused the standard to break down before useful readings could be taken and thus the standard was not included in the set.

Directly collected particulate ship emissions were analysed by XANES for the first time and were found to be similar to oil fly ash from power stations, containing highly soluble ferric sulfate as a major component of total Fe, although the proportion was seen to vary with fuel and engine type. The results demonstrate the merits of further investigation, particularly due to the role of ship emissions in global Fe distribution for atmosphere/ocean models.

The analysis of particulate samples from biomass burning indicate that the majority of Fe mobilised by large scale natural and agricultural combustion is present in the form of <60 µm sized mineral dust particles carried into the air by the more vigorous Brownian motion caused by the heat. While this provides a possible explanation for the wide variation in Fe solubility found in biomass ash in the literature, the low relative concentration of Fe in the ash itself meant that determining speciation was not feasible with the available samples.

The analysis of diesel emissions, meanwhile, appeared to indicate the presence of significant quantities of copper chloride among the particulates released by a model Euro-5 engine. XANES analysis implies that chlorinated organic molecules represent the majority of chlorine in the samples, but this cannot be stated for certain due to the aforementioned impacts of beamline conditions on the standards and therefore also the samples. The presence of chlorinated organics has implications for human health, but the copper chloride that is most likely released by copper-based oxidation catalyst regeneration cycles is of wider concern to the chemistry of the troposphere. Further sampling and analysis of newer Euro-6 engines for the same particulate emissions is highly recommended.

Analysis of the solubility of various elements (including Fe) in coal fly ash, and the response of Fe in ashes from three different power stations to simulated atmospheric processing, presented new information on speciation and the influence of other elements thereon. While the XANES fitting of all three ash types showed that ferrihydrite is the dominant Fe species, the relatively low solubility of

samples is indicative of heavy Al-substitution in the ferrihydrite crystal structure, and the rate of Al substitution appears to directly affect solubility. The high reported ferric sulfate content in most of the spectra are not reflected in solubility studies, casting doubt on the accuracy of the fittings and demonstrating the need for an expanded range of appropriate standards.

Simulated atmospheric processing was only seen to increase Fe solubility significantly in one of the three ash types, apparently in response to limited buffering capacity in that particular sample from low Ca content. Further processing experimentation with more representative timeframes and oxidising gas concentrations has the potential to yield more detailed information.

The remaining work was focussed on the influence of changes in relative humidity on the behaviour of suspended organic particulates. FLIM imaging of solutions of Green Fluorescent Protein (GFP) allowed the observation of changes in fluorescence lifetime caused by changes to the concentration of the surrounding solution, brought about by adjusting the relative humidity of the air around the trapped droplet. Repeated observations allowed a trendline to be constructed along with literature values to predict the refractive index of GFP in isolation, which has the potential to become a useful reference for researchers planning to use GFP as an aerosol probe or in high refractive index media.

Concern about the substantial rise in relative humidity and temperature surrounding inhalable pharmaceuticals as they travel from the outside air into the lungs of patients prompted the research presented in chapter 5. Monitoring hygroscopicity by observing changes in the Raman spectra of the hydrophilic functional groups of four asthma drugs was found to be effective, although the time required to develop a spectrum means that the timescales involved are not directly applicable to modelling the conditions of pharmaceutical application.

Salbutamol sulfate was seen to have hygroscopic properties, but SEM observation of particle size and modelling of hygroscopic growth implies that the drug particles would still be in the optimal size range to be rapidly absorbed in the lungs after gathering a water layer from the warm, wet air inside the respiratory system. Salmeterol xinafoate was not found to have hygroscopic properties despite its large number of hydrophilic sites due to the orientation of those sites in the crystal structure. The two steroid aerosols, ciclesonide and fluticasone propionate, were not expected to exhibit hygroscopic behaviour even at close to 100% relative humidity, and this expectation was borne out by the observations.

## Appendix

The following work was published in the **International Journal of Pharmaceutics**, 30 March 2017, volume 520 issues 1-2, pages 59-69

### **Measurement of the Raman spectra and hygroscopicity of four pharmaceutical aerosols as they travel from pressurised metered dose inhalers (pMDI) to a model lung**

N. Davidson<sup>a</sup>, H. -J. Tong<sup>b</sup>, M. Kalberer<sup>b</sup>, P. C. Seville<sup>c,d</sup>, A. D. Ward<sup>e</sup>, M. K. Kuimova<sup>f</sup> and F. D. Pope<sup>a\*</sup>

<sup>a</sup>School of Geography, Earth and Environmental Sciences, University of Birmingham, Edgbaston, Birmingham, B15 2TT, UK.

<sup>b</sup>Department of Chemistry, University of Cambridge, Lensfield Road, Cambridge, CB2 1EW, UK.

<sup>c</sup>School of Pharmacy, University of Birmingham, Edgbaston, Birmingham, B15 2TT, UK.

<sup>d</sup>School of Pharmacy and Biomedical Sciences, University of Central Lancashire, Preston, Lancs, PR1 2HE, UK.

<sup>e</sup>Central Laser Facility, Rutherford Appleton Laboratory, Harwell, Oxford, OX11 0QX, UK.

<sup>f</sup>Imperial College London, South Kensington Campus, London, SW7 2AZ, UK

## Abstract

Particle inhalation is an effective and rapid delivery method for a variety of pharmaceuticals, particularly bronchodilation drugs used for treating asthma and COPD. Conditions of relative humidity and temperature inside the lungs are generally very different from the outside ambient air, with the lung typically being warmer and more humid. Changes in humidity, from inhaler to lung, can cause hygroscopic phase transitions and particle growth. Increasing particle size and mass can negatively affect particle deposition within the lung leading to inefficient treatment, while deliquescence prior to impaction is liable to accelerate drug uptake. To better understand the hygroscopic properties of four pharmaceutical aerosol particles; pharmaceutical particles from four commercially available pressurised metered dose inhalers (pMDIs) were stably captured in an optical trap, and their composition was examined online via Raman spectroscopy. Micron-sized particles of salbutamol sulfate, salmeterol xinafoate, fluticasone propionate and ciclesonide were levitated and examined over a range of relative humidity values inside a chamber designed to be capable of mimicking conditions within the respiratory tract. The effect of temperature upon hygroscopicity was also investigated for salbutamol sulfate particles. Salbutamol sulfate was found to have significant hygroscopicity, salmeterol xinafoate showed some hygroscopic interactions, whilst fluticasone propionate and ciclesonide revealed no observable hygroscopicity. Thermodynamic and structural modelling is used to explain the observed experimental results.

## 1. Introduction

### 1.1 Respiratory drugs and drug delivery

Respiratory ailments in the form of asthma and Chronic Obstructive Pulmonary Disease (COPD) are often managed with inhalable drugs. These drugs include beta-2 agonists such as salbutamol and salmeterol, and corticosteroids like fluticasone and ciclesonide.

Salbutamol sulfate and salmeterol xinafoate are both *beta-2 adrenoceptor agonists*, meaning that they target the beta-2 receptors in bronchial muscle cells in a similar manner to adrenaline (Reisine, et al., 1983), forcing calcium out of the cells thus forcing them to relax, and opening the user's airways to allow easier breathing. Salbutamol (Ventalin™, Salamol™) has been a popular treatment for asthma and COPD since 1968 (Icha, 2007), while Salmeterol (Serevent™) was introduced in 1988 as a longer lasting alternative (Ullman & Svedmyr, 1988).

Fluticasone propionate (Flixotide™) is an artificial corticosteroid that assists breathing by reducing inflammation in the lung lining (Harding, 1990). Whilst steroids are useful in managing respiratory conditions, deposition of the drug in the oropharynx suppresses the local immune system, and patients often suffer from mouth and throat infections such as oral candidiasis as a result (Lee, et al., 2012), (Renner, et al., 2012). Fluticasone propionate is also supplied as a combination inhaler with salmeterol xinafoate (Seretide™) due to their complementary modes of action (Woolcock, et al., 1996) (Chapman, et al., 1999) (Calverley, et al., 2003). Pure compounds rather than mixtures were investigated in this study.

Ciclesonide (Alvesco™) is a recently developed inhaled corticosteroid used as a treatment for asthma, hay fever and other respiratory ailments. In order to reduce the mouth and throat infections associated with respiratory steroid application, ciclesonide is designed to be biologically inactive until it interacts with esterase enzymes present in the lung (Mutch, et al., 2007) at which point it is hydrolysed to the active form desisobutyryl-ciclesonide; these enzymes are not found in the oral cavity to the same extent, and hence the potential benefit of reduced oropharyngeal side effects.

Inhalable drugs are predominately administered by nebuliser, dry powder inhaler (DPI) or by pressurised metered dose inhaler (pMDI). Powdered nebulisers have been in use since the 19<sup>th</sup> century (Sanders, 2007), while cheaper and more portable pMDIs were invented in 1955 (Purewal & Grant, 1997). The pMDI is now the most popular device for delivering drugs to the human respiratory system in Great Britain and elsewhere (Lavorini, et al., 2011).

Modern pMDIs contain solid drug particles which are suspended in a liquefied hydrofluoroalkane propellant: most commonly HFA-134a (Cripps, et al., 2000) (Leach, 2005). Other co-solvents such as ethanol or oleic acid can be used depending on the drug (Bell & Newman, 2007). The solvent evaporates within a few milliseconds at ambient temperature upon activation of the pMDI (Stein, 2006), generating a fixed dose, inhalable aerosol of micron-sized solid drug particles travelling at a wide range of planar velocities into the user's trachea and lungs (Crosland, et al., 2009).

## **1.2 Significance of relative humidity and temperature on delivery efficiency**

Drugs acting within the respiratory tract are only effective if the particle aerodynamic diameters are in the 1-5 $\mu$ m range since larger particles cannot reach the receptor sites inside the lungs (Labiris & Dolovich, 2003). Hygroscopic particles can increase in size and mass as they collect water from the air (Broday & Georgopoulos, 2001) which means that particles manufactured in the appropriate range when dry may swell to larger than optimal size and higher than optimal mass by the time they pass through the moist air inside the trachea and towards the lungs. While larger particles are less likely to navigate to the regions where they can be absorbed most rapidly, more massive particles have greater momentum, are more likely to impact the back of the throat than pass into the lungs (Mansour, et al., 2016) and their direction of travel is less influenced by the Brownian diffusion processes that would drive them to their intended destination (Tsuda, et al., 2013).

Previous work has shown (Tong, et al., 2014) that salbutamol sulfate deliquesces at around 92% relative humidity (RH). Deliquescence describes the phase change of a crystalline solid to a saturated solution droplet using water collected from the surrounding air. Temperature can affect the RH level required to bring about deliquescence in hygroscopic substances but the effect varies between compounds (Lipasek, et al., 2013). Temperature also has a significant influence over the saturation vapour pressure of air (Lawrence, 2005) so the air inside the lungs at 37°C and near-100% RH contains three times the concentration of water as outside air at similar RH and 20°C (Nave, 2004). However, temperature influences the kinetics of drug dissolution only, rather than the thermodynamic behaviour of solid particles, which remain relatively unchanged, and it is not expected to significantly impact hygroscopic properties.

The rate of deliquescence dictates the rate of adsorption of drugs across lung epithelia, since a given drug cannot be absorbed until it has fully dissolved (Bikiaris, 2011). This lends a time-critical aspect to drug delivery since solid particles in the lungs are removed over time by ejection via the mucociliary

escalator in the ciliated regions of the lungs or partition into macrophages in the alveoli (Hardy & Chadwick, 2000) and dissolution appears to be the rate-limiting step for the uptake of inhalable drugs (Bur, et al., 2010). If more of a given drug is removed in these manners before it is fully dissolved, a greater dose must be administered and the resultant side effects such as immunosuppression with corticosteroids (Lee, et al., 2012) and hypoalkaemia with salbutamol (Hung, et al., 1999) will have greater impacts on patient health.

On the other hand, as mentioned in the previous section rapid deliquescence can lead to an increase in particle size that makes it more difficult for drugs to reach deep into the airways. Finding optimal values for both particle size and hygroscopicity is important for providing patients with the most efficiently delivered treatment with the least side effects, and is the primary motivation for this series of experiments. Additionally, a better understanding of the hygroscopic properties of drug molecules should inform which drugs are likely to be pre-wetted by the wicking effect of water uptake upon inhalation, thus kick starting the dissolution of drug particles upon impaction onto higher respiratory tract surfaces like the epithelium (Brain, et al., 2014).

Investigations are ongoing into the hygroscopic behaviour of drug aerosols delivered by nebuliser e.g. (Haddrell, et al., 2014). However, the popularity of pMDI delivery for bronchodilation medication and the logistical difficulties involved in modelling the pharmacokinetic behaviour of medication inside the lung of a living creature mean that similar studies on pMDI-delivered drugs are justified. DPI formulations have been shown to be vulnerable to high humidity conditions (Janson, et al., 2016) and the lower particle velocity of DPI inhalations compared to pMDI (Ibrahim, et al., 2015) also implies that high humidity conditions are a concern primarily for DPI devices. However, the sudden change in humidity surrounding drug particles from both types of device upon inhalation mean that changes to particles from pMDIs also merit attention.

It is worth noting that the lung deposition rate of pMDI-delivered material is normally less than 10% (Newman, et al., 1981) and with optimised inhalation technique and additional equipment such as spacers (Dolovich, et al., 1981) (Newman, 1996) maximum possible deposition appears to be around 25% of the total inhaled dose. Since larger particles are more likely to impact or be excluded by the processes discussed above, concern over hygroscopic particle growth is justified.

This series of experiments investigates the use of an optical trap to stably levitate drug aerosols released by popular pMDI devices and Raman spectroscopy to monitor signs of hygroscopic particle growth upon rapid increase in RH. The set up allows for the control of temperature and RH to more closely mimic the conditions inside the human lung than conventional cover slip analysis.

## **2. Methods and Materials**

The combination of optical trap, Raman spectroscopy and model lung was first described in Tong et al 2014 (Tong, et al., 2014). The optical trap uses a counter propagating dual beam (CPDB) trap configuration first described by Rkiouak et al. (Rkiouak, et al., 2014) and deployed in several subsequent experiments (Tang, et al., 2014) (Jones, et al., 2015) (Hunt, et al., 2015). This trapping setup is remarkable because it is capable of stably trapping micron-sized solid particles of non-spherical geometry for periods of time up to several hours.

## 2.1 Counter propagating dual beam optical trap

The trapping beams were generated by a 1064 nm Nd:Yag laser (Ventus, Laser Quantum) passed through a beam splitter (Oz optics) and fibre-coupled into two single-mode fibres. Each fibre output was delivered to beam expansion and collimation optics before entering the objective lenses. The laser power at output was 15 mW from the top objective lens and 10 mW through the bottom objective lens (figure 2). The asymmetry in power ensured that trapped particles were driven closer to the optical focus plane of the bottom objective through which the Raman laser is passed, ensuring better focus on the resulting images (Rkiouak, et al., 2014). The foci of the lasers were positioned  $\sim 10$   $\mu\text{m}$  apart, which created a trapping volume large enough to stably hold 1-5 $\mu\text{m}$  particles for long periods. Once all useful observations had been collected from a trapped particle, the particle was allowed to fall under gravity to the cover slip by blocking the 1064 nm trapping beams.

There are several reasons to prefer an optical trap to cover slip analysis. The most significant is that pharmaceutical aerosols are, until they reach the respiratory tract, suspended particles and attempts to recreate their conditions should be as close as possible. Interactions between collecting substrates and water can measurably alter the deliquescence point of hygroscopic particles (Eom, et al., 2014) with surfaces like glass reducing the deliquescence point of sodium chloride by 1.5% compared to a suspended particle. Previous work in our group has also observed changes in particle efflorescence upon a cover slip compared to optical trap. Any particle landing on a cover slip will have part of its surface in contact with the cover slip rather than exposed to the surrounding air (see figure 1), so a hygroscopic particle will form a water layer beginning with a halo around the contact point with the cover slip rather than across the surface dictated by the particle's geometry and density of hygroscopic sites. The shape of the resulting droplet and rate of adsorption will both be affected by the presence of a cover slip.

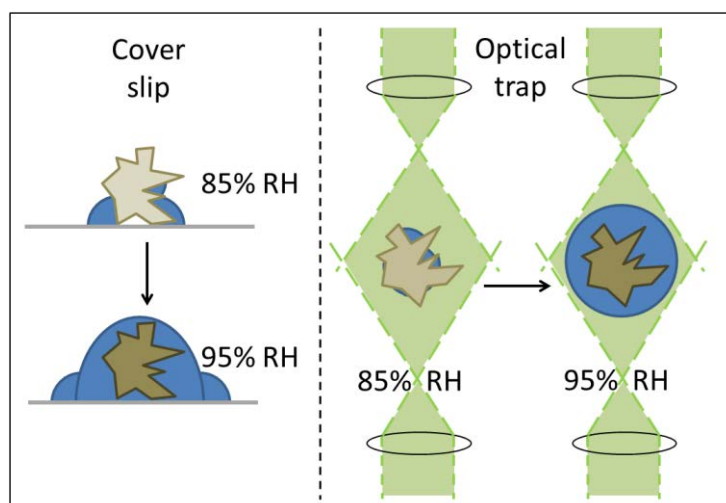


Figure 22. An illustration of the influence of coverslips on the formation of water layers on hygroscopic particles. Optical trapping allows particles to remain suspended as they deliquesce in a manner more representative of particles *in vivo*.

This is especially important in time-critical experiments such as those reported in this paper. Optical trapping represents the best current option for making detailed observations of physical and chemical changes on suspended particles in varying conditions, and yields better resolved Raman spectra than particles observed on a cover slip due to the removal of interfering spectral features associated with

the composition of the cover slip. Optical trapping is typically superior for single particle spectroscopy when compared to other single particle levitation techniques, such as electrodynamic balances or acoustic trapping, because the optical setup ensures good alignment between the studied particle and spectroscopic probe (Hargreaves, et al., 2010).

Optical trapping is easiest with spherical or spheroidal particles and droplets due to their symmetry (Ashkin, 1992). While the setup used in this work has demonstrated the capacity to trap non-spherical particles for periods of an hour or longer (Rkiouak, et al., 2014) (Tong, et al., 2014), particles that are closer to spheres are still easier to trap for the same reasons.

## **2.2 Raman Spectroscopy**

Raman spectroscopy is a powerful technique for examining the functional groups and intermolecular interactions of substances, requiring very small sample masses and no sample preparation (Hirschfeld & Chase, 1986) (Vankeirsbilck, et al., 2002) and making it ideal for the analysis of micrometer-scale drug particles. Raman spectroscopy has much lower signal-to-noise ratio than competing infrared analysis techniques because of the visible range detection region, and because the scattering wavelengths are separate from those of the excitation laser, so the technique can be effective with very small samples whose absorption would be indistinguishable against a standard FT-IR beam (PerkinElmer Inc, 2008). These experiments use a Raman setup which collects back-scattered photons along the same path as the excitation laser, but filtering the excitation photons with a Razoredge dichroic mirror and longpass edge filter combination (SemRock).

Raman scattering was generated using a 514.5nm Ar-ion laser (Innova 300C, Coherent), with a power of 4.3mW measured at the laser focus. Each Raman spectrum was generated by a 30 second exposure to the 514.5nm laser. This is longer than the residence time of particles in the respiratory system but is necessary to generate usable and reproducible spectra. These wavelength and power settings were selected based on previous experiments (Hunt, et al., 2013) as they were found to cause minimal heating of samples over long periods of exposure. Raman scattered light was collected in the region of 540-1830  $\text{cm}^{-1}$ .

Wavelength calibration of the Raman spectrometer was carried out using a cover slip with raised sides containing pure liquid toluene. The spectrum is collected from a focal point within the bulk liquid, away from the surface of the cover slip to avoid interference. The position of spectral peaks for toluene is well characterized and these are used as a reference for wavelength calibration.

## 2.3 Artificial Lung Chamber & Particle Imaging

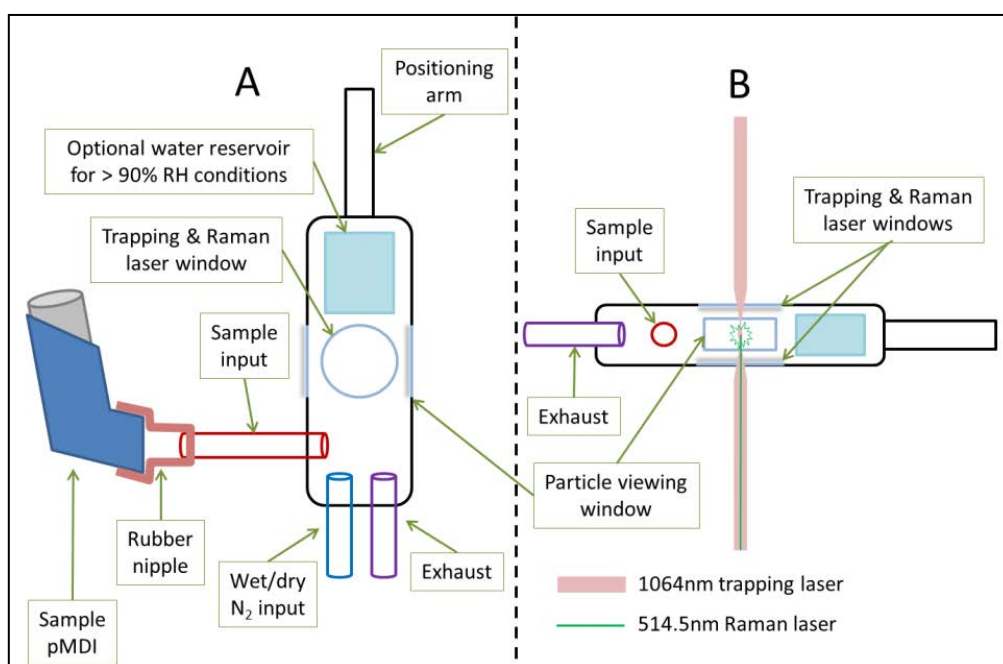


Figure 23 Top-down (A) and side (B) views of the artificial lung chamber (High RH conditions here defined as >93% @ 20°C)

The artificial lung (figure 2) was an aluminium chamber of internal dimensions approximately 10 x 2 x 1cm, with borosilicate cover slip windows at the top and bottom to admit laser light and also at the sides to observe particles using a Mitutoyo M Plan Apo 20x objective lens connected to a CCD camera (Princeton Instruments, Spec10), opposite an LED source (Comar Optics). A monitor attached to the CCD camera allowed users to observe particles passing around, through and into the optical trap.

RH and temperature were monitored using a Sensirion SHT-75 RH probe with a manufacturer-stated accuracy of  $\pm 1.8\%$  RH and  $\pm 0.3^\circ\text{C}$ . Raman spectra were collected within 3 minutes of reaching the desired RH. This is significantly longer than the 10 seconds recommended by the medical community for inhalation, holding an exhalation of a pMDI dose but is necessary for adjusting RH accurately and for developing clear and reproducible spectra. RH levels were altered using N<sub>2</sub> gas sourced from boiled off liquid nitrogen, using a flow rate of  $\sim 200\text{ cm}^3/\text{min}$  through a Bronkhorst MV-301 mass flow controller. A lower flow rate of  $100\text{ cm}^3/\text{min}$  was used for RH adjustment of the Salmeterol particles, since higher flow rates tended to dislodge the particles from the trap for reasons discussed in section 3.3. The input and exhaust ports were located on the same face of the cell in order to generate slow flow conditions around trapped particles and thus minimise turbulence that might dislodge the particle.

The gas was either run into the cell directly (low RH) or passed through a bubbler containing milli-Q grade deionized water before entering the cell (high RH). For very high RH conditions, a water reservoir was added inside the chamber. While the bubbler could provide RH up to  $\sim 90\%$ , the reservoir could generate RH as high as 93% at 30°C and up to 98% at 20°C.

Salmeterol xinafoate, fluticasone propionate and ciclesonide were analysed at ambient temperature at high and low RH. Salbutamol sulfate was analysed both at ambient temperature and at more

physiologically relevant temperatures by incubation of the microscope environment using Solent Scientific incubator components.

## **2.4 pMDI injection**

To dispense the aerosolised drug into the artificial lung chamber, a simple connector was built for the pMDI outlet involving a flexible rubber cap with a rigid 6mm (internal diameter) PTFE tube protruding through it. The tube was connected to a similar tube on the side of the artificial lung by a short length of flexible silicone tubing. The chamber was washed sequentially in deionized water and methanol to minimise potential cross-contamination with other drugs.

The propellant flow within the sample chamber carried material from each pMDI discharge into the path of the trapping beam. Drug particles passing across the side viewing window were illuminated by an LED and observed on a monitor. Scattering of the unfiltered trapping laser from a trapped particle was viewed on the same monitor to indicate the positional stability of the particle.

Based on the stated mass per release of each drug, the density of the solid material (Zhejiang NetSun Co., Ltd., 2010), the assumption that an average particle is solid and has a volume of approximately  $10 \mu\text{m}^3$ , a single release from each inhaler is estimated to deliver approximately  $10^6$  to  $10^7$  particles to the chamber. However, many of these particles are lost by impaction onto the walls of the chamber. A single trapped particle, which is at least  $2\mu\text{m}$  in diameter, has sufficient material to generate a Raman spectrum.

## **2.5 SEM imaging**

Each drug was actuated onto a glass cover slip and coated with 10nm gold particles in a Polaron SC7640 sputter coater. The cover slips were attached to Agar Scientific 25mm double sided sticky carbon tabs prior to imaging on a Philips XL30 ESEM FEG.

## 2.6 Chemical Structures of the asthma drugs investigated

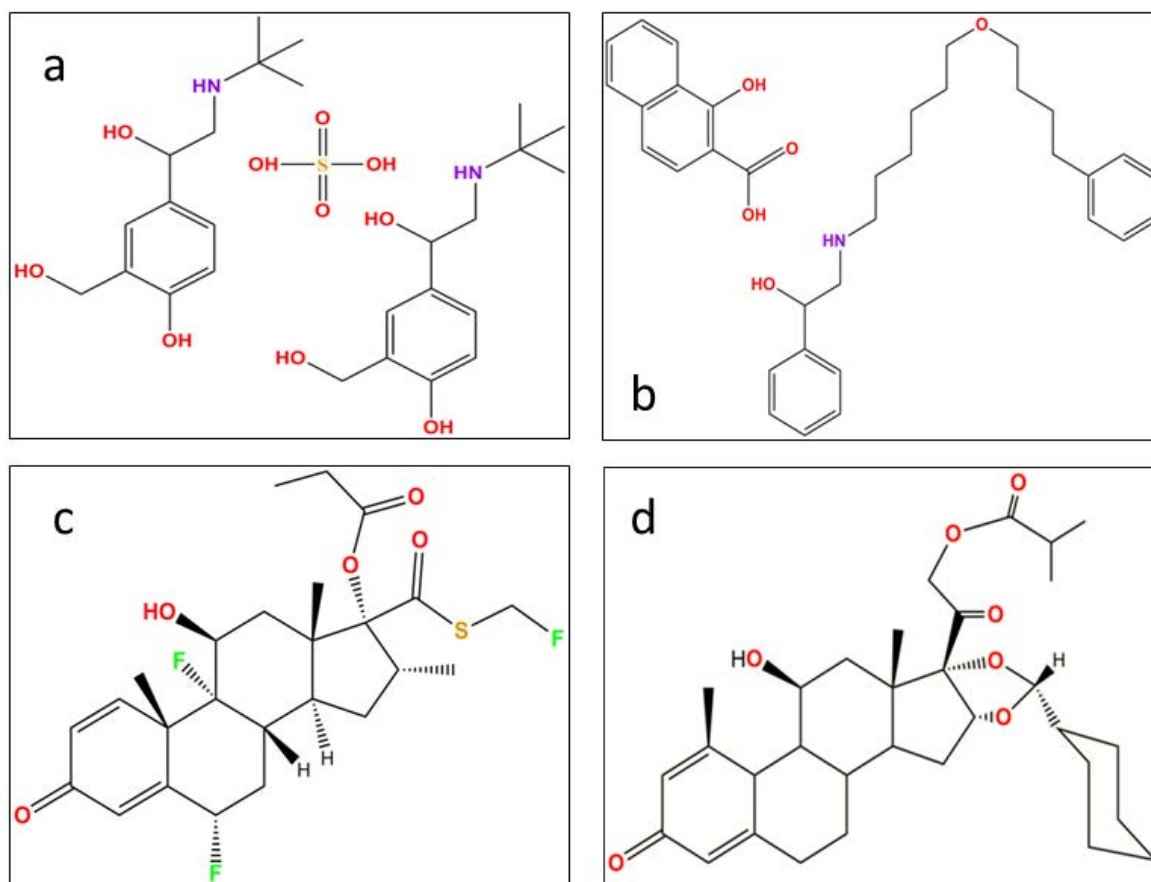


Figure 24 Chemical structures of single molecules of salbutamol sulfate (a), salmeterol xinafoate (b), fluticasone propionate (c), and ciclesonide (d)

Salbutamol sulfate particles were generated from a Salamol brand inhaler by Ivax Chemicals Ltd. Salbutamol sulfate contains several polar groups and no long aliphatic chains, and its hygroscopic character has been documented (Tong, et al., 2014). Salmeterol xinafoate particles were produced from a “Serevent” brand inhaler produced by Cipla Ltd. Salmeterol also contains multiple polar groups but also a long aliphatic chain. Its hygroscopic properties are to be determined.

Fluticasone propionate, generated from a “flixotide” brand inhaler, is manufactured by GlaxoSmithKline, and ciclesonide particles were generated by a “Ciclohale” brand inhaler also by Cipla Ltd. Ciclesonide is produced under license from Takeda UK Ltd. Fluticasone propionate and ciclesonide are both steroids and as such are relatively hydrophobic and are not expected to show hygroscopic properties.

### 3. Results and Discussion

#### 3.1 Thermodynamic Calculations of Particle Hygroscopicity

Thermodynamic calculations of aerosol particle hygroscopicity were carried out using the Extended Aerosol Inorganics Model (E-AIM) (Clegg, et al., 2001) (Engelhart, et al., 2011) (Ling & Chan, 2008). E-AIM is a thermodynamic model for predicting the water content of aerosol particles at different relative humidities. The model is appropriate for calculating the thermodynamic state of the drug aerosol for a given RH, however, the model does not take into account the time dependent kinetic limitations of water uptake to the particle within the respiratory tract. Within E-AIM, model III is used and the UNIFAC model is chosen to calculate the water activities of the organic fraction of the investigated drugs within the particle at different RH. The UNIFAC model parameterizes the molecular composition of the organic fractions of the investigated drug particle using a combination of structural and functional groups (Wittig, et al., 2003). The calculation of water activities of the sulfate group within salbutamol sulfate is also described by Clegg (Clegg & Brimblecombe, 1998). The type and quantity of UNIFAC parameters chosen to represent the four investigated drugs are provided in Table 1. It is noted in some cases exact matches for molecular composition, using UNIFAC, of the investigated drugs are not possible and in such cases the closest match was used. Standard dissociation constants for the carboxylic acid and amine functional groups were used. The model assumes that both salbutamol sulfate and salmeterol xinafoate dissociate into their respective ions dependent upon their dissociation constants. The formation of solid salts (salbutamol sulfate and salmeterol xinafoate) is disallowed since the activity products of the salts are unknown. Hence the modelled hygroscopicity provides an upper limit estimate.

The output from E-AIM allows for the prediction of the drug molecule hygroscopicity (Clegg, et al., 2001) (Engelhart, et al., 2011) (Ling & Chan, 2008). Figure 4 shows the mass growth factors for the four investigated drugs. Mass growth factor is defined as the mass increase, for a given RH, normalized to the dry mass. It can be seen that Figure 4 predicts two distinct types of interaction. The beta-2 agonists (salbutamol sulfate and salmeterol xinafoate) contain a higher proportion of hydrophilic groups and are thus predicted to be strongly hygroscopic, while the more lipophilic steroids (ciclesonide and fluticasone propionate) are expected to collect little water from the air even under near water saturated conditions. It is noted, that the bulk thermodynamic calculations in E-AIM do not take into account the crystal structure of solid particles which may block access to hydrophilic sites and prevent otherwise hydrophilic molecules from interacting with water in the air. Furthermore, the model runs do not take into account possible deliquescent barriers to water uptake due to the lack of product activity data.

Table 9 UNIFAC parameters used for thermodynamic modelling of the four investigated drugs. Note that the salmeterol xinafoate is modelled as two separate molecules: salmeterol and xinafoate. Also note that the sulphate in salbutamol sulphate is not modelled using UNIFAC hence its omission from the table.

UNIFAC Group	Salmeterol	Xinafoate	Salbutamol	Fluticasone propionate	Ciclesonide
Alkane (CH <sub>3</sub> )	-	-	3	4	3
Alkane (CH <sub>2</sub> )	10	-	1	1	9
Alkane (CH)	1	-	1	4	6
Alkene (CH=CH)	-	-	-	1	1
Alkene (CH=C)	-	-	-	1	1
Aromatic carbon (ACH)	8	6	3	-	-
Aromatic carbon (AC)	4	4	3	-	-
Alcohol (OH)	3	1	3	1	1
Carboxylic acid (COOH)	-	1	-	-	-
Carbonyl (CH <sub>2</sub> CO)	-	-	-	2	2
Ether (CH <sub>2</sub> O)	1	-	-	-	-
Ether (CHO)	-	-	-	-	2
Secondary amine (CH <sub>2</sub> NH)	1	-	1	-	-
Acetate (CH <sub>2</sub> COO)	-	-	-	1	1
Fluoroalkane (CF)	-	-	-	3	-

Ferron's kinetic model (Ferron, 1977), as used in the International Commission on Radiological Protection (ICRP, 1994) provides a parameterization with which to estimate of the time dependent growth of hygroscopic particles. pMDI particles are typically generated in the size range 2 – 5 µm to optimally deliver drugs to the central regions of the lung. The Ferron model suggests that a hygroscopic particle of initial size of 2–5 µm diameter will reach approximately 80–50% of its equilibrium size, respectively, within a typical 2–3 s long inhalation.

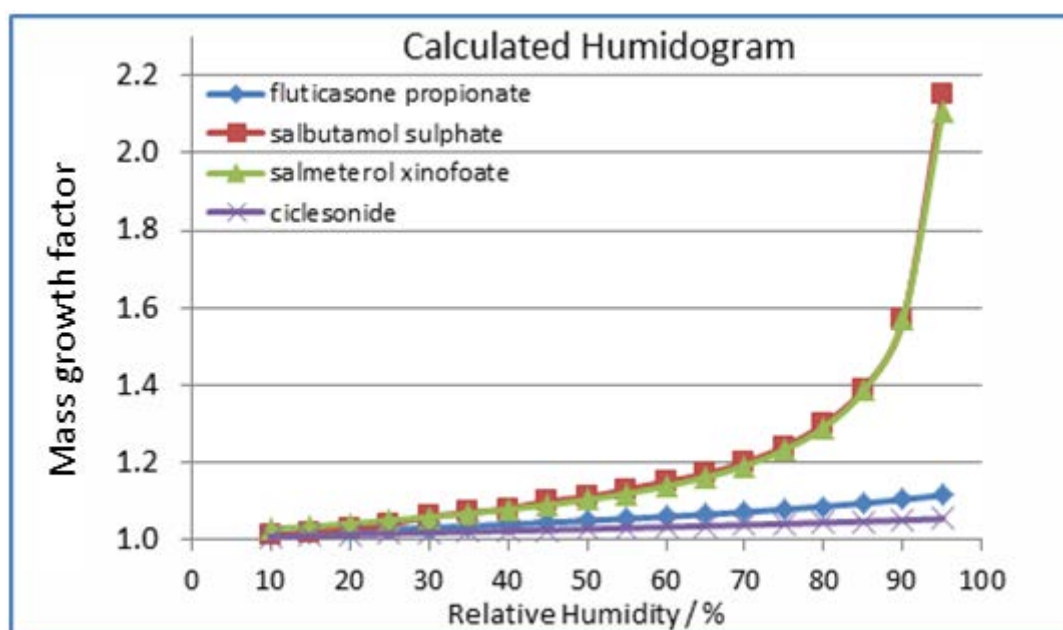


Figure 25 Influence of relative humidity on particle diameter predicted from chemical bonding

### 3.2 Drug Particle Crystallography

The Mercury 3.6 program (Macrae, et al., 2006) was used to simulate the crystal structure of all drugs whose structures had been added to the Cambridge Structural Database run by the Cambridge Crystallographic Data Centre (CCDC, 2015).

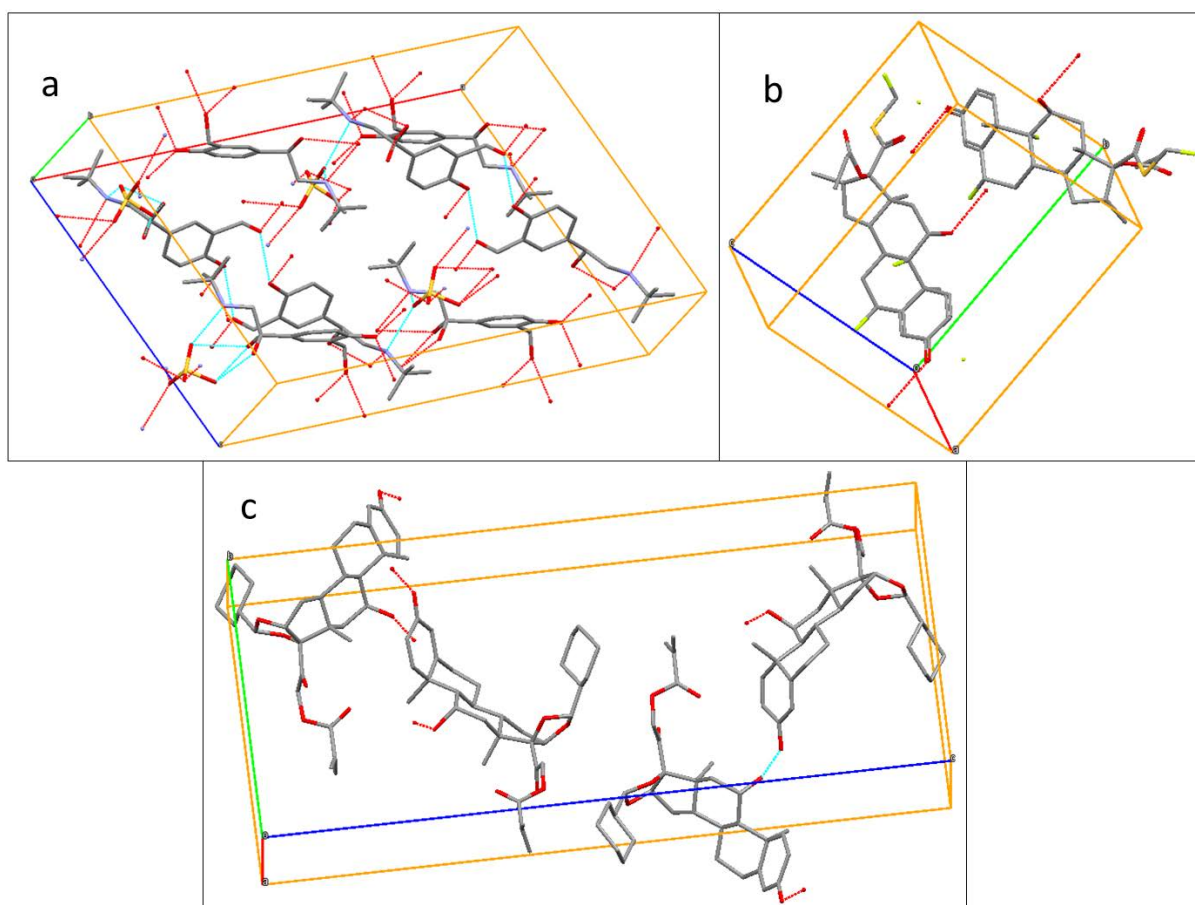


Figure 26 Model unit cells of salbutamol sulfate (a), fluticasone propionate (b), and ciclesonide (c). Salmeterol xinafoate's unit cell was not available at time of writing. Hydrogen bonding within the unit cell is illustrated with a cyan line, while hydrogen bonding external to the unit cell (thus contributing to hygroscopic behaviour) are illustrated with red dotted lines.

The chemical structure of salbutamol sulfate (figure 5a) shows hydrophilic sites across the molecule. The most likely crystal form generated by rapid solvent evaporation in air was first described in 1978 (Leger, et al., 1978), with an 8 molecule unit cell (figure 5a) that shows hydrogen bonding sites on every face. Hygroscopic behaviour is inferred from this structure and has been demonstrated in previous experiments at room temperature (Tong, et al., 2014).

Salmeterol is not found in the Cambridge Structural Database. Solid structures are variously described as either amorphous, or needle-like or plate-like crystals depending on the exact conditions of manufacture (York & Hanna, 1994) (Barjoan & Clotet, 2009). Salmeterol xinafoate is bound together by hydrogen bonding of the  $\delta$ -positive amine group on salmeterol to the  $\delta$ -negative carboxylic acid group on the xinafoic acid. The two groups are expected to cancel their respective charges, leaving few hydrophilic sites open to interaction with water while the particle is in a solid state.

As a steroid, fluticasone is expected to be lipophilic (Lipworth & Jackson, 2000). The structure of fluticasone (figure 5b) does have a number of polar groups. However, the documented crystal structure (Cejka, et al., 2005) describes a plate-like structure with any hydrogen bonding occurring

along the plane of growth (figure 5b) resulting in water interaction only along edges, and likely to result in little or no hygroscopic behaviour.

Ciclesonide (figure 5c) is found as either needle-like (Phull, et al., 2012) or needle-like and spherulitic crystals as well as amorphous solids (Feth, et al., 2007) depending on solvent type and evaporation time. Ciclesonide has multiple polar groups but the model unit cell described by Feth et al describes most of the oxygens arranged inside the crystal with the hydrophobic sites facing outward. Limited hydrogen bonding due to the hydroxyl and ketone groups on adjacent molecules have the potential to attract water molecules to crystal faces, but the hydrophobic nature of the rest of the exposed molecule implies that hygroscopic behaviour is unlikely.

### 3.3 SEM imaging and Trapping Logistics

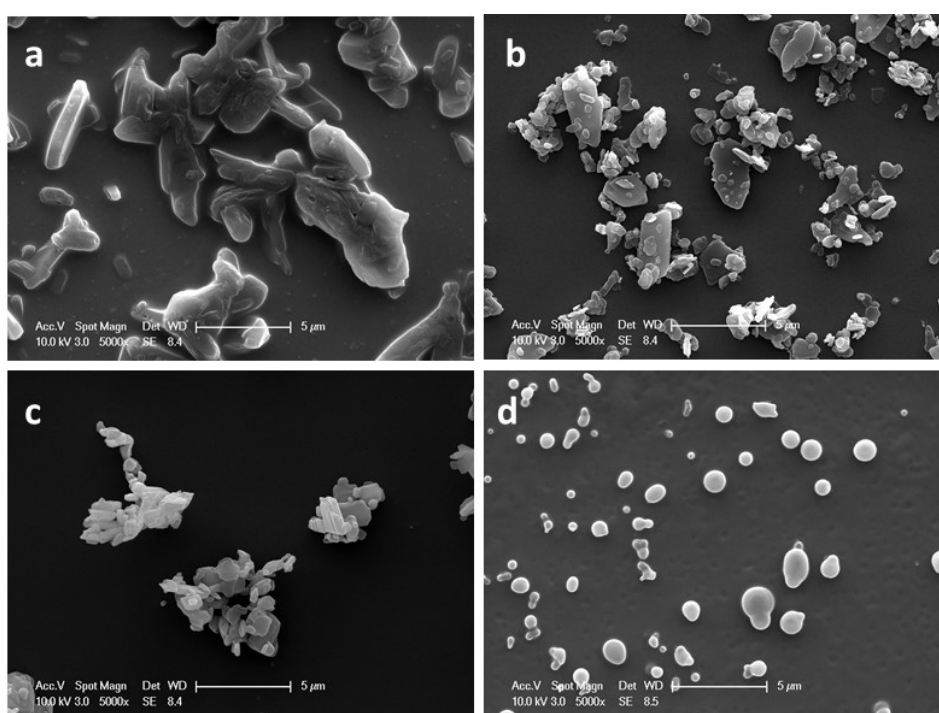


Figure 27 SEM images of: (a) salbutamol sulphate, (b) salmeterol xinafoate, (c) fluticasone propionate & (d) ciclesonide

SEM images of the drug particles were collected under dry conditions in order to determine shape and ease of capture. The likelihood of a particle being successfully caught in the optical trap is dictated by both particle shape and the number of particles generated per release. Salbutamol sulfate had been optically trapped previously on the same apparatus (Tong, et al., 2014). The thick, needle like shape of salbutamol sulfate particles (figure 6a) is well suited to entrapment for reasons detailed in section 2.4, and the 100 µg per release dose of the available inhalers resulted in a successfully suspended particle roughly once for every two releases. Salmeterol xinafoate was significantly harder to trap and retain than the others due to a combination of its low dose (20 µg per release) and flat, platelike aggregate structure (figure 6b). Fluticasone has a similar crystal structure to salmeterol but a much higher dose (250 µg per release) and was more reliably trapped than salbutamol sulfate. Ciclesonide was similar in trapping frequency to fluticasone since its lower dose (160 µg per release) was balanced by a more spherical particle shape (figure 6d).

### 3.4 Raman spectrum changes from hygroscopic properties and additional compounds

Hydrogen bonding with water molecules adjacent to the polar groups of organic molecules expands the range of vibrational energy states that can generate Raman scattering photons. This effect allows water uptake by hygroscopic particles to be monitored by Raman spectroscopy.

All four drugs use hydrofluoroalkane HFA 134a/Norflurane as a propellant. The salbutamol and ciclesonide inhalers also report anhydrous ethanol among their ingredients. Norflurane contains four C-F bonds, each of which generate a distinctive Raman scattering peak at  $1234\text{ cm}^{-1}$ . This peak is not expected to be visible in the Raman spectra of the drug molecules, apart from Fluticasone which has 3 C-F bonds of its own, due to Norflurane's low boiling point ( $-26.5^{\circ}\text{C}$ , (Lide, 1991)) at atmospheric pressure causing all of the propellant to boil off before readings can be collected. The spectra collected from particles other than fluticasone do not show peaks in the C-F stretching region, which implies that all propellant boils off before the particles are scanned.

### 3.5 Salbutamol sulfate / Salamol™

#### 3.5a Raman spectra and structural information

Each salbutamol molecule contains a single phenol group, two aliphatic hydroxyls and a secondary amine. One molecule of salbutamol contains two ionised salbutamol molecules bound to a single sulfate group. The S=O symmetric stretches on the sulfate show a small but distinctive peak at  $1154\text{ cm}^{-1}$ . The largest peaks in the salbutamol spectrum correspond to  $-\text{CH}$  wagging at  $656\text{ cm}^{-1}$ , aromatic ring vibration at  $752\text{ cm}^{-1}$ , C-C-O stretches in relation to the aliphatic hydroxyls at  $784\text{ cm}^{-1}$ , asymmetric hydroxyl stretches at  $969$ ,  $977$  and  $1008\text{ cm}^{-1}$ , phenyl ring vibrations at  $1059$  and  $1074\text{ cm}^{-1}$ , a prominent CH stretch at  $1257\text{ cm}^{-1}$  (this bond can be found in figure 3 just above the ring)  $\text{CH}_2$  and  $\text{CHOH}$  vibrations again from the aliphatic hydroxyls at  $1360\text{ cm}^{-1}$ , a broad ring stretching peak around  $1450\text{ cm}^{-1}$  followed by a  $\text{CH}_2\text{-N}$  amine peak at  $1463\text{ cm}^{-1}$ , and finally a strong peak at  $1615\text{ cm}^{-1}$  corresponding to the phenolic C-OH stretch. All of these peaks (figure 7) correspond well with those found in the literature (Ali, et al., 2009).

### 3.5b Impact of RH and Temperature on salbutamol spectra

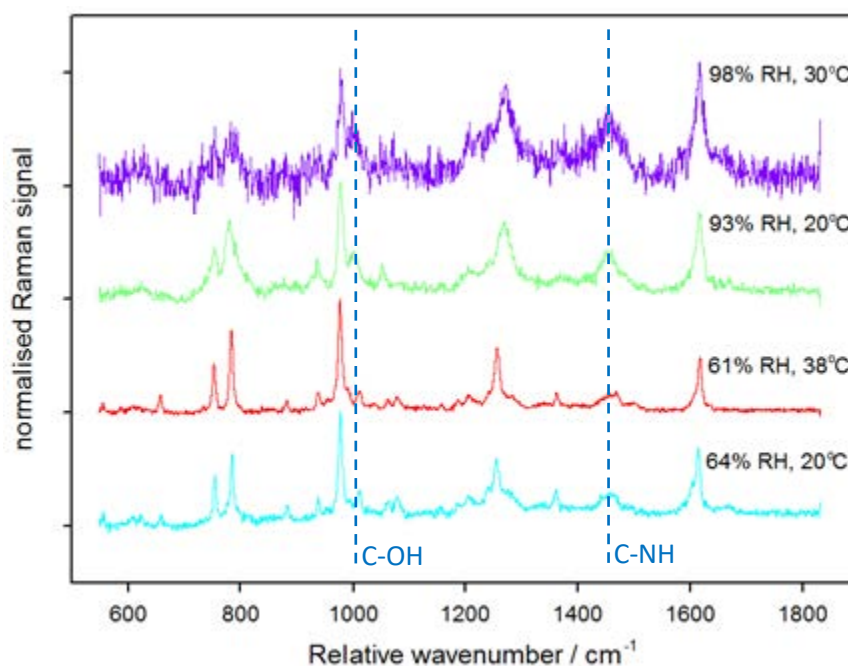


Figure 7 Raman spectra of optically trapped salbutamol sulfate particles at a range of RH and temperatures. Above salbutamol's deliquescence point of 92% RH, peak broadening is visible at the C–OH peak at  $1008\text{cm}^{-1}$  and at the C–NH peak at  $1463\text{cm}^{-1}$ , signifying water interaction with the bonds.

RH above 92%, the deliquescence point identified by Tong et al (Tong, et al., 2014), could not be maintained at physiological temperature ( $37^\circ\text{C}$ ) with the available equipment, so measurements were taken at  $30^\circ\text{C}$ - the highest temperature at which  $>92\%$  RH could be maintained. The particle trapped at 98% RH and  $30^\circ\text{C}$  was small, hence the poorer signal/noise ratio. The contrast between the relatively dry and relatively wet particles is clear to see as the peaks corresponding to hydrophilic bonds in the wet particles are broader, and some peaks such as the hydroxyl peak at  $1008\text{cm}^{-1}$  and the amine peak at  $1463\text{cm}^{-1}$  are more pronounced.

The spectral traces, recorded at similar RH but under contrasting temperatures, are very similar. Within the temperature range investigated ( $20\text{--}38^\circ\text{C}$ ), there are no observable temperature effects upon particle deliquescence. The deliquescence RH is measured to be ca. 92% RH in agreement with the measurement of Tong et al (Tong, et al., 2014). This implies that the temperature gradient experienced in the trajectory from pMDI to lung is likely to be unimportant in determining particle hygroscopicity; RH is the dominant determinant of particle hygroscopicity.

The modelling results from E-AIM suggested that salbutamol sulfate would show significant hygroscopicity if a deliquescence phase transition occurred. The experimental results confirm this model prediction. The presence of a phase transition and significant water uptake is in line with the high reported solubility of salbutamol sulfate ( $14.1\text{g/L}$ , (Walkowsky & He, 2003)).

### 3.6 Salmeterol xinafoate / Serevent™

#### 3.6a Raman spectra and structural information

Salmeterol xinafoate contains several aromatic rings, an ether group, a benzoic acid and a secondary amine. Benzoic acid is distinct from both aromatic rings and carboxylic acids due to the increased conjugation (Kwon, et al., 1994) and shows distinctive peaks in the solid state at  $1627\text{ cm}^{-1}$ ,  $994\text{ cm}^{-1}$  and  $788\text{ cm}^{-1}$ . These peaks are all present in our spectra (figure 8). Ring stretches are clearly visible at  $1580\text{--}1616\text{ cm}^{-1}$ ,  $1400\text{--}1420\text{ cm}^{-1}$  (the multiple strong peaks denoting ring stretches shifted by the various adjacent functional groups) and symmetric ring stretches are visible at  $1000\text{--}1028\text{ cm}^{-1}$ ,  $1215$  and  $1257\text{ cm}^{-1}$ . A strong amine vibration peak is visible at  $1204\text{ cm}^{-1}$ . A sharp peak at  $730\text{ cm}^{-1}$  corresponds to rotational peaks from  $\text{CH}_2$  groups, as would be expected by a molecule with a long aliphatic chain like salmeterol. The ether group can be identified by small peaks at  $554$  and  $1145\text{ cm}^{-1}$ . These spectra correspond well with previously published, well-defined Raman spectra (Ali, et al., 2008a).

Repeated exposure to the Raman laser caused some fluorescence effects in salmeterol xinafoate particles, so each spectrum had to be recorded on a freshly captured particle. The Raman laser was blocked except during the collection of spectra in order to minimise the effect. The fluorescence activity that occurs in salmeterol xinafoate after prolonged exposure to the Raman laser may possibly be avoided in future experiments by using a longer excitation wavelength.

#### 3.5b Impact of RH on salmeterol spectra

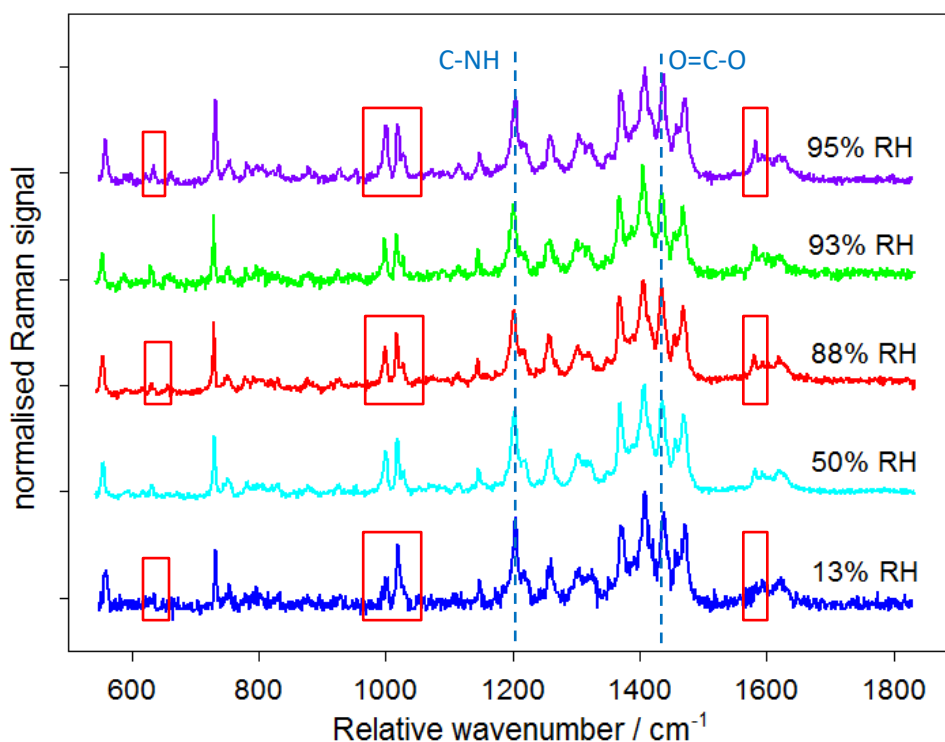


Figure 8 Raman spectra of salmeterol xinafoate at a range of RH values. Even at 95% RH, the amine vibrational peak at  $1204\text{ cm}^{-1}$  and carboxylic acid stretching peak at  $1420\text{ cm}^{-1}$  do not show signs of broadening, contrary to the predicted behaviour modelled by E-AIM. Intensity changes on the aromatic ring stretches at different RH are highlighted in red.

According to the Raman spectra collected in figure 8, salmeterol xinafoate does not demonstrate any visible broadening around peaks corresponding to either salmeterol's amine group or the carboxylic acid group on its xinafoic acid partner upon RH enhancement. This suggests that the salt does not undergo a deliquescent phase transition. The modelling results from E-AIM suggested that salmeterol xinafoate would show significant hygroscopicity if a deliquescence phase transition occurred. The observed lack of deliquescence is in line with the low predicted solubility of salmeterol xinafoate (22.6 mg/L according to ALOGPS (Tetko, 2001)).

The hygroscopic behaviour of salmeterol xinafoate, as predicted by E-AIM, may be limited by the steric hindrance of the hydrophilic sites by hydrophobic structures arranged around them in solid crystals. The relative enhancement of peaks corresponding to aromatic ring stretches at 650, 1000 and 1580  $\text{cm}^{-1}$  imply some interaction with water around some or all of the aromatic rings in salmeterol xinafoate at >88% RH. Most likely, the presence of the hydroxyl and carboxylate groups on the aromatic xinafoate section of the drug enhances water interaction.

### **3.4 Fluticasone propionate / Flixotide**

#### **3.4a Raman spectra and structural information**

Fluticasone contains several distinctive bonding types that would be expected to yield distinctive peaks in any resulting Raman spectra: a phenone, an ester, a thioether and three C-F bonds across the molecule. Fluticasone has been imaged by Raman spectroscopy previously and its spectra interpreted in depth (Ali, et al., 2008b) (Rogueda, et al., 2011) (Theophilus, et al., 2006) (Wang, et al., 2014), which provides useful references for the spectra generated here.

The raw fluticasone propionate spectra contained a very sharp and strong peak at 640 - 650  $\text{cm}^{-1}$ . This peak was not observed in other spectra in the literature. We believe this peak to be an artefact caused by second harmonic resonance effect from the 1064 nm trapping laser. Confirmation of the spectral artefact was achieved by measuring spectra of fluticasone propionate recorded on the cover slip without the trapping laser present. These spectra did not contain the peak. We have removed this artificial peak from the spectra shown in Figure 9.

The strongest peak in the spectrum of fluticasone is the C=O vibration at 1659 $\text{cm}^{-1}$ , followed by the  $-\text{CH}_3$  symmetric stretch (there are 4  $-\text{CH}_3$  groups in Fluticasone) at 1606 $\text{cm}^{-1}$ .  $-\text{CH}_2$  and  $-\text{CH}$  stretches occur at around 1380 and 1330  $\text{cm}^{-1}$  respectively and highly distinctive C-F and S-C-F bands occur at 1234 $\text{cm}^{-1}$  and 1022 $\text{cm}^{-1}$ . Fluticasone is the only compound among the samples that contains a C-F bond, and generated the only spectra showing C-F stretching peaks. This implies that that in all samples the Norflurane propellant had fully evaporated prior to analysis. The phenone group registers as an OOH/CCH aromatic deformation peak at 888 $\text{cm}^{-1}$ . A small C-H wagging peak can be seen at around 700 $\text{cm}^{-1}$ .

### 3.4b Impact of RH on fluticasone spectra

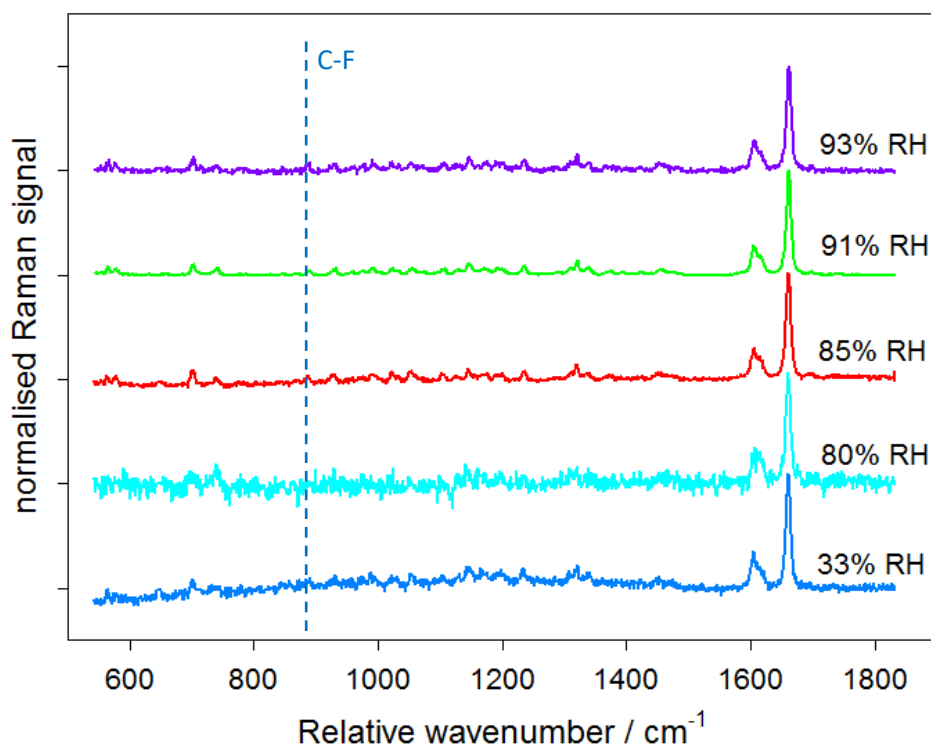


Figure 9 Raman spectra of fluticasone propionate at a range of RH values. The C-F stretching peak at  $888\text{ cm}^{-1}$  is present in this spectrum but not the others, confirming that the Norflurane propellant discussed in section 3.4 has boiled off

The spectrum collected at 80% RH was from a small particle- around  $1\mu\text{m}$  in diameter. This accounts for the greater noise in the signals. Otherwise, no peaks are displaced or strongly deformed by the rise in relative humidity. Fluticasone shows no signs of hygroscopic behaviour, in agreement with the results from E-AIM. Water solubility is low ( $11.4\text{ mg/L}$ ) as predicted by ALOGPS (Tetko, 2001).

### 3.5 Ciclesonide / Alvesco™

#### 3.5a Raman spectra and structural information

Ciclesonide (Feth, et al., 2008) has a diverse selection of functional groups, which generates a complicated Raman spectrum. The largest peak at  $1654\text{cm}^{-1}$  (figure 10) represents the stretching vibration of an  $\alpha$ ,  $\beta$ -unsaturated carbonyl, while the adjacent peak at  $1601\text{cm}^{-1}$  shows the neighbouring C=C bond. Ciclesonide contains four  $-\text{CH}_3$  groups and this corresponds to another large, broad peak at  $1443\text{cm}^{-1}$ . The three ether bonds generate another large peak at  $1112\text{cm}^{-1}$ , and the single ester linkage appears at  $1242\text{cm}^{-1}$ . Ciclesonide has a single hydroxyl group attached to a six-membered saturated ring, and a matching “cyclic alcohol” stretch appears at  $1029\text{cm}^{-1}$ . The C-C stretches of the two saturated six-membered rings are found at  $963\text{cm}^{-1}$ . Multiple small peaks around  $800\text{-}900\text{cm}^{-1}$  represent ring deformation in the phenol group adjacent to the saturated rings. Another region of small peaks around  $1330\text{cm}^{-1}$  corresponds to the various symmetric and antisymmetric stretches of the isopropyl group.

### 3.5b Impact of RH and Temperature on Ciclesonide Spectra

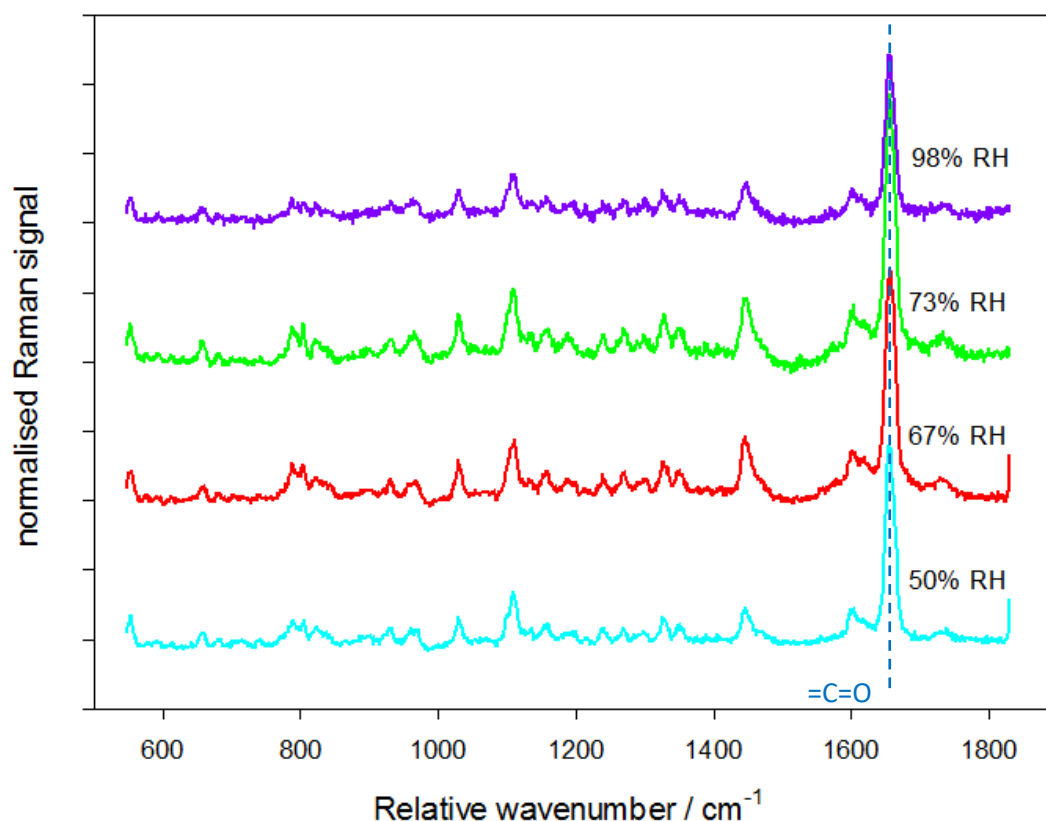


Figure 10 Raman spectra of ciclesonide at a range of RH values. The spectra show no signs of hygroscopic behaviour at up to 98% RH.

As a steroid, ciclesonide is not very hydrophilic and does not contain many polar groups. The crystal structure shows very little opportunity for water uptake on surfaces, and E-AIM predicts that ciclesonide has the lowest hygroscopic potential of any of the drugs analysed. Calculated water solubility is also the lowest of all the drugs (1.57mg/L, (Tetko, 2001)). It would not be expected to show hygroscopic behaviour, and no such behaviour was observed in the Raman spectra compiled in figure 10.

### 3.6 Specific advantages and limitations of procedure to drug delivery

The advantages of this setup and analytical technique to the examination of inhalable drugs do merit some discussion in addition to the general benefits of optical trapping over cover slip analysis documented in section 2.1. The current setup can monitor particle size with an external camera as well as directly monitoring water interactions with hydrophilic functional groups on particles by examining the Raman spectrum. On-board RH monitoring can determine deliquescence points for new drugs, or verify those of existing drugs, to a high degree of accuracy, factoring in the crystal structures of particles as well as their chemical structure in a manner that is difficult to reproduce with software modelling alone.

The main limitation of the technique is the length of time required to collect each Raman spectrum. Since deliquescence occurs faster than the thirty seconds required for the 514nm setup to generate a useful spectrum from a 2  $\mu\text{m}$  particle, the event cannot be monitored in real time with the existing

apparatus. Also, photosensitive compounds like salmeterol xinafoate have to be regularly replaced due to photodegradation of particle surfaces which negates the advantage of being able to observe a specific particle before and after deliquescence. This issue may be avoided by employing a longer wavelength of Raman laser, although this will require either a much more intense source or a longer exposure time to produce viable spectra.

## 4. Conclusions

This series of experiments has demonstrated a viable technique for examining individual particles of inhalable drugs supplied by pMDIs. With little modification, such as by attaching a vacuum pump to the outlet port of the sample chamber, this experimental setup may also be used to examine single particles from DPI devices.

The Raman spectra of four optically trapped drug particles (salbutamol sulfate, salmeterol xinafoate, fluticasone propionate and ciclesonide) were measured within a model lung. The model lung allowed for modification of local RH to test the drugs for hygroscopic behaviour, while the optical trap eliminated any surface effects from water droplets forming around a solid particle on a cover slip. Raman spectroscopy allowed for the direct observation of the hydrogen bonding with water in hydrophilic groups, where the broadening of peaks indicates hygroscopicity.

Spectral peak broadening was observed in salbutamol sulfate particles above their deliquescence point at 92% RH, at room temperature and more physiologically relevant temperatures, while spectra remained similar to dry particles at lower RH regardless of temperature within the observed range. Salmeterol xinafoate shows some spectral changes to the intensities of the peaks corresponding to its aromatic rings, but does not show any changes to the more hydrophilic functional groups which is interpreted as no deliquescence at RH up to 95%. Fluticasone propionate and ciclesonide show no hygroscopic properties at all, as would be expected with their lipophilic composition, low water solubility and the modelled particle growth factors generated using the E-AIM model.

## Acknowledgements

MKK is thankful to the EPSRC for the Career Acceleration Fellowship (EP/I003983/1). ND thanks

NERC for a personal studentship. MK was supported by ERC grant 279405. We are thankful to the

CLF RAL for a programmed access grant LSF1207 (FLIMOLA).

## Works Cited

Ali, Edwards, Kendrick & Scowen, 2008b. Vibrational spectroscopic study of fluticasone propionate. *Biomolecular Spectroscopy*, pp. 244-247.

Ali, Edwards, Kendrick & Scowen, 2009. Vibrational spectroscopic study of salbutamol hemisulphate. *Drug Testing and Analysis*, pp. 51-56.

- Ali, et al., 2008a. Vibrational spectroscopic characterisation of salmeterol xinafoate polymorphs and a preliminary investigation of their transformation using simultaneous in situ portable Raman spectroscopy and differential scanning calorimetry. *Analytica Chimica Acta*, pp. 103-112.
- Ashkin, 1992. Forces of a single-beam gradient laser trap on a dielectric sphere in the ray optics regime. *Biophysical Journal*, pp. 569-582.
- Barjoan & Clotet, 2009. Spain, Patent No. EP2127641A1.
- Bell & Newman, 2007. The rejuvenated pressurised metered dose inhaler. *Expert Opinion on Drug Delivery*, pp. 215-234.
- Bikiaris, 2011. Solid dispersions, Part I: recent evolutions and future opportunities in manufacturing methods for dissolution rate enhancement of poorly water-soluble drugs. *Expert Opinion on Drug Delivery*, pp. 1501-1519.
- Bloxham, Eicher-Lorka, J. & Niaura, 2002. The C-S bond in ethylthiols: a study of the characteristic Raman vibrational Spectral Band. *Chemija*, 13(4), pp. 190-193.
- Brain, Kreyling & Godleski, 2014. Inhalation Toxicology. In: Wallace & Kruger, eds. *Hayes' Principles and Methods of Toxicology, Sixth Edition*. Boca Raton, FL: CRC Press, pp. 1402-1414.
- Brodoy & Georgopoulos, 2001. Growth and Deposition of Hygroscopic Particulate Matter in the Human Lungs. *Aerosol Science and Technology*, p. 144-159.
- Bur, Huwer, Muys & Lehr, 2010. Drug Transport Across Pulmonary Epithelial Cell Monolayers: Effects of Particle Size, Apical Liquid Volume, and Deposition Technique. *Journal of Aerosol Medicine and Pulmonary Drug Delivery*, 3(23), pp. 119-127.
- Calverley, et al., 2003. Combined salmeterol and fluticasone in the treatment of chronic obstructive pulmonary disease: a randomised controlled trial. *The Lancet*, pp. 449-456.
- CCDC, 2015. *WebCSD v1.1.1*. [Online]  
Available at: <http://webcsd.cds.rsc.org/index.php>  
[Accessed 10 11 2015].
- Cejka, Kratochvil & Jegorov, 2005. Crystal Structure of Fluticasone Propionate, C<sub>25</sub>H<sub>31</sub>F<sub>3</sub>O<sub>5</sub>S. *Zeitschrift für Kristallographie - New Crystal Structures*, pp. 143-144.
- Chapman, et al., 1999. Salmeterol and fluticasone propionate (50/250 microg) administered via combination Diskus inhaler: as effective as when given via separate Diskus inhalers.. *Canadian Respiratory Journal: Journal of the Canadian Thoracic Society*, pp. 45-51.
- Clark, 1994. Medical Aerosol Inhalers: Past, Present, and Future. *Aerosol Science & Technology*, pp. 374-391.
- Clegg & Brimblecombe, 1998. A thermodynamic model of the system H<sup>+</sup> - NH<sub>4</sub><sup>+</sup> - Na<sup>+</sup> - SO<sub>4</sub><sup>2-</sup> - NO<sub>3</sub><sup>-</sup> - Cl<sup>-</sup> - H<sub>2</sub>O at 298.15 K. *The Journal of Physical Chemistry*, 12(102), pp. 2155 - 2171.

Clegg, Seinfeld & Brimblecombe, 2001. Thermodynamic modelling of aqueous aerosols containing electrolytes and dissolved organic compounds. *Journal of Aerosol Science*, Issue 32, pp. 713-738.

Coates, 2000. Interpretation of Infrared Spectra, A Practical Approach. In: *Encyclopedia of Analytical Chemistry*. Chichester: John Wiley & Sons Ltd, pp. 10815-10837.

Cripps, Riebe, Schulze & Woodhouse, 2000. Pharmaceutical transition to non-CFC pressurized metered dose inhalers. *Respiratory Medicine*, 94(2), pp. S3-S9.

Crosland, Johnson & Matida, 2009. Characterization of the spray velocities from a pressurized metered-dose inhaler. *Journal of Aerosol Medicine and Pulmonary Drug Delivery*, pp. 85-97.

Delgado, Chou, Silver & Crain, 2003. Nebulizers vs metered-dose inhalers with spacers for bronchodilator therapy to treat wheezing in children aged 2 to 24 months in a pediatric emergency department.. *Archives of Pediatric and Adolescent Medicine*, pp. 76-80.

Dodson, et al., 2011. Photophysical and photochemical properties of the pharmaceutical compound salbutamol in aqueous solutions. *Chemosphere*, pp. 1513-1523.

Dolovich, Ruffin, Roberts & Newhouse, 1981. Optimal delivery of aerosols from metered dose inhalers. *Chest*, 80(6), pp. 911-915.

Engelhart, et al., 2011. Water content of aged aerosol. *Atmospheric Chemistry & Physics*, Issue 11, pp. 911-920.

Eom, et al., 2014. Influence of collecting substrates on the characterization of hygroscopic properties of inorganic aerosol particles.. *Analytical Chemistry*, 4(86), pp. 2648-2656.

Ferron, 1977. The size of soluble aerosol particles as a function of the humidity of the air. Application to the human respiratory tract. *Journal of Aerosol Science*, Volume 8, pp. 251-277.

Feth, et al., 2008. USA, Patent No. US20100120737 A1.

Feth, et al., 2007. Physicochemical, Crystallographic, Thermal, and Spectroscopic Behavior of Crystalline and X-ray Amorphous Ciclesonide. *Pharmaceutics, Preformulation and Drug Delivery*, pp. 3765-3780.

Haddrell, et al., 2014. Dynamics of aerosol size during inhalation: Hygroscopic growth of commercial nebulizer formulations. *International Journal of Pharmaceutics*, pp. 50-61.

Harding, 1990. The human pharmacology of fluticasone propionate. *Respiratory Medicine*, pp. 25-29.

Hardy & Chadwick, 2000. Sustained Release Drug Delivery to the Lungs. *Clinical Pharmacokinetics*, pp. 1-4.

Hargreaves, et al., 2010. Measurements of the Equilibrium Size of Supersaturated Aqueous Sodium Chloride Droplets at Low Relative Humidity Using Aerosol Optical Tweezers and an Electrodynamic Balance. *The Journal of Physical Chemistry*, pp. 1806-1815.

- Hirschfeld & Chase, 1986. FT-Raman Spectroscopy: Development and Justification. *Applied Spectroscopy*, 08 January, pp. 133-137.
- Huang, et al., 2003. Near-infrared Raman spectroscopy for optical diagnosis of lung cancer. *International Journal of Cancer*, pp. 1047-1052.
- Hung, Chu, Wang & Yang, 1999. Hypoalkaemia and salbutamol therapy in asthma. *Pediatric Pulmonology*, pp. 27-31.
- Hunt, Ward & King, 2013. Laser heating of sulfuric acid droplets held in air by Raman tweezers. *RSC Advances*, pp. 19448-19454.
- Hunt, Ward & King, 2015. Heterogeneous oxidation of nitrite anion by gas phase ozone in an aqueous droplet levitated by laser tweezers (optical trap): is there any evidence for enhanced surface reaction?. *Physical Chemistry Chemical Physics*, pp. 2734-2741.
- Ibrahim, Verma & Garcia-Contreras, 2015. Inhalation drug delivery devices: technology update. *Medical Devices (Auckland)*, Volume 8, pp. 131-139.
- Icha, 2007. Ventolin remains a breath of fresh air for asthma sufferers, after 40 years. *The Pharmaceutical Journal*, p. 404.
- ICRP, 1994. *Ann. ICRP 24 (1-3) publication 66: Human Respiratory Tract Model for Radiological Protection*, s.l.: Elsevier Health Sciences.
- Janson, et al., 2016. Difference in resistance to humidity between commonly used dry powder inhalers: an in vitro study. *npj Primary Care Respiratory Medicine*, Issue 23, p. 16053.
- Jones, King & Ward, 2015. Atmospherically relevant core-shell aerosol studied using optical trapping and Mie scattering. *Chemical Communications*, pp. 4914-4917.
- Kwon, et al., 1994. Vibrational Spectroscopic Investigation of Benzoic Acid Adsorbed on Silver. *Journal of Physical Chemistry*, pp. 8481-8487.
- Labiris & Dolovich, 2003. Pulmonary drug delivery. Part I: Physiological factors affecting therapeutic effectiveness of aerosolized medications. *Journal of Clinical Pharmacology*, p. 588-599.
- Lavorini, et al., 2011. Retail sales of inhalation devices in European countries: So much for a global policy. *Respiratory Medicine*, pp. 1099-1103.
- Lawrence, 2005. The relationship between relative humidity and the dew point temperature in moist air: A simple conversion and applications. *Bulletin of the American Meteorological Society*, pp. 225-233.
- Leach, 2005. The CFC to HFA Transition and Its Impact on Pulmonary Drug Development. *Respiratory Care*, 50(9), pp. 1201-1208.
- Lee, et al., 2012. The Efficacy of Immediate Diet for Reducing Local Adverse Events of Inhaled Corticosteroid: A Pilot Study. *Tuberculosis and Respiratory Diseases*, pp. 93-99.

Leger, Goursolle & Gadret, 1978. Structure Cristalline du Sulfate de Salbutamol [tert-Butylamino-2 (Hydroxy-4 hydromethyl-3 phenyl)-1 Ethanol.1/2H<sub>2</sub>SO<sub>4</sub>]. *Acta Crystallographica Section B*, pp. 1203-1208.

Lide, 1991. *CRC Handbook of Chemistry and Physics*. Boca Raton, FL: CRC Press.

Ling & Chan, 2008. Partial crystallization and deliquescence of particles containing ammonium sulfate and dicarboxylic acids. *Journal of Geophysical Research*, 113(14), pp. 1-15.

Lipasek, et al., 2013. Effect of Temperature on the Deliquescence Properties of Food Ingredients and Blends. *Journal of Agricultural and Food Chemistry*, pp. 9241-9250.

Lipworth & Jackson, 2000. Safety of Inhaled & Intranasal Corticosteroids Lessons for the New Millennium. *Drug Safety*, 1(23), pp. 11-33.

Macrae, et al., 2006. Mercury: visualization and analysis of crystal structures. *Journal of Applied Crystallography*, Volume 39, pp. 453-457.

Mansour, et al., 2016. 11.4 Particle deposition in the airways. In: Hillary & Park, eds. *Drug Delivery: Fundamentals and Applications, Second Edition*. Boca Raton, FL: CRC Press.

Mutch, et al., 2007. The role of esterases in the metabolism of ciclesonide to desisobutyryl-ciclesonide in human tissue. *Biochemical Pharmacology*, pp. 1657-1664.

Nave, 2004. *Saturated Vapor Pressure, Density for Water*. [Online]  
Available at: <http://hyperphysics.phy-astr.gsu.edu/HBASE/Kinetic/watvap.html#c1>  
[Accessed 6th August 2014].

Newman, N., 1996. Effect of add-on devices for aerosol drug delivery: Deposition studies and clinical aspects. *Journal of Aerosol Medicine: Deposition, clearance and effects in the lung*, 9(1), pp. 55-70.

Newman, et al., 1981. Deposition of pressurised aerosols in the human respiratory tract. *Thorax*, Volume 36, pp. 52-55.

Pandya, Berawala, Khatri & Mehta, 2010. Spectrofluorimetric estimation of salbutamol sulphate in different dosage forms by formation of inclusion complex with  $\beta$ -cyclodextrin. *Pharmaceutical Methods*, pp. 49-53.

PerkinElmer Inc, 2008. *Advantages of Raman Spectroscopy when Analysing Materials through Glass or Polymer Containers and in Aqueous Solution*. [Online]  
Available at:  
[http://www.perkinelmer.co.uk/CMSResources/Images/APP\\_RamanAnalysisThrougGlassPolymerAqueous.pdf](http://www.perkinelmer.co.uk/CMSResources/Images/APP_RamanAnalysisThrougGlassPolymerAqueous.pdf)  
[Accessed 07 August 2014].

Phull, Rao & Kankan, 2012. United States of America, Patent No. US 8158780 B2.

Purewal & Grant, 1997. *Metered Dose Inhaler Technology (Illustrated ed.)*. s.l.:Informa Health Care.

Reisine, Heisler, Hook & Axelrod, 1983. Activation of beta 2-adrenergic receptors on mouse anterior pituitary tumor cells increases cyclic adenosine 3':5'-monophosphate synthesis and adrenocorticotropin release. *The Journal of Neuroscience*, pp. 725-732.

Renner, Mueller & Shephard, 2012. Environmental and non-infectious factors in the aetiology of pharyngitis (sore throat). *Inflammation Research*, pp. 1041-1052.

Rkiouak, et al., 2014. Optical trapping and Raman spectroscopy of solid particles. *Physical Chemistry Chemical Physics*, pp. 11426-11434.

Rogueda, et al., 2011. Particle synergy and aerosol performance in non-aqueous liquid of two combinations metered dose inhalation formulations: An AFM and Raman investigation. *Journal of Colloid and Interface Science*, pp. 649-655.

Sanders, 2007. Inhalation therapy: an historical review. *Primary Care Respiratory Journal*, pp. 71-81.

Sauer, Hofkens & Enderlein, 2011. *Handbook of Fluorescence Spectroscopy and Imaging*. Weinheim: WILEY-VCH Verlag GmbH.

Stein, M., 2006. The Relative Influence of Atomization and Evaporation on Metered Dose Inhaler Drug Delivery Efficiency. *Aerosol Science and Technology*, Issue 40, pp. 335-347.

Tang, et al., 2014. Heterogeneous interaction of SiO<sub>2</sub> with N<sub>2</sub>O<sub>5</sub>: single particle optical levitation-Raman spectroscopy and aerosol flow tube studies. *The Journal of Physical Chemistry*, pp. 8817-8827.

Tetko, 2001. *ALOGPS*. [Online]  
Available at: <http://www.vcclab.org/lab/alogps/>  
[Accessed 21 10 2016].

Theophilus, et al., 2006. Co-deposition of salmeterol and fluticasone propionate by a combination inhaler. *International Journal of Pharmaceuticals*, pp. 14-22.

Tong, et al., 2014. Rapid interrogation of the physical and chemical characteristics of salbutamol sulphate aerosol from a pressurised metered-dose inhaler (pMDI). *Chemical Communications*, pp. 15499-15502.

Tsuda, Henry & Butler, 2013. Particle transport and deposition: basic physics of particle kinetics. *Comprehensive Physiology*, Volume 4, pp. 1437-1471.

Ullman & Svedmyr, 1988. Salmeterol, a new long acting inhaled beta 2 adrenoceptor agonist: comparison with salbutamol in adult asthmatic patients. *Thorax*, pp. 674-678.

UNEP, 1987. *The Montreal Protocol on substances that deplete the ozone layer.*, Nairobi: UNEP.

Vankeirsbilck, et al., 2002. Applications of Raman spectroscopy in pharmaceutical analysis. *TrAC Trends in Analytical Chemistry*, pp. 869-877.

Walkowsky & He, 2003. *Handbook of aqueous solubility data*. 1st ed. Boca Raton, FL: CRC Press.

Wang, et al., 2014. Low-frequency shift dispersive Raman spectroscopy for the analysis of respirable dosage forms. *International Journal of Pharmaceutics*, Issue 469, pp. 197-205.

Wittig, Lohmann & Gmehling, 2003. Vapor–Liquid Equilibria by UNIFAC Group Contribution. 6. Revision and Extension. *Industrial & Engineering Chemical Research*, 42(1), pp. 183 - 188.

Woolcock, Lundback, Ringdal & Jacques, 1996. Comparison of addition of salmeterol to inhaled steroids with doubling of the dose of inhaled steroids.. *American Journal of Respiratory and Critical Care Medicine*, pp. 1481-1488.

York & Hanna, 1994. United States of America, Patent No. US5795594 A.

Zhejiang NetSun Co., Ltd., 2010. *ChemNet.com - Global Chemical Network*. [Online]  
Available at: <http://www.chemnet.com/cas/>  
[Accessed 21 09 2015].